SHAPE MEMORY POLYMER COMPOSITE FOR ADAPTIVE COMPONENTS FOR ORTHOSIS AND LOWER LIMB FRACTURE FIXATORS

A Thesis submitted by

Lama Hewage Janitha Jeewantha

BSc Eng. (Hons), PG Diploma

For the award of

Doctor of Philosophy

2023

ABSTRACT

Rapidly increasing engineering innovations have contributed invaluable new technologies to the biomedical field since the mid-20th century. This thesis is devoted to another vital development in the biomedical field with the invention of shape memory polymer (SMP) orthosis and lower limb fracture fixators. SMP is a smart material that can deform temporarily and recover its permanent shapes upon an external stimulus. This innovative product is an alternative to plaster of Paris casting which has been dominant in orthopaedic external fracture treatments. Bisphenol A base SMP was synthesised, and glass transition temperature was tailored to suit non-invasive biomedical applications. The manufacturing parameters of the product were optimised for the needs of orthopaedic bone immobilisation, using grey relational combined Taguchi analysis. The novel material is denoted as Ortho$^+$, and it contains one layer of E-glass fibre with 0.4 wt% of TiO_2. The concept was successfully proved with, a lower limb leg cylindrical cast using Ortho$^+$ on a mannequin in less than 10 mins. The Ortho$^+$ SP is lightweight, has less setting time, allows multiple alterations and optimal air circulation. Ortho$^+$ can be reused after disinfection; thus, it is ideal for first aid treatment where the required medical facilities are not freely available. This research has successfully established ground-breaking knowledge in the material development framework and opened up a new window to replace traditional orthopaedic materials with Ortho$^+$ to manufacture next-generation orthosis and fracture fixators.

CERTIFICATION OF THESIS

I, Lama Hewage Janitha Jeewantha, declare that the PhD Thesis entitled Shape memory polymer composite for adaptive components for orthosis and lower limb fracture fixators is not more than 100,000 words in length including quotes and exclusive of tables, figures, appendices, bibliography, references, and footnotes. The thesis contains no material that has been submitted previously, in whole or in part, for the award of any other academic degree or diploma. Except where otherwise indicated, this thesis is my own work.

Date: 16 January 2023

Endorsed by:

Associate Professor Jayantha Ananda Epaarachchi

Principal Supervisor

Associate Professor Mainul Islam

Associate Supervisor

Student and supervisors' signatures of endorsement are held at the University.

ACKNOWLEDGEMENTS

comments, encouragement, and the directions they provided me to conduct this research in a meaning full manner.

I owe a debt of gratitude to my primary, secondary, and tertiary teachers for encouraging me to pursue a challenging careers as a research

This dissertation is dedicated to my Father,

for love, sacrifice, and inspiration…

TABLE OF CONTENTS

LIST OF TABLES

LIST OF FIGURES

ABBREVIATIONS

ABS	Acrylonitrile-butadiene-styrene
ACPCL	(α-allyl carboxylate-ε-caprolactone)
ADP	Areal damage percentage
B	Billion
CFRSMPC	Carbon fibre reinforced shape memory polymer composite
DDH	Dysplasia of the hip
DEA	Dielectric analysis
DGEBA	Bisphenol A diglycidyl ether
DMA	Dynamic mechanical analysis
DOFN	Distributed optical fibre network
DSC	Differential scanning calorimetry
ECG	Electrocardiography
ED	Emergency department
EVA	Poly[ethylene- ran-(vinyl acetate)]
FDA	Food and drug administration
FEA	Finite element analysis
FLIR	Forward-looking infrared
FRSMPC	Fibre reinforced shape memory polymer composite
FTIR	Fourier transform infrared spectroscopy
GFRSMPC	Glass fibre reinforced shape memory polymer composite
GRA	Grey relational analysis
GRG	Grey relational grade

HBMSC	Human bone marrow mesenchymal stem cells
HDI	Hexamethylene diisocyanate
HPED	N,N,N'-tetrakis(2-hydroxypropyl)ethylenediamine
HPU	Hyperbranched polyurethane
LM	Loss modulus
M	Million
MBA	Butyl methacrylate
MDI	Methylene diphenyl diisocyanate
MMA	Methyl methacrylate
MWCNT	Multi-walled carbon nanotubes
NGDE	Neopentyl glycol diglycidyl ether
NIR	Near infraRed
NPs	Nanoparticles
NRSMPC	Nanoparticle reinforced shape memory polymer composite
OA	Oleic acid
OBR	Optical backscatter reflectometer
PBS	Phosphate buffered saline
PCL	Poly(ε-caprolactone)
PCHMA	Poly(cyclohexyl methacrylate
PCLA	Poly(d,l-lactide-co-ε-caprolactone)
PDLLA	Poly(D,L-lactic acid)
PDMS	Polydimethylsiloxane
PEEK	Polyether ether ketone

PEG	Polyethylene glycol
PGLA	Poly glycolic acid
PGMA	Poly(glycidyl methacrylate)
PHBV	Poly[(R)-hydroxybutyrate-co-(R)-3-hydroxyvalerate]
PLA	Poly-DL-lactide
PLGA	Poly glycolic acid
PLLA	Poly-l-lactic acid
POP	Plaster of Parise
PPC	Poly(propylene carbonate)
PTMEG	Polytetramethylene ether glycol
PU	Polyurethane
R & D	Research and development
R_f	Shape fixity ratio
$R_{f,30}$	Shape retention ratio (Shape fixity after 30 days)
R_r	Shape recovery ratio
RST	Minimum recovery start temperature
$\dot{R}_r$	Shape recovery rate
SEM	Scanning electron microscope
S/N ratio	Signal to noise ratio
SM	Storage modulus
SMA	Shape memory alloy
SME	Shape memory effect
SMP	Shape memory polymer

SMPC	Shape memory polymer composite
SP	Smart plaster
TEA	Triethanolamine
TEGDMA	Tetraethylene glycol dimethacrylate
TETA	Triethylenetetramine
T_g	Storage onset glass transition temperature
$\dot{T}_g$	Minimum of storage derivative transition temperature
TGA	Thermogravimetric analysis
TPU	Thermoplastic polyurethane
TTS	Time temperature superposition
UMAT	User-defined material subroutine
USQ-SMRTA	University of Southern Queensalnd - smart material research team Australia
UV	Ultraviolet
WHO	World Health Organisation
WLF	William-Landel-Ferry
wt%	Weight fraction

CHAPTER 1: INTRODUCTION

1.1   Background

The function of bone is to support and facilitate movements and protect the body's internal organs [1]. A fracture is a break or a crack in bone, mainly due to high impact force or stress. The common fracture types are illustrated in Figure 1.1. The majority of fractures are non-fatal but need immediate medical attention, including essential procedures to reduce mortality and disability [2].

Bone healing is a natural process. It requires time, from weeks to several months, and appropriate treatment would give optimum conditions for the bone to heal by itself [3, 4]. Orthosis plays an important role in fracture recovery by correctly lining up weak or deformed body parts, restricting or eliminating motion, increasing muscle activity, and providing continuous support to regain a full range of motion [5]. The fracture treatments may include plasters, splints, braces, traction, and surgically inserted metal rods or plates to hold the bone pieces together [6]. Among these, casting is the most popular treatment technique [7].

Usually, casts are made from plaster of Paris (POP) and moulded from rolls composed of a settable filler. POP plasters are uncomfortable, cumbersome, heavy, and bulky. They have a low strength-to-weight ratio, take a long time to set (24-72 hrs.), disintegrate in water, decrease X-ray transparency, and micro-organisms growing between the skin and the cast

may cause a series of problems [8, 9]. A skilful certified technician should make the POP cast since the process's success depends heavily on technical competence and experience [7]. However, until now, POP has been the most effective, efficient, and popular method to treat bone fractures [10].

Crushed; common in porous bones (older people)

Ends forced into each other; w/ outstretched arms

Incomplete like a green twig; common in children

Comminuted

Depressed

Spiral

Compression

Impacted

Greenstick

Many fragments; common in older brittle bones

Pressed inward; typical on skull

Ragged break due to twisting force; common in sports
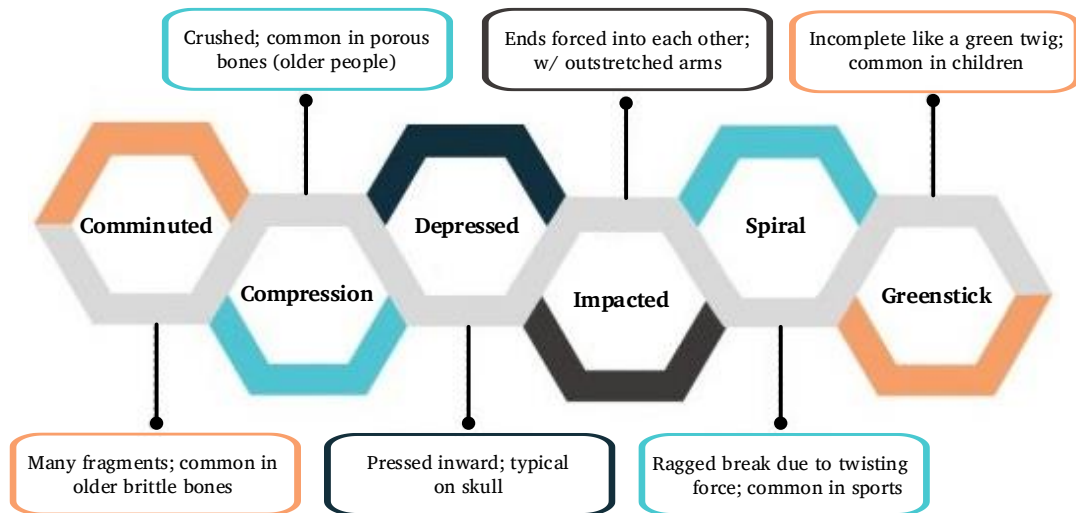
Figure 1.1: Common fracture types

Fibreglass casts are preferred if the bones are not out of position or if the healing process has already started. They are lighter in weight, longer wearing, easy to dress, available in different colours and need less maintenance. In several clinical studies, researchers have reported fibreglass casts being difficult to mould and have observed that they provoke asthmatic reactions [11]. On the other hand, undercast pressure creates compartment syndrome and limits blood flow to arteries and muscles during swelling [12]. Therefore, as cell damage may occur sooner when temperature and pressure

are coupled, this can lead to ulcers, nerve damage, or indeed the permanent loss of body parts [13].

Figure 1.2: (a) Plaster of Paris, (b) Fibreglass and (c) Wood composite, lower limb leg cylindrical cast

None of the bone immobilisation options are free from risk, but the latest developments can safely manage orthopaedic pathologies. With the recent advancement in materials and other innovations in the current century, researchers are in the race to synthesise functional materials for human benefit. In this research, the author introduces Bisphenol A based shape memory polymer (SMP), a smart material, to evade the negative experiences brought about by POP and fibreglass orthopaedic materials.

SMPs are smart materials that can be deformed into a temporary shape, be fixed, and then regain their original shape in response to an external stimulus [14-17]. This phenomenon is called the shape memory effect (SME).

3

It can be classified into one-way, two-way, and multiple SME [18]. The SME can be induced either physically (through temperature, UV light, electrical, magnetic and mechanical means) or chemically (through pH, water, solvents and biological agents). Some SMPs can respond to multiple stimuli as well [19-24]. From the molecular point of view, SME is an entropy-driven process explained through net-points and switching segments [25]. The permanent shape governed by the net-points and switching segments is sensitive to an external stimulus, which allows temporal material deformation [26]. The temporary shape is obtained through the switching segments' solidification. This can be achieved through chemical or physical changes.

SMPs generally have weak mechanical properties [27]. Therefore, they are often reinforced with fibres (e.g., carbon, glass and basalt) and fillers (nanoparticles (NPs) and microparticles)) [27-31]. Fillers can also be used to improve shape memory functional properties such as thermal conductivity, electrical conductivity, and photothermal effect [32-34]. SMPs show low density, large recovery strain, tailorable glass transition temperature, manufacturability, biocompatibility, biodegradability, and low cost, compared to other polymers [22, 35-38]. Therefore, SMPs are potential candidates in many engineering applications, including space, aerospace, civil infrastructure, textiles, and biomedical uses, as illustrated in Figure 1.3 [35, 38-42]. Most biomedical SMP applications can be seen in intravascular, vascular, general surgical, urogenital, ophthalmic, and orthodontic fields [17, 22, 26, 43-51]. Besides this, SMPs have already been successfully

experimented with for self-tightening sutures and staples, clot removals, controlled drug release, cardiac valves, stents, and tissue engineering prototypes [47, 52-57]. In 2009, USA based MedShape Inc. obtained a Food and Drug Administration (FDA) clearance for their suture anchor in soft tissue repair orthopaedic surgeries [21, 58].
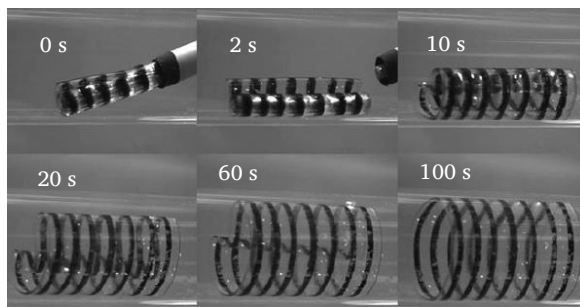
Biomedical: stent [59]
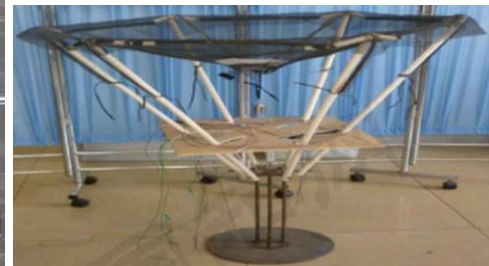
Space: deployable antenna [60]

Space: deployable antenna [61]

Textile: woven fabric [62]
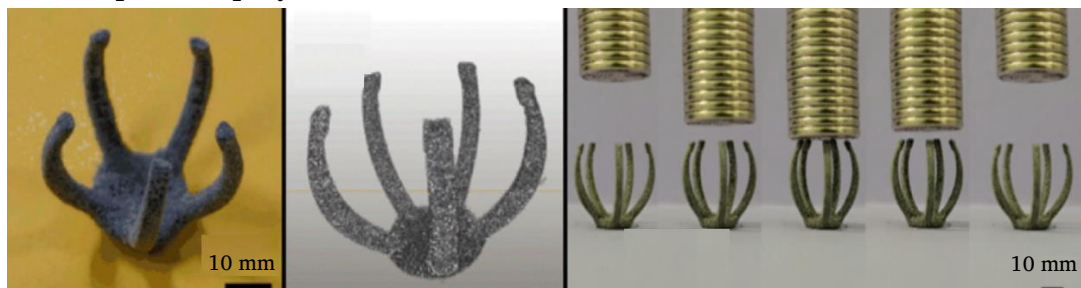
Soft robotics: gripper [63]
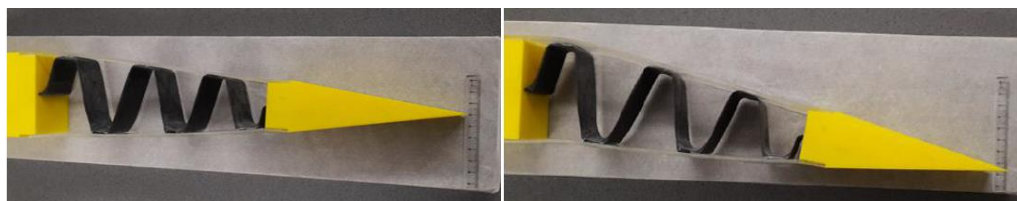
Aerospace: Morphing wing [64]
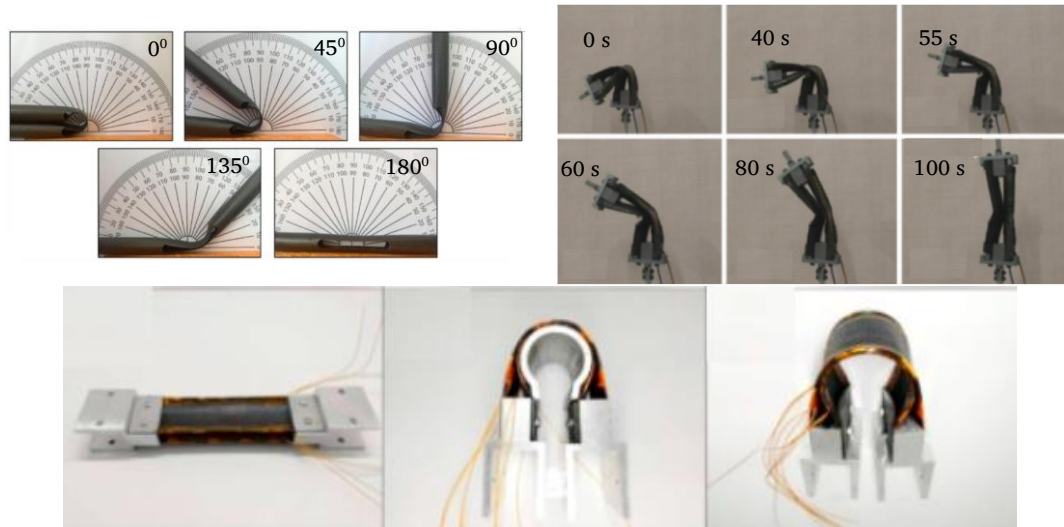
SMP hinges [65-67]

Figure 1.3: SMP applications

Most SMP researchers have confined themselves to a focused on restorative biomedical devices since SME can effectively facilitate the deployment of these devices with minimum invasiveness. Thus, most attention has been paid to invasive biomedical SMP application development to date [68]. In contrast, non-invasive orthopaedic applications demand mechanical and shape memory properties at body temperature, which was difficult to achieve with the recently invented SMPs.

On the other hand, commercial unavailability forced researchers to synthesise SMPs for their own requirements, based on their specific intended applications [69]. Therefore, SMP researchers have spent significant time on SMP synthesis and characterisation rather than on continued applied research with readily available SMPs. The author further noticed that most proposed conceptual SMP designs were not progressively continued until the governing

bodies authorised them. Therefore, it is hard to achieve the general, SMP specific, and other required attributes for the intended applications illustrated in Figure 1.4. Hence there is a significant research gap between the characterised SMP and its use in straightforward applications.
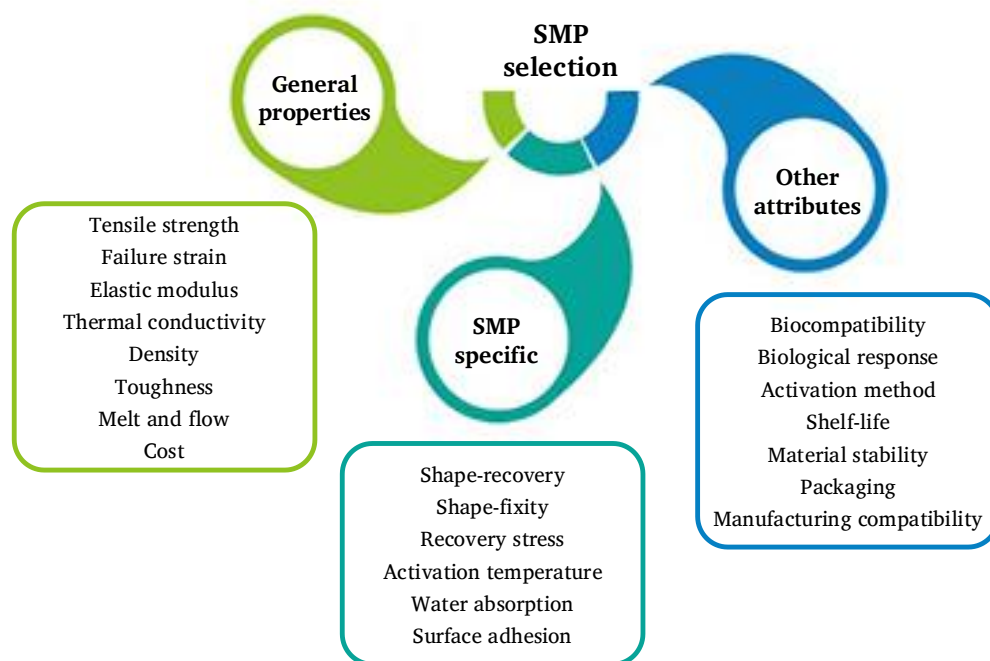
Figure 1.4: SMP material selection matrix for applications

Therefore, the author is highly motivated to introduce a novel Bisphenol A base hybrid shape memory polymer nanocomposite, which can drive next-generation external orthopaedic and biomedical applications. The achievements detailed in this thesis provide a novel solution to fabricate adaptive components and lower limb fracture fixators in the not-too-distant future.

1.2   Research problems

- The human skin comprises lipid membranes and is highly sensitive to temperature. Due to their nature, skin cells are potentially damaged in only several minutes with exposure to different magnitudes of thermal conditions. Williamson et al. presented a time-temperature relationship of 49°C acting over 3 mins. which caused first degree thermal injury [70]. In 1949, Read et al. revealed when human skin is exposed to a temperature of around 45°C for 2-3 hrs., this can cause skin burns [71]. The cell damage occurs sooner when temperature and pressure are combined [13]. Therefore, in SMP-based non-invasive applications, the activation temperature is crucial to avoid thermal burn injuries. During the last four decades, various SMPs have been synthesised for biomedical applications; however, to date, for non-invasive orthopaedic applications, SMP has not been comprehensively investigated.

- SMPs are not freely available for purchase in the commercial market [21, 42]. Therefore, SMP researchers have been obliged to synthesise and characterised them to fulfil their research requirements. The author observed that in this process, researchers generally chose curing cycle parameters for synthesised SMPs based on literature. The importance of selecting a proper curing cycle and its effect on shape memory properties have not been sufficiently addressed to

date by any SMP research group. Therefore, it is worth studying delicate shape memory properties and how they can be enhanced by introducing customised curing and post-curing cycles.

- To date, there has been no prominent research evidence for the use of SMPs for non-invasive biomedical applications due to their inherent weak mechanical properties. Therefore SMPs have often been reinforced with fibres or fillers [72, 73]. Fibres improve SMPs strength, recovery stress, and damping properties more remarkably than fillers [74]. However, low ($<45^{\circ}$C) glass transition temperature (T_g) SMPs mechanical and shape memory properties have not been comprehensively investigated and optimised. Therefore, it is essential to study the synthesised SMPs mechanical properties ((i) tensile, (ii) flexure, (iii) compression, and (iv) impact) and shape memory properties ((i) shape fixity ratio, (ii) shape retention ratio, and (iii) shape recovery ratio) before fabricating non-invasive adaptive orthosis and fracture fixators.

- SMP thermomechanical and shape memory properties depend upon chemical structure as well as fabrication parameters such as reinforcement type, fibre weight fraction (*wt*%), and thickness, among others [75]. The NPs are more influential in SMPs' functional properties such as their chemical, electrical, and thermal properties,

rather than their mechanical properties [76]. Therefore, it is crucial to study how fabrication parameters affect the overall performance of the composite and to optimise multiple variables to a single objective.

- The uniform distribution of NPs improves the base material's characteristics [39]. Among the different techniques for dispersing NPs, ultrasonic irradiation has shown excellent emulsifying and crushing performance [77]. Sonication is important to prevent agglomeration; however, prolonged sonication raises the temperature of the epoxy, causes micro-bubbles and, cavitation, and breaks molecules apart [78, 79]. Consequently, epoxy resin's performance may decline. Therefore, it is vital to research the optimum dispersion time for NPs to achieve anticipated functionalities and performances.

- Numerous modelling techniques have been proposed to describe the complex viscoelastic behaviour of SMPs [80-82]. The modelling approach consists of spring, dashpot, and frictional elements [83]. Finite element analysis (FEA) models are based on stress relaxation, and the parameters are obtained through thermomechanical experimentations [64]. This method does not require user material subroutines (UMAT in ABAQUS). The main advantage of this

approach is to calculate rate-dependent behaviours and the SME of the viscoelastic materials without fabricating physical prototypes. However, most FEA models for SMPs have not been validated since the model is built upon the experimental viscoelastic results. In addition, most SMP-based FEA viscoelastic models have not been validated; therefore, it is worth studying validation techniques to improve the reliability of predictions.

- SMP researchers have consistently focused on improving synthesised SMP's mechanical, thermal, and shape memory properties. However, these efforts have mostly been limited to fundamental material characterisation at room temperature. To perform will in extreme operational environments, the robustness of SMPs' long-term environmental durability is crucial [84, 85]. Thus, it is worth studying SMPs' environmental durability to gain more attention for applied research in the future.

- After 2003, SMP researchers experienced widespread enthusiasm due to breakthrough product innovations such as soft-tissue fasteners and suture-anchor systems [15, 47, 86, 87]. Therefore, research groups and biomedical industries are in the race to develop modern healthcare devices with maturing SMP technologies around the globe. However, the overall rate at which the concept has been

translated into approved products is extremely low [21]. Therefore, it is essential to introduce a new systematic approach and a well-defined framework during SMP research and development.

1.3   Research objectives and significance

The study's aim is to synthesise novel SMP for external orthopaedic applications that can be used to immobilise fractured bones. The synthesised SMP will be thermally activated, and the required thermomechanical and shape memory properties will be engineered to fulfil orthopaedic bone immobilisation requirements. Therefore, this research fills the remaining knowledge gap in SMP synthesis, curing, fabrication, FEA modelling, and *vitro* demonstration.

During the research, the following **main objectives** have been defined to achieve the aims.

1) Review and understand current orthopaedic fractured bone immobilisation methods, their limitation, and the potential of SMPs for non-invasive biomedical applications.

2) Synthesise novel SMP for non-invasive orthopaedic applications.

3) Experimentally evaluate and statistically optimise SMPC fabrication parameters prioritising, the required properties to immobilise fractured bones.

4) Develop and validate the FEA model to predict SMP stress when formed into complex shapes which require unique shape recovery behaviour.

12

5) Demonstrate a lower limb leg cylindrical cast with synthesised novel SMP and prove the concept.

The battles, automobile accidents and natural disasters around the globe cause massive injuries to the human race, among which are bone fracture injuries. The synthesised SMP is ideal for musculoskeletal-related injuries and emergencies in remote places where required first aid treatment is not freely accessible or available. Moreover, the synthesised SMP will offer the best use of custom-made prosthetic devices, formed quickly and at a low cost. Ultimately, synthesised SMP biomedical applications will provide a tremendous scientific return on investment.

1.4   Extended abstract

Rapidly increasing engineering innovations have contributed invaluable new technologies to the biomedical field from the mid-20th century. The global population's well-being has increased due to better healthcare and life expectancy is much longer than our ancestors' just a few generations ago. This thesis is devoted to developing another valuable contribution to the medical field, using innovative shape memory polymer (SMP). SMP is a smart material that can fix deformed temporary shapes and recover their permanent shapes upon an external stimulus such as temperature, light, electricity, water, pH or magnetism.

13

Fall-related injuries and accidents often demand orthopaedic emergency care in hospitals. Early and effective fracture treatment techniques are essential for repairing the patient's musculoskeletal system. Over many decades, plaster of Paris (POP) and fibreglass have been the dominant materials in orthopaedic external fracture treatments. However, they are cumbersome, have extended setting times, and micro-organisms under the cast lead to infections. In addition, internal pressure sores or hotspots can cause severe pain to the patient, leading to ulcers, nerve damage, or even permanent loss of body parts. With the advancement of polymer science during the past few decades, a significant number of bio-compatible polymeric materials are making inroads into the medical field. In particular, SMPs have shown tremendous potential to replace traditional non-invasive orthopaedic materials.

However, these applications demand structural and shape memory properties at body temperature ($\sim 37^{\circ}$C). Therefore, a Bisphenol A based SMP transition temperature was tailored to suit non-invasive orthopaedic applications in this research. The introduced curing cycle enhanced the delicate shape memory recovery properties by 25%. The SMP matrix was reinforced with carbon and glass fibres to improve mechanical properties, according to a robust Taguchi $L_{18(2 \times 3 \times 3)}$ mixed orthogonal array. This was followed by the addition of biocompatible nanoparticles (TiO_2, MWCNT and Graphene) in 0.4, 0.7 and 1.0 wt% according to a Taguchi L_9 array. The newly synthesised materials thermomechanical and physical properties were

14

obtained according to ASTM/ ISO standards. Thenceforth, fabrication parameters were optimised for the needs of orthopaedic bone immobilisation, using grey relational combined Taguchi analysis.

After that, A hybrid shape memory polymer composite was synthesised based on optimum fabrication parameters. The novel material is denoted as Ortho$^+$, and it contains one layer of E-glass fibre with 0.4 $wt\%$ of TiO_2. The Ortho$^+$ showed 74.4 ± 3.9 MPa, 71.3 ± 1.0 MPa, 129.7 ± 0.2 MPa and 0.036 J/mm tensile, compression, flexural, and impact strength at room temperature, respectively. Most importantly, Ortho$^+$ showed a 99.8% shape fixity ratio, 98.4% shape retention ratio, and 90.9% shape recovery ratio at 40°C. To predict Ortho$^+$ behaviour, ABAQUS finite element modelling was conducted and validated by comparing strain readings with a distributed optical fibre embedded firsthand experimental program.

During the proof of concept, a lower limb leg cylindrical smart plaster (SP) using Ortho$^+$ was successfully demonstrated on a mannequin in less than 10 mins. The best performances were given by circular patterned Ortho$^+$ SP with two layers of cotton webril at 50°C programming temperature. Interestingly, the Ortho$^+$ SP underneath temperature did not exceed 45°C and the intact pressure was less than 30.2 ± 5.2 mmHg at any instance, thus, offering assurance of safe external use. The Ortho$^+$ SP is lightweight, has less setting time, is easy to apply and the process is quicker and cleaner than POP and fibreglass. In addition, it offers the opportunity for multiple alterations, undercast pressure adjustments, and optimal air circulation. Most

importantly, Ortho$^+$ can be reused after disinfection. Therefore Ortho$^+$ SP is ideal for first aid treatment in remote or isolated locations where the required medical facilities and assistance are not freely available or accessible. Furthermore, this product can be easily used on bone fractured person at any remote location by a normal paramedic until the patient transfer to a hospital.

Building on the progressive use of SMPs in non-invasive biomedical applications, the research in this thesis has successfully developed ground-breaking knowledge in the synthesis, characterisation, optimisation, and material development framework. The outcomes of this study have opened up a new window for biomedical researchers to replace traditional orthopaedic materials with Ortho$^+$ and fabricate next-generation orthosis and fracture fixators.

1.5   Structure of the Thesis

The six chapters in the thesis cover the aforementioned research questions and objectives. The chapter content is briefly summarised below.

Chapter 1:   Introduction

The first chapter outlines the thesis significance, relevance, and original contribution to SMP based external applications. Finally, the research objectives are presented.

Chapter 2:   Literature review

The second chapter provides a comprehensive literature review. The research gap that addresses the first objective of this study is identified. SMP evolution, current market share, stimuli, reinforcements, and applications, including biomedical invasive and non-invasive, are briefly reviewed. Following this, the cause is highlighted of the limited number of commercialised applications. Furthermore, the chapter provides an extensive review of current popular orthopaedic materials and their complications. It is established that SMPC for non-invasive orthopaedic applications will benefit musculoskeletal patients who suffer from bone fractures.

Chapter 3:   Shape memory polymer synthesis

The third chapter consists of a description of SMP synthesis, tailoring activation temperature, and curing kinetics analysis. This chapter covers the second objective of the study.

Chapter 4:   Multi-attribute parametric optimisation of shape memory polymer properties

The fourth chapter comprises a discussion of SMP reinforcement with fibres and nanoparticles, multi-attribute parametric optimisation, and the performance of the newly

17

introduced Ortho$^+$. This chapter comprehensively addresses the third objective of this study.

Chapter 5:   Ortho$^+$ FEA modelling validation and demonstration

The fifth chapter is an analysis the viscoelastic properties, FEA model, and a lower limb leg cylindrical cast demonstration of Ortho$^+$. The chapter addresses the fourth and fifth objectives of this study.

Chapter 6:   Conclusion

The sixth chapter provides an examination of the findings related to research aims and research questions while highlighting the new scientific knowledge offered by this study. The study's research contribution to the field and its limitations are briefly outlined. Finally, recommendations for this field of research are make.

1.6 Associated publications

Journal articles (Q$_1$)

J$_1$ **Jeewantha, L.H.J.**, Jayalath, S., Emmanuel, K.D.C., Herath, H.M.C.M., Foster, E., Islam, M.M., Leng, J., and Epaarachchi, J.A., 2022. Shape memory polymer smart plaster for orthopaedic treatments. **Smart Materials and Structures**, 31 p. 115016

https://doi.org/10.1088/1361-665X/ac943b

J$_2$ **Jeewantha, L.H.J.**, Emmanuel, K.D.C., Herath, H.M.C.M., Islam, M.M., Fang, L. and Epaarachchi, J.A., 2022. Multi-attribute parametric optimisation of shape memory polymer properties for adaptive orthopaedic plasters. **Materialia**, 21, p.101325.

https://doi.org/10.1016/j.mtla.2022.101325

J$_3$ **Jeewantha, L.H.J.**, Emmanuel, K.D.C., Herath, H.M.C.M., Epaarachchi, J.A., Islam, M.M. and Leng, J., 2022. Investigation of curing kinetics and internal strains to enhance performances of bisphenol A based shape memory polymers. **Materialia**, 21, p.101264.

https://doi.org/10.1016/j.mtla.2021.101264

J$_4$ **Jeewantha, L.H.J.**, Epaarachchi, J.A., Forster, E., Islam, M. and Leng, J., 2022. Early research of shape memory polymer vascular stents. **Express Polymer Letters**, 16(9).

https://doi.org/10.3144/expresspolymlett.2022.66

Conference proceedings

C₁   **Jeewantha, L.H.J.**, Emmanuel, K.D.C., Epaarachchi, J.A., Islam, M.M. and Herath, H.M.C.M., 2021, January. Effects of biocompatible nanoparticles in DGEBA based shape memory polymers for biomedical applications. In ACAM10: 10ᵗʰ Australasian Congress on Applied Mechanics (pp. 100-116). Engineers Australia.

https://search.informit.org/doi/10.3316/informit.321636682295366

C₂   **Jeewantha, L.H.J.**, Emmanuel, K.D.C., Herath, H.M.C.M., Islam, M.M., and Epaarachchi, J.A., 2021, September. Development and characterization of shape memory polymers for non-invasive biomedical applications. In Smart Materials, Adaptive Structures and Intelligent Systems (Vol. 85499, p. V001T02A001). American Society of Mechanical Engineers.

https://doi.org/10.1115/SMASIS2021-66024

C₃   **Jeewantha, L.H.J.**, Epaarachchi, J.A. and Islam, M.M., 2022. Effect Of Dispersion Time for Nanoparticles DGEBA Shape Memory Polymer Composite Fabrication. In International Symposium on Polymeric Materials ISPM (2022) (PP.1-6). Advanced Engineering Materials and Composites Research Centre (AEMC), University Putra Malaysia.

C₄   **Jeewantha, L.H.J.**, Islam, M.M. and Epaarachchi, J.A., 2020. Development of Smart Materials for Invasive Medical Applications Using Shape Memory Polymers. In 6th International Conference on Mechanical, Industrial and Energy Engineering (ICMIEE 2020) (pp. 1-7). Khulna University of Engineering & Technology.

C₅   **Jeewantha, L.H.J.**, Islam, M.M. and Epaarachchi, J.A., 2019. Recent Progress in Shape Memory Polymers in Biomedical Applications. In Proceedings of the 1st International Conference on Mechanical and Manufacturing Engineering Research and Practice (iCMMERP-2019) (pp. 1-4). Global Circle for Scientific, Technological and Management Research (GCSTMR).

Media release

UniSQ	https://www.unisq.edu.au/news/2022/03/smart-plaster
Nursing review	https://www.nursingreview.com.au/2022/04/new-smart-plaster-a-turning-point-in-orthopaedic-care/
Manufacturing	https://www.aumanufacturing.com.au/new-plaster-is-faster-lighter-and-stronger-say-usq-researchers
IESL Newsletter	https://iesl.lk/SLEN/60/Smart_Polymers_in_Biomedical.php
Newswire	https://www.newswire.lk/2022/02/14/a-sustainable-smart-plaster-for-orthopaedic-treatments/

Video

Channel 7	https://www.facebook.com/watch/?v=1012792699638124

Associated awards

- Best poster at open day centre for future materials UniSQ - 2022

  https://composites.usq.edu.au/research/

1.7 Summary

Orthopaedic fracture fixators play a vital role in fracture recovery by supporting weak or deformed body parts and immobilising the motion in fractured fragments until they regain the full range of motion. Fibreglass is the most popular alternative to POP, which is typically used to immobilise fractured bones. However, POP and fibreglass casting materials have many disadvantages, such as causing hotspots and pressure sores, their low strength-to-weight ratio, and their long setting time among other issues. Therefore, orthopaedic materials with novel, exciting characteristics are in demand.

The author proposes a novel SMP material for external orthopaedic applications to meet such demand. This thesis has six chapters. It starts with an introduction and a literature review. After these, three comprehensive technical chapters are presented, in which the SMP activation temperature suited for external biomedical applications is designed. SMP properties are then evaluated and statistically optimised, prioritising orthopaedic bone immobilisation requirements. Further, a FEA model is developed and validated to predict behaviour when the SMP is formed into complex body shapes which require unique shape recovery. Finally, a leg-cylindrical cast is

demonstrated on a human mannequin. The last chapter is a summary of the

research contribution, followed by recommendations for future work.

CHAPTER 2: LITERATURE REVIEW

2.1   Introduction

Shape memory materials (SMMs) can memorise the temporary shape and recover their permanent shape upon an external stimulus, which is called the SME [72, 88-91]. In early 1932 this phenomenon was observed in AuCd alloy and later found in NiTi alloy [92]. NiTi, Cu, and Fe based alloys have been comprehensively investigated, and their electro-thermomechanical properties are highly valuable commercially [93-96]. The property of the SME is not intrinsic or invariable for materials which have this capacity. It depends on programming and recovery parameters such as deformation temperature, loading and cooling and heating rates [97-102]. The capacity for shape memory is not limited to metallic alloys (SMAs), and later, the same phenomenon was observed in polymers and ceramics (SMCs)[103-105]. However, SMPs have been shown to have a significant advantage over SMAs due to their availability, easier synthesis process and wide range of mechanical and physical properties [106, 107]. In addition, SMPs offer superior recoverable strain, tailorable glass transition temperature, a wide range of stimuli, and recyclability [17, 27, 75, 108-114]. Most SMPs are biocompatible, and some are even biodegradable [38, 57, 115-118]. Thus, SMPs are of particular interest.

Based on their particular kind of SME, SMPs are categorised into one-way, two-way and multiple-way SMPs. In one-way SMPs, the process is

irreversible. Interestingly, two-way SMPs' shape change is reversible; thus, the shape changes back and forth upon stimulus [114]. They have one permanent shape and one temporary shape. On the other hand, multiple-way SMPs have one permanent shape and several temporary shapes. Therefore due to the reversible effect, two-way and multiple-way SMPs are promising candidates in soft robotics and many more engineering applications [119]. Figure 2.1 gives the overview of this chapter.
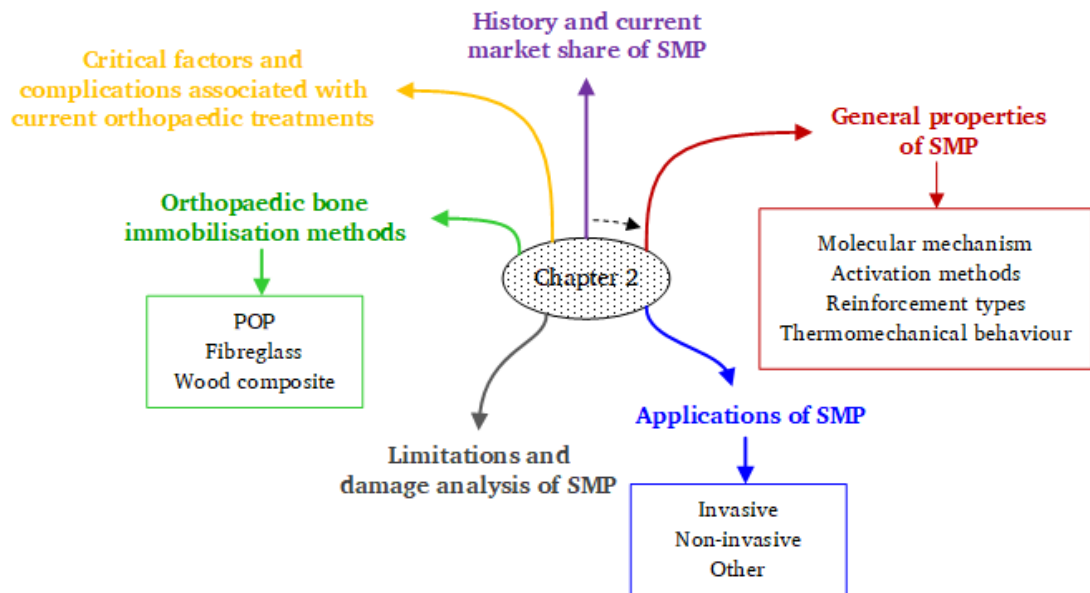
Figure 2.1: Overview of Chapter 2

During the SMP product design stage, general, SMP-specific, and other attributes need to be addressed. Figure 2.2 illustrates a comprehensive overview of SMP design needs, including activation, functionality, mechanical properties, environmental aspects, shape recovery, and manufacturing.
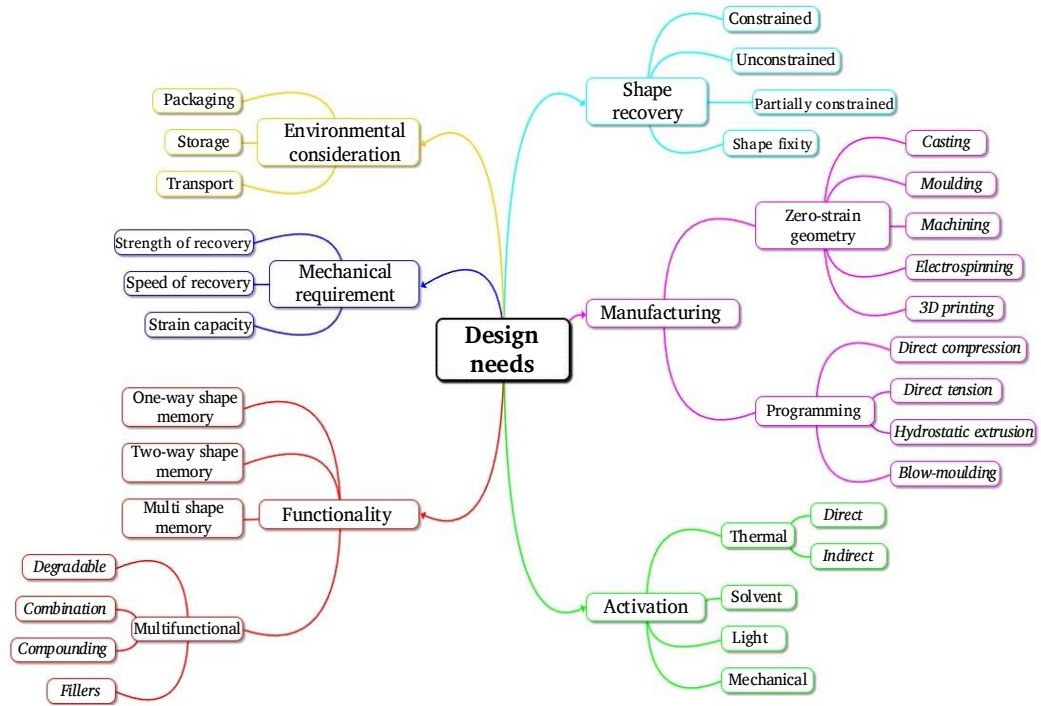
Figure 2.2: SMP design needs. Reproduced from [21]

2.2 History and current market share of SMPs

Synthetic polymers with "elastic memory" became widespread after World War II. The first use of the elastic memory effect was to replace the glass in cockpits of aircraft with acrylic plastic [120]. In the 1950s, Paul Cook proposed heat-shrink tube cross-linking polyethylene [121]. The "elastic memory" or "memory effect" describes the recovery process, while the "crystalline clutch mechanism" was used to describe the shape fixity [122]. In the late 1980s, Japan Mitsubishi Heavy Industry (MHI) explored polynorbornenes and polyurethane-based SMP applications [42, 123]. From then onward, the term "shape-memory" started to be used, and researchers put significant effort into studying the molecular mechanism, activation

26

methods, reinforcement and their potential applications [124]. After 2003, enthusiasm became widespread for SMPs due to soft tissue fasteners and suture anchor product innovations [86]. Several global research groups are committing their immeasurable time to developing devices with maturing SMP technologies. Lendlein A., Larock R. C., Gall K. A., Osada Y., Wilson T. S., Kremer F., Mather T., and the University of Southern Queensalnd – Smart Material Research Team Australia (UniSQ-SMRTA / Jayantha A. E.) among many other academic research groups, are particularly interested in SMPs [15, 125].
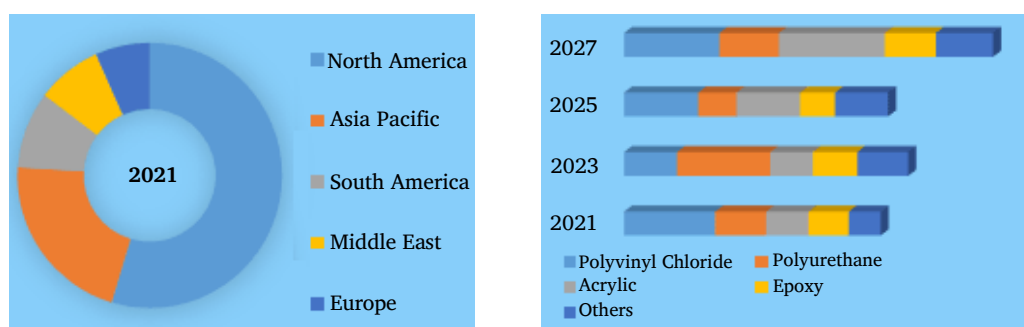
Figure 2.3: SMP market, (a) Regional analysis in 2021 (%), (b) Material with market projections.

According to global market insight, in 2021, the SMP market share was valued at around $ 450.4 M and this is forecast to sustain 26.9% growth till 2023 gaining a total value of $ 3.5 B. According to the analysis in 2021, pharmaceutical research and development activities across the biomedical field dominate the SMP market, with funding reported at 0.1 B. Interestingly,

due to the ease of manufacturing and shorter production time, Polyurethane (PU) is expected to hold over 40% of the revenue in the SMP market in 2030.
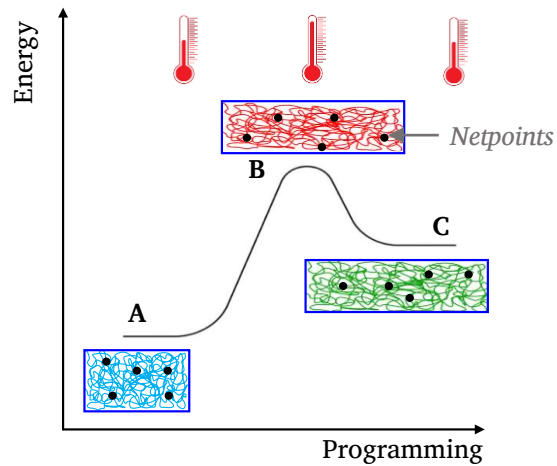
Figure 2.4: Energy diagram of a thermos-responsive shape memory polymer. Reproduced from [23]

2.2.1 Molecular mechanism

The molecular architecture drives the SME but does not require a specific chemical structure in the repeating units [75]. The energy and molecular structure theories are utilised to explain the SME [126]. In Figure 2.4, "A" shows an entropically favourable permanent shape; hence it is more stable. In the above transition temperature ($\leq T_{trans}$), the material deforms and transforms into the less favourable "B" and, upon cooling with constrained forces, "C" is obtained. Again, beyond the T_{trans}, the driving force provides the stored energy for the material to quickly regain its permanent shape [127].

The SMP network thereby releases energy and becomes a stable, permanent shape.

From a molecular point of view, the SMP network is incorporated with chain segments and netpoints [26, 75]. The netpoints associated with cross-links govern the permanent shape [128]. The polymer cross-links can be either chemical (covalent bonds) or physical (intermolecular interactions), and the temporary shape fixation is obtained by solidifying the switching domain [26]. Lu et al. classified SMPs into four categories based on their chemical structure [15]. The thermally activated amorphous shape memory polymer molecular mechanism is illustrated in Figure 2.5.

i) Chemically cross-linked glassy thermosets (T_g)

ii) Chemically cross-linked semi-crystalline rubber (T_m)

iii) Physically cross-linked thermoplastics (T_g)

iv) Physically cross-linked block copolymers (T_m)

Dynamic mechanical analysis (DMA) storage modulus *vs* temperature is plotted to identify these properties, and the amorphous cases T_g and the crystalline cases T_m are defined. The chemically cross-linked thermoset SMPs do not melt; these are the most popular and simplest. The 3-dimensional covalent bonds lead to attractive tailorable shape memory characteristics and either burn or decompose [129]. Due to their chemical bonds, thermoset SMPs have more stiffness than physically cross-linked thermoplastic SMPs. On the

other hand, physically cross-linked thermoplastic SMPs are easy to deform and reform; they show superelastic properties due to the phase separation of block copolymers [130]. These elastic properties can be further customised by changing hard and soft segments.
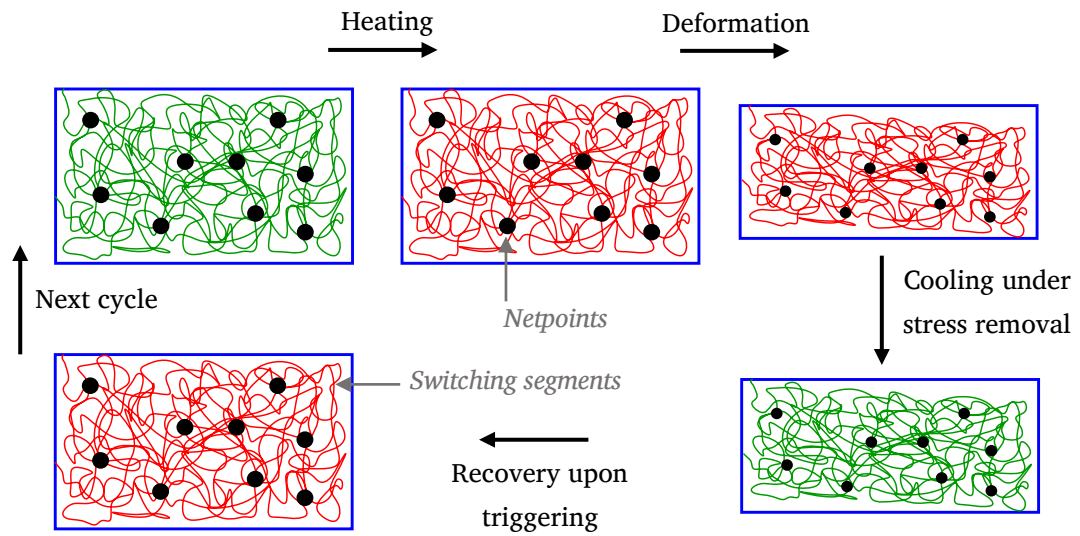
Figure 2.5: Molecular mechanism of amorphous shape memory polymer

2.2.2 Activation methods

The SME relies on stored strain energy and needs the required entropy to change the material's shape, which is called activation or recovery [131]. It is important to note that cross-linking restrains the polymer chain relaxation during recovery and does not drive recovery. The energy drives the recovery process, which can be done using various methods [132]. The most common stimulus types are heat, electrical current, magnetic field, solvents, moisture,

chemical, pH, pressure, mechanical, microwave and light [112, 133-140]. A detailed illustration is given in Figure 2.6.
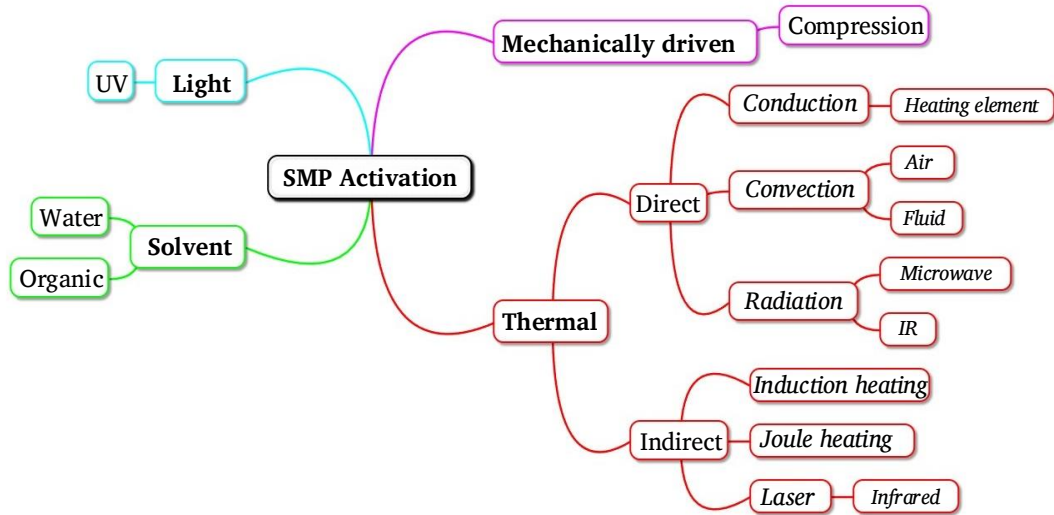
Figure 2.6: SMP activation methods

Thermally activated SMPs are common. These are classified into those requiring direct and indirect heating. In direct heating, the localised area or bulk material is exposed to temperatures above the transition temperature. On the other hand, indirect heating involves fillers, particles, and macroscopic filaments, which are dispersed uniformly within the material [132]. Upon the correct stimulus, these fillers generate heat; thus, the SMP can be activated both locally and remotely. Joules heating is the most commonly used indirect actuation method, with electrical conductive fillers [140]. In addition, Fe_3O_4 particles reinforce SMPC activation using a magnetic field-induced eddy current without applying a direct electric field [76]. Utilising multiple stimuli

31

allows for synthesising robust materials to tackle complex engineering challenges while serving various applications [141]. The total work done is a function of temperature, and the effectiveness of the SME is governed by the cross-linking density [21].

2.2.3 Reinforcement type

SMPs can be weak in strength depending on their chemical and physical structure [142]. To improve SMPs' mechanical and structural properties, they are often reinforced with fibres and fillers [72, 73, 143]. Fibres are classified into continuous woven, unidirectional, and chopped strands. They remarkably improve the mechanical, recovery stress, and damping properties of their polymer [72, 74, 144]. SMP researchers have comprehensively studied and characterised carbon and glass fibre-reinforced SMPCs and their properties [40, 90]. Occasionally, basalt, kevlar, aramid, and natural fibres have been experimented with [41, 145, 146]. On the other hand, nano and microparticles improve SMPC functional properties such as thermal conductivity, electrical conductivity and light emission, rather than the mechanical strength [76, 147, 148]. Jordan et al. observed higher strain failure with regard to declined NP size in amorphous polymers [149]. The addition of NPs can introduce multiple triggering options, and NPs have been demonstrated to affect the T_g [49, 132, 150]. To date, SMP researchers have thoroughly investigated Carbon nanotubes (CNT), Multi-walled carbon nanotubes (MWCNT), Carbon black, Carbon dot, Graphene, Titanium dioxide

(TiO$_2$), Silicon carbide (SiC), and Iron (II, III) oxide (Fe$_3$O$_4$) NPs [73, 76, 97, 125, 133, 151-153].

2.3 SMP thermomechanical behaviour

During the thermomechanical cycle, the SMP undergoes large deformation upon stress or strain and this significantly varies the elastic modulus as a function of many parameters [154]. However, until the material reaches its transition temperature (T$_{trans}$), the storage modulus (SM) remains constant, but then the material's SM undergoes a drastic drop [155]. Liu et al. stated that to have a better SME, the SM drop should be of more than two orders compared to their glassy stage [156]. Thus the SMP displays a certain rigidity and flexibility due to the micro-Brownian movements below and above T$_{trans}$ [59]. To quantitatively analyse this, R$_f$ and R$_r$ are defined to standardise the SMP functionality [157]. The most widely accepted SMP thermomechanical cycle is shown in Figure 2.7.

① Deformation to the desired temporary shape

② The desired temporary shape is achieved

②−③ Decrease of the temperature below T_{trans}

③−④ Removal of the stress by removing the material out of the testing machine

②−④ Fixation of the temporary shape

④−⑤ Increase of the temperature above T_{trans}
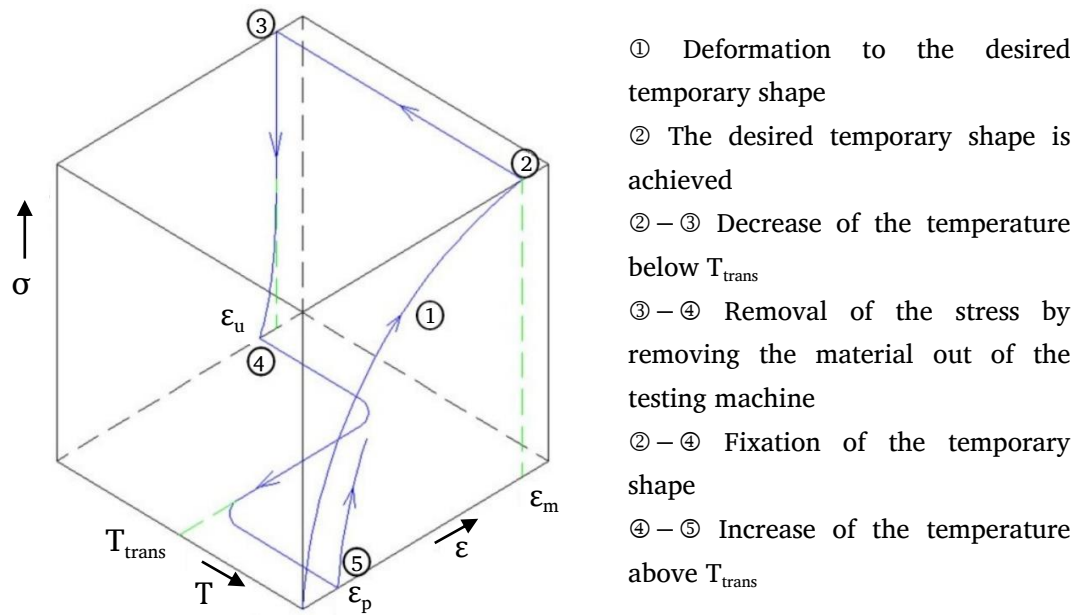
Figure 2.7: Schematic representation of thermomechanical cycle.

Reproduced from [158]

Programming	The SMP is heated close to or above the T_{trans} and can be formed into a specified shape by compression, extrusion or injection moulding [159].
Storage	The SMP is cooled and held in its temporary shape. This occurs below the T_{trans} and constraints are released once cooling has finished.
Recovery	Upon reheating to a point above, the T_{trans} SMP returns to its permanent shape.

During the thermomechanical cycle, the elastic portion stores energy and the viscous portion dissipates energy [123]. To describe this phenomenon, the storage elastic modulus (E") and loss elastic modulus (E') are defined, and

their ratio is taken as the loss tangent modulus (Tan $\delta = E''/E'$) [160]. DMA equipment is used to obtain these parameters. It is important to note that the SMP should retain its initial strength for reliable product design after going through a complete shape memory thermomechanical cycle.

2.4 Applications of SMPs

SMPs and their blends have promising applications in various fields, from domestic to advanced engineering in products such as automobiles to aerospace transport, smart textiles to intelligent packaging, switches to sensors, and most importantly, biomedical applications [39, 111, 161-164]. SMPs have been a strong candidate for aerospace applications since their introduction; however, SMP synthesis to withstand harsh environments like a vacuum, high or low temperature cycles, UV radiation, and cosmic rays are challenging [165, 166]. Recent developments focus on low-cost deployable structures such as booms, morphing skins, trusses, hinges, and antennas [29, 40, 61, 65, 72, 112, 167-170].

SMPs have been extended to many biomedical branchers since SMP-based medical instruments and auxiliaries support minimally invasive surgeries [171-173]. Both academics and industry practitioners have shown strong interest in SMP biomedical applications, which can be categorised as having general surgical, intravascular, urogenital, ophthalmics, orthopaedics and orthodontics uses [17, 21, 23, 24, 161, 171, 174-176].

2.4.1 SMP invasive biomedical applications

During the past decade, significant attention has been given to invasive SMP biomedical application development and commercialisation [47, 106, 177]. Selected invasive biomedical outcomes are summarised in Table 2-1. SMP stents are prominent in both biodegradable and nondegradable cardiovascular applications. Most fabricated SMP stents are self-expanding at body temperature [68, 178]. On the other hand, using biodegradable medical devices avoids a painful second surgery. Hence the development of minimally invasive, self-expandable, and biodegradable SMP devices add value to laparoscopic aids diagnosis or therapeutic procedures [53]. The SMP degradation can either be surface or bulk and starts linearly before turning nonlinear [179]. Because of biocompatibility and biodegradability, poly(ε-caprolactone) (PCL), polylactic acid (PLA) and poly (D, L-lactide acid) (PDLLA) polymer families and their composite blends are popular in invasive application developments [20, 180-185]. Polyurethane-based SMPs are regularly used due to their physicochemical, mechanical and structural performances [26, 186].

Table 2-1: A brief summary of SMP invasive biomedical applications

Application	Author	Activation method	Material and remarks
Vascular stent	Tamai et al. [187]	Thermal	0.17 mm thick stent was made of poly-l-lactic acid (PLLA). Deployed in a hot liquid balloon and stent took 0.2 s at 70°C and 20 min. at 37°C. The stent was installed in 15 patients and no deaths were reported.
	Venkatraman et al. [188]		The first bi-layered biodegradable 0.15 mm thick stent was made of PLLA, poly glycolic acid (PLGA) and polyethylene glycol (PEG). The minimum recoil (36%) percentage occurred at thickness ratios of PLLA/PLGA:8/7 within 8 min. at 37°C water.
	Sonawane et al. [189]		The 0.25 mm thick stent was made of PLA and PGLA ratio of 3:2. The stent was installed in a goat vessel at 37°C and specially checked for antibacterial effect and biofilm formation.
	Lauto et al. [190]		Helically wound 0.055 mm thick deacetylated chitosan (4 w/v%) stent was tested with Wistar rats. No granuloma was observed after two weeks. The stent self-expanded over 50% of its initial diameter within 3 min. and the expansion process was irreversible.

Chen et al. [191]	The hydrophilic Chitosan stent supports swells in an aqueous environment and recovered permanent shape within 150 s in 37°C. The vascular stent was coated with heparin to avoid thrombogenicity and sterilised with ethylene oxide. The stent successfully implanted in the rabbit artery.
Chen et al. [192]	Chitosan-based epoxy cross-linked sirolimus-eluting hydrophobic heparin-coated biodegradable 3 mm diameter stent developed. The stent was rinsed with Phosphate Buffered Saline (PBS) solution to remove residual cross-linking. The drug release rate was controlled with the outer heparin layer.
Wache et al. [56]	The drugs loaded stent was made of thermoplastic polyurethane (TPU). Maximally the stent can be loaded with drugs 35% by weight in a 30 mm long stent. The activation temperature was between (80-120)°C, which is significantly high for biomedical applications.
Duarah et al. [193]	Hyperbranched polyurethane (HPU) synthesised with biocompatible carbon dot-silver (CD-Ag) nanohybrid in different weight ratios and fabricated a rapid self-expanding infection-resistant stent. Mechanical and thermal stability significantly improved with 5% nanohybrid materials in the HPU/CD-Ag stent

	due to strong H-bonding, covalent bonding and polar-polar interactions. The stent self-expanded ($>99\%$) diameter from 3.45 mm to 5.40 mm within 20 s.
Zeng et al. [194]	The stent was made by melt blending amorphous poly(propylene carbonate) (PPC) with elastic TPU. The PPC has improved ductility, recovery speed, R_r but lower the R_f. The most optimal properties were obtained with 50% of each PPC and TPU. The stent recovered its original shape within 20 s at 37°C.
Yu et al. [195]	The ring-opening copolymerisation technique was used to synthesise and the material named poly(ε-caprolactone-co-DL-lactide)/ PCLA. The stent was triggered at 37°C, the geometrical length was 13 mm, and the inner and outer diameters were 28 and 30 mm, respectively. The stent was implanted in a dog's oesophagus within 5 min. and 30 s.
Xue et al. [184]	The self-expandable stent contained three arms of PCL, methylene diphenyl diisocyanate (MDI) and crystallisable microbial polyester, poly[(R)-hydroxybutyrate-co-(R)-3-hydroxyvalerate] (PHBV). The activation temperature is around (39-40)°C. A sharp actuation was observed within 25 s in the body's fluid environment.

Boire et al. [185]	The stent was mainly PCL and poly (α-allyl carboxylate-ϵ-caprolactone) (ACPCL). Varying molecular weight and gel content, the transition temperature was reduced to 37°C. An 89% PCL and 11% ACPCL copolymer with a 1.5 cm length and 1.2 cm outer diameter SMP circular stent was implanted in A/J mice thigh muscle. A successful cellularisation and fibrotic tissue formation were observed.
Zheng et al. [194]	The stent was made of poly (propylene carbonate) (PPC) and PCL using the melt blend technique. The stent was submerged in 37°C water and the original shape was recovered within 15 s. The mass loss of the stent was controlled by the ratio of PCL to PPC by weight.
Ajili et al. [196]	The stent material was obtained with PU/PCL: 70/30 by weight ratios and T_g was found around 37°C. The study conducted on human bone marrow mesenchymal stem cells (HBMSCs) has proved the biocompatibility of stent supporting cell adhesion and proliferation.
Ansari et al. [197]	Two types of PU, LARIPUR 107-93A and LARIPUR 2102-85AE have been fabricated with Young's modulus 9.0 MPa, 4.3 MPa, respectively. The shape memory behaviour was not observed in

	LARIPUR 107-93A due to the high elastic modulus. A minimum recovery start temperature (RST) was achieved from minimum diameter/thickness ratios. Therefore, it is concluded that the geometrical changes greatly affected recovery response.
Chasse et al. [198]	The helical flow device was 3D printed with acrylonitrile-butadiene-styrene (ABS), and the device structural integrity was enhanced with polydimethylsiloxane (PDMS). The flow device was kept inside the testing chamber and immersed in a 37°C static water bath. The PBS was circulated approximately 1 cm^{3}s^{-1} and volume flow rate, pH and temperature were controlled. The PCL activation temperature can be varied upon different copolymers, which is a breakthrough in the development of bio-compatible material research.
Park et al. [199]	The stent material was synthesised with PCL and poly(glycidyl methacrylate) PGMA ratios of 94% and 6%, respectively. The triggering temperature (32-44)°C controls the crystallinity and net-point spacing by varying PCL/PGMA molar and cross-linking ratios. The stent is resistant to bacterial infection and the performance was observed in a short period with rabbits.

Gu et al. [200, 201]	Thermal/ Magnetic	The stent synthesised polylactide-base polyurethane (PLAU) and Fe_3O_4. and oleic acid (OA) was used to assure the homogeneity of Fe_3O_4 NPs. The 0%, 3%, 6% and 9% Fe_3O_4 rations took 15, 19, 14 and 11 s to recover permanent shape, respectively, at 55°C Further, PCLAU obtained synthesising Poly(d,l-lactide-co-ε-caprolactone) (PCLA) with polytetramethylene ether glycol (PTMEG) and hexamethylene diisocyanate (HDI). The PCLAU/ Fe_3O_4 dual-induced self-expandable stent was obtained by adding Fe_3O_4 that operated at 40°C. The stent showed 100% R_f and more than 82% R_r. In *vitro* degradation, cracks were observed after 3 weeks, and 67% weight loss was recorded after 13 weeks of implantation.
Zou et al. [202]	Magnetic	The stent was made of solution casting and composed of commercially available PU and Fe_3O_4 NPs and OA. Fe_3O_4 was used to improve the dispersibility of the compound material and the transition temperature was 42°C. It was found the R_f and R_r were not affected by added NPs until they reached 20% by volume. Further, 1% NPs contained stent recovered its permanent shape within 30 s.

	Baer et al. [203]	Light	The stent was synthesised with TPU, HDI, N,N,N'-tetrakis(2-hydroxypropyl)ethylenediamine (HPED), triethanolamine (TEA) and Epolight 4121. The stent was crimped over a fibre-optic light diffuser coupled to an IR diode laser. Under zero flow, the stent was fully recovered within 6 min. at a laser power of 8 W.
Intravascular thrombectomy	Small et al [43]	Light	Thermoplastic SMP (MM6520 and MM5520), Platinum dye (Epolight™ 4121). The actuation was complete within 3 s. The temperature rise of the blood near the device is approximately 12°C. Tissue damage is possible with extended use.
Self-tightening suture/ knot	Lendlein et al. [17, 115]	Thermal	Thermoplastic SMP was programmed by stretching about 200%. After forming a loose knot, both ends of the suture were fixed. The knot was tightened in 20 s when heated to 40°C. During the animal experiment, 0.1 N could be detected in the surrounding tissue.
	Zhang et al. [204]		The thermo-sensitive suture was synthesised with styrene-butadiene-styrene tri-block copolymer and PCL. The thread was able to automatically knot within 10 s in a water bath at 70°C. The activation temperature is too high for biomedical applications.

	Goraltchouk et al. [205]		The stimulus was applied before, during, or after the deployment of the suture in tissue. In particular, the SMP was used to enhance the formation or deployment of the retainers.
	Toncheva et al. [206]	Light	The SMP contained PCL and Ag NPs. The knot was tightened at 30 s and the temperature was increased from 21°C to 37°C.
Embolic coil	Maitland et al. [44]	Light	The SMP coil was made of thermoset polyurethane (MP5510). The device actuation temperatures are in the range of 65 to 85°C.
Macrophage phagocytosis	Guo et al. [207]	Light	The synthesised SMP contained thermoplastic PDLLA and Gold NPs. The activation temperature was between 37°C to 45°C. The actuation was due to 532 nm viable light and the maximum power was 2 W.
Soft actuator	Fang et al. [208]	Light	The actuator was made of Poly[ethylene- ran-(vinyl acetate)] (EVA) and Aniline black. Photothermal actuation due to 808 nm NIR light. Recovery temperature from 85 to 74°C and $R_r > 98\%$.
Surgical fastener	Bettuchi et al. [209]	Thermal	The polyurethane based surgical faster introduced for meshes used in hernia repair. The fastener recovered its permanent shape within 1-5 s after insertion into tissue.
Dialysis Needle	Ortega et al. [210]	Thermal	The SMP needle made of MM-5520 SMP (DiAPLEX Company, Ltd.).

			T_g is lowered to near body temperature and the external energy required to activate needle is eliminated. SMP adapter was introduced to reduce the hemodynamic stress caused by dialysis needle flow impingement within an arteriovenous graft.
Clot removal	Metzger et al. [211]	Thermal	The clot removal contained two different ester based thermoset polyurethanes MP4510 and MP 5510 from MHI. The T_g set between 37°C-65°C. The device was capable of holding a clot against pressures over ten times greater than typical pressures.
Neuronal electrode	Sharp et al. [212]	Thermal	A micro-casting method was developed to fabricate neuronal electrodes from an epoxy based SMP from Composite Technology Development, Lafayette, CO. The shape recovery rate is low (35% after ~20 hrs).
Aneurysm occlusion	Hampikian et al. [213]	Thermal	The Polymer Technology Group, Inc, supplied the polyurethane-based polymer. The SMP reported T_g of 33°C and a melting point of 140°C. The straightened fibres deployed into the aneurysm model and once introduced flow, SMP recovered the helical coil configuration.
Intragastric implants	Marco et al. [214]	pH	Self-inflating implant actuated by acidic pH or at 3.7°C.

Orthodontic therapy	Mather et al. [215]	Thermal	The SMP contained butyl methacrylate (BMA, 66.7 *wt*%), methyl methacrylate (MMA, 28.6 *wt*%) and tetraethylene glycol dimethacrylate (TEGDMA, 4.8 *wt*%). The two-stage SMP is particularly useful in orthodontic brackets, "O-rings" applications. Two temporary shapes can be stored in memory, allowing for complex deployment on simple heating.
	Nakasima et al. [216]		The SMP plastic wire of 1 mm in diameter stretched to two to three times its original length at a temperature of 50°C. The SMP wire gave a stable force of 119-156 g to move the teeth.
	Jung et al. [49]		The orthodontic wire made from melt-spinning of PU block copolymer which was synthesized in a two-step process from a reaction of 4,4'-methylene bis(phenylisocyanate), poly(ε-caprolactone) diol and 1,4-butanediol. The hard and soft segments improve orthodontic wires' flexibility and mechanical resistance to correct misaligned teeth at body temperature.
	Masuda et al. [217]		The material elastic modulus can be adjustable by varying the 1-butanol amount at synthesis, thus allowing appropriate orthodontic force.

A stent is a tiny tube or circular lattice widely used to prevent the narrowing of the arteries and maintain the required blood flow to the myocardium [157]. Currently stents are made of stainless steel 316L, Tantlum, Nitinol (Ni-Ti), Cobalt, Platinum and Iridium [56, 195, 218]. Despite the fact that metal stents have been widely used in clinical practices, there are many drawbacks associated with metallic vascular stents, such as rejection by the body's immunity system, damage to vessel walls due to high stiffness, high cost of fabrication, and clinical issues such as allergies [219, 220]. The introduction of cardiovascular SMP stents has dramatically changed surgical procedures since SMP stents can be deployed with minimum invasiveness. Most SMP stents have been fabricated with thermoplastic SMPs using micro-electro discharge machining, electroforming, solvent casting, die-casting, 3D-printing, laser cutting and braiding [68, 221]. In addition, a significant number of SMP stents are self-deployed, and performances are mainly governed by T_g, cross-links, a triggering mechanism, geometry, and programming conditions.

In 2008, Chen et al. developed a chitosan-based epoxy cross-linked sirolimus-eluting hydrophobic heparin-coated biodegradable SMP vascular stent [192]. The uniformly 0.10 ± 0.001 mm thickened chitosan film was cut into 100×1.2 mm^2 and wound on a 3 mm diameter mandrel before being immersed in an epoxy compound, as shown in Figure 2.8. Finally, it was rinsed with PBS solution to remove residual cross-linking and was allowed to dry. During the drying process, the stent was shrunk and returned to a temporary

shape. This allowed it to be implanted through small incisions in narrow arteries and to then recover its permanent shape by hydration. The mechanical stability of the stent was verified, and Chen et al. revealed that 85% of the cross-linked stent had achieved the best mechanical properties.
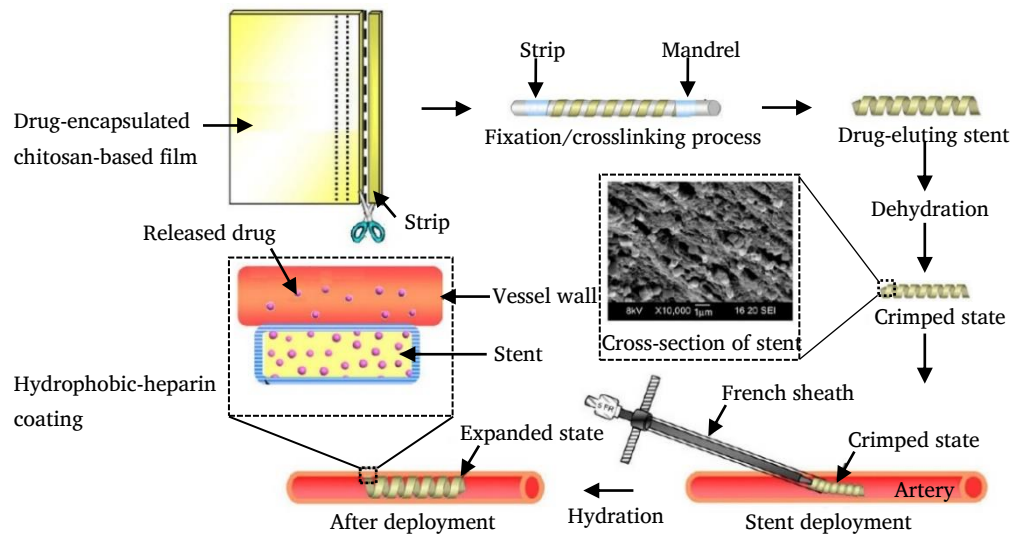
Figure 2.8: Schematic illustrations of the development process of the sirolimus-eluting polymeric stent and the deployment of the stent in an artery via a French sheath in an animal study. Reproduced from [192]

According to *vivo* results, the drug release rate remained constant and controlled with the outer heparin layer. The reduction of drug release rate delays arterial healing and may lead to late thrombosis development. Hence the optimum drug release rate needs to be investigated in future experiments. After one month of clinical examinations, results verified that none of the stents migrated in the animals' infrarenal abdominal aorta. Hence it was

concluded that proper expansion had taken place during the deployment. According to the literature, sirolimus also reduced migration, delayed healing, and reduced neointimal formation [222]. Therefore, during the SMP vascular stent fabrication, careful consideration of other affected parameters is crucial to improve reliability.

Further, Chen et al. discussed the optimum period for biodegradable vascular stents before total deterioration with enzymatic reaction. It was found that the strength should remain for more than six months in humans' bodies to achieve optimum medical requirements [223]. Chen et al. identified that cross-linking may affect the degradation of the stent, and further investigation will be required before clinical trials. The proposed stent has shown greater potential than earlier chitosan stents and is one of the best vascular stent designs found in the literature; however, after Chen et al., researchers' interest in chitosan stents has sharply declined.

PCL is another widely used SMP in biomedical vascular stent applications. However, the PCL T_m is around 60ºC, and it is difficult for human tissues to withstand that temperature. PCL's relatively low strength was increased by mixing different copolymers and hard segments such as PLA, MDI, and PPC. Bellin et al. investigated a triple SME stent. This stent's transition from its initial to second shape is fixed by physical cross-links and the transition from second to third shape is derived by covalent cross-links [224]. The initial two shapes are defined through thermomechanical programming, while netpoints defined the final shape of the stent. The Three

triggering temperatures are as follows 20°C, 40°C and 60°C. The polymer structure is divided into two networks.
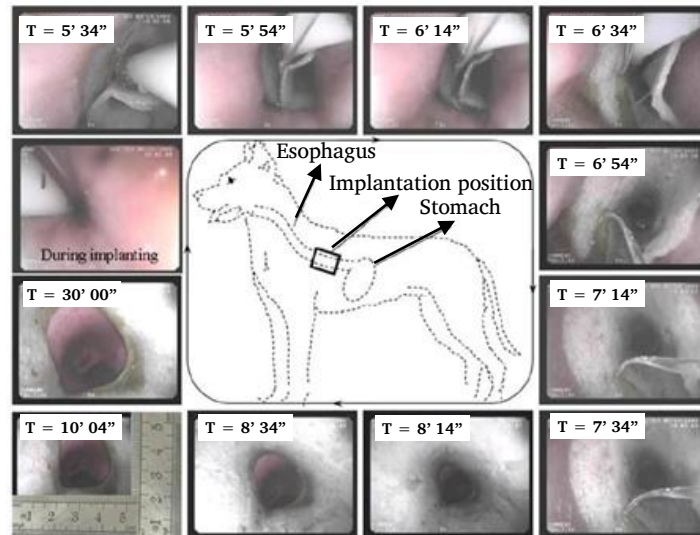
Figure 2.9: Schematic illustration and endoscopic photos showing the process of shape memory recovery of a PCLA stent implanted in a dog's esophagus. Reproduced from [195]

The first polymer network, named MACL consists of PCL and poly(cyclohexyl methacrylate)(PCHMA). The second network, called CLEG, consists of PCL and PEG. The triple SME allows the insertion of a vascular stent in a compressed shape, followed by expansion into the second position, and a third contracted shape that facilitates the removal of the stent later. Hager et al. presented a list of triple and multiple SMPs, but further studies on triple SME polymeric stents are limited in the existing literature [114].

Yu et al. further studied the properties of PCL and found substantial degradation over 14 weeks; thus, PCL is limited in clinical applications [195].

Due to this, Yu et al. chose the popular PLA homopolymer, which has verified biocompatibility and biodegradability, to improve PCL's properties. The proposed new polymeric material was synthesised with ε-caprolactone (ε-CL) and DL-LA with 10/90 weight ratios. The ring-opening copolymerisation technique was used to synthesise, and the new material was named PCLA. PCLA's material properties were compared with commercially available metallic (Ni-Ti alloy) stents, and a nearly equal mechanical strength was observed. Further, Yu et al. noted that PCLA's compressive strength unexpectedly increases with degradation. The vascular stent is triggered at 37°C, its geometrical length is 13 mm, and the inner and outer diameters are 28 and 30 mm, respectively. During *vivo* experiments, a vascular stent was implanted in a dog's oesophagus through a minimally invasive technique (Figure 2.9). The surgical team finished implantation within 5 min. and 30 s. Frequently observed endoscopic results verified that the stent prevented restenosis before slipping into the stomach.

Embolization is a medical technique currently used by most surgeons to block the blood flow to a particular area inside the body. It helps to prevent massive internal bleeding, control the blood flow, block the blood flow to tumours and eliminate abnormal connections to veins. SMP researchers developed embolization techniques with the help of SME. Redriguez et al. tested filling-type embolization and used polyurethane-based material as a filler [25]. During a swine *vivo* modelling, Landsman et al. studied the time required to deploy it in the correct place without activation [225]. The

efficiency of the device was verified by performing blood flow studies. The swelling capacity is essential to avoid tissue damage during the process. The pilot study revealed that at 37°C water did not exceed 0.6 N, and cell damage is unlikely to happen with this load. Nathan et al. further stated that without damaging cells, foams could be used to block the blood vessels [16]. Therefore, these authors concluded that SMP foams are potential candidates for embolization devices.
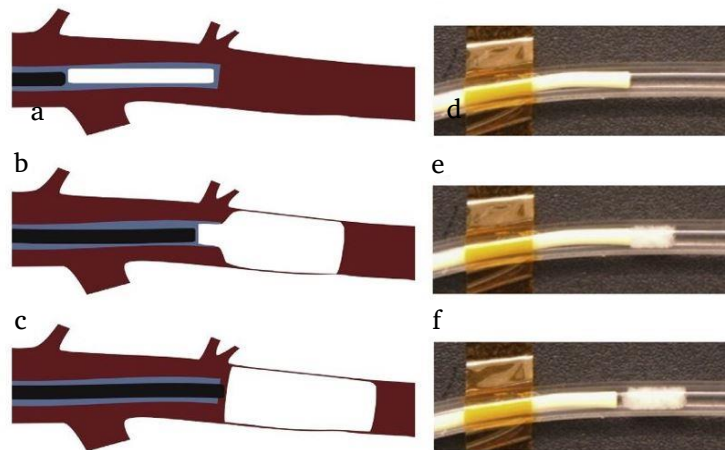
Figure 2.10: Endovascular deployment of the SMP, (a) Device is pushed near the catheter tip by the guidewire, (b) Guidewire pushes the self-actuating device out of the catheter, (c) Deployed device fills the vessel lumen, (d–f) In *vitro* demonstration of a developed occlusion device in body temperature. Reproduced from [226]

Small et al. developed a novel bool clot removal method from thermoplastic polyurethane from MHI Japan [43]. The SMP micro-actuator tip is made of optical fibre, which can be activated at 810 nm laser light. The

corkscrew SMP specimen was heated before being straightened manually into a temporary rod shape. The device was tested under 37°C static water and actuated within 3 s in 4.89 W laser power. During the *vitro* test, the device successfully captured the artificial blood clot in the water-filled bifurcated vessel.
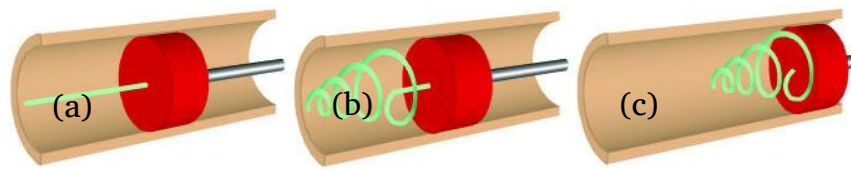
Figure 2.11: Laser-activated SMP micro-actuator. (a) Temporary straight rod form, (b) Permanent corkscrew from laser heating, (c) Deployed micro-actuator is retracted to capture the thrombus. Reproduced from [43]
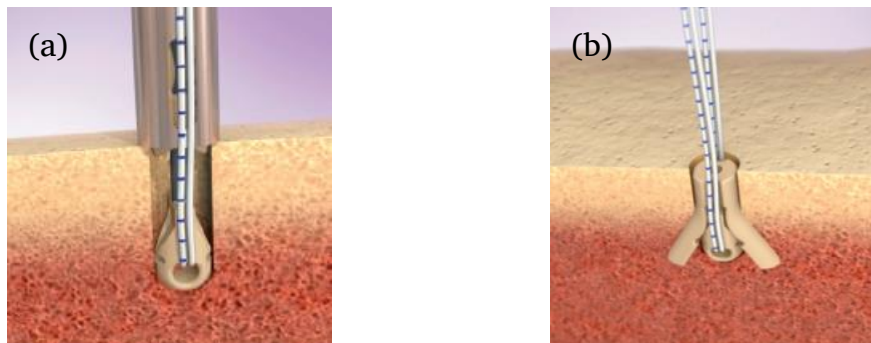
Figure 2.12: Suture anchor (a) Driver positioned over site of implantation, (b) Implanted suture anchor. Reproduced from [227]

In current SMP biomedical product realisation, MedShape is leading the clearing of two products with FDA approval. The first is a suture anchor

used in soft tissue reconstruction which is made of the chemically cross-linked thermoset-acrylic-based copolymer. Theis suture anchor is activated over 50°C and stable over 40% of strain for up to two years.

MedShape's other suture anchor was made with thermoplastic polyetheretherketone (PEEK) [227]. This suture anchor show ~3 GPa Young's modulus at body temperature and has 4 years of storage stability. In traditional bone fixation, screw-based devices lead to soft tissue damage during their insertion. MedShape has successfully addressed this challenge by introducing mechanically activated soft tissue fasteners named ExoShape® and Eclipse™ as shown in Figure 2.13 and Figure 2.14 [142, 227]. During the ExoShape® and Eclipse™ insertion, the fastener is deploying axially. Therefore, more uniform force is applied, causing less damage to surrounding soft tissues. According to experimental evaluation, ExoShape® has a pull-out strength of over 1200 N for synthetic and porcine bones, respectively [228].
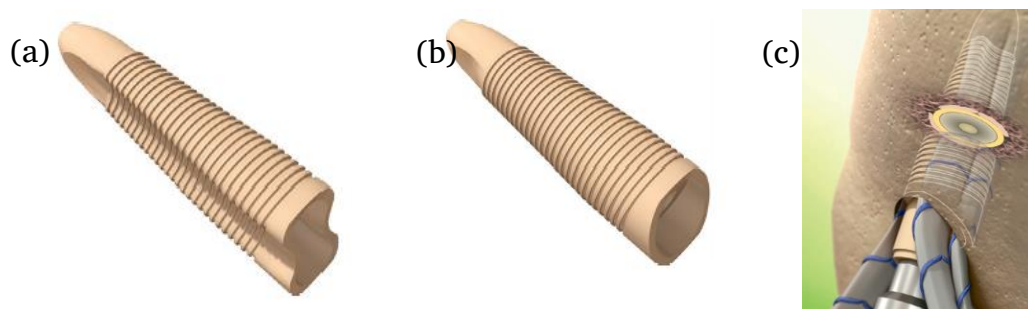
Figure 2.13: ExoShape® soft tissue fastener (a) Temporary programmed shape, (b) Deployed shape, (c) Deploying into the bone tunnel with soft tissue. Reproduced from [142]
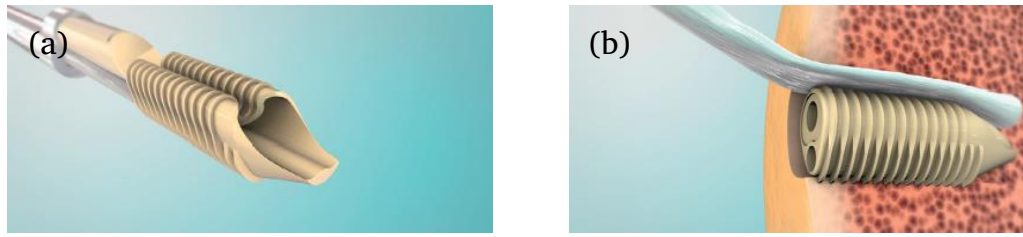
Figure 2.14: Eclipse™ soft tissue fastener (a) Pre-deployed (programmed) state and loaded on driver, (b) Deployed in bone tunnel. Reproduced from [21]

Around 30 kinds of thermoplastic and thermoset SMPs, such as DiAPLEX, Veriflex®, Verilyte™, Veritex™, Tecoflex®, and TEMBO are in the commercial market. However, most are not yet of medical grade quality. Therefore limiting their translation to clinical applications [47]. On the other hand, the literature presented above shows that orthopaedic devices have gained limited attention despite their tremendous potential.

2.4.2 Non-invasive biomedical SMP applications

Due to the demand for thermomechanical properties at body temperature, SMPs were hardly seen in non-invasive biomedical applications; thus, a significant research gap remains. Kumar et al. fabricated SMPU stockings to manage chronic venous disorders [229]. The SMPU filament (linear density 18.6 tex) and Nylon (linear density 18.9 tex) were combined using a circular knitting machine in the smart stocking. The developed yarn

T_g was at 30°C and the SMPU stocking was heated for 10 min. before applying it over a cylindrical tube, as shown in Figure 2.15.
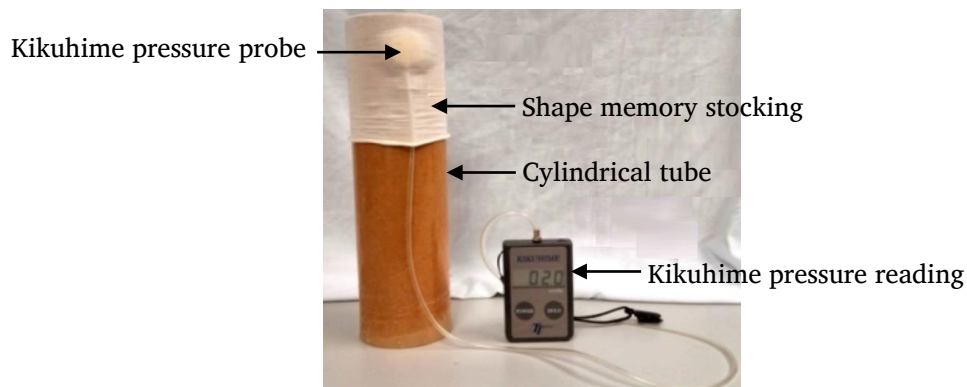
Figure 2.15: Shape memory smart medical stocking [229]

The baseline pressure was selected as 30 mmHg. However, by varying the temperature levels and strain, a maximum of 46.2 mmHg was obtained. Thus, up to 50% of extra pressure was generated by heating the stocking. Therefore, it was established that an SMPU stocking provides the additional freedom to adjust pressure levels during compression therapy externally. Moreover, Kumar et al. verified the repeatability of the stocking, demonstrating five cycles at 40°C, as shown in Figure 2.16. Ahmad et al. pre-stretched SMPU strips, offering the required pressure gradient, which is an alternative to current treatment choices. The PCL-based SMPU contained 58% and 42% of soft and hard segments, respectively [230]. The material has shown a transition temperature of 45°C, and R_r of 82% and a maximum failure strain of over 800%.

56

In Ahmad et al.'s experiment, during the pressure bandage fabrication, SMPU film was cut into 70×30 mm strips and stretched to a pre-defined strain of 25, 50 and 75% in the heated chamber. After that, the free ends of each strip were attached to a piece of fabric using Araldite Rapid glue. The two configurations of pressure bandages are shown in Figure 2.17 a and b. The pressure bandage generated 25 mmHg maximum pressure at 60°C; however, the pressure dropped to 14 mmHg (at 25°C) upon cooling. On the other hand, it was found that the generated pressure decreases with the increase in test cycles due to internal molecular rearrangement and chain disentanglement. Ahmad et al. stated that SMP pressure bandages could be used without additional training and are reusable and cost-effective.
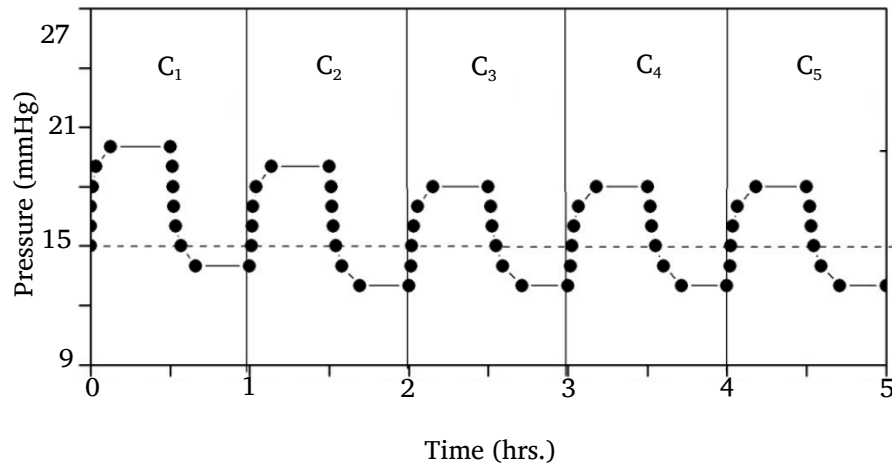
Figure 2.16: Pressure variation during sequential heating and cooling of the stocking up to 5 cycles (C_1-C_5: individual cycles). Each cycle includes heating the stocking for 30 min. in a heated chamber (40°C), then cooling down for another 30 min. at room temperature [229].

57
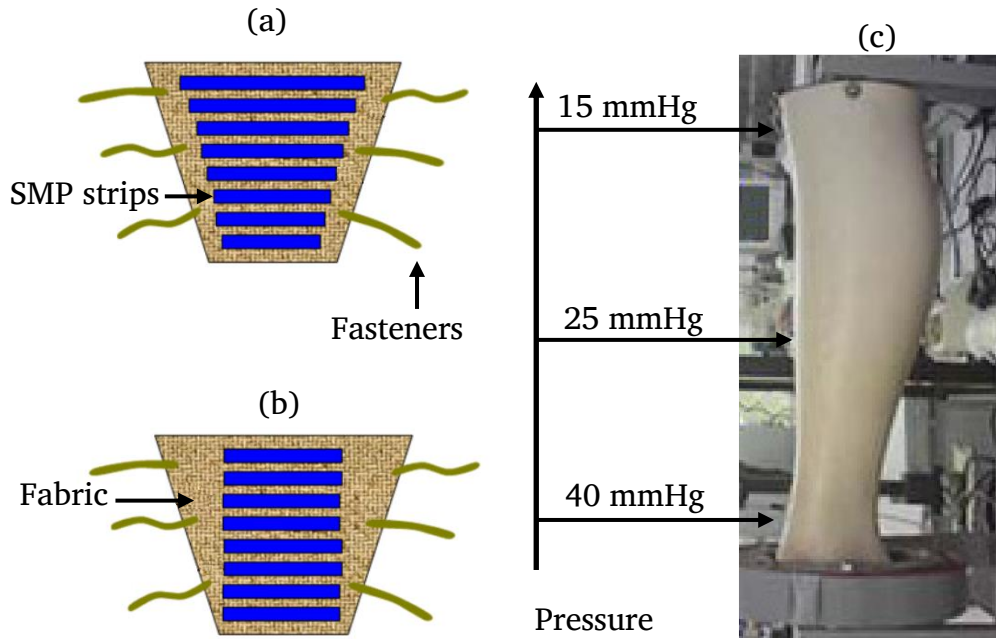
Figure 2.17: (a) and (b) SMP bandage, (c) Pressure required for leg ulcer

treatment. Reproduced from [230]

Zhao et al. detailed the fabrication process of styrene-based SMP forearm, finger and wrist fracture fixators [91]. The SMP sheet was dipped in a hot water bath, wrapped around the limb, and the fracture fixators' fixity and operability were verified. During the mechanical characterisation, the SMP obtained 421 MPa flexural modulus, which was closer to that of gypsum. The SMP T_g was 66.85°C and the cyclic test revealed properties remained until 30 cycles. However, the SMP T_g was higher for external biomedical applications, and the study did not progress to product realisation.
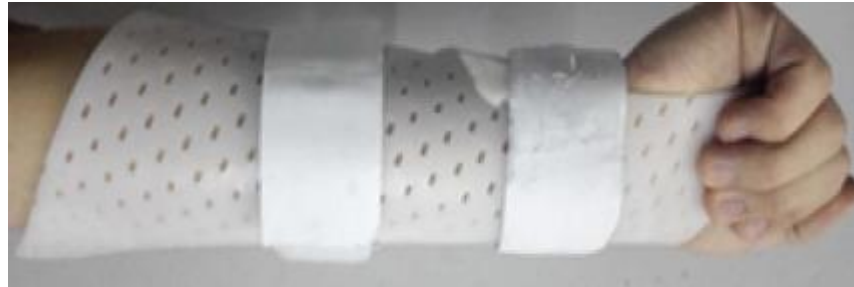
Figure 2.18: SMP-based arm fixators (a) Wrist, (b) Figure, (c) Arm.

Reproduced from [91]

2.5   Limitations and damage of SMPs

SMPs have gained substantial attention in the development of biomedical applications. However, to date, there are limited FDA approved SMP medical devices, as summarised in Table 2-2. During the literature survey, the author discovered a significant number of characterised SMPs for various invasive biomedical applications. Thermomechanical properties were often investigated at room temperature and the properties in a complex body fluid environment have hardly been explored. On the other hand, designers must be fully aware of biomaterial properties to get maximum product efficiency. Due to this critical knowledge gap and the strict certification

process, a number of preliminary studies have not been continued to complete the commercialisation process. Table 2-3 illustrates the SMPs' strengths and limitations for invasive applications.

Table 2-2: Commercialized SMP-based medical devices

Name	Manufacture	Application
All Fit [110]†	All Fit China Co., Ltd.	Shape-memory polymer surgical splint
ExoShape [21]‡	Medshape Inc.	Soft-tissue fastener made of PEEK to fix soft-tissue grafts
Morphlx [21]‡	Medshape Inc.	Suture anchor for repairing worn tendons and ligaments

† *Technical data unavailable, ‡ FDA approved*

On the other hand, the potential for SMPs in non-invasive biomedical applications is underestimated due to the significant damage which occurs during programming; thus, they are currently at their preliminary stage. This damage can be categorised into mechanical and functional damage, as shown in Figure 2.19 [231].

Table 2-3: SMP strengths and limitations in invasive applications

Strengths	Limitations
Good recovery strain	Low recovery force
Easy fabrication	Poor mechanical properties
Cost-effective	Poor electrical conductivity
Lightweight and non-toxic	Packaging and storage issues
Biocompatible	Transporting issues
Biodegradable	Fatigue susceptibility
Tuneable thermal properties	Short life cycle
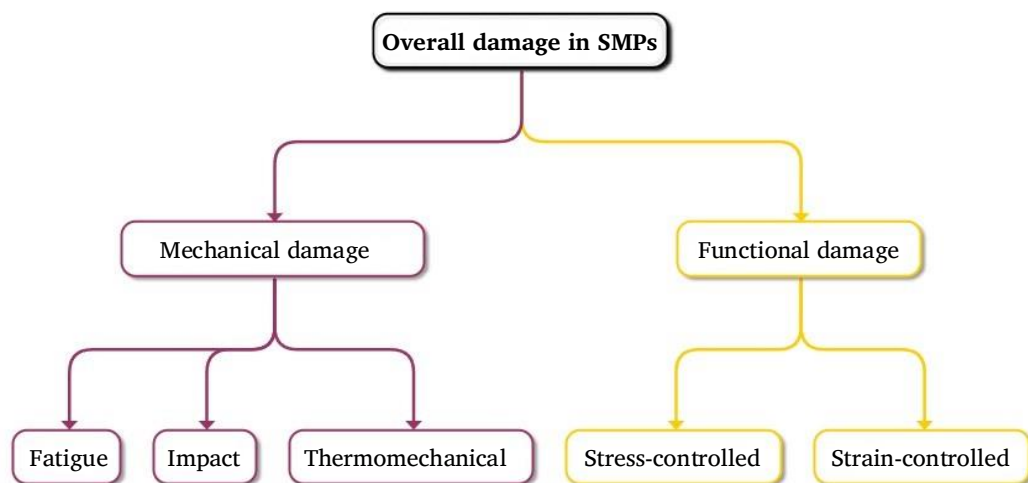
Figure 2.19: SMP damage categories. Reproduced from [232]

The mechanical damage is due to molecular chain failures in the polymeric network, resulting in a reduction in tensile, compression, and flexural mechanical properties [233]. In addition, SMP programming and recovery are also associated with the rearrangement of the polymeric chain. However, these changes are highly dependent on the thermomechanical cycle

conditions. Emmanuel et al. observed that fibre-reinforced SMPCs have a high risk of damage since the matrix tends to lose its fibre adhesion properties at higher temperatures due to softening [234]. In addition, these undesirable effects become prominent according to the material thickness, fibre type, and fibre fraction. For the first time in SMP research, Emmanuel et al. introduced the dimensionless "Areal Damage Percentage" (ADP %), as shown in equation 01 to quantify SMP damage [146].

$$ADP \% = \frac{A_d}{A_t} \times 100\% \qquad (01)$$

Where,

A_d Damage area

A_t Total deformed area
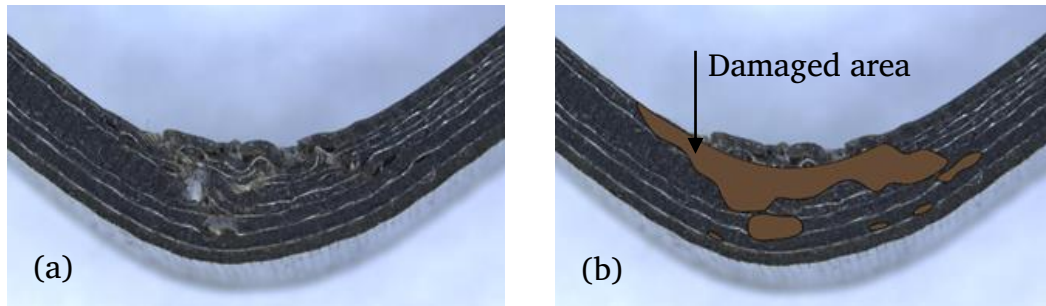
Figure 2.20: Analysis of SMP damage at programming (a) Partially damaged sample (b) Evaluation of A_d. Reproduced from [146]

The outer surface may experience tensile strain and at this stage, the polymer is flexible and weak. Hence SMPC cannot withstand such strain levels. To reduce the damage Gall et al. proposed to tailor the fibre

configuration during synthesis [28]. In addition, Emmanuel et al. identified that firstly, the storage onset temperature is the most appropriate temperature for programming and secondly, unidirectional fibres at the compression side significantly reduce the SMPC damage [234].

The SMP functional damage causes a loss of SME, R_f and R_r due to the number of programming cycles and permanent (inelastic) deformation. Therefore, in order to enhance SMP's potential in non-invasive biomedical applications, it is worth studying SMPC damage criteria and limitations.

2.6 Optimisation of polymer composites

Statistical evaluation methods are used in SMP optimization to analyse the data obtained from experiments and determine the significance of the results. Design of experiments (DOE) and analysis of variance (ANOVA) are used to identify the most significant factors and their optimal levels to achieve the desired properties of the polymer. This approach allows for a systematic and efficient way to optimize polymer materials, reducing the need for costly and time-consuming trial-and-error methods.

ANOVA is a statistical method that can be used to identify the most important factors that affect the properties of SMPs and optimize their performance. Also, ANOVA allows for quantifying the contributions of different aspects to the overall variability in a response variable, which can measure SMP/SMPC properties such as the degree of shape recovery or the transition temperature. Palanikumar et al. used ANOVA to analyse the data

obtained from the experimental study on machining glass fibre-reinforced polymer composites (GFRPC). The study aimed to identify the factors that significantly affect the surface roughness of the composites during machining [235]. Latha et al. used ANOVA analysis to determine the significant parameters affecting the thrust force during the drilling of GFRPC. This helped them develop a fuzzy logic-based model to predict the thrust force. The study provides valuable insights into the machining of GFRP composites and can aid in optimising the drilling parameters to achieve better performance [236]. The GFRPC machinability during end milling was studied by Azmi et al. using the Taguchi method [237]. The study conducted experiments by varying cutting parameters, such as cutting speed, feed rate, and depth of cut, and analysed the resulting cutting forces, surface roughness, and chip formation. The results showed that cutting speed and feed rate significantly affected cutting force and surface roughness, while the depth of cut had a minor effect. The authors also observed that the chips formed during milling were discontinuous and short in length, indicating a brittle fracture mode of the GFRPC [237]. Noryani et al. proposed a statistical framework that involves selecting the natural fibre and polymer matrix based on their mechanical properties using the regression models [238]. Applications of this method include developing high-performance polymer materials for various industries, such as automotive, construction, aerospace, and biomedical.

2.7 Orthopaedic bone immobilisation methods

The adult human skeleton (Figure 2.21) comprises 206 bones, accounts for approximately 15% of total body weight, and is the largest organ in the human body [239]. Bone is complex, living, constantly changing tissue, 30% of which consists of a soft framework of collagen protein and 70% of which is composed of Calcium phosphate mineral which provides more mechanical resistance to the tissue [240, 241].
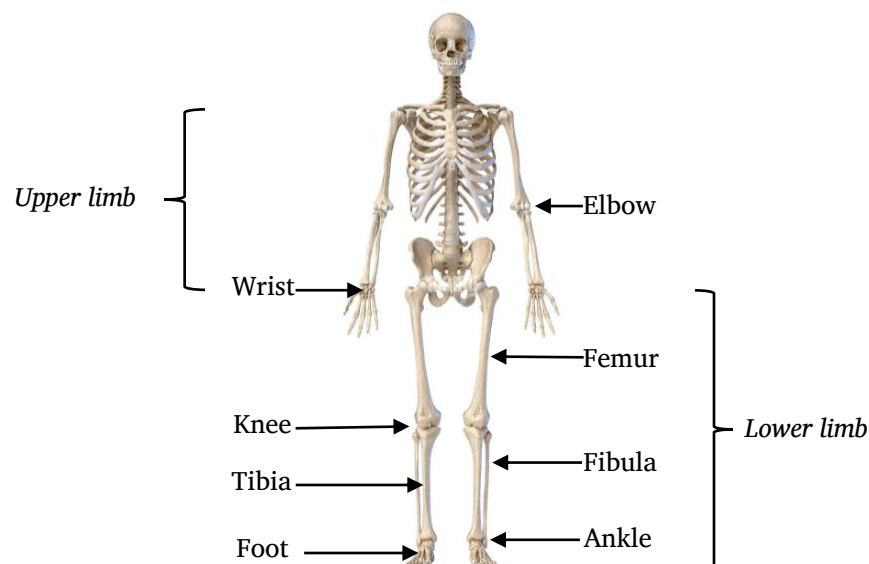
Figure 2.21: Human skeleton. Reproduced from [242]

A fracture is a break or cracks in a bone due to force that the bone cannot structurally bear [243]. Bone healing is a natural process and depends on the extent of injury; usually, an upper limb takes 2-3 weeks, while a lower limb takes 4 weeks [244]. Orthosis plays a vital role in fracture recovery by supporting weak or deformed body parts, restricting or immobilising the

motion in fractured fragments of the body, and providing continuous support to regain the full range of motion of the concerned body part. The treatments include plaster cast or surgically inserting metal rods.

Table 2-4: Commonly used splints and casts [233]

Location	Type of splint	Type of cast
Hand/ figure	Ulnar gutter, radial gutter, thumb spica, figure	Ulnar gutter, radial gutter, thumb spica
Forearm/ wrist	Volar/ dorsal forearm, single sugar-tong	Short arm, long arm
Elbow/ forearm	Long arm posterior, double sugar-tong	Long arm
Knee	Posterior knee, off-the-shelf immobiliser	Long leg
Tibia/ fibula	Posterior ankle, bulk joints	Long leg
Ankle	Posterior ankle, stirrup, bulky jones, high-top walking boot	Short leg
Foot	Posterior ankle with or without toe box, hard-soled shoe, high-top walking boot	Short leg, short leg with toe box for phalanx fracture

The author of this thesis is interested in closed fractures, commonly treated with casts and splints [245]. Casts are categorised into five types: upper extremity, lower extremity, cylinder, body and spica casts [246]. Splints are noncircumferential immobilisers that allow the fractured limb to swell. On

the other hand, casts provide less tolerance, but perfect circumferential immobilization, both of which are associated with high complication rates [247]. Cast or splint type selection depends on the injury's severity, location and stability. Commonly used types of casts and splints are shown in Table 2-4. In addition, selecting the appropriate cast or splint materials will speed up the healing, prevent complications, and enhance patient satisfaction [248]. Different types of synthetic materials for orthopaedic fracture immobilisation are available on the commercial market; some are listed in Table 2-5. Among them, plaster of Paris (POP) or fibreglass materials are more popular and widely used in clinical practices.

Table 2-5: Orthopaedic materials [249]

Material	Description
Delta-cast[1]	Cotton bandage impregnated with prepolymer
Delta-light[1]	Knitted glass fibre bandage impregnated with polyurethane prepolymer
Duraset lite[2]	Knitted fibreglass bandage impregnated with polyurethane resin
Hexcelite NS[2]	Thermoplastic linear polyester polymer with inorganic filler on a cotton base
Dynacast XR[3]	Knitted 100% glass fibre fabric impregnated with a polyurethane resin
Plaster of Paris	
Scotch cast[4]	Knitted fibreglass fabric impregnated with polyurethane resin

[1]Johnson & Johnson Orthopaedic, [2]Hexcel Medical, [3]Smith and Nephew Medical Ltd., [4]M Health Care

2.7.1 POP casting

Before POP casting technics were developed, orthopaedic surgeons made splints with bamboo, wood, plastic, plywood, aluminium, wax, starch, and leather, but all ended up with unsatisfactory results [8, 10]. Early POP casts were created by positioning the fractured body parts inside a wooden box and then filled with POP [10]. Hence the cast was too bulky and difficult for patients. Antonius and Nikolai, orthopaedic surgeons, improved on this method by suggesting the current POP bandages in the 1850s [10, 250]. Nowadays, the POP technique is extensively used in congenital issues such as paediatric management of club foot, developmental dysplasia of the hip (DDH) spica, deformities in the spine, scoliosis, pott's spine and immediate management of open and close fractures. Until now, compared with other alternatives, POP has been significantly preferred in emergency departments (ED).
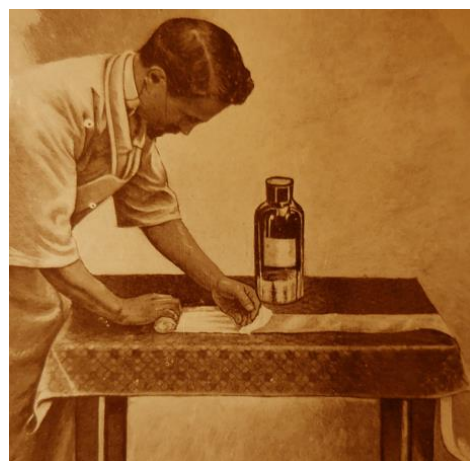
Figure 2.22: POP plastering history [10]

Gypsum is a raw state of POP comprised of fine white powder. Its chemical name is Calcium Sulphate Hemihydrate; adding water causes an exothermic reaction [251]. Due to this exothermic reaction, the temperature inside will rise and then cool down after 2~5 min. [252]. Eventually, 80% of the water evaporates, while the remaining 20% is absorbed into a hydrated crystal lattice [253]. Setting up starts just after 10 min. of mixing and continues for around 72 hrs. [254]. The POP technique offers many advantages and disadvantages, which are listed in Table 2-6.

Chemical Reaction

$$2 \, (CaSO_4 \cdot \tfrac{1}{2} H_2O) \; + \; 3H_2O \; \rightarrow \; 2 \, (CaSO_4 \cdot 2H_2O) \; + \; Heat \; [246]$$
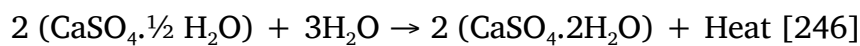
calcium sulfate hemihydrate   calcium sulfate dihydrate

Table 2-6: Advantages and disadvantages of POP casting [8, 249, 255-258]

Advantages
• Safer for external medical application
• Can be moulded
• A short casting process time
• Cheap and easily available

Disadvantages
• Needs a high level of skill, with success relying on experience

- Pressure sore or hot spots cause severe pain and might lead to ulcers or nerves damage

- Needs special attention (encourage patient to move fingers or toes to improve blood circulation; advisable not to put small objects, powders, lotions, or food spills inside the cast)

- Poor mechanical and radiographic properties
- Needs frequent communication with patient during the casting
- Sticky when applying
- Difficult to handle in a humid environment
- Messy and difficult to keep the process clean
- Susceptible to complications with allergies and prevent sores
- Cumbersome
- Needs special tools to be removed

POP casts are typically removed by manually cutting them using plaster-cutting pliers and separators. Robert Stryker introduced the first electric plaster cutter in 1945 [259]. Since then, electric oscillators have been popular; however, the instrument noise and the rotary blade are frightening, particularly for young children [260]. According to current safety protocols, electric oscillators are allowed only for padded casts and usage must be stopped if the patient feels any heat [261]. Therefore, water soaking is an ideal solution to remove children's POP casts, but this takes over 30 min. [262]. Figure 2.23 illustrates typical POP cast removal techniques and tools.

Figure 2.23: POP cast removing tools

2.7.2 Fibreglass casting

The first successful alternative for POP was introduced in 1980, with a material composed of fibreglass with polyurethane resin [263]. In the 1950s, fibreglass tape bandages were introduced [264]. The properties of fibreglass (strength, rigidity and elasticity) encourage its use as a casting material. David et al. compared two fibreglass casting techniques. In the standard method, the fibreglass was stretched, and it warped, with substantial tension causing more compressive stress during the curing. In contrast, the stretch-relax technique involved a process in which the fibreglass was stretched, then allowed to relax before being laid around the fractured segment [263, 265].

There are two types of fibreglass used in the medical field. In the first method, the fibreglass reel comes with in-built polyurethane resins [263]. The chemical reaction and setting up start after its package is opened up and it is taken out. In the second method, water or gel initiates the hardening process [265]. Compared to POP, the fibreglass casting technique is more sophisticated, and it is preferred in order to avoid structural failures.

Moreover, fibreglass's durability is almost twice that of POP [256]. In humid conditions, a fibreglass cast is up to 33% stronger than a POP cast [265].
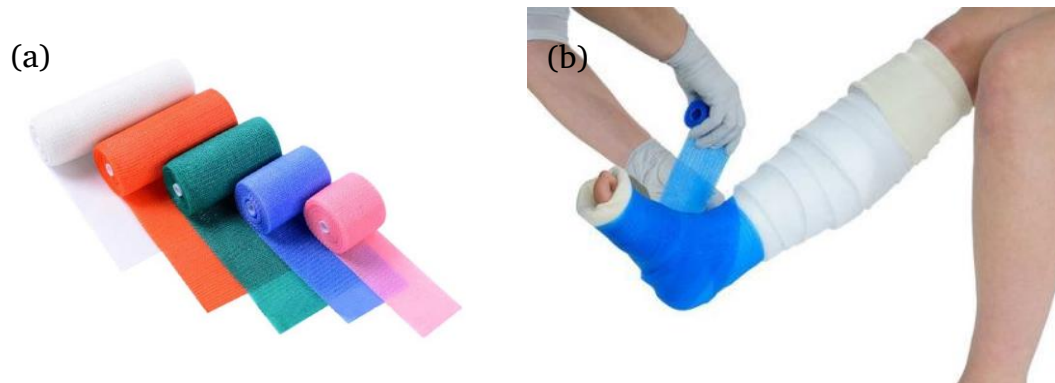
Figure 2.24: Fibreglass casting, (a) Casting tape, (b) Lower limb casting

Table 2-7: Advantages and disadvantages of fibreglass casting [258, 266-269]

Advantages
• Cleaner process
• Greater strength, porosity, lighter weight and radiolucency
• Durable, convenient, and with uniform thickness
• Quick to set up and comfortable
• Resistant to water, thus beneficial for military and paediatric applications

Disadvantages
• Difficult to mould
• Containing toxic or harmful components (e.g. cyanates)
• Eliciting asthmatic responses, itching, redness and dryness

2.7.3 Wood composite casting

As an alternative to POP and fibreglass casting, in 2010, an innovative wood composite material was introduced for fracture treatment [258]. This product incorporates wood chips in a thermoplastic polymer that comes in 2 mm and 4 mm thick sheets or 4 cm and 8 cm casting tapes [257].

(a)　(b)

Figure 2.25: Wood composite cast, (a) Non-removable rigid cast, (b) Removable semi-rigid orthosis [258].

The wood composite is heated to 65°C prior to the application, after which the desired shape can be easily moulded. The material regains its original strength at 45°C, offering extended work time for moulding [258]. Making changes after the cast has solidified is impossible with POP or fibreglass casting. On the other hand, wood composite tapes are self-adhesive when warm; thus, their high pliability allows readjustments of the shape [7]. Additionally, Pirhonen et al. investigated the mechanical properties and found that the ideal thickness for a wood composite cast is 2 mm when flexibility is needed [257].

Hirsimäki et al. investigated wood composite cast performance with 30 patients aged between 24 to 76 years. These patients were treated with semi-rigid orthosis, as shown in Figure 2.25. Due to its multiple layers, it was reported that applying the cast in the correct position was difficult and the preheating process was not fast enough [258]. Nevertheless, the researchers revealed that the semi-rigid open wood composite cast was strong enough to stabilize ankle fracture.

2.8   Critical factors and complications in orthopaedic plaster treatment

Various factors are significant during the preparation and provision of orthopaedic plaster treatment. An exothermic chemical reaction takes place during POP and fibreglass cast solidification. During POP casting, the plaster roll must be soaked vertically for sufficient time, usually indicated by bubbles ceasing to rise to the surface. The water in the container should be deep enough to cover the POP plaster. Only clean water must be utilised, and any previously used water should be avoided; otherwise, the setting time will be accelerated. In addition, it is important to use water at temperature ideally between 21°C and 23°C, and not exceeding 35°C [248]. This is because the combined effect of the POP chemical reaction and hot water may generate significantly higher temperatures. Hutchinson et al. revealed that the cast thickness increases the temperature under the cast [70]. Interestingly, the undercast padding and thickness are not influenced by the temperature profile beneath the cast after it is applied [270].

74

On the other hand, the undercast temperature is crucial since human skin comprises a lipid membrane of highly thermal-sensitive cells. Within a matter of several minutes, the skin cells may become damaged with exposure to heat. Williamson et al. presented the injury threshold temperature that human skin can withstand without forming epidermolysis symptoms such as vesicles, bullas and blisters [271]. The depth of the burn depends upon the degree of temperature, nature of the exciting agent, duration of contact, and susceptibility, as illustrated in Figure 2.26. The developed time-temperature relationship is such that at 49°C for 3 min. this causes the first degree of thermal injury. Further, Hutchinson et al. classified thermal burns based on Williamson et al.'s findings [70]. Following Moritz and Henriqures experiments in 1949, Read et al. revealed that when human skin is exposed to a temperature of around 45°C for 2-3 hrs., this could cause skin burns [71]. Thus, splints are safer since the absence of circumferential surfaces lets heat dissipates fast.

Compartment syndrome is a commonly reported painful and dangerous complication in POP and fibreglass casting which occurs due to the tightness of the applied cast [263]. A higher undercast pressure damage muscles, nerves or blood vessels in the area covered by the cast. This damage might be irreversible if the orthopaedic technician does not detect it immediately [272]. It is worth noting that cell damage occurs sooner when temperature and pressure are combined [13].

First-degree burn   Second-degree burn   Third-degree burn

Skin   *Skin*   *Skin*

1
2
3

1 - Epidermis   2 - Dermis   3 - Fat
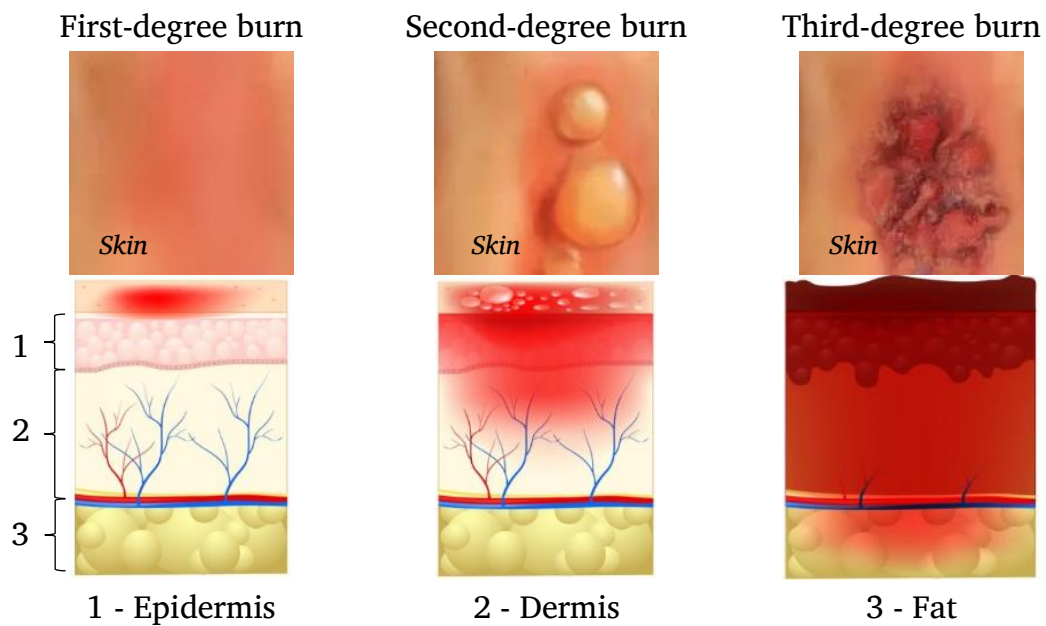
Figure 2.26: Burn injury attorney

Plaster complications can be divided into systemic complications, which affect the whole body and local complications, which occurs only where the plaster has been applied [273, 274]. The complications range from minor to severe, varying with the time the cast is worn. These complications can be minimised with good nursing practices and physiotherapy, leading to speedy recovery [275, 276]. In this section, the author outlines local complications that occur just after a period of time; some common complications are listed in Figure 2.27. Interestingly, around 72% of orthopaedic injuries are reported during cast removal [277]. Therefore orthopaedic casting and removal cannot be performed without training, knowledge, and good judgement [261].
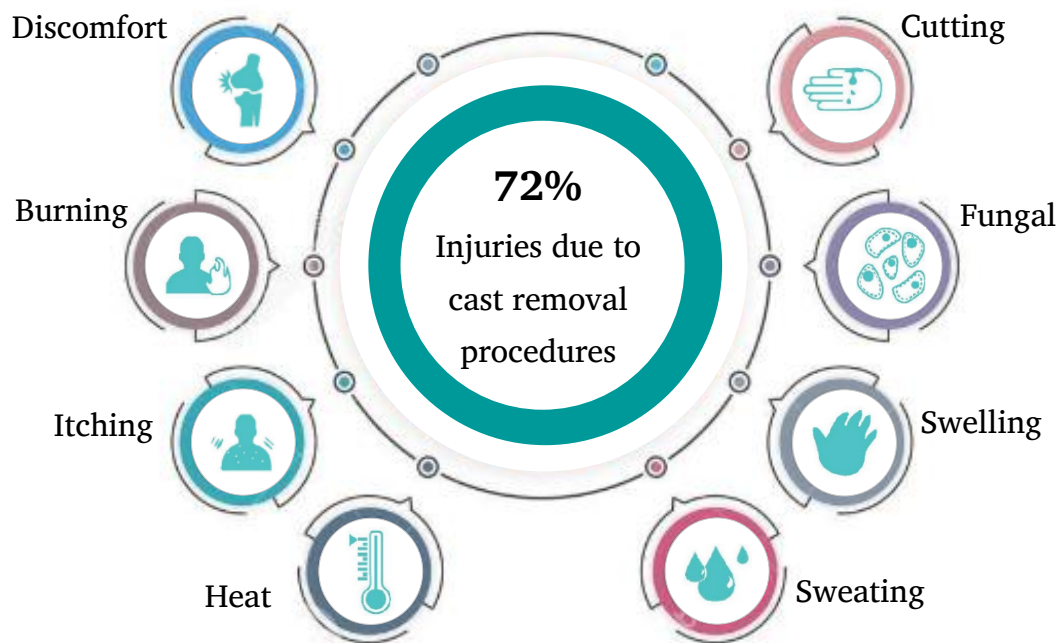
Figure 2.27: Complications of orthopaedic casts. Reproduced from [277]

The author of this thesis strongly believes SME can be effectively used to eliminate the current drawbacks and complications associated with the orthopaedic casting and removal process. To date, plenty of SMP-based research work has been published for invasive biomedical applications. However, there is insufficient attention as yet to non-invasive applications. Thus, in this thesis, a novel SMP material will be introduced which will benefit patients' who suffer from bone fractures as well as staff working in the orthopaedic area.

2.9   Finite element analysis of SMPs

FEA is a computational technique used to analyse and predict the behaviour of materials and structures under various physical conditions. FEA can be used to simulate the behaviour of SMPs under different conditions, such as temperature changes, mechanical loading, and deformation [278]. Viscoelastic modelling is an essential component of FEA for SMP/SMPCs. Viscoelasticity refers to the time-dependent, nonlinear behaviour of materials under stress. Viscoelastic modelling allows for the characterization of the time-dependent behaviour of the material, which is essential for predicting the response of SMPs to loading over time [279]. These properties can be obtained through experimental characterization techniques such as DSC and DMA. Additionally, viscoelastic modelling can help account for the effect of temperature on the material's properties, which is critical for accurately predicting shape recovery behaviour under different conditions.

SMP viscoelastic models use the Prony series, which can be used to represent the material's time-dependent behaviour over a range of temperatures [280]. Another commonly used model is Maxwell and Kelvin-Voigt, which consists of a series of springs and dashpots that can represent the viscoelastic behaviour of the material.

Mailen et al. presented a comprehensive FEA model for the self-folding behaviour of SMP sheets, considering the effects of both thermal and mechanical stress on the material's behaviour [281]. The model is based on a

thermal-stress coupling approach and the material properties of the SMP, such as the modulus of elasticity and coefficient of thermal expansion, as well as the temperature distribution across the sheet. To validate the model author observed folding angles under different heating conditions. Additionally, Mailen et al. investigated the effects of sheet thickness against the folding angle, which provides insights into the design and optimisation of SMP-based devices and systems. The author comprehensively discusses currently published SMP FEA viscoelastic models in Chapter 5.2.

2.10 Summary

SMPs are evolving as a promising material for smart engineering applications due to their ability to undergo shape changes upon exposure to external stimuli such as temperature, light, electricity, water, pH, magnetism, and specific ions. The phenomenon of shape change and reversal is called SME and is due to an entropy change in polymer molecules. The SME is driven by cross-links which are of two types: chemical and physical. The chemically cross-linked glassy thermosets offered greater flexibility to tailor the activation temperature and are soft at elevated temperatures. SMPs are generally weak in strength; thus, they are often reinforced with fibres and fillers. Carbon and glass fibres and carbon-based NPs are more popular among SMP researchers. The SMP/ SMPC programming and shape recovery behaviour is characterised by their thermomechanical cycle.

SMPs exhibit superior characteristics such as a tailorable glass transition temperature, responsiveness to various stimuli, large recoverable strains, low density, low cost, recyclability, manufacturability, biodegradability, and biocompatibility. The growing number of published journal articles concerning SMPs demonstrated researchers' continued interest in them, and they can be seen in applications for space, aerospace, flexible electronics, and smart textiles. In addition, SMPs have also shown tremendous potential for biomedical applications since surgical implants can be deployed with minimal invasiveness. With the advancement of polymer chemistry, recently developed SMPs demonstrate advanced features such as minimal systemic toxicity, low rejection by the host, stability, and natural biodegradability. Research over the years has proved a number of SMP biomedical applications in self-tightening sutures, catheters, vascular stents, tissue engineering, drug delivery, orthodontics, and orthopaedics. To date, USA MedShape has successfully commercialised SMP suture anchor and soft tissue fasteners with FDA approval. Still, many research outcomes have been terminated without successful progression due to deficiencies in synthesis and processing.

POP and fibreglass plastering techniques are widely used for fractured bone immobilisation. Nevertheless, these traditional casts are associated with many drawbacks, such as their being uncomfortable and cumbersome, and their success depending on technicians' competence and experience. Moreover, the internally developed compartment syndrome limits blood flow

to arteries, and hotspots can cause severe pain, which leads to ulcers, nerve damage, or permanent loss of body parts. Interestingly, SMPs can effectively address POP and fibreglass casting complications; thus, SMPs have shown immense potential in orthopaedic applications.

However, rarely are characterised and suitable SMPs available, and a significant material gap must be solved before they are used in non-invasive orthopaedic applications. Therefore, synthesising a novel SMP and a comprehensive characterisation is mandatory to verify the required structural properties at body temperature. Continuous research is warranted to cater for SMP orthopaedic non-invasive orthopaedic applications that benefit musculoskeletal patients.

CHAPTER 3: SHAPE MEMORY POLYMER

SYNTHESIS

3.1 Introduction

Natural and synthetic polymers play a significant role in advanced biomedical applications and have grown rapidly over the past two decades. Among the polymers, SMPs extensively studied and successfully delivered promising applications in the field of biomedical. However, the early reported biomedical applications mainly focused on minimally invasive surgeries and devices. To date, external applications with SMP are hardly found. This is due to the unavailability of promising SMP for external biomedical applications in the commercial market.

The author identified that using SMP in external biomedical applications such as fracture fixators and orthosis requires rigidity at body temperature (37°C) [230]. Moreover, above 49°C over 3 min. can cause the first degree of thermal injury [271]. Therefore, tailoring activation temperature without sacrificing shape memory properties is much needed but challenging. Thus, in this chapter, four chemicals were synthesised according to their stoichiometric ratios and tailored the SMP activation temperature to a greater extent until they suit external biomedical applications. To find the best match for orthopaedic external applications, shape fixity ratio, shape retention ratio and shape recovery ratio were comprehensively analysed, and the best-synthesised ratio is selected for further experimentation.
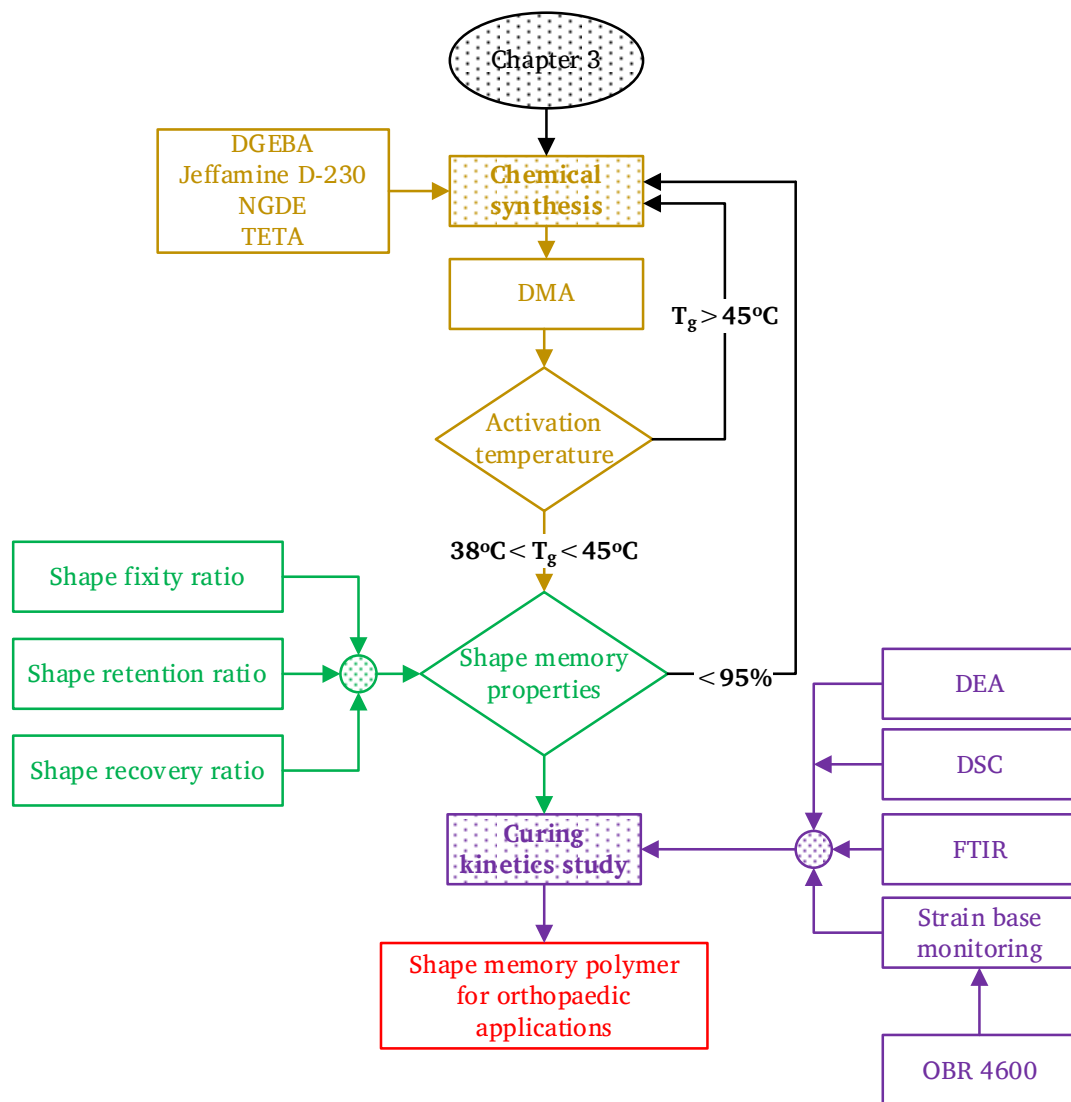
Figure 3.1: Technical overview of Chapter 3

During the literature review, the author identified that curing cycles may also influence delicate SMEs. Thus, with the aid of DEA, DSC and FTIR, the curing kinetics have been systemically studied, and a novel curing cycle was introduced in this chapter. According to the referred literature, the proposed novel curing cycle improved SME by 25%. A brief technical overview of Chapter 3 is illustrated in Figure 3.1. This chapter's primary outcome is finding a suitable SMP for orthopaedic external biomedical

applications and how delicate SME can be further enhanced with the aid of curing kinetics. The detailed new knowledge is highly important since most SMP researchers have to synthesise SMPs for their research requirements since they are not available to purchase commercially. Therefore, this chapter helps to create an SMP synthesis framework for future application-oriented SMP-based research and developments. The content of this chapter is published in J_1 and C_1 as listed in Chapter 1.6 of the thesis.

3.2   Materials and SMP synthesis

Bisphenol A is an organic compound that was synthesized in 1981[282]. Since then, diglycidyl ether of bisphenol-A (DGEBA) monomer is a key building block of many biomedical engineering applications due to the tailorable activation temperature, simplicity of the chemistry involved, availability and better mechanical and structural properties [283, 284]. The introduced aliphatic and aromatic amines varied the crosslinked density and chain flexibility for the purpose [14, 284-287].

DGEBA monomer with epoxy value of 190 g/eq and Neopentyl glycol diglycidyl ether (NGDE) chain extender were purchased from Huntsman Australia. Epoxy value of 59.5 g/eq poly(propylene glyol)bis(2-aminopropyl)ether (Jeffamine D-230) di-amine and triethylenetetramine (TETA) hardeners were purchased from Sigma Aldrich Australia. All chemicals and materials were used as received and their chemical structures are shown

in Figure 3.2. Initially, eighteen SMP specimens were fabricated according to their stoichiometric mass ratios and compositions are detailed in Table 3-1.

DGEBA   NGDE

D-230   TETA
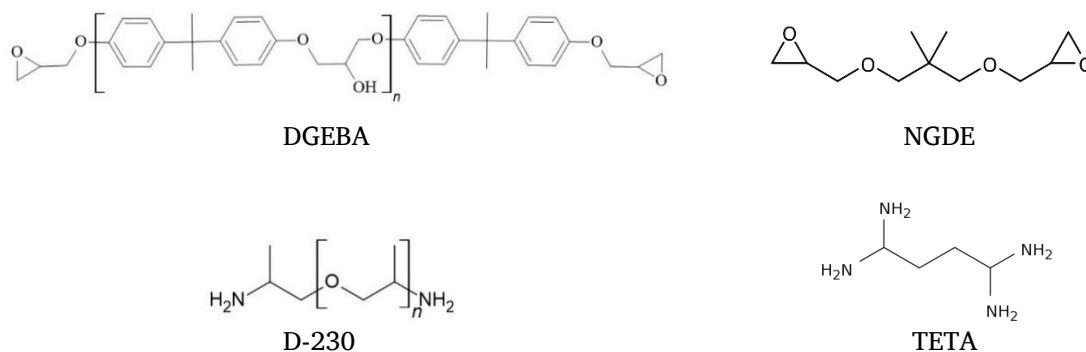
Figure 3.2: Chemical structures

The mould was made of two $400 \times 400 \times 5$ mm^3 tempered glass plates. To remove the fabricated SMP sheet without breaking it, a non-stick peel fly sticker was pasted as a release agent on the inner surfaces of the glasses. Seven metal spacers were then placed carefully to control the uniform thickness, as seen in Figure 3.3. The side walls were then sealed with a thick layer of temperature-resistant silicone, leaving an opening on the top. The mould was closed with a second tempered glass plate, and bulldog clips were employed to keep everything together. The mould was kept at room temperature for a day to dry before epoxy pouring.
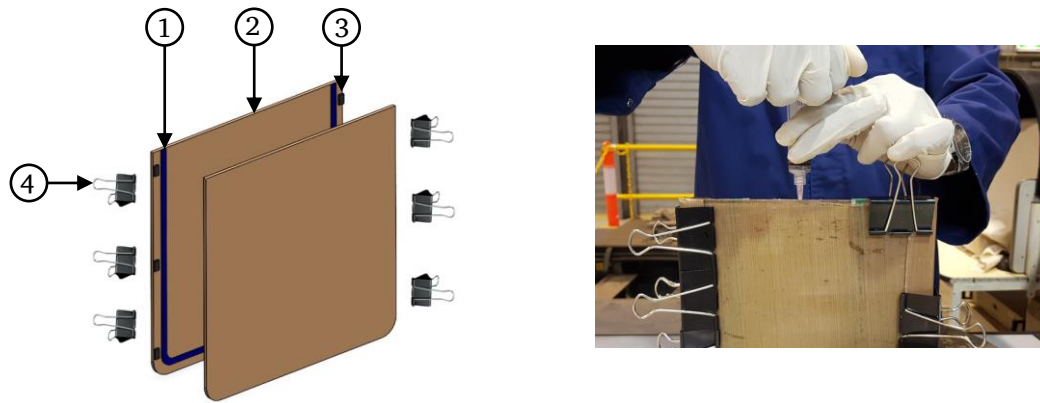
1   Silicon layer
2   5 mm thick tempered glass plate
3   Metal spacer (minimum 7)
4   55 mm bulldog clip (minimum 6)

Figure 3.3: SMP mould and preparation

Once the mould was ready, according to the prescribed weight ratio, synthesised the epoxy and degassed it in the vacuum chamber for 15 min. After that, epoxy was gradually poured into a glass mould from one side allowing air to escape from the other side. This was done to ensure no air traps within fibre layers creating voids. Subsequently, the synthesised SMPs were cured in a temperature-controlled electric oven for 1.5 hrs. at 100°C and followed post-curing at 135°C for an hour (Curing cycle named DGEBA-100). Then using a water jet cutter, SMPs were cut into the standard test specimens as shown in Table 3-2 for DMA and shape memory experiments.

Table 3-1: SMP synthesised mass ratios

Sample number		DGEBA	TETA	D-230	NGDE
Group 1	1A	07.819	1.000	--	--
	1B	03.193	--	1.000	--
	1C	09.774	1.000	0.612	--
	1D	13.032	1.000	1.632	--
	1E	19.547	1.000	3.673	--
	1F	39.095	1.000	9.794	--
Group 2	2A	--	--	1.000	2.521
	2B	0.639	--	1.000	2.017
	2C	1.277	--	1.000	1.513
	2D	1.916	--	1.000	1.008
	2E	2.555	--	1.000	0.504
	2F	3.193	--	1.000	--
Group 3	3A	--	1.000	--	6.173
	3B	1.564	1.000	--	4.938
	3C	3.128	1.000	--	3.704
	3D	4.691	1.000	--	2.469
	3E	6.255	1.000	--	1.235
	3F	7.819	1.000	--	--

Table 3-2: SMP standard test specimens

Experiment	Dimension, mm	
	Length	Width
DMA	45	8
Shape fixity, retention and recovery	100	10

3.3   SMP Characterisation techniques

In this section, the author comprehensively investigates the viscoelastic and shape memory properties of Table 3-1 synthesised SMPs. DMA analysis was performed with a TA instrument hybrid rheometer (Discovery HR-2)

under the ASTM D7028 standard. The specimens were kept for 5 min. at -20°C before starting a 5°C/min. temperature ramping up till reaching 120°C in DMA oscillation mode with 1 Hz frequency. Subsequently, the shape memory properties, R_f, $R_{f,30}$ and R_r were measured. In this study, SMP properties were established through the fold-deploy method and related equations are shown in 3.1 and 3.2. The fabricated stainless steel SMP 60°, 90° and 180° programming tools are illustrated in Figure 3.4. During the evaluation, SMP specimens were kept at respective T_g for 10 min. in an electric oven until they reached their thermal equilibrium. After that, SMP specimens were programmed using a 90° bend tool which has a 12 mm diameter. The constrain forces were kept until the SMP specimen reached room temperature (~23°C). Then the constraining forces were removed, and the spring-back angle was measured for R_f analysis. Next, the SMPs were heated to their respective T_g and recovery behaviour was video recorded. After that, recovered angles were measured and the R_r was calculated by referring to equation 3.2. In addition, the 90° programmed SMPs were kept at room temperature for 30 days and shape fixity ratios were calculated every five consecutive days. The retained shape after 30 days was defined as the shape retention ($R_{f,30}$) of SMP. The average results of the five specimens are considered in R_f, $R_{f,30}$ and R_r analysis. Gwyddion open-source software was used for data analysis and smoothed using the GRG nonlinear engine, as shown in equation 3.3. All the experiments were conducted at room temperature and 40%-60% humidity unless otherwise specified.
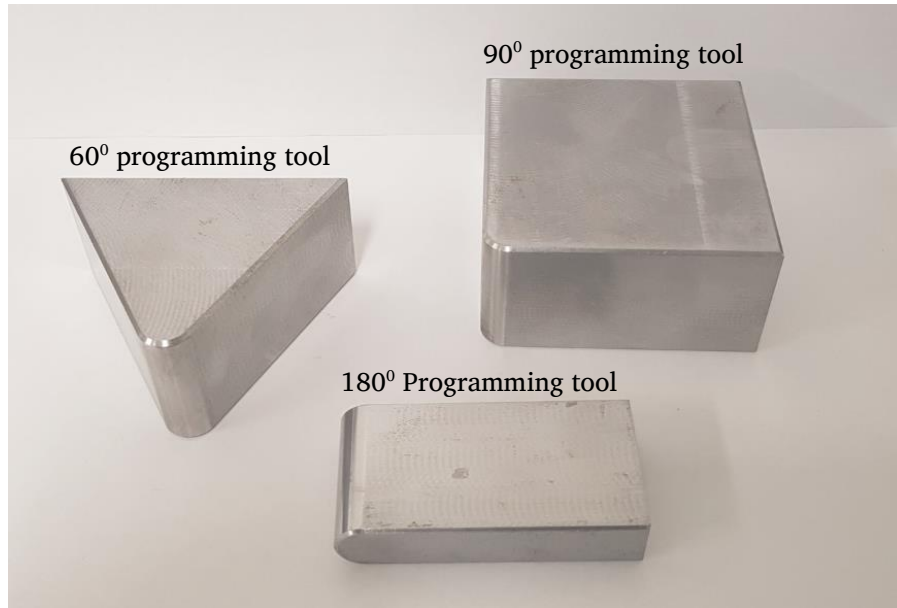
Figure 3.4: SMP 60°, 90° and 180° programming tools

$$R_f = \frac{\theta_{fixed}}{\theta_{max}} \times 100\% \tag{3.1}$$

$$R_r = \frac{\theta_{max} - \theta_i}{\theta_{max}} \times 100\% \tag{3.2}$$

Where,

θ_{fixed} Measured bending angle

θ_{max} Programmed bending angle

θ_i Recovered bending angle

GRG nonlinear engine

$$R_t = A(1 - e^{(-q^{tm})}) \tag{3.3}$$

Where,

R_t Recovery at time

A, q and m are constant
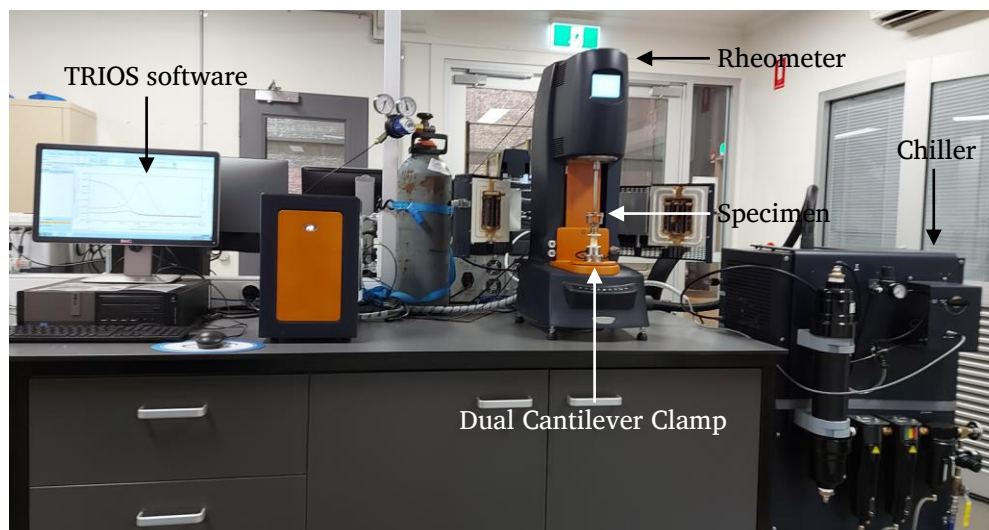
Figure 3.5: DMA hybrid rheometer experimental setup

To monitor the cure state of thermosetting SMPs, NETZSCH DEA 288 Ionic instrument was used with an IDEX115L DE sensor and J-type PFA insulated thermocouples. The DEA method uses a capacitor arrangement to apply an alternating electrical field in order to measure dielectric changes. The IDEX 115L sensor contained nickel electrodes on a flexible polyimide substrate in a comb structure with an electrode distance of 115 μm. During the DEA test, a $10 \times 10 \times 0.2$ cm^3 neat polymer specimen was synthesised. The DEA was carried out in multi-frequency mode from 1 Hz to 100 kHz and the data were analysed with NETZSCH Proteus 8.0 software.

To measure the synthesised SMP cured percentage, isothermal and non-isothermal analyses were conducted with a TA Instrument Discovery DSC-25. The instrument is shown in Figure 3.6. The cured solid samples were heated from -50ºC to 300ºC with a 5 ºC/min. constant heating rate. Both liquid and solid samples were kept in hermetically sealed aluminium pans. During the

DSC experiments, the liquid samples' weight was kept at 8 ± 0.1 mg, and the solid sample weights were maintained at 12 ± 0.1 mg.

Figure 3.6: TA instrument DSC-25

The FTIR analysis was conducted with a Nicolet iS50 spectrometer from Thermo Fisher Scientific, Inc. The uncured SMP resin and the cured solid SMP specimens were analysed with an attenuated total reflection module. The spectrum (Vector 32) data were recorded through 400-4000 cm^{-1} (2000-2500 nm) wavenumbers with a resolution of 0.5 cm^{-1} and analysed through OMNIC software.

At curing, the polymers are simultaneously undergone expansion or shrinkage. This effect was captured using a distributed optical fibre network (DOFN) and compared with DEA results. Thus, the author aims to introduce a real-time curing kinetics monitoring novel method which can avoid single-point sensing. A single-mode 125 μm optical fibre was embedded in SMP, as shown in Figure 3.7. The SMP specimen was connected to ODiSI OBR 4600

optical backscatter reflectometer and the strain readings were acquired at curing, post-curing and natural cooling. Due to the long duration of the curing process, single scans were taken every minute during the first hour. Afterwards, data were recorded every 5 min. The effect of temperature was compensated during the strain data analysis.
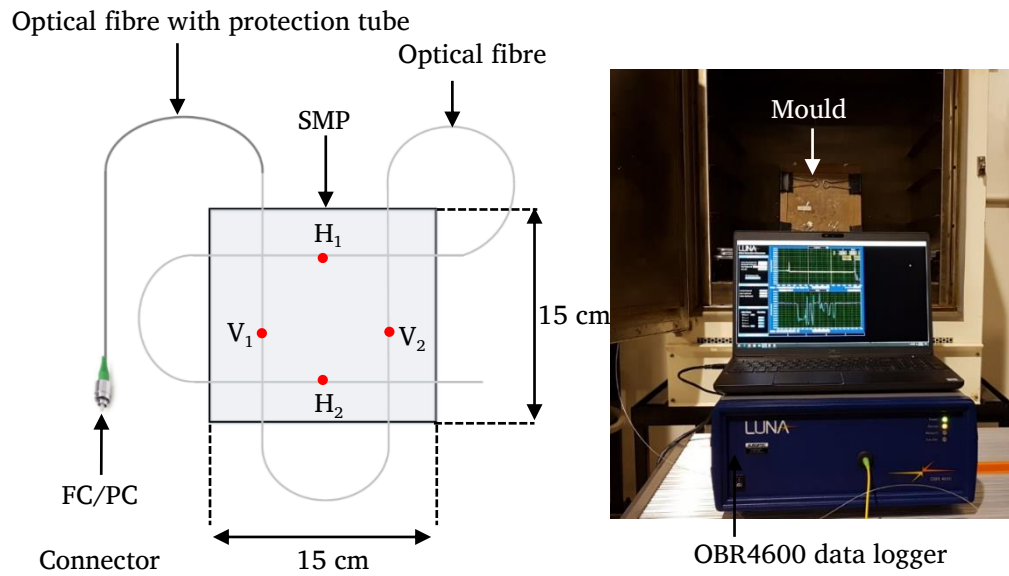
Figure 3.7: Distributed optical fibre sensing arrangement in SMP specimen for strain measurement

3.4 SMP synthesis and selection

According to the stoichiometric ratio, the synthesized mass ratios are present in Table 3-1. In Group 1, TETA was kept constant and the DGEBA was varied with the D-230 hardener. In Group 2, D-230 was kept constant and DGEBA and NGDE epoxies were changed according to their stoichiometric ratios.

Table 3-3 presents the calculated T_g, R_f, $R_{f,30}$ and R_r of synthesised SMPs. For Group 1, T_g occurred over 50°C, which is slightly high for external biomedical applications. However, adding D-230 drops the T_g of Group 1, but a clear pattern could not be identified.

Table 3-3: SMP T_g, R_f, $R_{f,30}$ and R_r properties

Sample number		T_g (°C)‡	R_f (%)*	$R_{f,30}$ (%)*	R_r (%)*
Group 1	1A	$59.13^{\pm 0.15}$	--	--	--
	1B	$50.34^{\pm 0.24}$	--	--	--
	1C	$54.73^{\pm 0.78}$	--	--	--
	1D	$58.84^{\pm 0.35}$	--	--	--
	1E	$53.03^{\pm 0.11}$	--	--	--
	1F	$52.10^{\pm 0.51}$	--	--	--
Group 2	2A†	--	--	--	--
	2B†	--	--	--	--
	2C	$18.83^{\pm 0.21}$	60.83	00.00	99.36
	2D	$27.51^{\pm 0.33}$	99.80	50.52	98.61
	2E	$46.56^{\pm 0.12}$	99.50	97.00	99.57
	2F	$50.34^{\pm 0.52}$	99.09	94.39	94.38
Group 3	3A	$17.22^{\pm 0.27}$	94.48	00.00	91.52
	3B	$21.45^{\pm 0.20}$	95.13	39.78	89.28
	3C	$40.14^{\pm 0.46}$	90.97	82.11	83.01
	3D	$49.35^{\pm 0.78}$	91.04	84.22	79.93
	3E	$59.29^{\pm 0.11}$	92.48	88.56	80.02
	3F	$59.14^{\pm 0.08}$	--	--	--

‡   Storage onset transition temperature

*   Standard deviation is within ± 0.25

†   Rubbery state at room temperature

Due to the absence of TETA, Group 2 showed a distinctive T_g behaviour. 2A and 2B SMP specimens were at their rubbery stage at room temperature;

thus not interested in calculating the 2A and 2B T_g and shape memory properties.

In Group 2, a maximum T_g of 50.34°C was observed in 2F, which had DGEBA and D-230 for 3.193:1.000 mass ratios. The addition of aromatic DGEBA over NGDE increased the T_g and a clear trend can be seen in Figure 3.8. On the other hand, TETA was kept constant in Group 3, and the obtained T_g ranged from 17.22°C to 59.14°C.
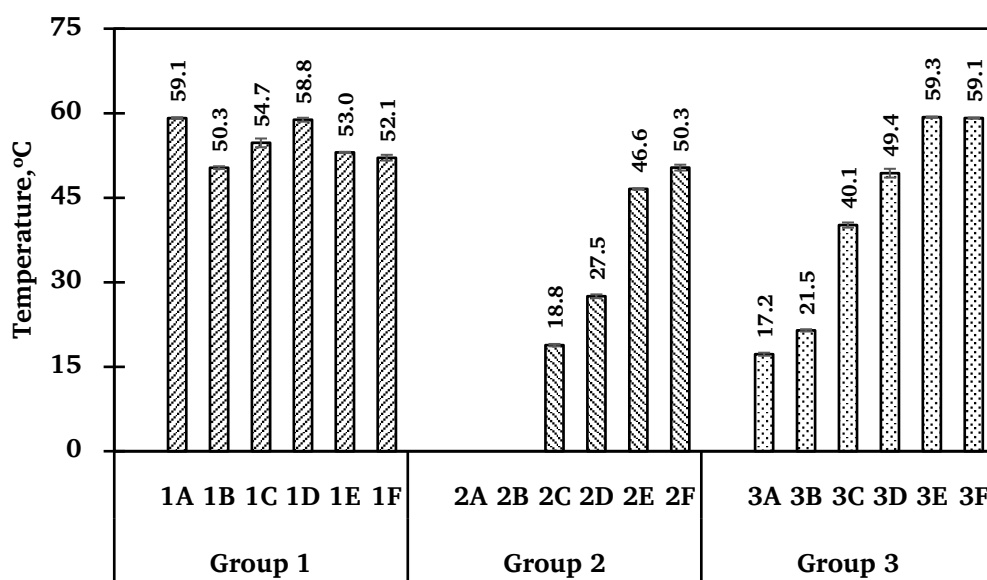
Figure 3.8: Storage onset T_g

Figure 3.9 presents the Group 2 storage modulus obtained from DMA trials. It has been observed that the glassy storage modulus behaves relatively constant until the temperature reached their glassy onset temperature. The difference between maximum and minimum at 0°C was 0.34 GPa. On the other hand, 2D and 2E storage modulus remained constant until the

temperature reached 20°C. For 2F, a higher storage modulus was recorded compared to other SMPs and this could be due to the absence of NGDE.
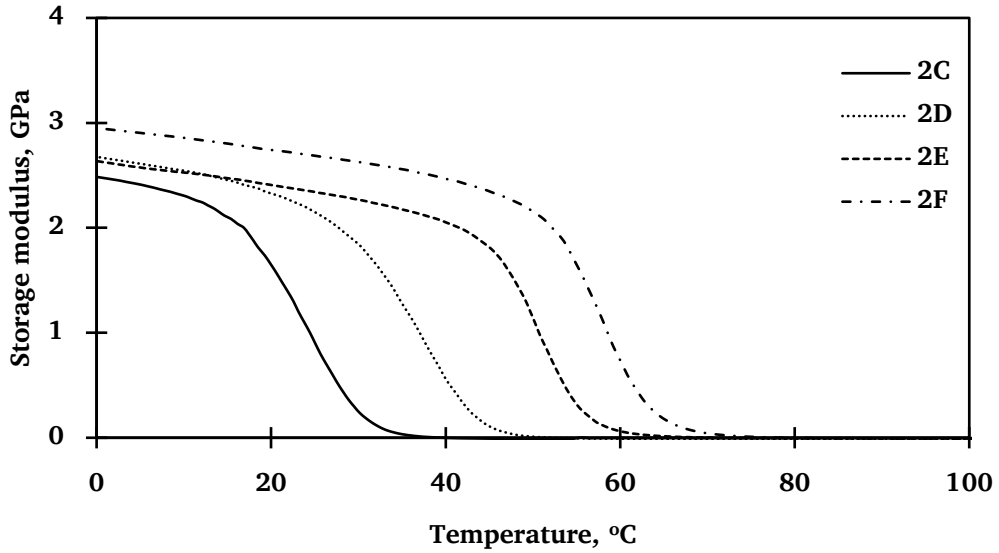
Figure 3.9: Storage modulus of Group 2

The ratio of glassy to rubbery storage modules was found to be above 1×10^3, indicating that all SMPs indicated a better SME [156]. Further, it was observed that a narrow transition region is ideal for quick activation and maintain deformed shape until the triggering temperature is met. [284]. In 2E, a 5.4°C transition range was observed; hence it is more suitable for quick response applications.

Next, the R_f, $R_{f,30}$ and R_r were evaluated, and the results are given in Table 3-3. The Group 1 SMPs were too stiff to program at storage onset T_g; therefore, Group 1 ignored without further analysis. Additionally, Table 3-3 revealed 2D, 2E and 2F obtained over 99% R_f and significantly higher R_r

(>94%). Besides that, Group 2 R_f and R_r are higher than the respective Group 3 SMP specimens.
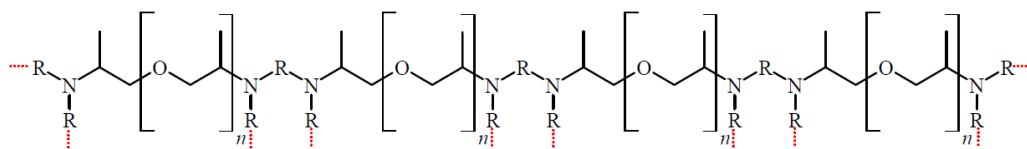
Where R,
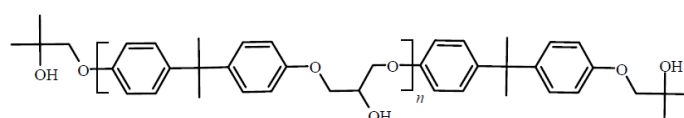
Figure 3.10: 2E SMP polymer chain

Isothermal free strain recovery can negatively affect the SMP applications. Therefore, SMPs shape retention ratio was closely monitored and noticed recovery angle changing rates in the first five-day period were higher than in the rest of the period. 2F recovered at a rate of 0.54 degrees/day for the first five consecutive days, followed by a rate of 0.02 degrees/day for the rest of the 25 days. Similarly, a 0.22 degrees/day recovery rate was obtained for 2E for the first five days; this showed higher shape memory retention performances than other specimens. In addition, 2E's shape retention ratio was 2.61% higher than 2F's. Moreover, the 2E storage onset activation temperature was 3.78°C less than 2F's and within the safe margin of Hutchinson et al.'s skin damage model; thus, the 2E activation temperature is safer for fabricated non-invasive devices than 2F's [70]. Therefore, it can be

96

concluded that 2E offered the best chemical configuration for fabricating non-invasive biomedical devices with reference to activation temperature, shape fixity ratio and shape retention ratio. Thus, from this onwards in this thesis, the author will only consider DGEBA: NGDE: D-230 for 2.555: 0.504: 1.000 (2E) synthesis mass ratio. The 2E chemical structure is shown in Figure 3.10.

To the completion of this chapter, the author presented the mechanical properties of selected 2E chemical configuration in Table A01 which is shown in Appendix. According to the Table A01, the synthesised 2E reported 40.51 MPa, 43.60 MPa and 78.86 MPa tensile, compression and flexural strength, respectively. Additionally, 2E specimen 0.048 J/mm impact resistance is shown. The standards and the equipment's used to evaluate mechanical properties were comprehensively discussed and compared in Chapter 4.4.

3.5   Curing kinetics experimentation

Curing involves a chemical reaction process; as part of this process, cross-links are formed between molecules. In the first phase, DEA equipment logged the reaction process with respect to time, which provides insight into the curing process. The log viscosity and permittivity were analysed through DEA and then compared with DSC results. The kinetic parameters such as activation energy and pre-exponential factor were calculated from Ozawa and Kissinger methods and discussed. The Kissinger method is the most popular and unbeatably simple way of estimating activation energy in thermally stimulated processes [288]. The methods used by Ozawa and Kissinger to

calculate activation energy made the assumption that chemical reactions were first order; however, if the temperature ram is not linear, this leads to an extreme error. The main advantage is Kissinger method can present a single value of the activation energy regardless of the process complexity. After that, the theoretical time required to cure was calculated and proved.

Further, SMP curing results were verified with non-destructive FTIR analytical method. The internal changes at curing analysed with an embedded optical fibre network experimental model. To the authors' knowledge, this is the first time that rheological changes were monitored using strain data. The validity and repeatability of the polymer composites' experimental results depend on synthesis materials' purity, instrumentation, and human errors. To avoid the uncertainty of results, the experimental program was conducted strictly following the standers and conditions. Further, synthesised SMP properties have shown an excellent consistency in Chapter 4.

3.5.1 Dielectric analysis

DEA measures changes in a polymer's dielectric properties and cures resin as a function of the temperature, time and frequency of the applied alternating electrical field. The synthesized chemical has negatively and positively charged ionic compounds and, with the alternate field, would be able to move back and forth during the DEA test. Thus, the IDEX sensor can measure the resistance of the ionic movements and the inverse of that is called the log ion viscosity.
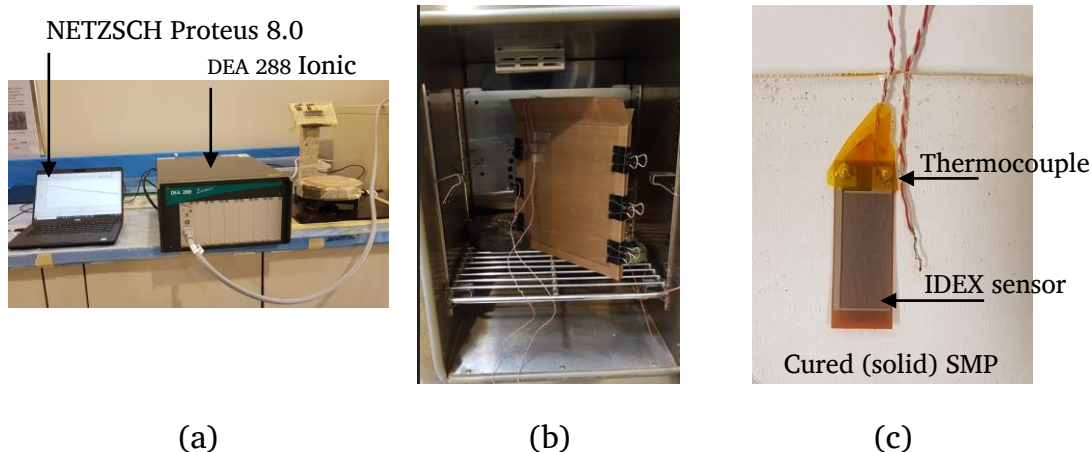
Figure 3.11: DEA experimentation (a) DEA 288 equipment, (b) SMP

specimen curing, (c) Cured SMP specimen with IDEX sensor

The DEA 288 equipment and the experimentation setup is shown in Figure 3.11. Figure 3.12 represents the 1 Hz ion viscosity curve, where a dramatic drop in ion viscosity can be seen due to the softening of the chemical solution. The ion viscosity reached a minimum within 20 min., attaining its best flow behaviour. Until the epoxy gained a minimum log ion viscosity, the temperature was the dominating factor and the chemical reaction had yet to be started. After that, the chemical reaction kicked off, and the ion viscosity rose. Because the chemical reaction surpasses the temperature effect on ion viscosity, from here onwards, the degree of cure was directly proportional to the log ion viscosity. The ion viscosity gradually progressed, and 11 Hz/Ωcm ion viscosity was recorded after 350 min.. Therefore, this demonstrates that the dielectric cure index can be an accurate indicator for illustrating the degree of cure.
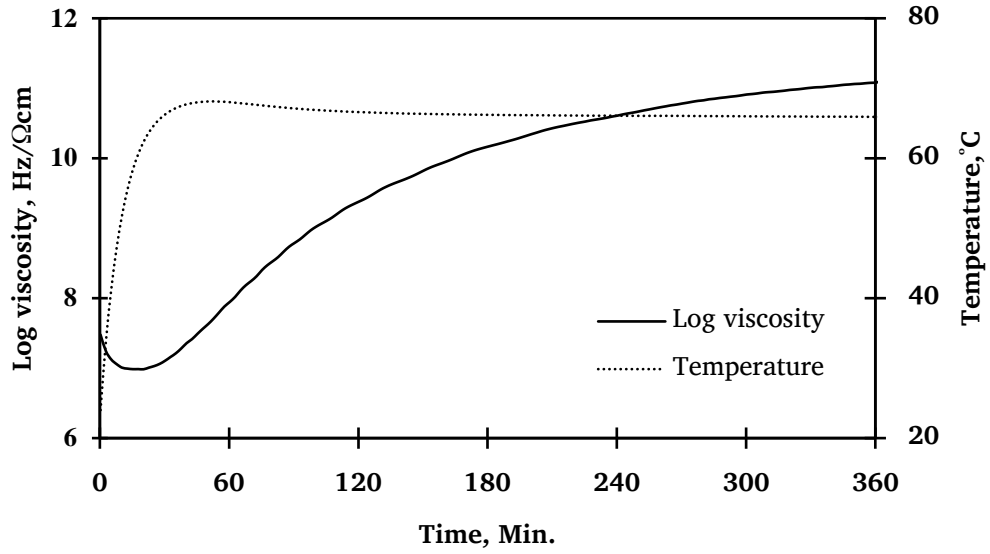
Figure 3.12: Log viscosity
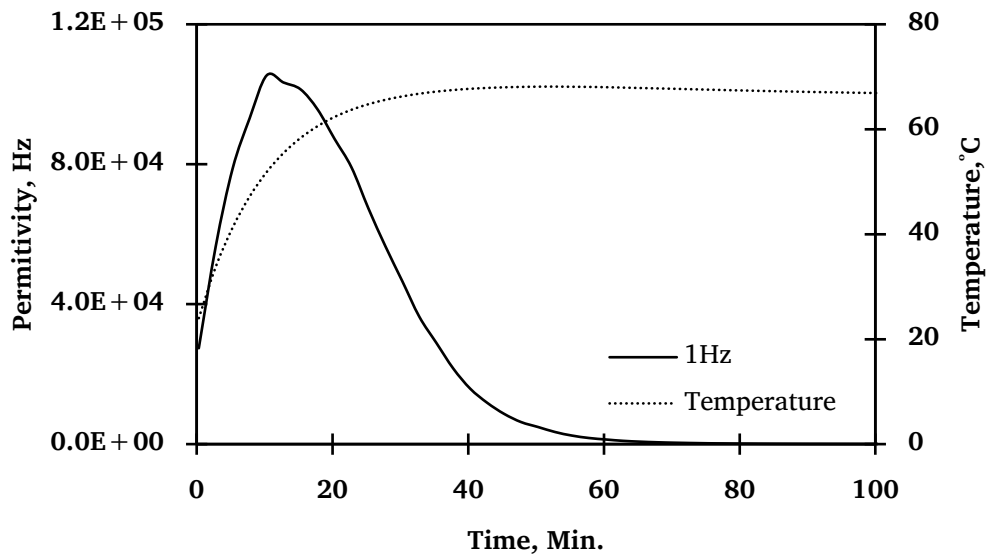
Figure 3.13: Permittivity

Permittivity is another crucial parameter which can be measured during DEA trials. In Figure 3.13, a shape peak at 10 min. represents the curing kick-off time. When the crosslinking has taken place, the permittivity

100

drops, and the time taken to reach onset can be considered the curing cycle time. According to Figure 3.13, the current DGEBA chemical combination was cured within 42 min.

3.5.2 Differential scanning calorimetry analysis

A comprehensive study is essential before introducing the curing cycle for epoxy polymers. To justify the proposed curing cycle, DSC analysis was conducted with variable heat rates of 2°C/min., 5°C/min., 7°C/min., 10°C/min. and 15°C/min. The maximum peak temperatures (T_{max}) are shown in Table 3-4 against these different heat rates. Further, T_{max} increased with the heating rate, and the maximum peak temperature was observed at 15°C/min. heat rate.

To calculate the activation energy (E), Ozawa and Kissinger methods have been used with variable heating rates. The simplest form of the Kissinger equation for estimating the E is as follows.

Ozawa method $\qquad E \cong 2.15R \dfrac{d(\log\beta)}{d(1/T)}$ $\qquad\qquad$ (3.4)

Kissinger method $\qquad -\dfrac{E}{R} \cong \dfrac{d\ln(\beta/T^2)}{d(1/T)}$ $\qquad\qquad$ (3.5)

Pre-exponential factor $\qquad A = \beta(\dfrac{E}{RT^2})e^{E/RT}$ $\qquad\qquad$ (3.6)

Rate constant $\qquad k = Ae^{-E/RT}$ $\qquad\qquad$ (3.7)

Where,

R is the universal gas constant

The Ozawa plot, Figure 3.14 shows the logarithmic values of the heating rates (β) in °C/min. versus reciprocal of peak temperature (1/T) in Kelvin are shown. Similarly, in the Kissinger plot, $\ln(\beta/T^2)$ versus $1/T$ is shown in Figure 3.15. Both Ozawa and Kissinger plots give straight lines, and the gradient used to calculate the activation energy is as per equations 3.4 and 3.5. The calculated activation energy, the average value of the pre-exponential factor (A) for different heat rates and the rate constant (k) are presented in Table 3-5.
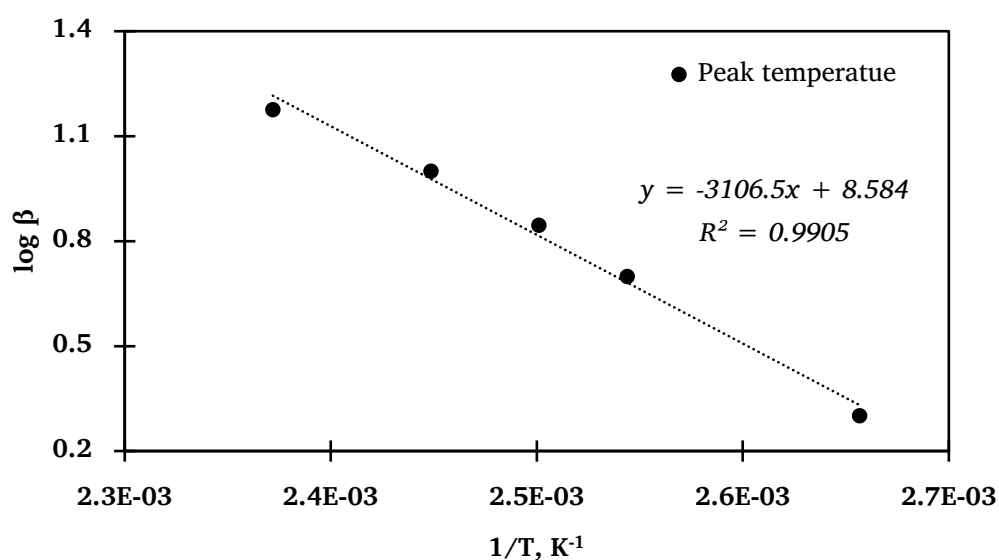
Figure 3.14: Ozawa plot for thermal degradation of 2E SMP

Table 3-4: T_{max} for different heating rates

	T_{max} from DSC heating rates (°C/min.)				
	2	5	7	10	15
BGEBA epoxy	103.26	119.95	126.70	135.25	148.45

The difference between activation energy from both methods was less than 2.7 kJ/mol and thus effectively identical. The rate constants calculated with respect to T_{max} of a 2°C/min. heating rate and obtained values were similar in both methods. The activation energy and pre-exponential factors are useful to predict the isothermal conversion time of the chemical reaction. The fractional conversion (α) and time (t) are given by equation 3.8.
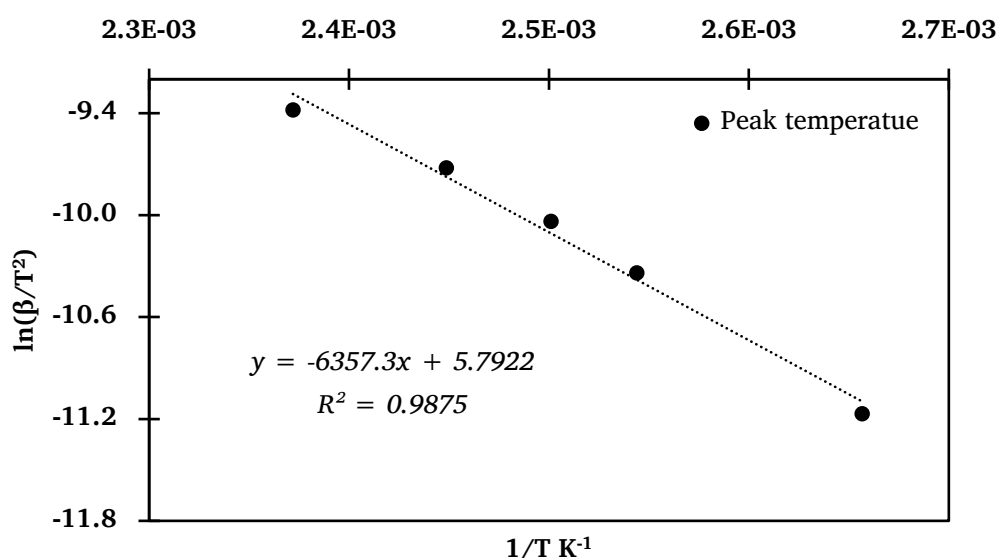
Figure 3.15: Kissinger plot for thermal degradation of 2E SMP

Fractional conversion $\qquad -\ln(1 - \alpha) = kt$ $\qquad\qquad$ (3.8)

Figure 3.16 shows the predicted time required to complete the reaction for the same chemical composition for the respective T_{max} of the different heating rates. Both Ozawa and Kissinger methods showed similar results for the same heating rates. However, results revealed the higher the heating rate,

the shorter time the curing cycle takes. According to Figure 3.16, at a 2°C/min. heating rate, it took 60 min. to complete the curing cycle; on the other hand, 5°C/min. heating rate consumed only 25 min. to complete the curing cycle.

According to the DSC model, the proposed curing cycle takes 43 min. to reach 100% curing, which complies with DEA permittivity results. DSC curing kinetic data are useful to schedule curing parameters and optimise existing curing cycles. Moreover, DGEBA epoxy was kept under 65°C for another 320 min. to assure complete conversion before introducing a 1 hr. post-curing cycle. Thus, the author of this thesis would conclude 65°C for 6 hrs. followed by another hour at 115°C is ideal for cure 2E configuration and the proposed curing cycle is named DGEBA-65. The above predictions were made by assuming a first-order chemical reaction.

Table 3-5: SMP kinetic parameters from DSC

	Ozawa			Kissinger		
	E	$A \times 10^6$	K for $\beta = 2$	E	$A \times 10^6$	K for $\beta = 2$
	(kJ/mol)	(1/min)	(1/min)	(kJ/mol)	(1/min)	(1/min)
DGEBA	55.53	4.91	0.09	52.85	2.09	0.09

Curing percentage calculation:

$$\% \, Cure \; = \frac{[\Delta H_{uncured} - \Delta H_{cured}]}{[\Delta H_{uncured}]} \times 100\% \tag{3.8}$$
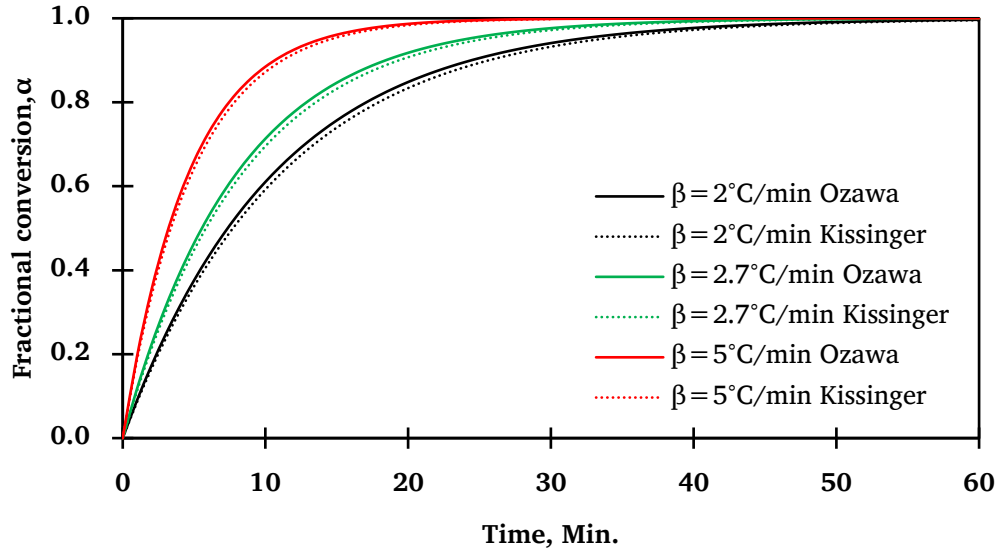
Figure 3.16: Curing completion time
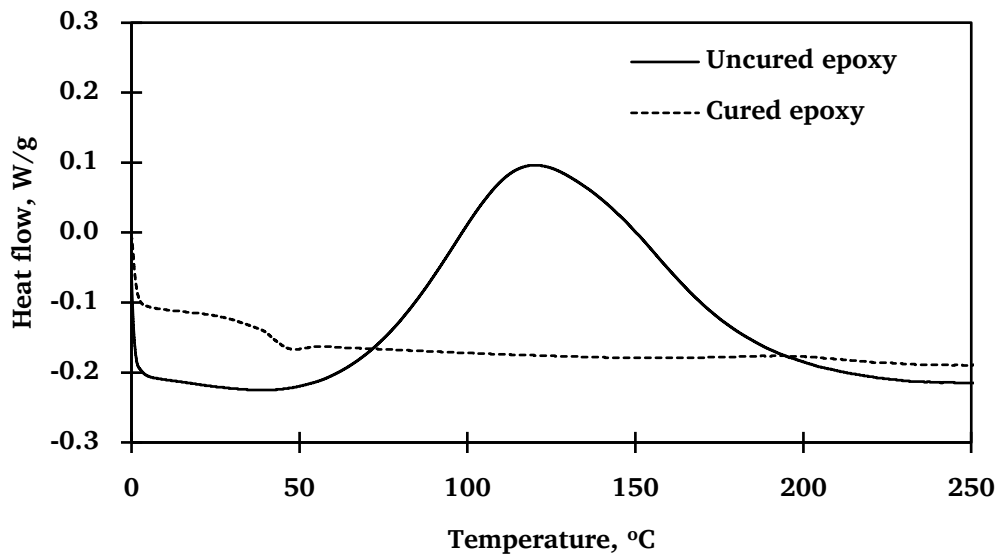
Figure 3.17: Curing percentage

Figure 3.17 illustrates the immediate DSC results of uncured epoxy resin and the cured solid sample with the DGEBA-65 curing cycle. The uncured epoxy resin has undergone a large exothermic peak, while cured solid

sample showed a quasi-liner response. The area under exothermic peaks represents the required heat of cure, and equation 3.8 is used to determine the curing percentage. The calculated cure percentage of SMP was equal to $98.72 \pm 0.5\%$, which provides a solid platform to compare the thermo-mechanical and shape memory properties of fibre reinforced shape memory polymer composite (FRSMPC) and nanoparticle reinforced shape memory polymer nanocomposite (NRSMPC) detailed in Chapter 4.

3.5.3 Fourier-transform infrared spectroscopy experimentation

FTIR spectrum is an effective tool for monitoring polymers and composites' curing process, phase separation and ageing [19]. The peak intensity of FTIR means the amount of the functional group in the composition and is a good indicator to identify SMPs' structural behaviour. Therefore, FTIR spectrum results can be used to identify and compare different curing cycles. DGEBA-65, DGEBA-100 and uncured SMP epoxy mixture FTIR results are presented in Figure 3.18. In this graph, IR absorbance is considered for an 850 cm^{-1} to 1000 cm^{-1} range. The IR absorbance peak at 914 cm^{-1} was highest for uncured resin, and this peak disappeared in cured epoxy polymers. According to the literature, the band 914 cm^{-1} represents the C−O oxirane group and its absence confirms curing completion in the SMP epoxy [14, 289].
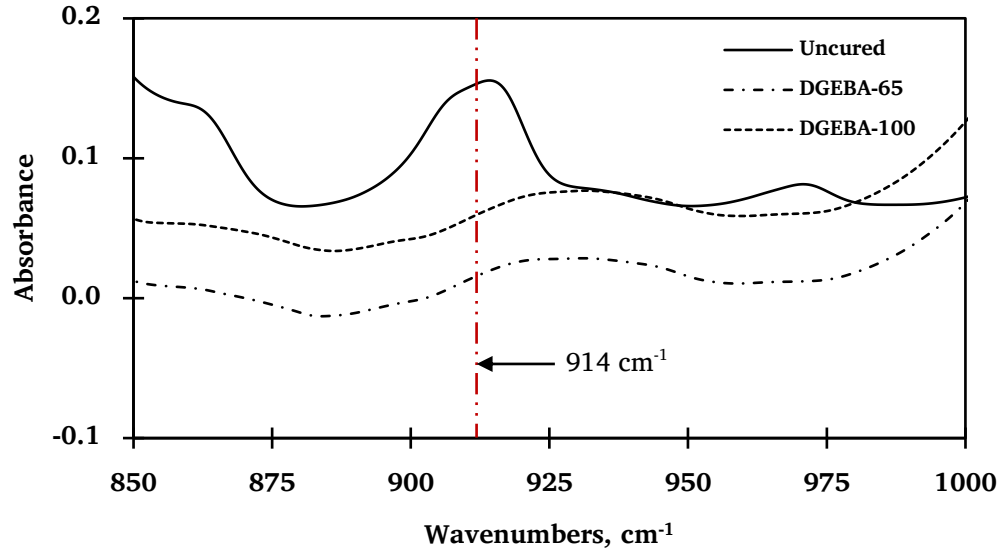
Figure 3.18: FTIR spectrum for cured and uncured SMP

3.5.4 Strain base curing measurement

The strain behaviours under DGEBA-65 and DGEBA-100 were measured and investigated. Experimentally measured strain values are illustrated in Figure 3.19 for DGEBA-65. According to Figure 3.19, within the first 10-15 min., the liquid samples showed negative strain, which indicated the SMP's solidification process. Most importantly, the optical backscatter reflectometer first extracted a drastic strain change time interval complying with the DEA chemical reaction kick-off time shown in Figure 3.12 and Figure 3.13. During the solidification, the DGEBA-65 SMP V_1 and H_1 strains were reached at -275 $\mu\varepsilon$ and -254 $\mu\varepsilon$, respectively and are effectively identical.
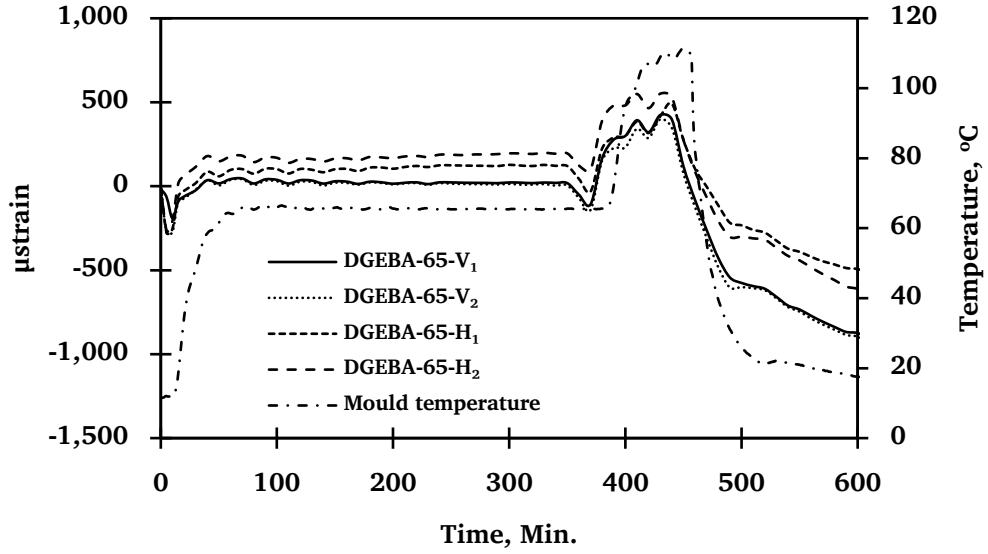
Figure 3.19: DGEBA-65 strain variation

At curing, the SMP solidified, and the volume of the material was reduced, which can be observed as a shrinkage. Thus, the negative strain reflects the material solidification during the chemical reaction. However, the SMP specimen thermally expanded with the continuation of the curing cycle until the start of post-curing. At the initiation of the post-curing process, the SMP internal strain again turned negative, and V_1 and H_1 were recorded as 50 $\mu\varepsilon$ and 43 $\mu\varepsilon$, respectively. During the post-curing, 423 $\mu\varepsilon$ and 461 $\mu\varepsilon$ maximum positive strains were obtained in V_1 and H_1. The post-curing process released the residual stresses, and further, it allowed the SMP to expand thermally. After the completion of curing, the SMP specimen was allowed to cool naturally. In this step, the SMP sample again gained a negative strain. The lowest negative strain was recorded as -930 $\mu\varepsilon$ and V_1 and V_2 strain values

108

were always lower than H_1 and H_2. The average strain difference between V_1,

V_2 and H_1, H_2 was ~280 με.
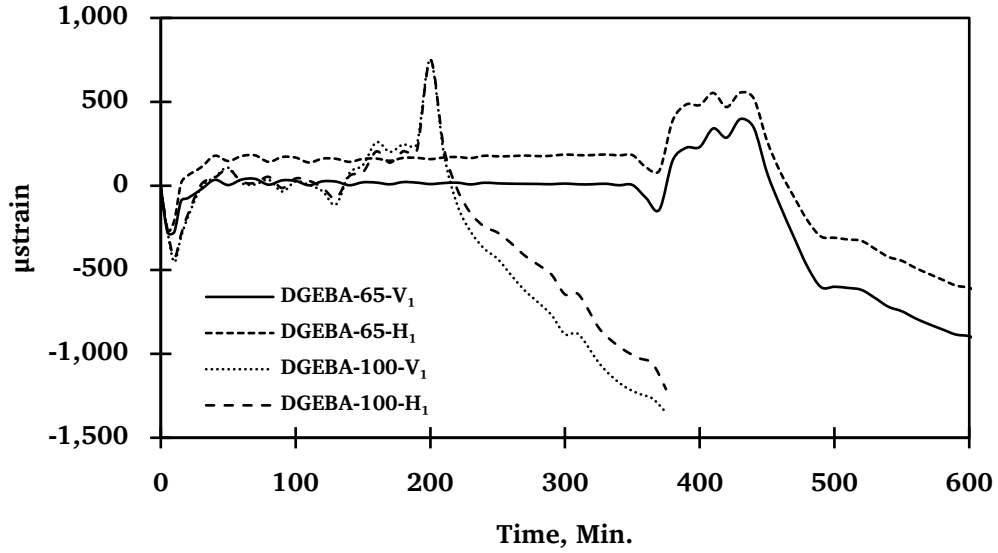
Figure 3.20: DGEBA-65 and DGEBA-100 strain variation

The SMP internal strains were compared for two different curing conditions, as shown in Figure 3.20. The overall strain behaviour was similar, as explained in Figure 3.19. However, the condition of DGEBA-100 obtained the maximum positive strain during the post-curing cycle, which was 752 με and in comparison, 47.2% higher than DGEBA-65. In both curing conditions, the SMP reached a minimum strain at room temperature, and in DGEBA-100, the minimum strain of -1349 με was recorded, which was 31% higher than DGEBA-65. Similarly, as explained in Figure 3.19, the measured strain values for H_1, H_2 were always lower than V_1, V_2. The final V_1 and H_1 strain values were significantly higher in the condition of DGEBA-100 than in DGEBA-65.

Therefore, there is a high probability of micro-cracks occurring in thicker DGEBA-100 cured SMPs, especially in fibre-reinforced SMPCs.

The preliminary analysis of captured strain data from the optical fibre network has shown that SMP undergoes rheological changes such as in its curing kick-off time. The statement can be further validated by comparing DEA and DOFN results with time. After 10 min. of curing, maximum permittivity was recorded, representing the kick-off. At the same time, DOFN showed the least amount of strain. However, a comprehensive analysis is required to establish the proper relationship of the curing index against the measured strains and temperatures. Additionally, it is possible to monitor and eliminate internal residual strain by introducing an optimised curing cycle to avoid unnecessary shrinkage, cracks and dry patches in the specimens. In order to assess the key qualitative feature of curing kinetics, the author advises taking strain measurements into consideration. The optical fibres can become embedded during the material synthesis and fabrication without affecting the material's thermomechanical properties. The advantage is that the optical fibre network can be used to monitor the structural health of the final components. In addition, the embedded optical fibres can be used to activate SMPs remotely and develop light-activated sophisticated real-life applications for space exploration [290, 291]. Therefore, it can be concluded that the embedded optical fibres enable the identification of the curing kinetics, rheological properties, and structural health monitoring of components made of SMPs.

DGEBA-65

| 97° | 117° | 148° | 180° |
| 50 s | 100 s | 150 s | 200 s |

DGEBA-100

| 95° | 108° | 130° | 158° |
| 50 s | 100 s | 150 s | 200 s |
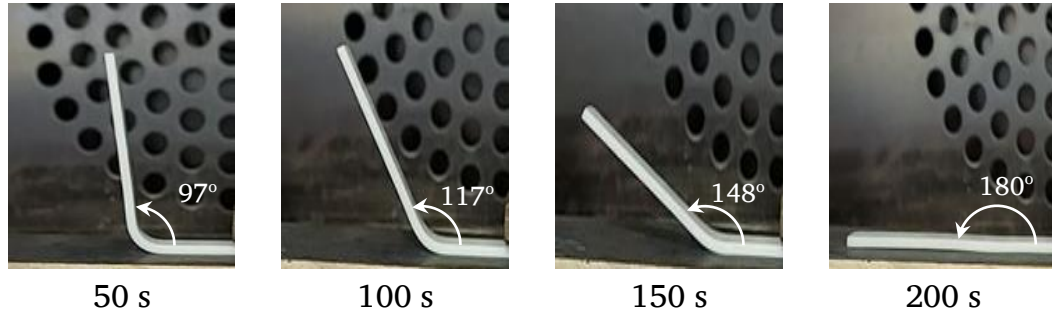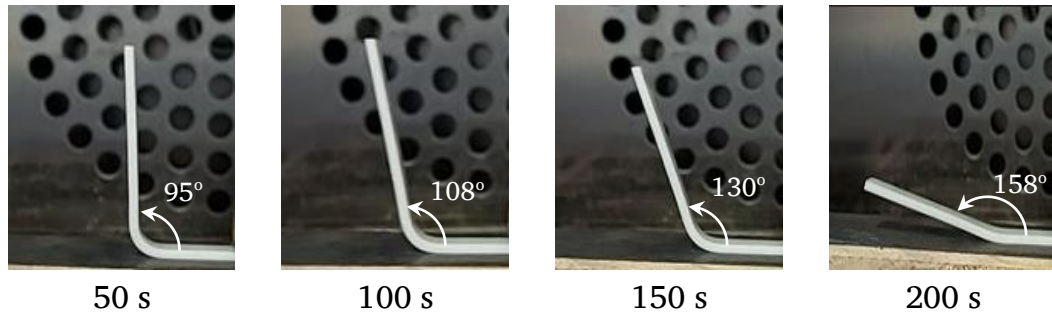
Figure 3.21: 2E recovery for DGEBA-65 and DGEBA-100 at T_g

3.6   Curing cycle effect on shape memory properties

Figure 3.21 illustrates the sequence of the shape recovery for DGEBA-65 and DGEBA-100 curing cycles at 50 s, 100 s, 150 s and 200 s. According to Figure 3.21, within 200 s DGEBA-65 fully recovered whereas DGEBA-100 recovered 158^0.

In addition, both the specimen's recovery process is compared in Figure 3.22 and clearly illustrates that SMP specimens showed a delayed response of around 25 s. This may be due to the polymer's low thermal conductivity or poor heat circulation inside the electric oven. Further, most SMP specimens

were linearly recovered at between a 25% to 90% recovery range. These are exciting factors to consider for SMP application developments.
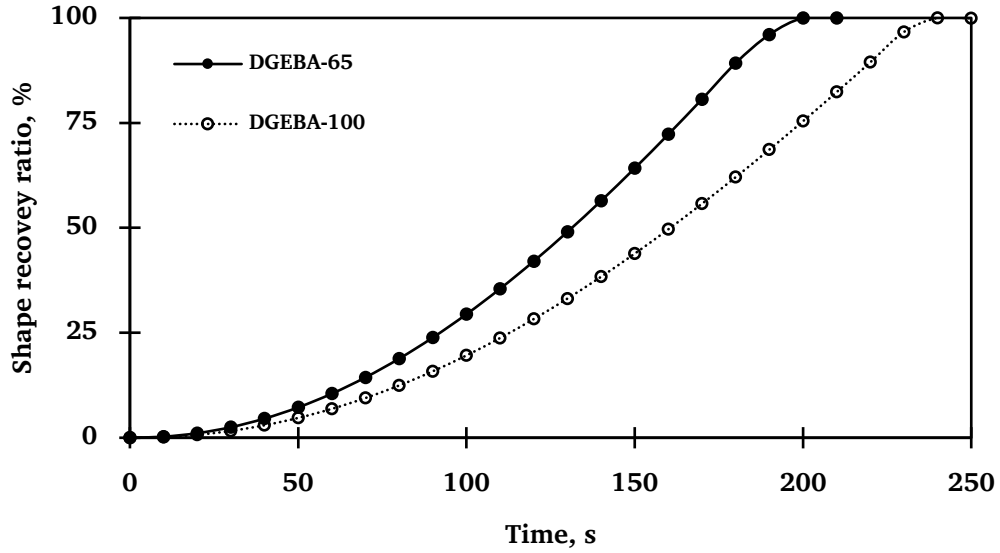
Figure 3.22: Shape recovery ratio *vs* recovery time

3.7   Summary

In this chapter, DGEBA epoxy-based SMPs were synthesized with an amine-based hardener and fabricated eighteen SMP specimens with different chemical configurations. After that, thoroughly studied the viscoelastic and shape memory characteristics of fabricated specimens. Based on transition temperature (46.56°C), shape fixity ratio, shape recovery ratio and shape retention ratio 2E, DGEBA:D-230:NGDE for 2.555:1.000:0.504 *wt*% gives the best chemical configuration to fabricate non-invasive biomedical devices. The fold-deploy technique is used to calculate shape memory properties at storage onset temperature, and this shows an excellent shape fixity ratio of 99.5%,

which reduces the uncertain behaviour of SMP for biomedical orthopaedic external applications. In addition, the programmed shapes were closely monitored over 30 days at room temperature and 97% shape retention ratio was found.

After that, SMP curing kinetics were comprehensively analysed through DEA and DSC trials and proposed a new curing schedule. Also, for the first time, DOFN techniques were used to monitor the SMP rheological changes at a macro level. The proposed curing cycle (DGEBA-65) showed higher recovery rates and saved 50 s and recovery time has been improved by 25% compared to the reference (DGEBA-100) curing cycle. Therefore, it is worth stating that delicate shape memory recovery properties can be further improved by studying curing kinetics. In addition, the innovative idea of using a DOFN has successfully shown its capability to measure in-situ data throughout the SMP curing and can be used in quality control in mass-scale production. However, the author endorses further studies on the DOFSN to breakthrough technological advancement to correlate with DEA readings. In view of this, Chapter 4 will be focused on enhancing mechanical properties and optimisation to select the best SMP configuration before fabricating an orthopaedic bone fracture fixator.

CHAPTER 4: MULTI-ATTRIBUTE PARAMETRIC OPTIMISATION OF SHAPE MEMORY POLYMER PROPERTIES

4.1   Introduction

During past decades, SMPs have rapidly been developed and exhibited their potential to replace traditional plaster of Paris, fibreglass and wood casting orthopaedic treatment practices. In this context, to demand SMP in orthopaedics must adhere to all the structural specifications of traditional materials while keeping unique features such as adjustability, ease of removal and reuse. On the other hand, SMP-based orthopaedic materials should provide unconditional support to fractured bones until they heal and avoid unforeseen disastrous situations. Therefore, critical fabrication parameters identification and a thorough study of them must be needed during the material synthesis and characterisation processors to provide absolute assurance (zero risk). Thus, researchers use robust parametric analysis and statistical optimisation tools to make logically placed arguments, resulting in higher quality products in fewer redesign cycles.

Chapter 4 provides comprehensive knowledge on SMP reinforcement with carbon and E-glass fibres and bio-compatible TiO_2, MWCNT, and graphene nanoparticles. Followed by thermo-mechanical properties were obtained according to the ASTM/ISO standards. The best available fabrication parameters guarantee better thermo-mechanical properties and a highly

reliable SMP material for extended use in external orthopaedics. Thus, the author of this thesis identified the importance of using parametric statistical optimisation since it can provide optimal results even the experimental results could have small or larger amount variability.
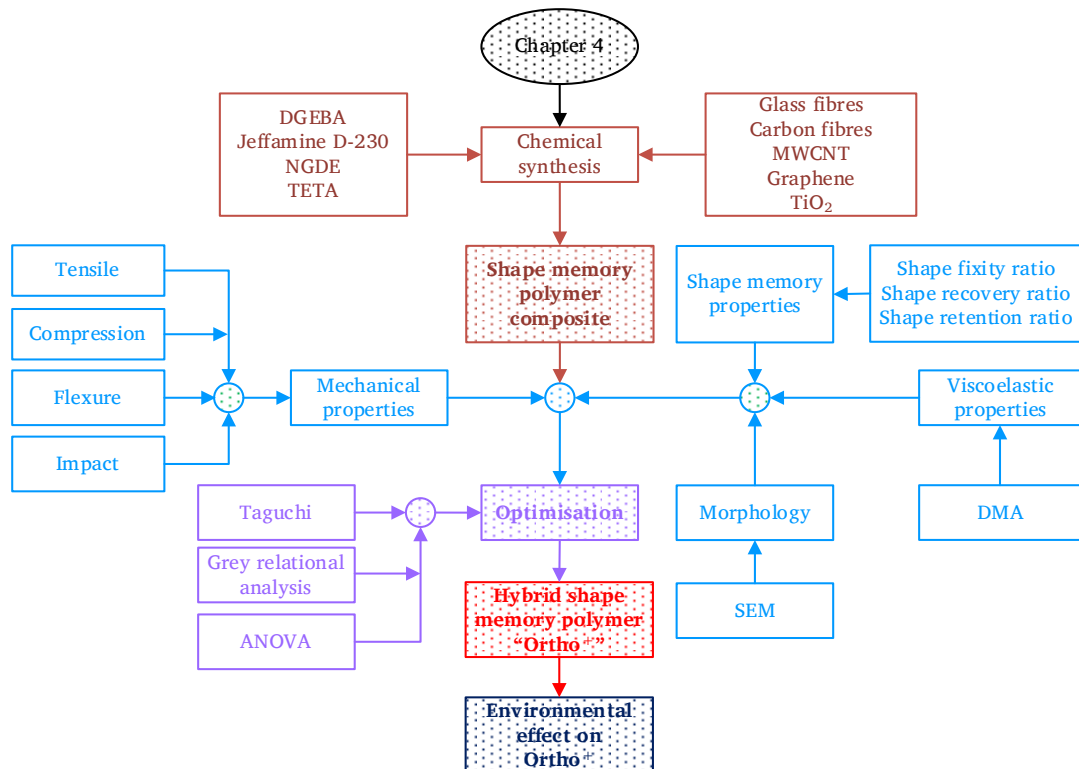
Figure 4.1: Technical overview of Chapter 4

Therefore, FRSMPC and NRSMPC multiple objectives were simplified individually while prioritising orthopaedic material requirements and optimised fabrication parameters using grey relational (GRA) combined Taguchi method. Chapters 4.5 and 4.6 present in-depth procedures of FRSMPC and NRSMPC optimisation. After considering optimum FRSMPC and NRSMPC

fabrication parameters, the novel shape memory polymer orthopaedic material was synthesised using a single layer of E-glass fibre with 0.4 $wt\%$ of TiO_2 and named Ortho$^+$. Further in Chapter 4.7, environmental effect on Ortho$^+$ was thoroughly investigated, and a comprehensive overview was provided before conduct *vitro* experiments. The technical content of Chapter 4 is illustrated in Figure 4.1.

The methodology detailed in this chapter can be extended to optimise any application-oriented micro to macro scale numerous polymer composites synthesis and characterisation processors. The revealed details in this chapter were published in J_1, J_2, C_1 and C_3 as listed in Chapter 1.6.

4.2 Taguchi and grey relational analysis

The design of an experiment is a most important preliminary task in engineering problem solving, where many complex relationships exist between input variables and outputs. The classical experimental design methods, response surface methodology and the Taguchi philosophy, are widely used to optimise the relationship between inputs and outputs [292]. An appropriately planned Taguchi experimental program provides important factors affecting product quality and optimal process conditions with minimum effort, time and cost [293]. However, the Taguchi principle is used to optimise single quality characteristics. In order to further enhance the effectiveness and robustness of multiple quality characteristics in a system,

116

grey relational analysis (GRA) was incorporated with the Taguchi method [294].

Taguchi signal to noise (S/N) ratios:

$$Smaller - the - better \ S/N \ ratio \ = -10\log\left(\frac{1}{n}\sum_{j=1}^{n} y_j^2\right) \qquad (4.1)$$

$$Larger - the - better \ S/N \ ratio \ = -10\log\left(\frac{1}{n}\sum_{j=1}^{n} \frac{1}{y_j^2}\right) \qquad (4.2)$$

Where,

y_j is the experimental result of the jth experiment

j is the number of experiments

n is the total number of experiments

Normalised GRA:

$$Smaller - the - better, y_j^*(k) = \frac{max \ x_j^0(k) - x_j^0(k)}{max \ x_j^0(k) - min \ x_j^0(k)} \qquad (4.3)$$

$$Larger - the - better, y_j^*(k) = \frac{x_j^0(k) - min \ x_j^0(k)}{max \ x_j^0(k) - min \ x_j^0(k)} \qquad (4.4)$$

Where,

$x_j^0(k)$ is measured results

$min \ x_j^0(k)$ is the measured minimum value of $x_j^0(k)$

$max \ x_j^0(k)$ is the measured maximum value of $x_j^0(k)$

k is the number of quality characteristics (k = 1, 2, 3….18)

Grey relational coefficient $\xi_j(k)$:

$$\xi_j(k) = \frac{\Delta_{min} + \xi\Delta_{max}}{\Delta_{0j}(k) + \xi\Delta_{max}} \tag{4.5}$$

Where,

Δ_{min} is the smallest value of $\Delta_{0j}(k)$

Δ_{max} is the maximum value of $\Delta_{0j}(k)$

ξ is the distinguishing coefficient which is equal to 0.5

Grey relational grade (GRG):

$$\gamma_j(k) = \frac{1}{n}\sum_{k=1}^{n} \xi_i(k) \tag{4.6}$$

Where,

$\gamma_j(k)$ is a grey relational grade (changes from 0 to1)

n is the number of experiments

4.3 Materials

As already mentioned in Chapter 3.2, Diglycidyl ether of bisphenol A (DGEBA) aromatic epoxy resin and neopentyl glycol diglycidyl ether (NGDE) aliphatic chain extender were purchased from Huntsman Australia. Poly(propylene glyol)bis(2-aminopropyl)ether (Jeffamine D-230) di-amine hardener was purchased from Sigma Aldrich Australia. In addition to the following materials, Carbon and E-glass 200 g/m² single woven fabrics were obtained from ATL Composites Australia. The industrial-grade (purity $>99\%$) NPs TiO_2 (particle size 20-40 nm), MWCNT (outer diameter 20-40 nm, inner

diameter 5-10 nm, tube length 10-30 μm) and graphene (conductivity 800-1100 S/cm, apparent density 0.07-0.11 g/cm^3) were ordered from XFNANO China. All chemicals and materials were used as received.

4.4   Characterisation techniques

The FRSMPC/NRSMPC was observed through Jeol Benchtop (JCM-6000) Scanning Electron Microscope (SEM). The fibre weight fraction was determined according to ISO 1172 calcination method-A. The dynamic mechanical analysis of FRSMPC/NRSMPC was performed with TA instrument hybrid rheometer (Discovery HR-2) as described in Chapter 3.3. FRSMPC and NRSMPC tensile strength were evaluated under ISO 527-5:2009 and ASTM 638-14, respectively. FRSMPC and NRSMPC compression strength, flexural strength and impact strength were determined according to ASTM D6641, ASTM D790, and ASTM D256 standards.

An MTS 100 kN (Insight Electromechanical) uni-axial testing machine was used to evaluate the tensile strength and compression strength, while an MTS 10 kN was used to evaluate the flexural strength of the FRSMPC and NRSPMs. An Instron Dynatup 8200 drop weight impactor was used to conduct the impact test. The mechanical test experimental instruments are illustrated in Figure 4.2. Additionally, the FRSMPC and NRSMPC R_f, $R_{f,30}$ and R_r were evaluated per the fold-deploy test method as detailed in Chapter 3.6.
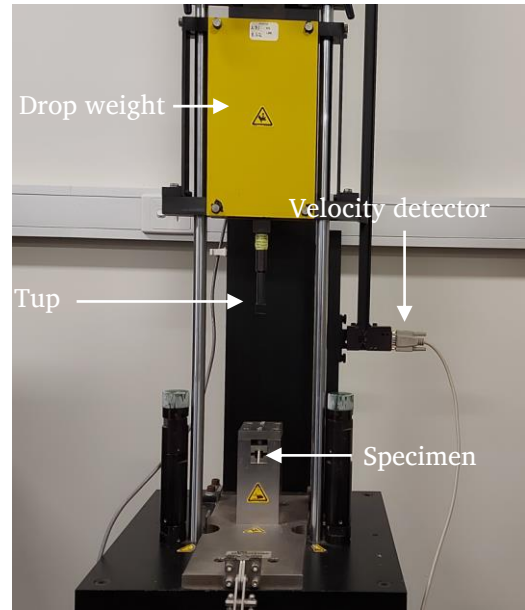
Figure 4.2: Mechanical properties evaluation, (a) Tensile equipment, (b) Impact equipment, (c) Compression equipment, (d) Flexural equipment

4.5   Fibre reinforced shape memory polymer composites

SMPs are weak in strength; thus, they are not popular in load-bearing actual structural applications [295]. Consequently, the research interest in

SMP increased due to the reinforcement materials and they are often reinforced with carbon, glass, and aramid fibres. Fibres can also be divided into nanofibers, short fibres and continuous fibres [296]. However, due to low strength and low stiffness, nanoparticles are slightly increased mechanical properties than fibres; as a result, they are hardly used in structural applications [297-302]. On the other hand, continuous fibre-reinforced SMPC have shown potential in many advanced applications such as morphing structures, space habitats etc… [19, 29, 40]. The adhesion between fibre and the matric is important to transfer stress effectively to achieve desirable properties [303]. Usually, the fibre selection is based on a particular application's required strength, stiffness, and budget. Carbon fibres are used in high-performance applications [304]. They have less impact-resistant but cause corrosion since higher electrical conductivity [305]. E-glass is the most economical glass fibre for composites and is mainly used as an electrical insulator when required for radio-signal transparency, printed circuit boards, antennas and aircraft randoms [306].

In this chapter, the author synthesised SMP with commonly available low-cost carbon and E-glass fibres and comprehensively analysed properties that are essential for immobilising orthopaedic bones.

4.5.1 FRSMPC preparation

Based on Chapter 3.4 experimental results, the best synthesis ratio (2E) was selected to fabricate carbon fibre reinforced shape memory polymer

composites (CFRSMPCs) and glass fibre reinforced shape memory polymer composites (GFRSMPCs). The detailed experimental structure is mentioned in Table 4-1. The introduced sample names for the eighteen SMPC samples against their fabrication configuration is shown in Table A01.

(a)

(b)

(c)
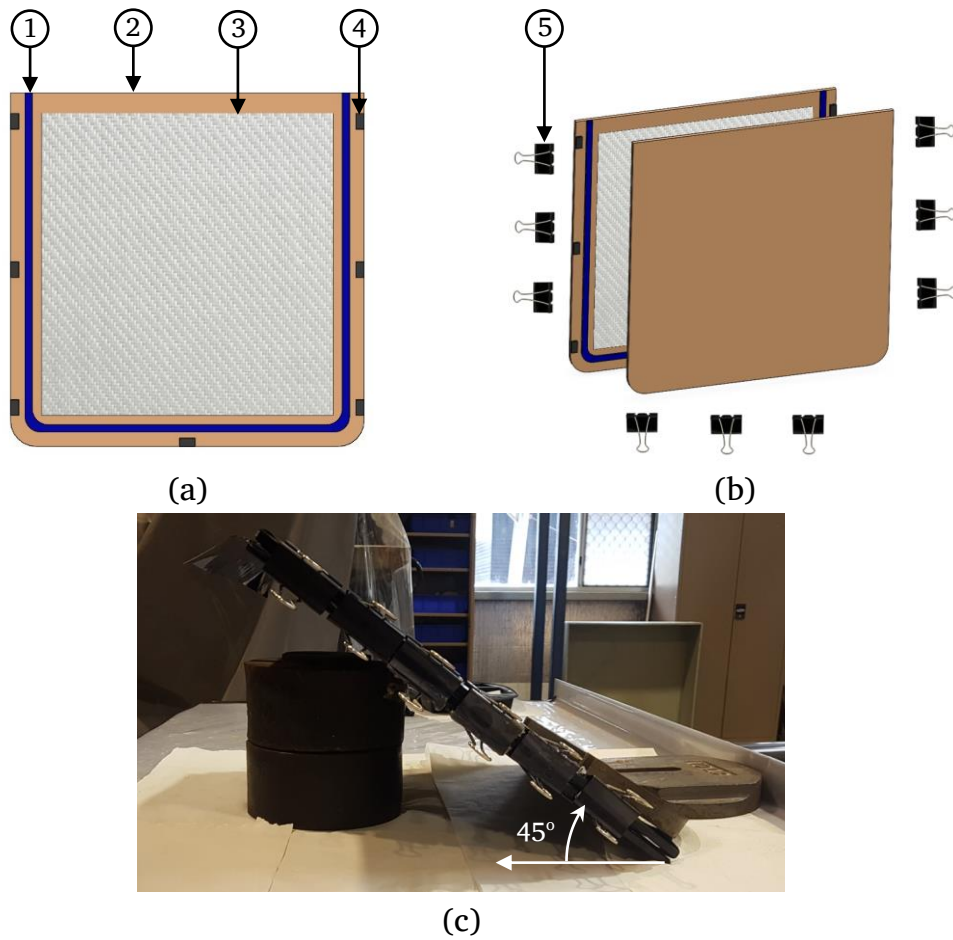
1   Silicon layer

2   5 mm thick tempered glass plate

3   E-glass fibre (300 x 300 mm^2)

4   Metal spacer (minimum 7)

5   55 mm bulldog clip (minimum 9)

Figure 4.3: Mould and SMPC preparation

Table 4-1: FRSMPC process parameters and Taguchi levels

Process parameters	Levels		
	Level 1	Level 2	Level 3
Fibre type	Carbon	E-glass	-
Number of layers	1	2	3
Thickness (mm)	1.0	2.5	3.0
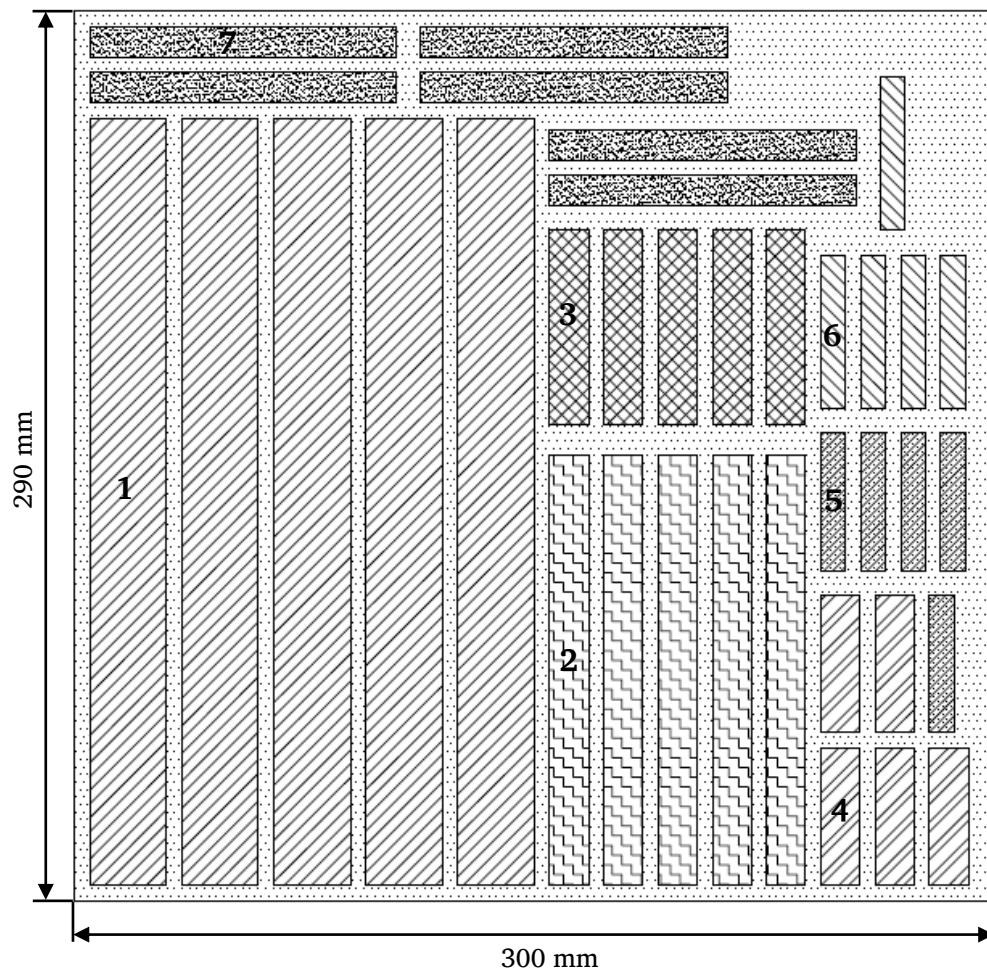
Part	Specimen name	Dimensions (mm)
1	Tensile specimen	250×25
2	Compression specimen	140×12.7
3	Impact specimen	63.5×8
4	Flexure specimen	44.8×12.7
5	DMA (Rheometer) specimen	45×8

6	DMA Q800 specimen	50×8
7	Shape memory specimen	100×10

Figure 4.4: FRSMPC water jet DXF cutting layout

The epoxy was poured into the glass mould, as illustrated in Figure 4.3, which contained fabric layers. After adding the chemicals, the mould was tilted 45° to release trapped air bubbles out and left at room temperature for 15 min. Then synthesised SMPC was cured at 65°C for 6 hrs., followed by post-curing at 115°C for another hour (DGEBA-65). After that, fabricated panels were cut using a water jet cutter per the ASTM /ISO standards described in Figure 4.4 and Chapter 4.4. Due to the water jet cutter limitation the specimens were placed with at least 5 mm of space between them.

(a)	(b)	(c)
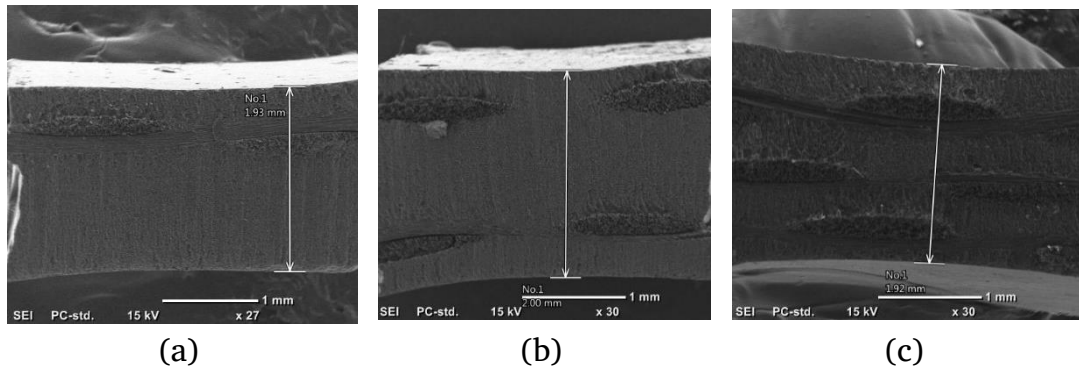
Figure 4.5: SEM images of CFRSMPC (a) 1C-2.0, (b) 2C-2.0, (c) 3C-2.0

The specimens were named starting from the number of fibre layers and then fibre type. Carbon fibres were represented by the "C" and glass by

"G". After the dash, the thickness of the specimen was mentioned in millimetres. For example, 2C-2.0 denotes 2 mm thick, two layers of carbon fibre specimen.

The fabricated CFRSMPC 1C-2.0, 2C-2.0 and 3C-2.0 SEM images are shown in Figure 4.5. According to the SEM images, it is clear that specimens are within the geometrical tolerance level and are free of voids and cracks, allowing for effective comparison and analysis of the thermomechanical and shape memory properties.

4.5.2 FRSMPC weight fractions

A common platform was needed to compare, build up and analyse relationships between multi variables; thus, the SMP weight fraction was effectively chosen. Experimentally obtained average SMP weight fractions are illustrated in Figure 4.6 and the specimens were arranged and grouped according to the fibre type and thickness.

Areal density

$$Areal\ density = \frac{Mass\ of\ the\ composite}{Volume\ of\ the\ composite} \qquad (4.7)$$

The minimum and maximum fibre weight fraction was $2.8 \pm 0.2\%$ and $25.1 \pm 0.1\%$, respectively. In addition to that, GFRSMPC's fibre fractions are always higher than respective CFRSMPCs by 3.8%, 4.5%, 4.3%, 6.1%, 6.3%, 5.9%, 5.7%, 7.3% and 7.4%. The average areal densities of CFRSMPCs and

GFRSMPCs were recorded 1151 ± 27.98 kg/m^3 and 1219 ± 64.97 kg/m^3 as per the equation 4.7. Due to the low density, SMPs are potential in many applications and Liu et al. stated that composites may vary between 900-1100 kg/m^3 [15]. Thus, it is clear that the synthesised SMP orthopaedic material will be more lightweight than POP, resulting in a higher level of patient satisfaction.
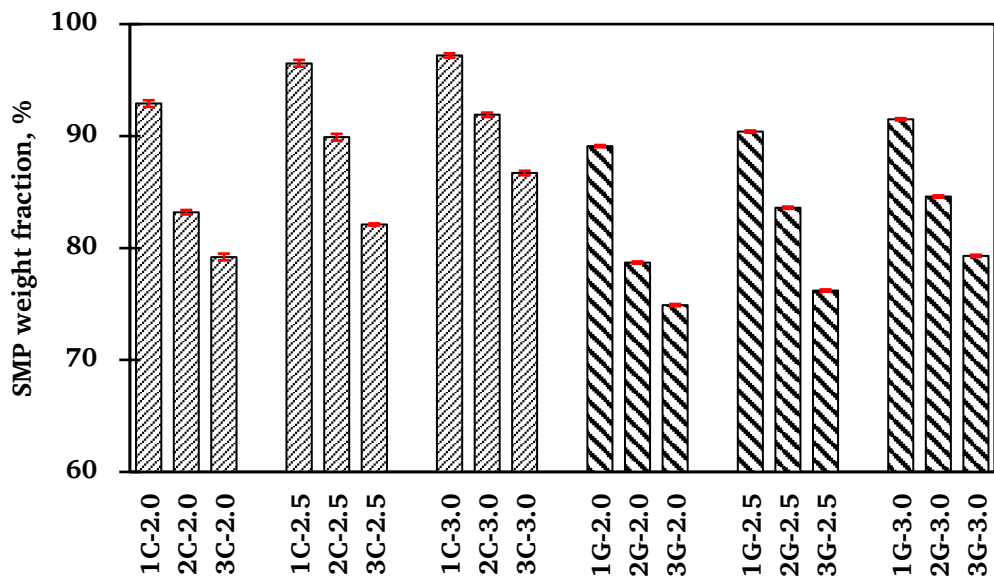
Figure 4.6: FRSMPC SMP weight fraction

4.5.3 FRSMPC viscoelastic properties

In polymers, the storage modulus (SM) almost remains constant in room temperature. However, the storage modulus decreases as the temperature rises. The onset represents T_g and the SM minimum derivative glass transition temperature is denoted as $\dot{T}_g$. The chain flexibility, intermolecular interaction, molecular weight, co-polymerization, cross-

linking and plasticizer are greatly affected by T_g [307]. These properties can influence physical geometry and reinforcements such as fabrics and fillers [283, 308].
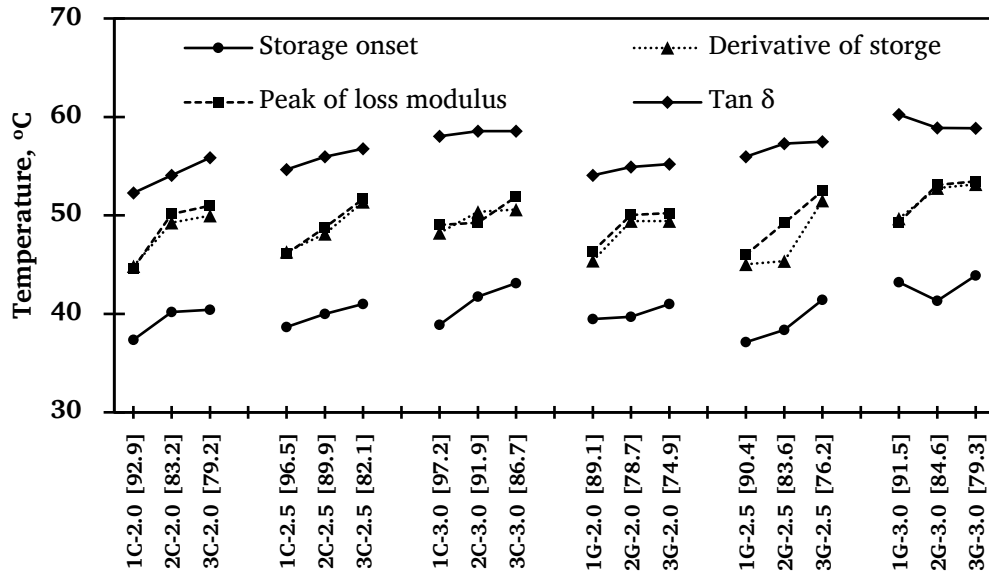
Figure 4.7: FRSMPC activation temperatures

Experimentally obtained storage onset, derivative storage onset, loss modulus peak (LM) and Tan δ peak transition temperatures are illustrated in Figure 4.7. The data is arranged according to the fibre type and thickness. The average FRSMPC T_g is 40.39 ± 1.92°C, $\dot{T}_g$ is 48.93 ± 2.63°C and Tan δ peak is 56.54 ± 2.12°C. The T_g and $\dot{T}_g$ are within the safe margins for non-invasive biomedical applications [71]. The maximum standard deviation, ± 2.63°C was reported in derivative storage onset; however, this was not significant compared to experimental errors. Thus, statistical optimisation is necessarily

required to find the most impacted fabrication parameter for T_g. The transition temperatures were dropped with the SMP weight fraction and the thickness. This could be due to the low thermal conductivity of the SMP matrix and incorporated fibres [15].

For an extensive viscoelastic comparison, 3G-2.0, 3G-2.5 and 3G-3.0 GFRSMPC were selected, and these are illustrated in Figure 4.8. Among these three SMPC specimens, the highest SM 5.9 GPa was recorded in 3G-2.0, which had a 74.9% SMP weight fraction. Moreover, 4.5 GPa and 3.9 GPa SM were recorded for 76.2% and 79.3% SMP weight fractions of 2.5 mm and 3.0 mm GFRSMPCs. Generally, DGEBA-based SMPs' storage modulus improved with the reinforcement. The ratio between storage and rubbery modulus is over 15 times, representing a better SME of synthesised FRSMPCs [156]. The Tan δ peak reached 0.885, 0.901 and 0.944 in 3G-2.0, 3G-2.5 and 3G-3.0, respectively. Tan δ is a measure of internal friction in a viscoelastic system, and a low Tan δ represents higher elasticity. On the other hand, glass fibres have better elastic properties; therefore, a higher glass fibre weight fraction (25.1 *wt*%) in 3G-2.0 accounted for its more improved elastic properties compared with 3G-2.5 and 3G-3.0.
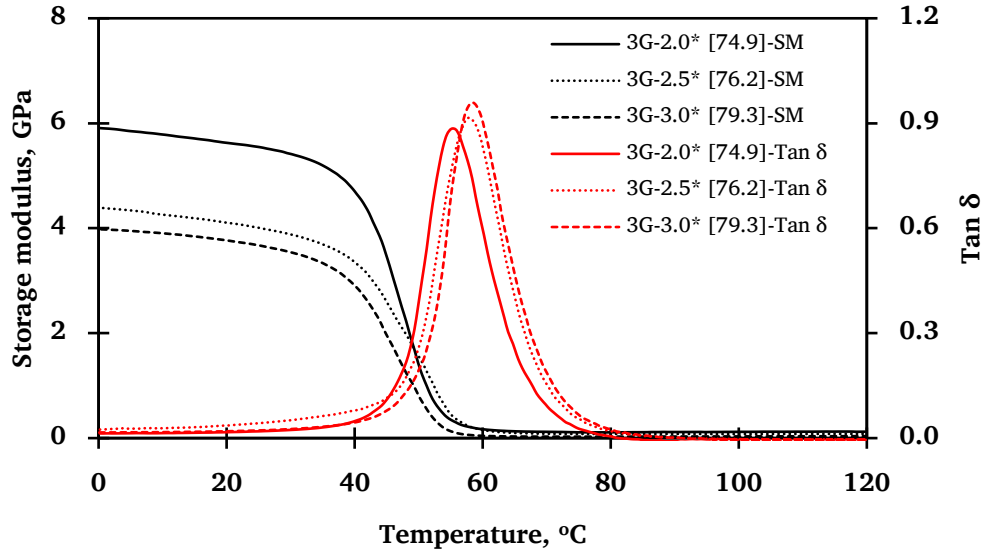
Figure 4.8: Storage modulus and Tan δ, as a function of temperature

*Presented experimentally received individual specimen data

The general viscoelastic trend of FRSMPC is illustrated against the SMP weight fraction in Figure 4.9 and the data tabulated in Table C01. According to the general trend, composites showed improved elasticity with the SMP weight fraction.

4.5.4 FRSMPC mechanical properties

The relationship of mechanical properties to SMP weight fraction is presented in Figure 4.10 and tabulated in Table C02. The data point trend was matched with exponential, linear, logarithmic, polynomial, power and moving average trendline options. The author identified, liner and second-order polynomial functions were given the best fit with minimum error. Thus, based on error (R^2), the author decided to use the linear trend pattern option. Using

129

these equations respective property can be predicted for over 70% SMP weight fraction with 95% confidence. Carbon fibres dominates the tensile, compression, and flexural properties. Also, FRSMPC's mechanical properties are substantially influenced by the fibre weight fraction. Moreover, the change rates in tensile, compression and flexural strength are effectively identical in both CFRSMPCs and GFRSMPCs.

During the tensile test, CFRSMPCs failed under the "LGM" mode. In contrast, Herath et al.'s styrene-based 0/90 woven CFRSMPC prepreg failure was identified as "XMV" [19]. Most GFRSMPCs failed under the "AGM" three-part failure mode; however, specimens with an SMP weight fraction of less than 89% failed explosively under the "XGM". The highest tensile strength was 286 MPa, observed in 3C-2.0. This was an enhancement of 348% compared to the specimen with the minimum tensile strength.

The compression properties are depended on matrix material type, specimen preparation method, fibre stacking sequence, fibre volume fraction, fabrication defects, test environment, and compression rate/speed. The compression stress versus strain is illustrated in Figure 4.10 (c) and (d).
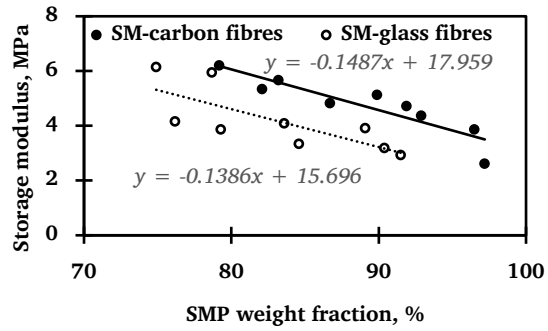
(a)
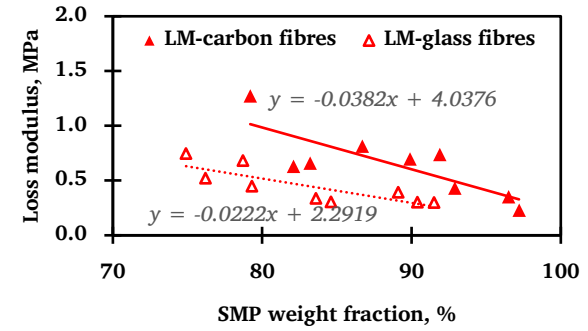
(b)
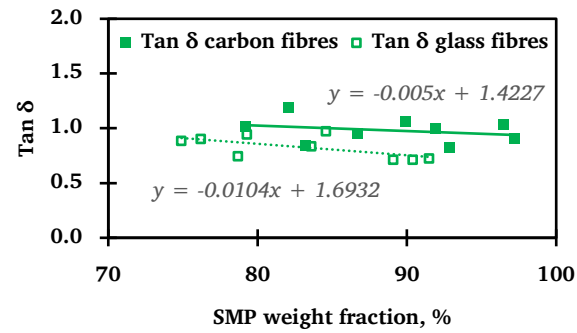
(c)

Figure 4.9: FRSMPC viscoelastic properties (a) Storage modulus, (b) Loss modulus, (c) Tan δ

(a)

(b)

(c)

(d)

132
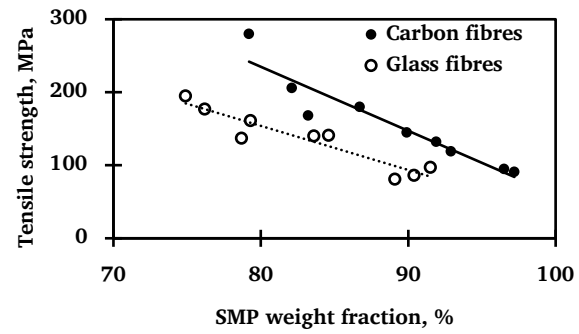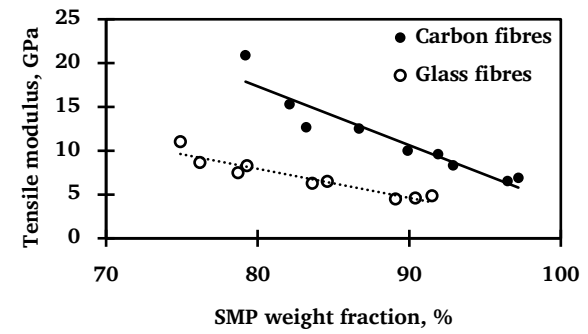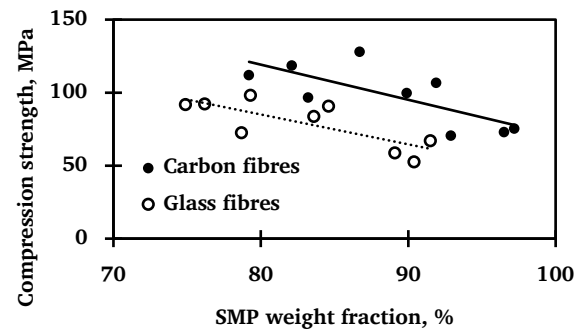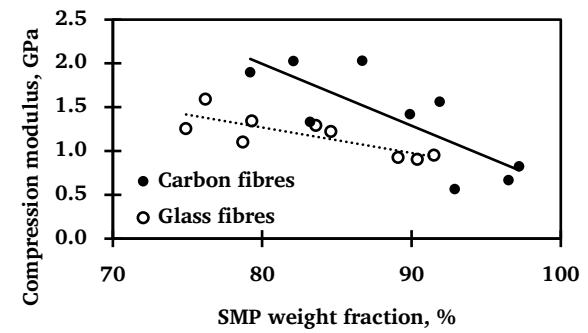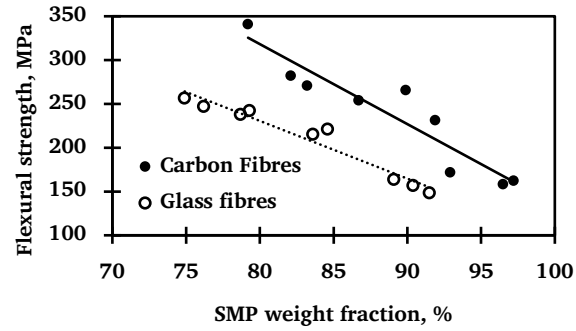
(e)
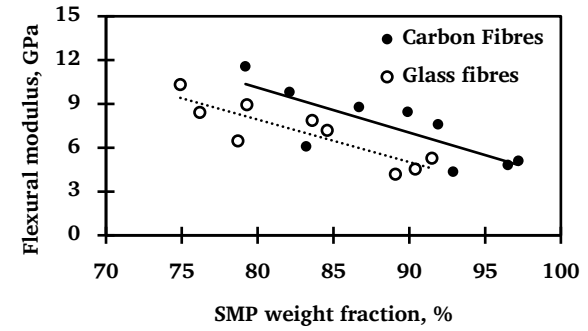
(f)
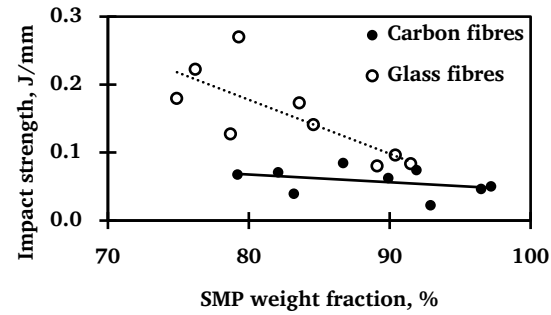
(g)

Figure 4.10: FRSMPC mechanical properties (a) Tensile strength, (b) Tensile modulus, (c) Compression strength, (d) Compression modulus, (e) Flexural strength, (f) Flexural modulus, (g) Impact strength

133

According to the ASTM D6641 compression test, HAT (Through-thickness/ at grip/ top) three-part failure mode was identified. The highest compression strength was 128 MPa which was 58% higher than the minimum compression strength. The compression strength varied within a limited range between 75 MPa in all the FRSMPCs. During the compression test, it was observed that CFRSMPCs were delaminated before they failed; however, 2 mm thick GFRSMPCs buckled without failing due to low stiffness. Nevertheless, CFRSMPCs' compression strengths were higher than the respective GFRSMPCs.

Flexural properties of thermosetting materials depended on the transition temperature, molecular weight between cross-links, free volume, chemical structure, network regularity and perfection [309]. The highest flexural strength was 341 ± 9 MPa. This was recorded for 79.2% SMP loaded CFRSMPC and exhibited an enhancement of 56% compared to the minimum flexural strength. Due to their low stiffness, the 2 mm thick FRSMPCs showed higher deflection with an average of 160 MPa flexural strength. Rimdusit et al. synthesised DGEBA with NGDE and D-230 with a 1:1:1 molar ratio and evaluated 59.5 MPa for flexural strength at room temperature [309]. In addition, D'Elia et al. synthesised DGEBA-based SMP and obtained 43 ± 4 MPa flexural strength, but this was 28% less than Rimdusit et al.'s findings [310]. However, in the present experiment, synthesised FRSMPCs' flexural results were 2.4 and 3.4 times higher than those of Rimdusit et al. and D'Elia et al.

The GFRSMPC's glass fibre fraction varied between 74% and 91% while CFRSMPC's carbon fibre fraction varied between 79% and 97%. This difference is mainly due to the fibre density. According to Artemenko et al. Carbon density varies between 1600 – 1350 kg/m^3 and glass fibre density varies between 1900 - 1650 kg/m^3 [311]. Therefore, the density of carbon fibre is less than glass fibre; thus, carbon fibres offer a better solution in applications where weight is an important factor. The maximum and minimum impact energies of the FRSMPCs were 0.27 J/mm and 0.02 J/mm, respectively. 1C-2.0 absorbed minimum energy at impact failure; in contrast, 3G-3.0 absorbed the highest impact energy. Additionally, the CFRSMPCs' impact strength was lower than respective GFRSMPCs' regardless of the SMP weight fraction and the thickness of the specimens. The overall CFRSMPCs' and GFRSMPCs' average impact strengths were 0.058 ± 0.019 J/mm and 0.153 ± 0.065 J/mm, respectively. Thus, GFRSMPCs absorbed 2.6 times of energy before they failed compared to CFRSMPCs. Consequently, E-glass fibres with higher strain-to-failure exhibit enhanced resistance to crack propagation in composite materials, resulting in a synergistic effect [312, 313]. Due to this reason the impact performance of GFRSMPCs was observed to improve in correlation with the percentage of fibres present, whereas no significant effect was observed in the case of CFRSMPCs. This is consistent with the findings of Yang et al., who revealed that glass fibre reinforced composites have higher impact resistance and impact energy depends upon the fibre fraction [314].

It is clear that mechanical properties are significantly dependent on selected fabrication parameters. Therefore, ANOVA and multi-parametric analysis is required to find the optimum and the most influential parameter for the final solution without compromising the overall design.

4.5.5 FRSMPC shape memory properties

The calculated R_f, $R_{f,30}$ and R_r are illustrated in Figure 4.11. The highest R_f, 99.95%, was recorded in 2.5 mm thick GFRSMPC, containing a 90.4% SMP weight fraction and the highest $R_{f,30}$, 98.4%, was recorded in 2.0 mm thick GFRSMPC, which contained 89.1% SMP weight fraction. Similarly, the highest R_r, ~100%, was seen in 3.0 mm thick CFRSMPC, which had a 91.9% SMP weight fraction. R_f and R_r achieved over 80%; however, $R_{f,30}$ data were spread in a wider range between 46.0% and 98.4%. Further, it has been noted that in 13 FRSMPC specimens, over 90% of R_f and R_r were recorded, while in only two FRSMPC specimens, over 90% of $R_{f,30}$ were recorded. For orthopaedic bone immobilisation, the applied cast should stay in place for a minimum of 3 weeks, depending on the nature of the fracture, its location, and the patient's age [315]. Therefore, variables taken into consideration, $R_{f,30}$ is the most important parameter for orthopaedic fractured bone immobilisation materials [316].
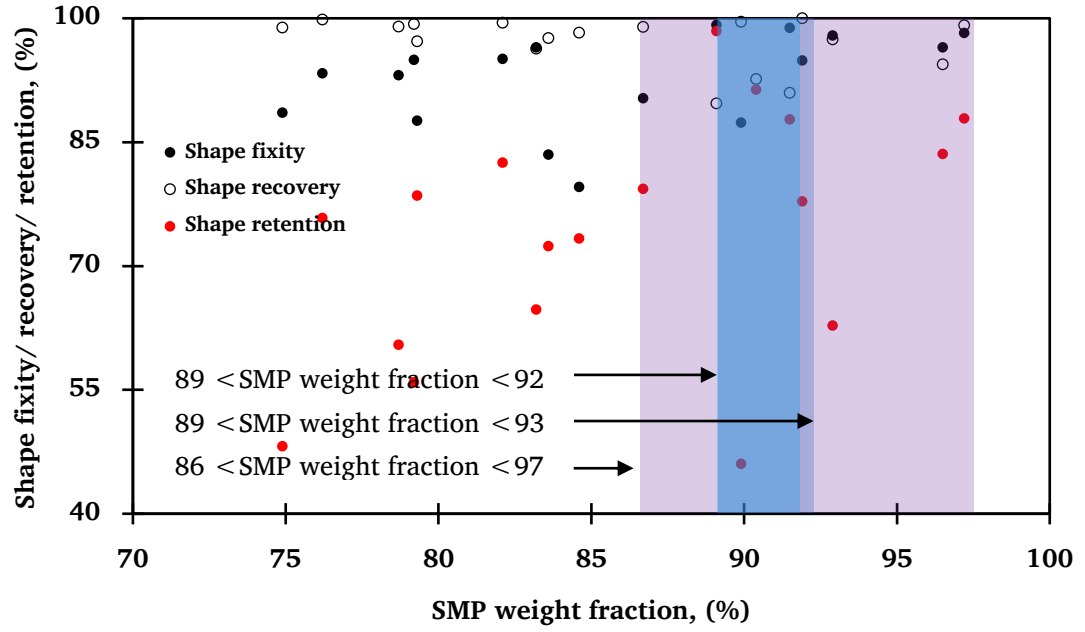
Figure 4.11: FRSMPC R_f, $R_{f,30}$ and R_r optimum region

Figure 4.11 further reveals that R_f and $R_{f,30}$ drastically dropped with fibre weight fraction due to the elastic properties provided by the fibres; in contrast, R_r improved in all FRSMPCs [21, 317]. Therefore, finding the optimum fabrication process variables is vital before the initial prototyping. It is clearly seen that at 89% to 92% SMP weight fraction, the overlapped region is optimum for R_f, $R_{f,30}$ and R_r. Thus, the author strongly suggests SMP weight fractions of 89% to 92% for the fabrication of adaptive orthopaedic plasters.
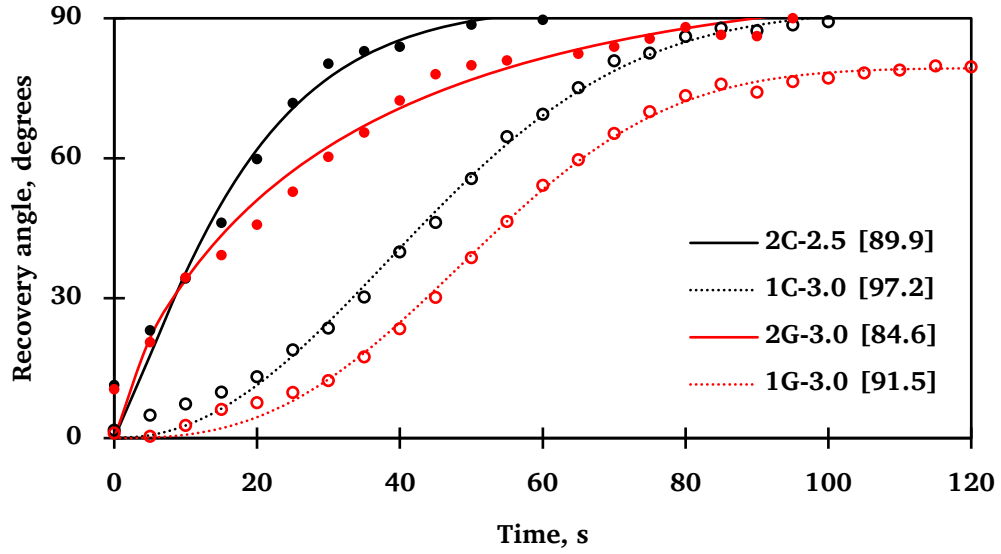
Figure 4.12: FRSMPC recovery behaviour

The CFRSMPCs' and GFRSMPCs' fastest and slowest recovery behaviours are illustrated in Figure 4.12. The fastest FRSMPC recovered its original shape within 60 s and the slowest specimen recovered 79.6° (88.4%) after 120 s. Due to the low thermal conductivity of matrix material and fibres, the initial recovery was slow; for example, 2C-2.5 recovered 60° within the first 20 s, but 1C-3.0 recovered only 13° (14.4%). The only significant difference between the two specimens was a 7.3% SMP weight fraction. Therefore, it can be concluded that incorporated fibres improved FRSMPCs' recovery rate ($\dot{R}_r$) remarkably. Figure 4.12 further reveals that the CFRSMPC recovery process was faster than the respective GFRSMPC. Overall, CFRSMPCs showed better recovery characteristics compared to GFRSMPCs. It is evident that the relationship between $R_{f,30}$ and R_r is relatively inverse. Therefore, it is necessary optimal, and the Taguchi design method utilises orthogonal arrays

which distribute the variables in a balanced manner while reducing the required number of experiments. Therefore, the author decided to conduct multi-attribute parametric optimisation prioritising the orthopaedic material requirements.

4.5.6 FRSMPC optimisation

The detailed design of the experiment is illustrated in Table 4-1 and Table A01. Density (ρ), minimum derivative of storage onset temperature ($\dot{T}_g$), tensile strength (σ_t), compression strength (σ_c), flexural strength (σ_f), impact strength (σ_i), shape fixity ratio (R_f), shape retention ratio ($R_{f,30}$) and shape recovery ratio (R_r) responses calculated Taguchi signal to noise (S/N) are presented in Table 4-2. Among the types of quality characterising tools, the criterion of the smaller-the-better was used to calculate density and transition temperature. The remaining responses were calculated under the principle of the larger-the-better, as shown in equations 4.1 and 4.2 [318].

Table 4-2: FRSMPC S/N ratios summary

Sample name	Performance evaluation characteristics									S/N ratios								
	ρ	$T\grave{}_g$	σ_t	σ_c	σ_f	σ_i	R_f	$R_{f,30}$	R_r	ρ	$T\grave{}_g$	σ_t	σ_c	σ_f	σ_i	R_f	$R_{f,30}$	R_r
	Kgm^{-3}	^{o}C	MPa	MPa	MPa	Jmm^{-1}	%	%	%									
1C-2.0	1140	44.8	119	71.0	172	0.023	97.9	62.8	97.4	-61.14	-33.03	41.51	37.03	44.71	-32.77	39.82	35.96	39.77
1C-2.5	1134	46.3	95.0	73.0	158	0.046	96.5	83.6	94.4	-61.09	-33.31	39.55	37.27	43.97	-26.74	39.69	38.44	39.50
1C-3.0	1116	48.2	91.0	75.0	162	0.050	98.2	87.9	99.1	-60.95	-33.66	39.18	37.50	44.19	-26.02	39.84	38.88	39.92
2C-2.0	1164	49.3	168	97.0	271	0.040	96.5	64.7	98.3	-61.32	-33.86	44.51	39.74	48.66	-27.96	39.69	36.22	39.85
2C-2.5	1138	48.1	145	100	266	0.062	95.4	46.0	98.5	-61.13	-33.64	43.23	40.00	48.50	-24.15	39.59	33.26	39.87
2C-3.0	1136	50.4	132	107	231	0.074	94.9	77.8	100.0	-61.11	-34.05	42.41	40.59	47.27	-22.62	39.54	37.82	40.00
3C-2.0	1211	50.0	280	112	341	0.068	95.0	55.9	99.3	-61.67	-33.98	48.94	40.98	50.66	-23.35	39.55	34.95	39.94
3C-2.5	1171	51.4	206	119	282	0.071	94.2	82.5	99.4	-61.37	-34.22	46.28	41.51	49.00	-22.97	39.48	38.33	39.95
3C-3.0	1152	50.6	180	128	254	0.085	90.0	79.3	100.0	-61.23	-34.08	45.11	42.14	48.10	-21.41	39.08	37.99	40.00
1G-2.0	1177	45.4	81.0	59.0	164	0.081	99.2	98.4	92.7	-61.41	-33.14	38.17	35.42	44.30	-21.83	39.93	39.86	39.34
1G-2.5	1160	45.0	86.0	53.0	157	0.096	100	98.3	92.6	-61.29	-33.06	38.69	34.49	43.92	-20.35	40.00	39.21	39.34
1G-3.0	1159	49.7	97.0	67.0	148	0.084	98.8	87.7	91.0	-61.28	-33.93	39.74	36.52	43.41	-21.51	39.90	38.86	39.18
2G-2.0	1248	49.4	137	72.0	238	0.127	93.1	60.4	98.0	-61.92	-33.87	42.73	37.15	47.53	-17.92	39.38	35.62	39.82
2G-2.5	1219	45.4	140	84.0	215	0.173	93.5	72.4	97.6	-61.72	-33.14	42.92	38.49	46.65	-15.24	39.42	37.19	39.79
2G-3.0	1172	52.8	141	91.0	221	0.141	89.5	73.3	98.2	-61.38	-34.45	42.98	39.18	46.89	-17.02	39.04	37.30	39.85
3G-2.0	1361	49.4	195	92.0	257	0.180	88.6	48.2	98.9	-62.68	-33.87	45.80	39.28	48.20	-14.89	38.95	33.66	39.90
3G-2.5	1261	51.5	177	92.0	247	0.222	92.4	75.8	99.8	-62.01	-34.24	44.96	39.28	47.85	-13.07	39.32	37.59	39.98
3G-3.0	1218	53.2	161	98.0	242	0.270	87.6	78.5	99.2	-61.71	-34.52	44.14	39.82	47.68	-11.37	38.85	37.90	39.93

4.5.7 FRSMPC Taguchi optimisation

The optimal fabrication process parameters were determined based on the highest signal-to-noise (S/N) [319, 320]. The obtained control variables against each response are presented and ranked in Table 4-3. The relative contribution of each control variable to the process parameter is shown within the square bracket.

Table 4-3: FRSMPC control variable ranking summary

Responses	Fibre type	Number of layers	Thickness
Density	Carbon[†],[35.35%]	1[*],[33.92%]	3.0[§],[16.93%]
Transition temperature[‡]	Carbon[§],[0.34%]	1[*],[50.52%]	2.5[†],[26.75%]
Tensile strength	Carbon[†],[5.13%]	3[*],[75.80%]	2.0[§],[6.49%]
Compression strength	Carbon[†],[22.97%]	3[*],[68.69%]	3.0[§],[4.79%]
Flexural strength	Carbon[§],[6.98%]	3[*],[79.68%]	2.0[†],[5.97%]
Impact strength	E-glass[*],[52.59%]	3[†],[28.79%]	3.0[§],[4.18%]
Shape fixity ratio	Carbon[§],[5.65%]	1[*],[65.64%]	2.5[†],[6.82%]
Shape retention ratio	E-glass[§],[3.12%]	1[*],[34.31%]	3.0[†],[20.64%]
Shape recovery ratio	Carbon[†],[14.28%]	3[*],[60.01%]	3.0[§],[1.58%]

* Rank 1, † Rank 2, § Rank 3, [] Relative contribution, ‡ $\dot{T}_g$

The minimum density was for a single layer of carbon fibre with a 3 mm thick composite. Similarly, the $\dot{T}_g$ was lowest for a single layer of carbon fibre with a 2 mm thick specimen. The thickness of the FRSMPC made a critical impact on $\dot{T}_g$ and showed a relative contribution of over 50%, while fibre types were minimally influenced. In addition, the highest tensile

141

properties were obtained with three layers of carbon fibres in a 2 mm thick FRSMPC specimen. The number of layers contributed 75.80% to the tensile strength, followed by thickness (6.49%) and fibre type (5.13%). Interestingly, the same fabrication configuration was optimised for flexural properties as well.

The glass fibres mainly dominated impact properties with a relative contribution of over 50%, followed by the number of layers (28.79%) and thickness (4.18%). The R_f and $R_{f,30}$ were optimum for a single layer of carbon and glass fibres, accounting for relative contributions of 65.64% and 34.31%, respectively. The FRSMPC R_r was optimum for three layers of carbon fibres in a 3.0 mm thick FRSMPC specimen. Moreover, the number of layers dominated R_f and R_r and with relative contributions of over 60%. Therefore $R_{f,30}$ was driven by both the number of layers and the thickness of the specimen. The findings that were obtained do not show how the parameters impact the materials' general performance; thus, GRA is required.

4.5.8 FRSMPC grey relational analysis

In Section 4.5.7, fabrication parameters were optimised against each response. However, it is important to find optimum fabrication parameters after considering multiple responses to improve overall product performance of orthopaedic material [321]. Therefore, grey relational theory is popular as an engineering decision making tool. In this chapter the author combined the GRA with Taguchi method. After evaluating the orthopaedic requirements,

FRSMPCs', $\dot{T}_g$, σ_i and $R_{f,30}$ responses were selected for GRA. The smaller-the-better principle was used to normalise $\dot{T}_g$ and the larger-the-better principle was used to normalise all other chosen responses. The characteristic equations are shown in equations 4.3 and 4.4 [322]. After that, grey relation coefficients were determined for each process parameter using equation 4.5 [322]. The calculated grey relation values and grey relation coefficients are shown in Table 4-4.

Table 4-4: FRSMPC grey relational analysis

Sample name	Normalized values			Grey relational coefficients			Grey relational grade	
	$\dot{T}_g$	σ_i	$R_{f,30}$	$\dot{T}_g$	σ_i	$R_{f,30}$	Value	Rank
1C-2.0	1.0000	0.0000	0.3206	1.0000	0.3333	0.4239	0.5858	5
1C-2.5	0.8214	0.0931	0.7176	0.7368	0.3554	0.6390	0.5771	6
1C-3.0	0.5952	0.1093	0.7996	0.5526	0.3595	0.7139	0.5420	8
2C-2.0	0.4643	0.0688	0.3569	0.4828	0.3494	0.4374	0.4232	16
2C-2.5	0.6071	0.1579	0.0000	0.5600	0.3725	0.3333	0.4220	17
2C-3.0	0.3333	0.2065	0.6069	0.4286	0.3865	0.5598	0.4583	13
3C-2.0	0.3810	0.1822	0.1889	0.4468	0.3794	0.3814	0.4025	18
3C-2.5	0.2143	0.1943	0.6966	0.3889	0.3829	0.6223	0.4647	12
3C-3.0	0.3095	0.2510	0.6355	0.4200	0.4003	0.5784	0.4662	10
1G-2.0	**0.9286**	**0.2348**	**1.0000**	**0.8750**	**0.3952**	**1.0000**	**0.7567**	**1**
1G-2.5	0.9762	0.2955	0.8645	0.9545	0.4151	0.7868	0.7188	2
1G-3.0	0.4167	0.2470	0.7958	0.4615	0.3990	0.7100	0.5235	9
2G-2.0	0.4524	0.4211	0.2748	0.4773	0.4634	0.4081	0.4496	14
2G-2.5	0.9286	0.6073	0.5038	0.8750	0.5601	0.5019	0.6457	3
2G-3.0	0.0476	0.4777	0.5210	0.3443	0.4891	0.5107	0.4480	15
3G-2.0	0.4524	0.6356	0.0420	0.4773	0.5785	0.3429	0.4662	11
3G-2.5	0.2024	0.8057	0.5687	0.3853	0.7201	0.5369	0.5474	7
3G-3.0	0.0000	1.0000	0.6202	0.3333	1.0000	0.5683	0.6339	4
Overall mean							**0.5295**	

The overall GRGs were calculated after averaging the grey relation coefficients. Thus, multiple objectives were simplified to a single GRG. The optimum FRSMPC fabricating parameters were found based on grey relation S/N ratios [321]. The overall GRG equals 0.5295, and the higher GRGs are closer to the optimal. In this analysis, 2G-3.0, 2C-2.0, 2C-2.5, 3C-2.0 GRGs are less than 0.450 and ranked as 15, 16, 17 and 18, respectively. The means of the GRG and S/N ratios were calculated based on the larger-the-better principle, as expressed in equation 4.6 and these are presented in Table 4-5 and Figure 4.13.

Table 4-5: FRSMPC grey relational S/N ratios and means

Levels	Control factors		
	Fibre type	Number of layers	Thickness
$\dot{T}_g$, σ_i and $R_{f,30}$ grey relational S/N ratios (Larger is better)			
1	-6.408	-4.275	-6.002
2	-4.939	-6.576	-5.138
3		-6.169	-5.880
Delta	1.469	2.301	0.864
Rank	2	1	3
$\dot{T}_g$, σ_i and $R_{f,30}$ mean grey relational grade			
1	0.4824	0.6173	0.5140
2	0.5766	0.4745	0.5626
3		0.4968	0.5120
Delta	0.0942	0.1428	0.0506
Rank	2	1	3
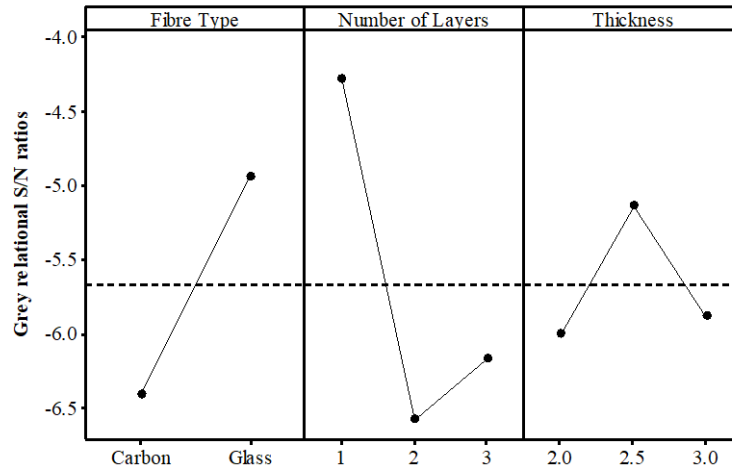
Figure 4.13: FRSMPC grey relational S/N ratio

The most optimum control factors were given with a single layer (grey relational, mean 0.6173 and S/N ratio -4.275) of glass fibre (grey relational, mean .5766 and S/N ratio -4.939) with 2.5 mm thick (grey relational, mean 0.5626 and S/N ratio -5.138) FRSMPCs. The number of layers mainly drives the FRSMPCs properties, followed by the fibre type and the thickness of the specimen.

4.5.9 FRSMPC ANOVA analysis

The Taguchi method cannot describe each control variable's impact on the final objective. Therefore, grey relational ANOVA analysis is conducted to determine the individualistic impact on the main objective. The result revealed that the fibre type and the number of layers are significant in selected responses since the P-value was less than 0.05 (95% confident level).

145

Table 4-6:FRSMPC grey relational ANOVA

Variance source	Degree of freedom	Sum of squares	Mean square	F ratio	P-value	Contribution (%)
Fibre type	1	0.039950	0.039950	7.22	**0.020**	**21.35**
Layers	2	0.070852	0.035426	6.40	**0.013**	**37.86**
Thickness	2	0.009863	0.004931	0.89	0.436	5.27
Error	12	0.066433	0.005536			
Total	17	0.187098				

According to Table 4-6, the highest relative contribution was 37.86%, given by the number of layers, while the fibre type and the thickness of the specimen contributed 21.35% and 5.27%, respectively. Thus, the thickness of the FRSMPC was not significant for overall performance. The most optimal mechanical and shape memory functional properties were given by 1G-2.5 (one layer of glass fibre in 2.5 mm thick FRSMPC). Therefore, the authors concluded that one layer of glass fibre is advisable to manufacture next generation orthopaedic smart materials on demand.

4.6 Nanoparticle reinforced shape memory polymer composites

NPs are having sizes ranging from 1 to 100 nm. These obtained wide interest from SMP researchers due to their superior physical, chemical, electrical, mechanical, and thermal properties and their high surface area and low density to-volume ratio [323]. NPs are often used to enhance the base material's properties [324]. In addition, NPs demonstrate antimicrobial effects, self-cleaning, scratch or abrasion resistance, and act like a UV protective coating [325, 326].

In this chapter, the author is interested in incorporating biocompatible NPs with synthesised SMP; thus, TiO_2, MWCNT and graphene NPs were selected. Moreover, TiO_2 is research friendly material and it has the ability to decompose organic pollutants under an aqueous environment [327-329]. The thermomechanical and shape memory functional properties can alter with NPs [330]. Therefore, in this section, NRSMPC's thermomechanical and shape memory properties were comprehensively investigated. Finally, the GRA combined Taguchi method effectively identified the optimum NP type and weight percentage that could use to fabricate orthopaedic bone fracture fixators.

4.6.1 Nanoparticle dispersion with DGEBA

Among the different techniques for dispersing NPs, ultrasonic irradiation has shown excellent emulsifying and crushing performance [331]. The sonication process is essential for mitigating agglomerates; however, prolonged sonication time probably increases epoxy temperature, micro-bubbles, cavitation, breaking apart molecules and finally degrading the epoxy resin performance [79]. Therefore, the author of this thesis provides critical insight into finding optimum NP dispersion time for DGEBA before fabricating NRSMPCs. The process parameters such as amplitude, mode, epoxy volume and the weight percentage of NPs were kept constant. After each sonication step (5 min.), FTIR was performed using Thermo Scientific™ and analysed through OMNIC™ Professional quantitation software.
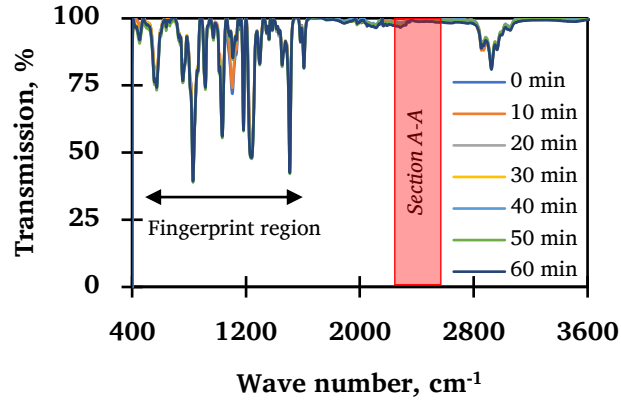
(a)
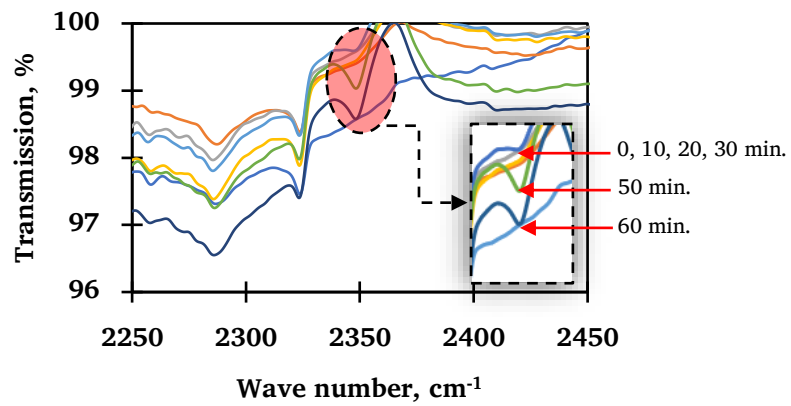
(b) Section A-A

Figure 4.14: FTIR analysis of DGEBA epoxy with TiO_2 NPs

Figure 4.14 revealed that the fingerprint region (600-1500 cm^{-1}) transmittance remained unchanged during 60 min. of sonication. However, the 2000-2500 cm^{-1} region shows an interesting behaviour and a further enlarged view is shown in Figure 4.14 (b). It can be seen that at 2350 cm^{-1}, there is a slight drop in transmittance after 40 min. of sonication and this could be an initial clue for the degradation of the resin due to the ultrasonic dispersion. The FTIR analysis leads the author to conclude that 30 min. of

short dispersion avoids DGEBA matrix degradation; thus, the settings are economically worthwhile. This method is more convenient since researchers can understand optimum dispersion time without processing solid specimens. As a result, the author used 200 W, 20 kHz, pulse mode (5s on, 5s off) ultrasonic settings to disperse NPs for 30 min.

Table 4-7: NRSMPC Taguchi L_9 design of experiment

Sample name	Nanoparticle type	Weight percentage, ($wt\%$)
T0.4	TiO$_2$	0.4
T0.7	TiO$_2$	0.7
T1.0	TiO$_2$	1.0
M0.4	MWCNT	0.4
T0.7	MWCNT	0.7
T1.0	MWCNT	1.0
G0.4	Graphene	0.4
G0.7	Graphene	0.7
G1.0	Graphene	1.0

4.6.2 NRSMPC preparation

The NPs were measured and DGABA and NGDE resins were introduced and stirred with an HB502 laboratory mixing device. The epoxy mixture was degassed and heated to 30°C to reduce the viscosity before sonication for 30 min. with pulse mode (5 s on and 5 s off) in cold water (~10°C) circulation bath. The epoxy temperature was consistently held below 60°C while 400 ml at a time were being sonicated. After the sonication process, entrapped air

was removed, and the dissolver was kept until it reached room temperature before introducing hardeners. Then cured at 65°C for 6 hrs., followed by a post-curing cycle at 115°C for 1 hr. (DGEBA-65). The fabrication configuration of NRSMPCs is illustrated in Table 4-7. Finally, the panels were cut using a water jet cutter per the ASTM /ISO standards described in Chapter 4.4. The water jet cutting layout is shown in Figure 4.15.
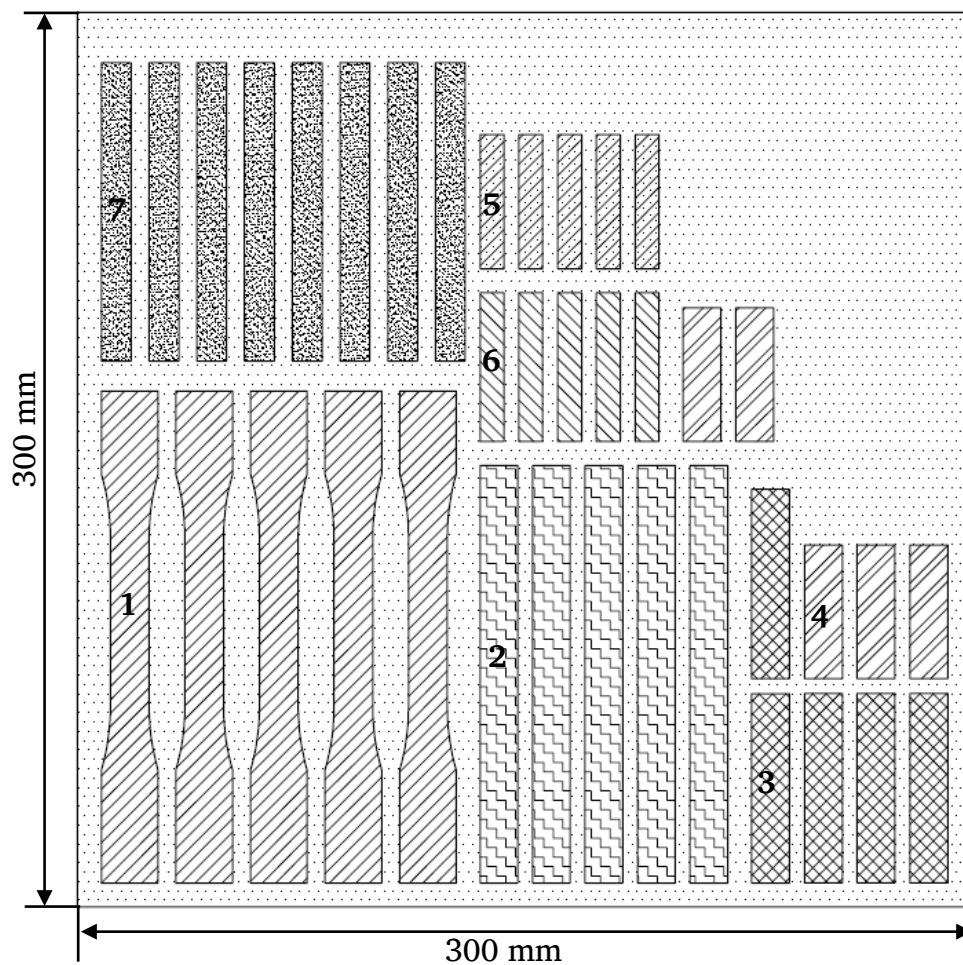
Part	Specimen name	Dimensions (mm)
1	Tensile specimen	165×13
2	Compression specimen	140×12.7
3	Impact specimen	63.5×8

4	Flexure specimen	44.8×12.7
5	DMA (Rheometre) specimen	45×8
6	DMA Q800 specimen	50×8
7	Shape memory specimen	100×10

Figure 4.15: NRSMPC water jet DXF cutting layout

4.6.3 NRSMPC viscoelastic and mechanical properties evaluation

The TiO_2 and MWCNT nanocomposites' surface morphology is shown in Figure 4.16. It was found that TiO_2, MWCNT and graphene NPs were uniformly dispersed without agglomeration and voids within the SMP matrix.

T0.4   M0.4
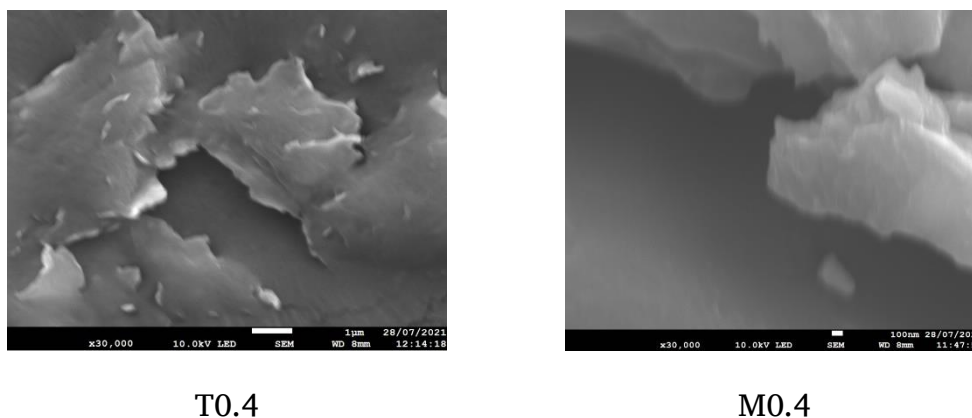
Figure 4.16: NRSMPC SEM images (a) T0.4, (b) M0.4

NRSMPCs viscoelastic, tensile, flexural and shape recovery behaviour are illustrated in Figure 4.18. (a), (b), (c), and (d). Moreover, neat SMP (SMP-0) and NRSMPCs average viscoelastic and thermomechanical experimental data are summarised in Table 4-8. The minimum SM is seen in SMP-0, and the T1.0 SM increased by 16.5% than the SMP-0. The highest σ_t was observed in

TiO_2 nanocomposites, followed by MWCNT and graphene nanocomposites. During the failure analysis it was observed that, T0.4, T0.7 and T1.0 were plastically deformed. According to the ASTM D3039-17, LGM and AGM failure modes are frequently identified and T0.4, M0.4 and G0.4 specimens are present in Figure 4.17. Interestingly, a higher percentage of NP's (>0.7 *wt*%) recorded lesser σ_t than SMP-0. The same tendency was observed in σ_c and σ_f as well. However, NRSMPCs σ_i has significantly dropped (~89%) compared to the SMP-0.

| T0.4 | T0.4 | G0.4 |
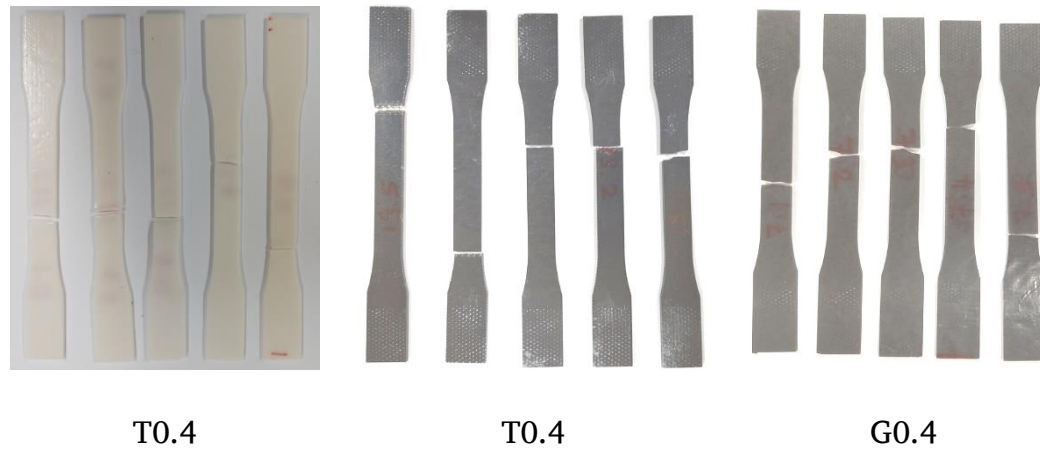
Figure 4.17: NRSMPC tensile failure

According to the fold deploy experimental results, TiO_2 nanocomposites $R_{f,30}$ is minimum compared to other respective NRSMPCs. However, $R_{f,30}$ increased with the TiO_2, MWCNT and graphene NPs weight percentage compared to SMP-0. On the other hand, the highest R_r was recorded in SMP-0 and dropped significantly with weight percentages of NPs.

Overall, it was hard to differentiate the NPs effect and select optimum fabrication parameters without proper statistical optimisation technique.

Table 4-8: NRSMPC experimental summary

Sample name	$\dot{T}_g$ °C	SM	σ_t	σ_c	σ_f	σ_i J/mm	R_f	$R_{f,30}$	R_r
				MPa				%	
2E	45.93	2323	40.51	43.60	78.86	0.048	100.0	90.8	89.3
T0.4	45.12	3030	45.52	52.26	93.97	0.004	99.9	97.6	80.3
T0.7	45.49	2884	43.21	52.01	84.91	0.004	100.0	93.7	75.7
T1.0	45.89	2707	36.98	43.02	38.36	0.006	98.7	91.0	72.8
M0.4	46.13	2895	39.47	49.66	94.25	0.007	98.5	91.6	86.9
M0.7	46.84	3023	37.25	48.63	86.30	0.006	99.3	91.2	74.4
M1.0	45.65	3589	23.06	40.43	35.79	0.006	98.9	90.4	82.1
G0.4	44.50	2951	30.59	52.49	94.38	0.004	99.1	93.5	92.2
G0.7	45.51	3021	28.88	51.65	78.59	0.005	98.6	86.7	73.3
G1.0	46.88	3290	9.72	43.18	48.40	0.006	97.2	77.1	49.6

Neat 2 mm thickness

The average $\dot{T}_g$ of NRSMPCs was 45.79 ± 0.72°C, with a narrow range of 2.38°C. The data ranged over a narrow region in σ_t, σ_c, σ_f, $R_{f,30}$, and R_r. The overall average variations of σ_i (0.05 ± 0.001 J/mm), and R_f ($98.91 \pm 0.83\%$) were insignificant. Therefore, $\dot{T}_g$, SM, σ_t, σ_c, σ_f, σ_i, $R_{f,30}$, R_r were considered during the Taguchi analysis of the NRSMPCs.

4.6.4 NRSMPC Taguchi optimisation

During the NRSMPC S/N ratio calculation, smaller-the-better (equation 4.1) was considered for the $\dot{T}_g$ and the rest of the parameters were calculated using the larger-the-better quality characteristic tool (equation 4.2).
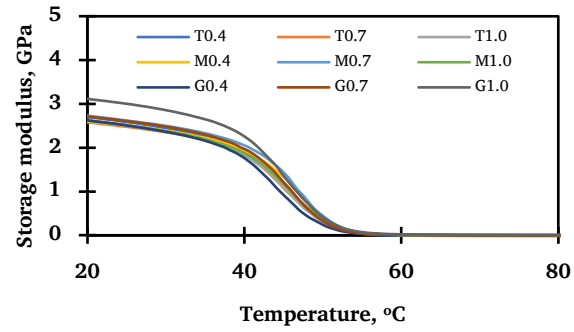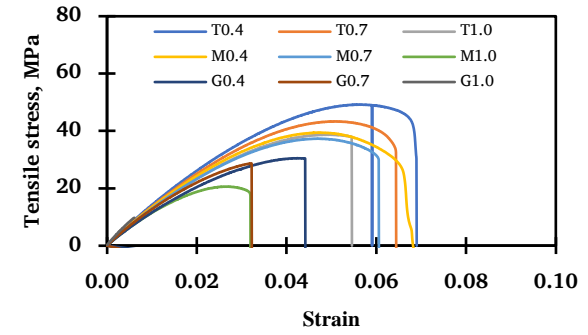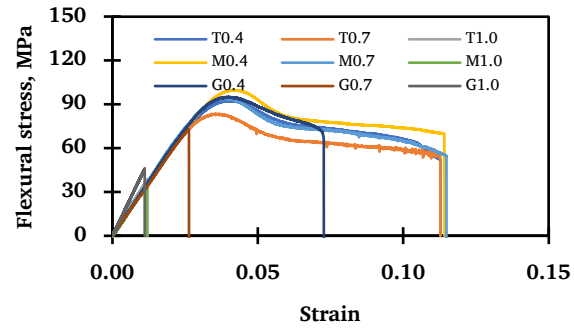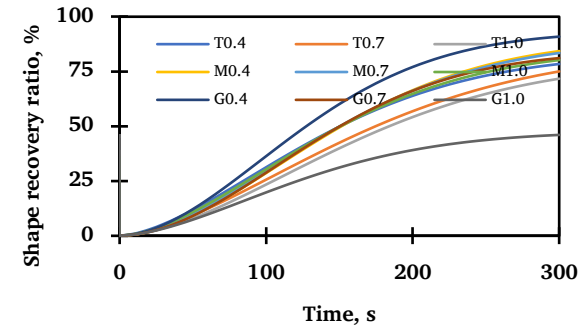
Figure 4.18: NRSMPC (a) Viscoelastic, (b) Tensile, (c) Flexural, (d) Shape recovery properties

According to the Taguchi analysis, the highest S/N ratio represents the optimal choice among the parameters. $\dot{T}_g$ of the NRSMPCs was the minimum for 0.4 *wt*% (S/N -33.11) of TiO_2 (S/N -33.16) NPs.

Table 4-9: NRSMPC control variable ranking summary

Responses	Nanoparticle type	Weight percentage, (*wt*%)
Transition temperature	TiO_2	0.4[†]
Storage modulus	MWCNT[†]	1.0
Tensile strength	TiO_2[†]	0.4
Compression modulus	Graphene	0.4[†]
Flexural strength	Graphene	0.4[†]
Impact strength	MWCNT[†]	1.0
Shape fixity after 30 days	TiO_2[†]	0.4
Shape recovery after 300 s at 47°C	MWCNT	0.4[†]

The optimal levels of the control factors for dependent parameters are summarised and ranked in Table 4-9. NRSMPC analysis offered an optimal R_r of 0.7 *wt*% (S/N 38.72) of MWCNT (S/N 38.17). On the other hand, in orthopaedic biomedical applications, R_f is critical and should retain a prolonged period. The robust Taguchi analysis offered the highest R_f for 0.4 *wt*% (S/N 39.48) with TiO_2 (S/N 39.47) NPs. In the next chapter, the author decided to simply multi objectives to a single objective function with the aid of GRA.

4.6.5 NRSMPC grey relational analysis

$\dot{T}_g$, SM, σ_t, σ_f, $R_{f,30}$ and R_r were considered during the GRA. $\dot{T}_g$ was normalised concerning smaller-the-better and other responses were normalised against the larger-the-better as per equations (4.3) and (4.4). Based on the normalised grey relational data, the grey relational coefficients were calculated and averaged into an overall grey relational grade (Equations 4.5 and 4.6). The normalised grey relational values and grey relational coefficients are mentioned in Table 4-10. The mean grey relation was 0.604, while the T0.4 specimen recorded a 0.788 Grey relational grade. Table 4-11 and Figure 4.19 illustrate the S/N ratios and respective mean grey relational grades. According to Table 4-11, the overall optimal fabrication parameters were given T0.4 specimen, which contained 0.4 *wt*% (S/N -2.597) of TiO_2 (S/N -4.022). Therefore, the authors strongly recommend using 0.4 *wt*% of TiO_2 to fabricate orthopaedic fracture fixators and splints.

Table 4-10: NRSMPC grey relational analysis

Sample name	Normalised value						Grey relational coefficients						Grey relational grade	
	$\dot{T}_g$	SM	σ_t	σ_f	$R_{f,30}$	R_r	$\dot{T}_g$	SM	σ_t	σ_f	$R_{f,30}$	R_r	Value	Rank
T0.4	0.742	0.366	1.000	0.993	1.000	0.721	0.659	0.441	1.000	0.986	1.000	0.642	0.788	1
T0.7	0.584	0.200	0.936	0.838	0.811	0.613	0.546	0.385	0.886	0.756	0.726	0.564	0.644	4
T1.0	0.416	0.000	0.761	0.044	0.680	0.546	0.461	0.333	0.677	0.343	0.610	0.524	0.491	8
M0.4	0.317	0.213	0.831	0.998	0.711	0.877	0.423	0.389	0.748	0.996	0.634	0.802	0.665	3
M0.7	0.019	0.358	0.769	0.862	0.688	0.583	0.338	0.438	0.684	0.784	0.615	0.545	0.567	6
M1.0	0.519	1.000	0.373	0.000	0.651	0.764	0.510	1.000	0.443	0.333	0.589	0.679	0.592	5
G0.4	1.000	0.276	0.583	1.000	0.801	1.000	1.000	0.409	0.545	1.000	0.715	1.000	0.778	2
G0.7	0.576	0.356	0.535	0.731	0.469	0.557	0.541	0.437	0.518	0.650	0.485	0.530	0.527	7
G1.0	0.000	0.661	0.000	0.215	0.000	0.000	0.333	0.596	0.333	0.389	0.333	0.333	0.386	9
Overall mean													**0.604**	

Table 4-11: NRSMPC grey relational S/N ratios and means

Levels	Control factors	
	Nanoparticle type	Weight Percentage
$\dot{T}_g$, SM, σ_t, σ_f, $R_{f,30}$, R_r Grey relational S/N ratios (larger is better)		
1	-4.022	-2.597
2	-4.337	-4.772
3	-5.335	-6.325
Delta	1.313	3.729
Rank	2	1
$\dot{T}_g$, SM, σ_t, σ_f, $R_{f,30}$, R_r Mean grey relational grade		
1	0.6411	0.7438
2	0.6083	0.5793
3	0.5638	0.4901
Delta	0.0773	0.2537
Rank	2	1
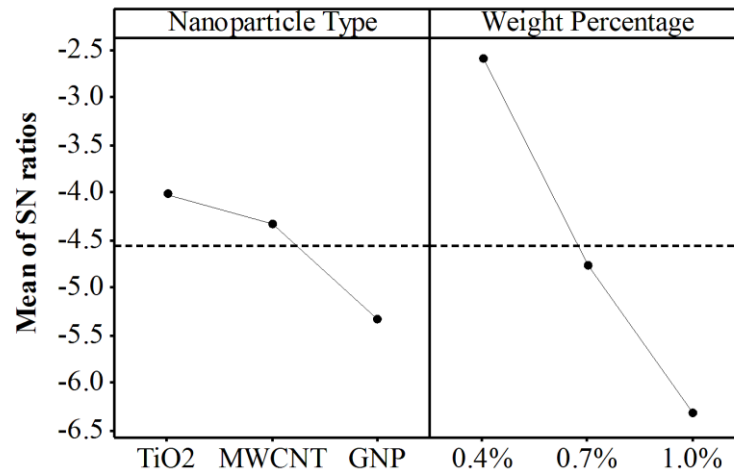
Figure 4.19: NRSMPC grey relational S/N ratios

4.6.6 NRSMPC ANOVA analysis

The grey relational ANOVA is shown in Table 4-12. According to the results, the NP weight percentage is the most dominant factor, which recorded a 72.545% relative contribution. Further, it can be seen that the P-value of NP

type is 0.578 and the weight percentage P-value is 0.050. Therefore, the NP's weight percentage is more dominant for the overall objective with a 95% confidence level.

Table 4-12: NRSMPC grey relational ANOVA

Variance source	Degree of freedom	Sum of squares	Mean square	F-value	P-value	Contribution (%)
Nanoparticle type	2	0.009025	0.004513	0.63	0.578	6.59%
wt %	2	0.099356	0.049678	6.95	0.050	72.54%
Error	4	0.028588	0.007147			
Total	8	0.136969				

In this research author synthesised fibre reinforced shape memory polymer composites according to L_{18} orthogonal Taguchi experimental array. Fibre type, number of layers and thickness were taken as process parameters. Therefore, it is clear that fibre type and number layers are discreet variables. The only continuous variable is thickness, in which was range from 2.0 mm to 3.0 mm with 0.5 mm step. Since the step size is smaller (≤ 0.5 mm), it was expected that the optimised results are in highest confident level. In addition to that NPRSMPCs synthesised according to L_9 orthogonal experimental array. The nanoparticle type and nanoparticle weight percentage (*wt*%) were used as process parameters. In this case nanoparticle type is a discrete variable and nanoparticle *wt*% is a continuous variable. During the experimentation the author varied nanoparticle weight percentage from 0.4% to 1.0% with 0.3% step size. The selected step size is smaller (≤ 0.3 *wt*%). Before finding an

optimum set of fabrication parameters, among the multiple responses, the critical once is chosen. For example, according to the grey relational ANOVA analysis, the effect of thickness on FRSMPC performances was insignificant (P > 0.05). Also, in literature author found that many published journal articles with similar or even larger step sizes [294, 332-337]. Thus, the author was highly confident about the optimised results.

4.7 Ortho$^+$ synthesis and characterisation

After considering optimum FRSMPC (Chapter 4.5) and NRSMPC (Chapter 4.6) fabrication parameters, the author synthesised novel shape memory polymer hybrid composite for non-invasive orthopaedic bone immobilisation and denoted as Ortho$^+$. The Ortho$^+$ fabrication process flow chart is shown in Figure 4.20. Next the synthesis process of Ortho$^+$ is briefly described. First, the DGABA and NGDE were introduced to the 0.4 *wt*% TiO$_2$ and stirred with an HB502 laboratory mixing device. Following this, epoxy was sonicated for 30 min. (pulse mode, 5 s on and 5 s off) using a 200 W Sonoplus GM2200 ultrasonic generator. At a time, 400 ml of epoxy was sonicated while strictly maintaining the solution temperature below 60°C. Finally, the epoxy was poured into the glass mould, which contained an E-glass fabric layer, and this was cured at 65°C for 6 hrs., followed by post-curing at 115°C for another hour (DGEBA-65) and cut into the standard specimen sizes.
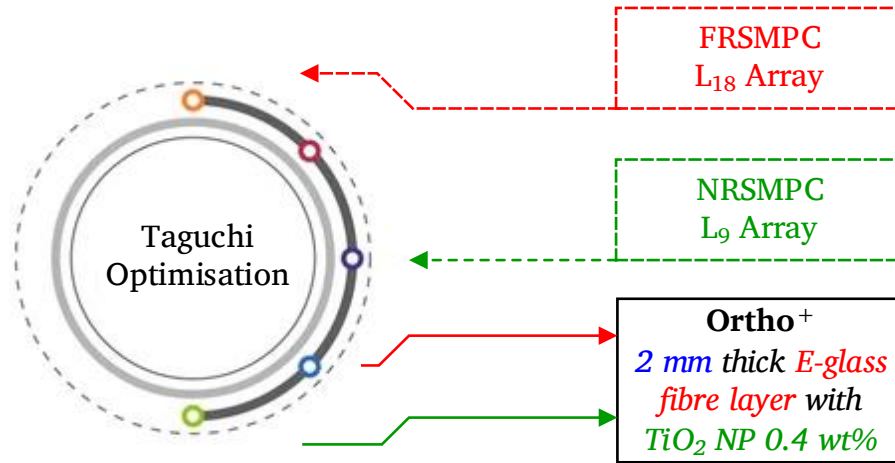
Figure 4.20: Ortho$^+$ fabrication: process chart

D-0	Ortho$^+$ kept at 0°C for 90 days
D-23	Ortho$^+$ kept at 23°C for 90 days
D-40	Ortho$^+$ kept at 40°C for 90 days
D-60	Ortho$^+$ kept at 60°C for 90 days
D-40/98	Ortho$^+$ kept at 40°C and 98% relative humidity for 90 days

A detailed examination of Ortho$^+$'s thermo-mechanical and shape memory properties was undertaken to identify the limitations and functionality in different environments. First Ortho$^+$ specimens were kept at five different environmental configurations for 3 months and properties are presented at room temperature. Interestingly, the measured D-23 properties are effectively identical to immediate Ortho$^+$ thermomechanical and shape memory properties; thus, the author of this thesis presents D-23.

The Ortho$^+$ thermogravimetric analysis (TGA) was performed in aluminium crucibles using a TA Instruments Discovery SDT 650. In an air

atmosphere, the temperature was raised from room temperature to 800°C at a rate of 5°C/min. Additionally the characterisation procedure of FTIR, DMA, tensile, compression, flexure, impact and shape memory properties are detailed in Chapters 4.7.1 to 4.8.

4.7.1 Ortho$^+$ decomposition temperature
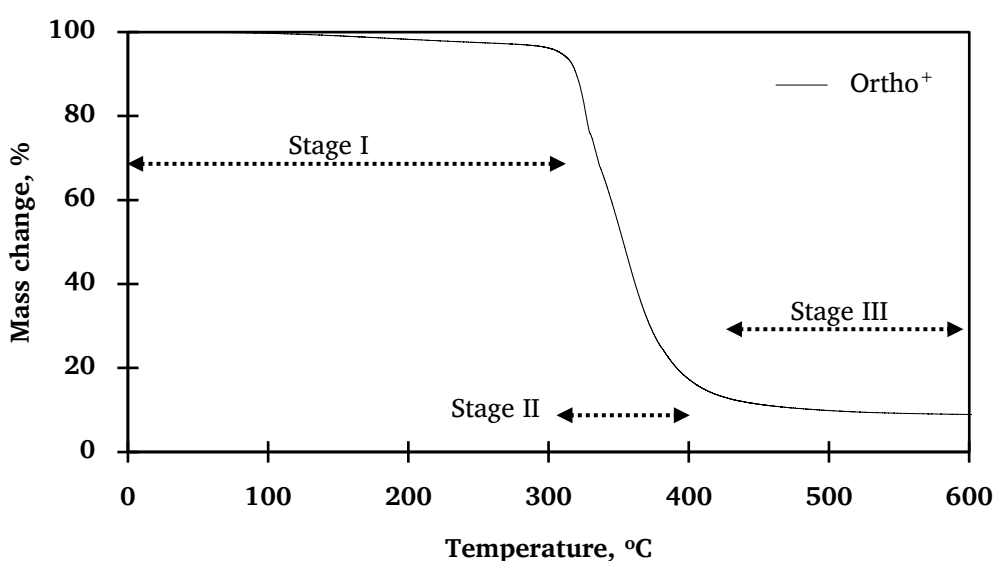
Figure 4.21: Ortho$^+$ decomposition temperature

The TGA result is illustrated as a function of mass loss against temperature. According to Figure 4.21, three stages of mass loss from room temperature to 600°C are identified, Stages I ($<$315°C), II (315°C-420°C) and III ($>$420°C). The rapid mass loss in stage II is due to the carbonate phase's decomposition, which releases carbon dioxide. Thus, the Ortho$^+$ is thermally stable and durable for orthopaedic applications between 40°C and 70°C.

162

4.7.2 Ortho$^+$ viscoelastic properties

The Ortho$^+$ viscoelastic properties are illustrated in Figure 4.22 and tabulated in Table 4-13. The D-40/98 specimen recorded the highest storage modulus, while the lowest was seen in D-60. However, no significant changes were found between D-23, D-40, and D-60 SM, whereas D-40/98 SM improved by 131.77% compared to D-23. Moreover, D-0 SM was enhanced by 58.69% compared to D-23 due to the hydrogen bonds.
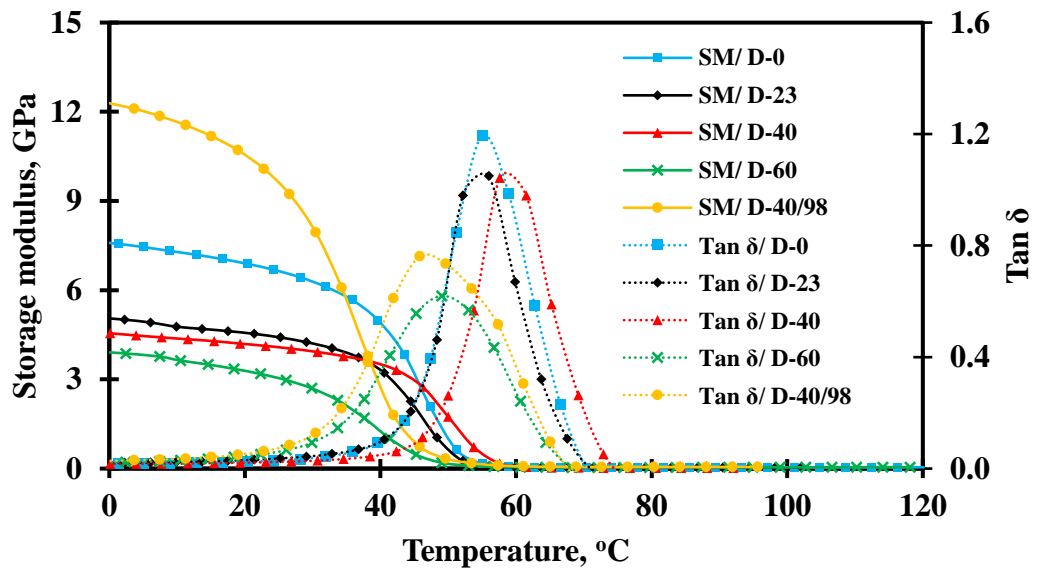
Figure 4.22: Smart plaster viscoelastic properties.

On the other hand, D-0, D-23 and D-40 Tan δ peaks were comparable, while the D-60 Tan δ peak dropped by 39.08% compared to D-23. For D-60 and D-40/98, less transition temperatures were recorded than for D-0, D-23 and D-40. For example, D-40/98 dropped storage onset and Tan δ transition temperatures by 28.83% and 12.24%, respectively, compared to D-23.

Without considering D-60 and D-40/98, the Ortho$^+$ had average T_g and Tan δ transition temperatures of 40.19 ± 2.4°C and 56.12 ± 2.83°C, respectively. After thoroughly examining viscoelastic properties, it is concluded that storing Ortho$^+$ at room temperature or below has no major influence on viscoelastic properties.

4.7.3 Ortho$^+$ mechanical properties

Ortho$^+$ tensile, compression and flexural properties are illustrated in Figure 4.23 and tabulated in Table 4-14. D-0, D-23 and D-40 tensile strengths and modulus are identical, but a higher failure strain was seen in D-0. A low level of gross plastic deformation and localised plasticity was observed due to TiO$_2$ NPs before the brittle fracture. During the tensile test, most specimens (>90%) failed under "AGM" mode, and the stress versus strain relationship was linear until the failure, as shown in Figure 4.23.(a). The highest compression strength and modulus were seen in D-23. The specimen reached 71.3 ± 1.0 MPa maximum compression strength at 0.068 strain before rapidly dropping. Compared to D-23, D-0 and D-40 experienced reduced compression strength by 47.6% and 27.5%, respectively. Overall, D-0, D-40, D-60 and D-40/98 Ortho$^+$ specimens buckled before falling sharply.

The Ortho$^+$ flexural properties are illustrated in Figure 4.23.(c). Interestingly the maximum failure stress of 160.2 MPa and flexural modulus of 4.08 GPa were seen in D-40. Compared to D-23, D-40's flexural strength and modulus were improved by 19.0% and 15.2%, respectively. D-23, on the

other hand, had a maximum failure strain of 0.056. Moreover, D-40/98's flexural strength and modulus dropped by 76.6% and 66.1%, respectively, compared to D-23. According to the tabulated impact properties in Table 4-14, the highest impact strength was seen in D-0, double that of D-23. The least impact energy, 0.013 J/mm, was seen in D-40/98, with a 63.9% reduction compared to D-23. It is clear that the stored environments influenced Ortho$^+$ mechanical properties positively and negatively. Overall, a significant reduction was observed in the mechanical properties of D-60 and D-40/98 compared to D-0, D-23 and D-40. Thus, the environments to which the Ortho$^+$ is exposed are crucial for retaining their characterised properties in accordance with the specifications.
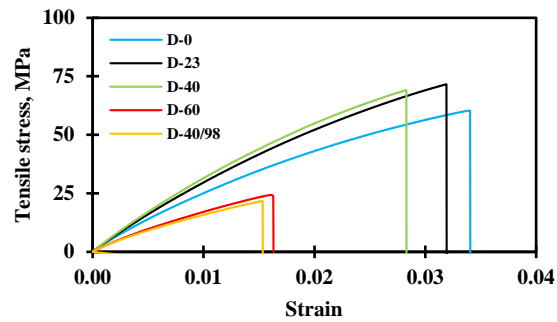
(a)
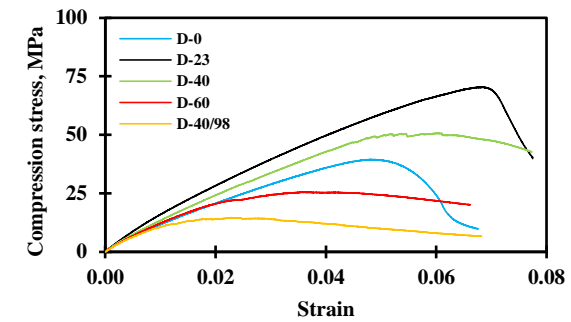
(b)
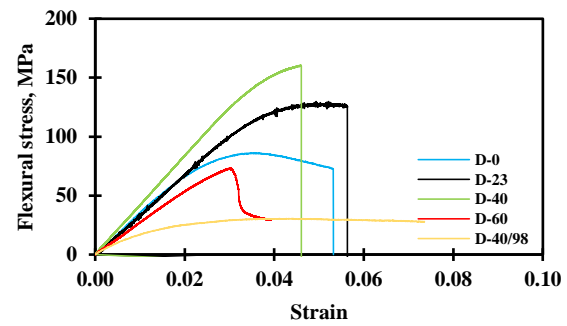
(c

Figure 4.23: Ortho$^+$ (a) Tensile, (b) Compression, (c) Flexural properties

166

Table 4-13: Ortho$^+$ viscoelastic properties

Sample name	T$_g$, (ºC)				†Storage modulus, (GPa)	Peak of loss modulus, (GPa)	Peak of Tan δ
	Storage onset	Min. derivation	Peak of loss	Peak of Tan δ			
D-0	38.27 ± 0.14	47.25 ± 0.70	47.90 ± 0.71	54.94 ± 0.12	6.943 ± 0.268	1.184 ± 0.035	1.033 ± 0.228
D-23	39.47 ± 0.07	45.40 ± 0.52	46.38 ± 0.94	54.07 ± 0.01	4.375 ± 0.141	0.395 ± 0.015	1.108 ± 0.170
D-40	42.84 ± 0.76	49.72 ± 0.38	51.31 ± 0.05	59.35 ± 0.56	4.045 ± 0.114	0.459 ± 0.015	1.205 ± 0.148
D-60	30.92 ± 0.82	39.43 ± 1.09	39.43 ± 0.48	50.94 ± 2.12	3.218 ± 0.123	0.436 ± 0.007	0.675 ± 0.053
D-40/98	28.09 ± 0.72	37.61 ± 1.97	37.94 ± .0.57	47.45 ± 0.58	10.14 ± 0.26	1.436 ± 0.019	0.786 ± 0.023

† The storage modulus at room temperature is reported

Table 4-14: Ortho$^+$ mechanical properties at room temperature

Sample name	Tensile properties, (MPa)		Compression properties, (MPa)		Flexural properties, (MPa)		Impact strength, (J/mm)
	Strength	Modulus	Strength	Modulus	Strength	Modulus	
D-0	60.3 ± 3.8	3735.4 ± 100.4	37.3 ± 3.1	881.9 ± 40.4	87.6 ± 2.1	3546.7 ± 89.7	0.075
D-23	74.4 ± 3.9	4440.3 ± 115.6	71.3 ± 1.0	1221.3 ± 43.0	129.7 ± 0.2	3463.2 ± 53.0	0.036
D-40	71.7 ± 1.6	4577.2 ± 47.6	51.7 ± 0.9	1098.7 ± 15.3	160.2 ± 5.4	4086.3 ± 92.6	0.024
D-60	23.2 ± 1.2	2432.9 ± 61.3	22.0 ± 1.4	807.8 ± 3.9	74.0 ± 1.0	2800.6 ± 36.0	0.013
D-40/98	23.6 ± 3.4	2367.6 ± 94.8	13.1 ± 1.2	771.0 ± 51.3	30.3 ± 1.0	1174.3 ± 77.2	0.017
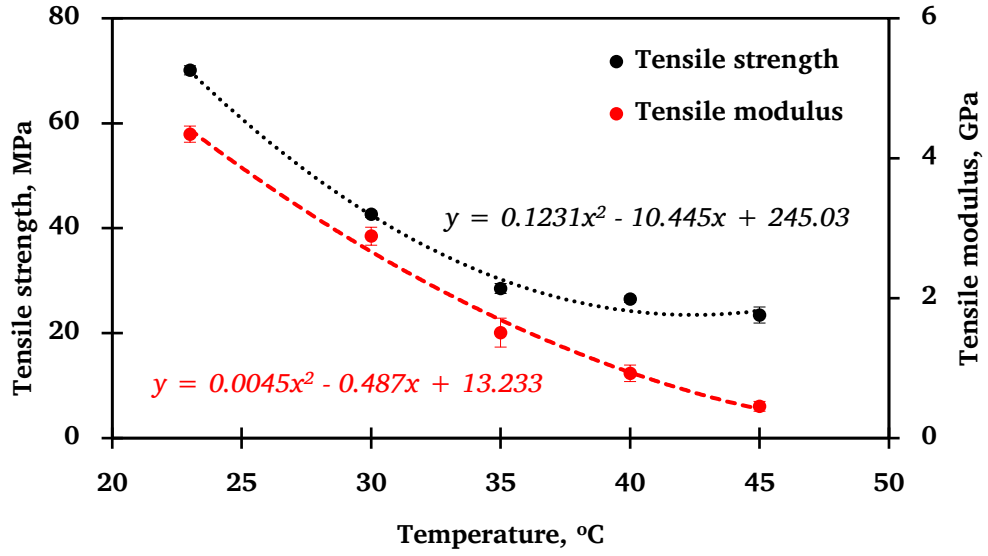
Figure 4.24: Ortho+ tensile properties at elevated temperature
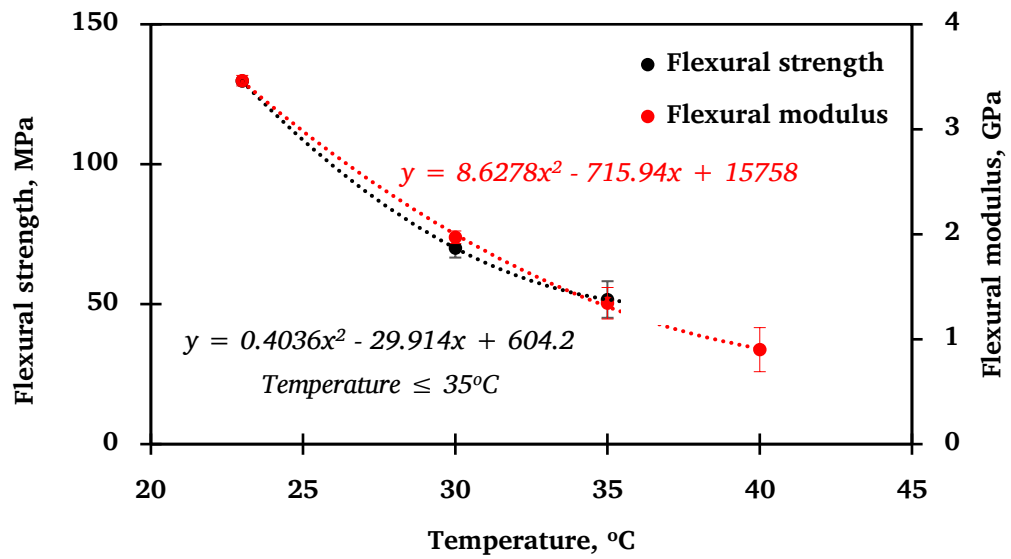
Figure 4.25: Ortho+ flexural properties at elevated temperature

In addition, the Ortho+ tensile and flexural properties were investigated at the elevated temperatures of 30°C, 35°C, 40°C and 45°C, with results illustrated in Figure 4.24 and Figure 4.25 and tabulated in Table 4-15.

The highest tensile and flexural properties were seen at 23°C, and these gradually dropped due to the temperature effect. For example, at 30°C, tensile and flexural strengths dropped by 42.7% and 46.0% compared to their strengths at 23°C. The relationship of strength versus temperature was represented through second-order polynomial functions with $R^2 > 99\%$.
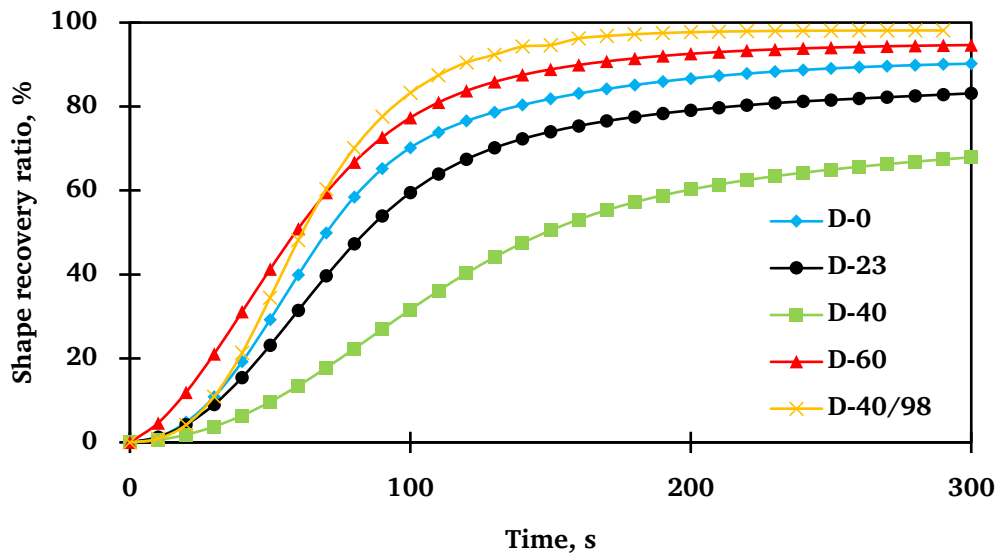
Figure 4.26: Average Ortho$^+$ shape recovery at 40°C and 50°C for 90° and 180° programme angles

4.8 Ortho$^+$ shape memory properties

Ortho$^+$ shape memory functional properties were evaluated at 40°C and 50°C. Figure 4.26 illustrates the average R_r at 40°C and 50°C for 90° and 180° angles for D-0, D-23, D-40 and D-60. According to Figure 4.26, D-40/98 and D-40 obtained the maximum and minimum R_r and $\dot{R}_r$, respectively. Further, it was noticed that 90° programmed D-40 specimens recovered

169

linearly, although ultimate R_r was less than 60% for 40ºC and 50ºC programming temperatures.

Additionally, R_r was averaged based on programmed angles and temperatures, as presented in Figure 4.27. It is clear that 180º programmed specimens had higher R_r and $\dot{R}_r$ while following a sigmoidal function, regardless of the recovery temperature. On the other hand, 90º programmed specimens at 40ºC a higher R_r was recorded than at 50ºC. This is likely due to the higher residual stress for Ortho$^+$ programmed at the lower temperature.
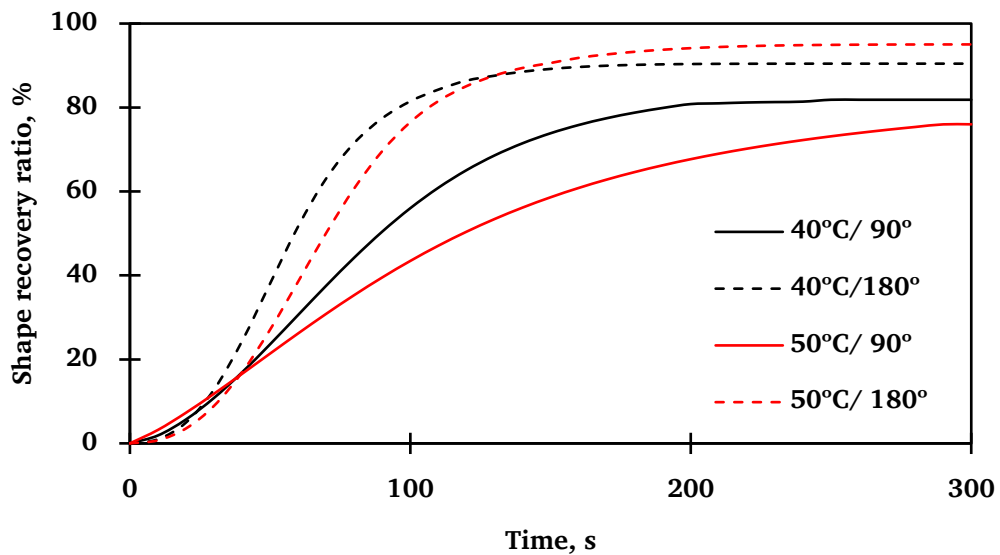
Figure 4.27: Average Ortho$^+$ shape recovery based on programming temperature and angle

Figure 4.28 illustrates the average five cycles of Ortho$^+$ R_r for a 90º programmed angle at 50ºC. The overall $R_r > 80\%$, while D-23 $\dot{R}_r$ was the lowest. Interestingly, the standard deviation of D-0 was significantly higher

than those of other configurations, which might be attributed to the trapped residual energy. However, as illustrated in Figure 4.26, Figure 4.27 and Figure 4.28, R_r was within the acceptable range for biomedical orthopaedic applications.
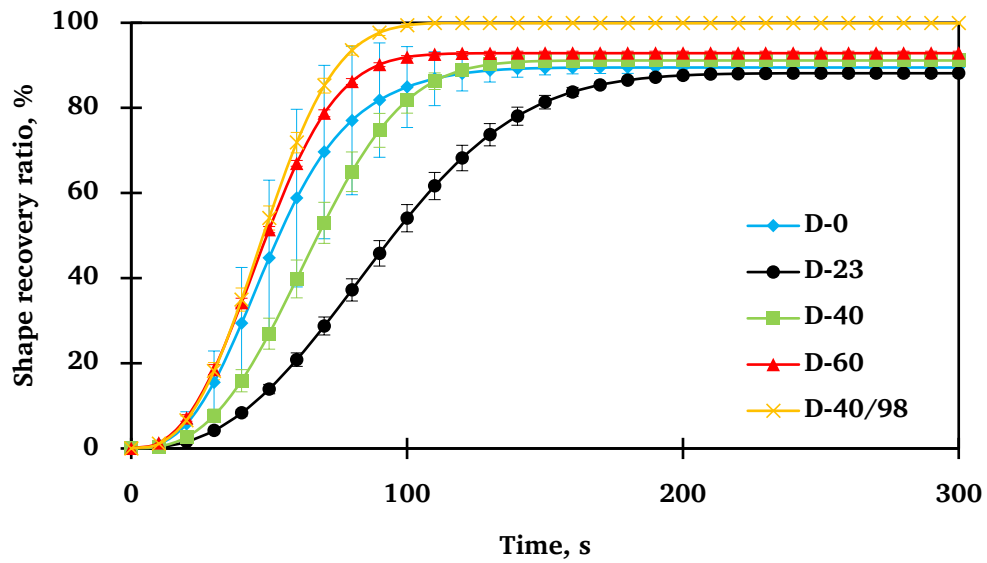
Figure 4.28: Ortho$^+$ recovery cycles

The calculated R_f and $R_{f,30}$ are summarised in Table 4-16 and the average R_r versus time (days) is shown in Figure 4.29. According to Figure 4.29, D-0 and D-60 self-recovered around 40% and 35% from their initial programmed shape within 30 days. The self-recovery behaviour of 90° and 180° programmed D-60 Ortho$^+$ differed; hence, the standard deviation was significant compared to other specimens. On the other hand, D-23 R_r variation is not significant; thus, it is concluded that storing conditions influence Ortho$^+$ shape memory properties.

Table 4-15: Ortho[+] tensile and flexural properties at elevated temperatures

Temperature, ºC	Tensile properties		Flexural properties	
	Strength, (MPa)	Modulus, (GPa)	Strength, (MPa)	Modulus, (GPa)
23	74.40 ± 3.90	4.44 ± 0.11	129.70 ± 0.25	3.46 ± 0.05
30	42.66 ± 0.60	2.89 ± 0.13	70.05 ± 3.41	1.97 ± 0.06
35	28.52 ± 0.95	1.51 ± 0.21	51.67 ± 6.54	1.34 ± 0.15
40	26.47 ± 0.59	0.93 ± 0.12	n/a	0.90 ± 0.21
45	23.46 ± 1.53	0.45 ± 0.07	n/a	n/a

Table 4-16: Ortho[+] shape memory properties

Sample name	R_f, (%)				R_r, (%)				$R_{f,30}$ (%)[‡]
	40ºC/90º	40ºC/180º	50ºC/90º	50ºC/180º	40ºC/90º	40ºC/180º	50ºC/90º	50ºC/180º	
D-0	95.31	99.48	97.05	98.94	91.17	85.61	84.47	99.14	66.3 ± 3.1
D-23	96.17	99.89	96.49	98.35	98.93	90.96	51.45	90.72	98.4 ± 1.9
D-40	99.35	99.41	97.73	99.13	49.10	80.00	54.44	87.74	88.7 ± 4.3
D-60	96.80	92.71	96.97	96.06	92.10	96.57	94.63	97.23	56.8 ± 23.4
D-40/98	97.79	96.22	99.92	98.21	94.84	99.70	98.29	99.68	40.6 ± 26.4

Note: 40ºC/90º – programmed to 90º after kept 5 min. at 40ºC

‡ Average of 60º, 90º and 180º programmed at 50ºC
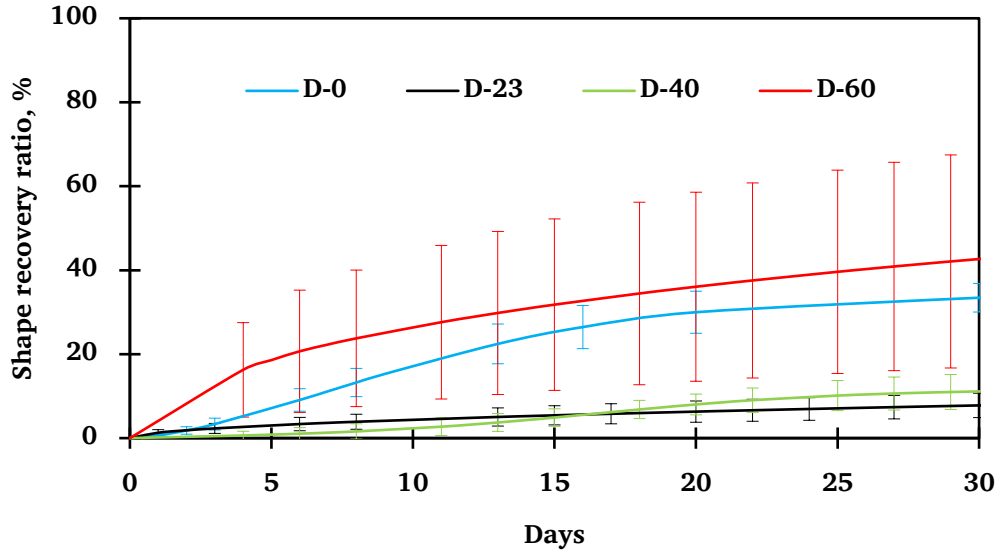
Figure 4.29: Average Ortho$^+$ shape recovery ratios for 60°, 90° and 180° programmed shapes at 50°C

According to Figure 4.26-Figure 4.29, the environmental factors affected Ortho$^+$ performance. For example. Th the strength of SMP/SMPCs is reduced when subjected to high temperatures. This is because thermal exposure can cause molecular degradation, leading to the loss material's mechanical properties. Additionally, SMPs can undergo a change in their morphology and crystallinity at high temperatures, which can also impact their strength [338].

When SMPs are stored at elevated temperatures for extended periods, they can experience shape recovery and strain behaviour changes. This is because the thermal history of the material can affect its microstructure and lead to changes in the crystallinity and morphology of the material [141]. As a result, the recovery behaviour and strain response of the SMP can be

affected. For example, studies have shown that storing SMPs at elevated temperatures for prolonged periods can decrease the material's recovery stress and strain [75]. This is due to changes in the material's morphology, such as reducing the number and size of the shape-memory domains.

Furthermore, the strain response of the material can also be affected, as storage at elevated temperatures can cause changes in the polymer's molecular weight distribution, leading to changes in the material's viscoelastic behaviour. After carefully considering Ortho$^+$ thermo mechanical and shape memory properties at 0°C, 23°C, 40°C, 60°C and 40°C with 98% relative humidity, the author recommends storing Ortho$^+$ between 23°C to 30°C ($<$40°C). Thus, users can avoid functional reduction of the material. On the other hand, to avoid unexpected recovery, the author introduced stretchy elastic bandages, which help users continue normal daily activities concerning medical advice.

4.9   Summary

In this chapter, the author reinforced SMP with fibres and NPs to provide the required structural integrity and functional properties to fabricate SMP material for orthopaedic treatments. An extensive experimental program was conducted under a Taguchi L_{18} ($2 \times 3 \times 3$) mixed full factorial orthogonal array with fibre type, number of layers and thickness control variables. Before finding an optimum set of fabrication parameters, among the multiple

responses, the critical once chosen. According to the grey relational ANOVA analysis, the effect of thickness on FRSMPC performances was insignificant (P > 0.05). In parallel, the author fabricated NRSMPC incorporating TiO_2, MWCNT and graphene, adding 0.4, 0.7 and 1.0 *wt*% with respect to L_9 Taguchi array. The thermomechanical and shape memory properties were analysed, and optimum fabrication parameters were found using grey relational analysis combined Taguchi method. After that, considering both FRSMPC and NRSMPC optimum control variables, the author synthesised hybrid shape memory polymer, which can be used to immobilise fractured bones in orthopaedic treatments and named the novel material "Ortho$^+$". In the final configuration, the Ortho$^+$ thickness was 2 mm and contained DGEBA: NGDE: D-230: TiO_2 *wt*% of 2.555:1.000:0.504:0.400 with 200 g/m^2 single woven E-glass fibre layer. Thus, Taguchi technique successfully found the optimum Ortho$^+$ fabrication parameters in a limited number of experiments, minimum time and cost. The same procedure could be applied to optimise fabrication parameters in any fibre-reinforced composites.

To verify the long-term Ortho$^+$ performance and durability, Ortho$^+$ is kept in four selected extreme environments and properties are compared at room temperature. The results revealed that the environment influenced Ortho$^+$ properties positively and negatively. Therefore, to maintain characterised features in line with the standards, the conditions to which it is exposed are crucial. In view of this, Chapter 5 will focus on ABAQUS

viscoelastic modelling, validation, and the *vitro* demonstration of lower limb

orthopaedic bone fracture fixator.

CHAPTER 5: ORTHO$^+$ FEA MODELLING

VALIDATION AND DEMONSTRATION

5.1   Introduction

In this chapter, the author developed ABAQUS finite element model for synthesised viscoelastic material and validated it through distributed sensor network. The resulting FEA model can forecast Ortho$^+$ SME, stress concentration zones when it forms into complex shapes. The geometrical features and their dimensions of Ortho$^+$ can be further optimised using the proposed FEA model. Additionally, the same methodology can be used to model any viscoelastic material in ABAQUS without fabricating physical prototypes.

Biomedical materials need unconditional assurance of providing accurate performance throughout the intended period. Thus, a lower limb leg cylindrical cast was successfully demonstrated on a human mannequin to prove the Ortho$^+$ usability in orthopaedics. The undercast temperature profile and pressure were continuously monitored and the results are comparable with POP and fibreglass casting methods. Therefore, the synthesised Ortho$^+$ showed a favourable solution to addressing existing orthopaedic fractured bone immobilisation challenges.
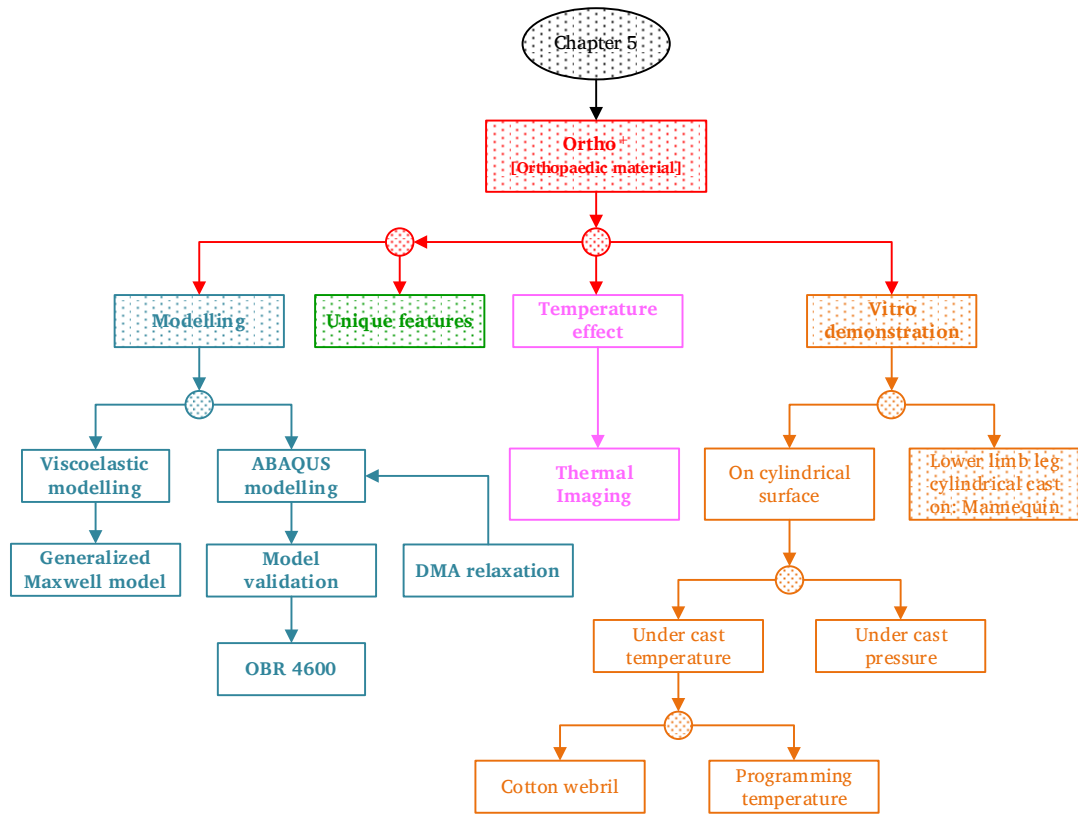
Figure 5.1: Technical overview of Chapter 5

Figure 5.1 briefly illustrates the technical content of this chapter. Additionally, the technical content presented in this chapter is published in J_1 and C_2 and listed in Chapter 1.6. In addition, two web stories have been published in UniSQ and Australia's nursing digital print, "Nursing Review".

5.2 SMP viscoelastic modelling

A number of modelling techniques have been presented recently to describe thermomechanical behaviour, and they can be divided into two categories: based on phase transition and viscoelasticity [231, 339]. In this thesis, the author is interested in SMP viscoelastic modelling techniques.
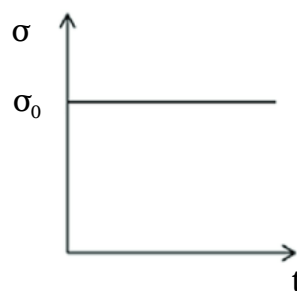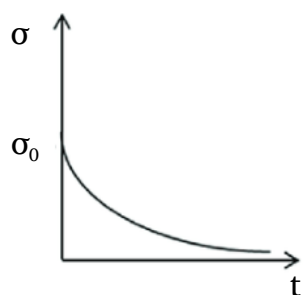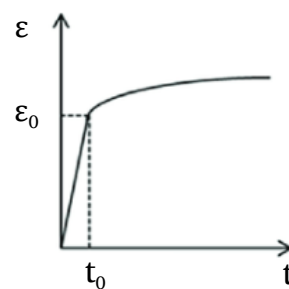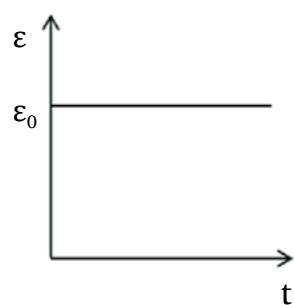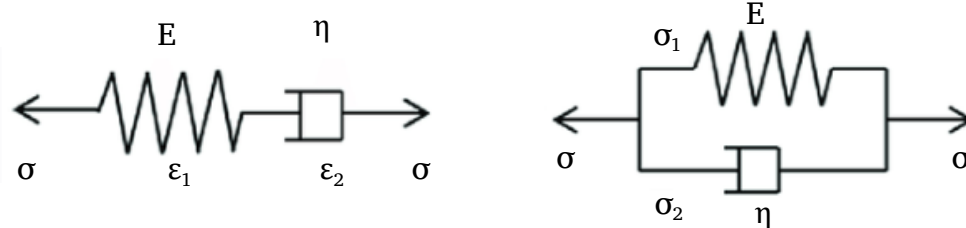
Where,

    E   Elastic modulus

    η Viscosity coefficient

    ε_0 Strain of the elastic element E_0

    σ_0 Stress of the elastic element E_0

Figure 5.2: One-dimensional viscoelastic models (a) Maxwell, (b) Kelvin

[340]

Massless Hookean springs and Newtonian dashpots are the fundamental elements used in various combinations in the SMP viscoelastic models [339].

The basic Maxwell and Kelvin models are shown in Figure 5.2. (a) and (b). If a constant strain (ε) is applied to the Maxwell model, the spring's instantaneous extension creates a stress (σ) [231]. However, the dashpot extends with time, decaying the initial stress developed. Thus, Maxwell model represents stress relaxation behaviour. On the other hand, the dashpot prevents instantaneous deformation when constant stress is applied to the Kelvin model. Interestingly, the Kelvin model exhibits increasing strain over time, similar to creep deformation [341]. Maxwell and Kelvin models are combined in the standard linear model, which can predict the overall behaviour of a viscoelastic material [342, 343]. This model has two forms: Maxwell form and Kelvin form, and the Maxwell form is shown in Figure 5.3. The standard linear model produces only three parameters; thus, it is simpler to understand.[344]. Hydrogels and PCL scaffolds biomaterials viscoelastic behaviour were studied using the standard linear viscoelasticity model [231, 345, 346].

To predict the multitude of physical entanglements and chemically crosslinks SMP viscoelastic behaviour more precisely, the generalized Maxwell model was derived and illustrated in Figure 5.4 [347]. In this model, a spring and an infinite number of Maxwell bodies are connected in parallel

[344]. The generalized Maxwell model assumes that the relaxation process happens over time rather than instantly [64].
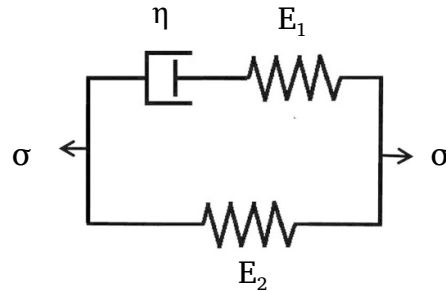
Figure 5.3: Standard linear model of viscoelasticity (Maxwell form) [341]
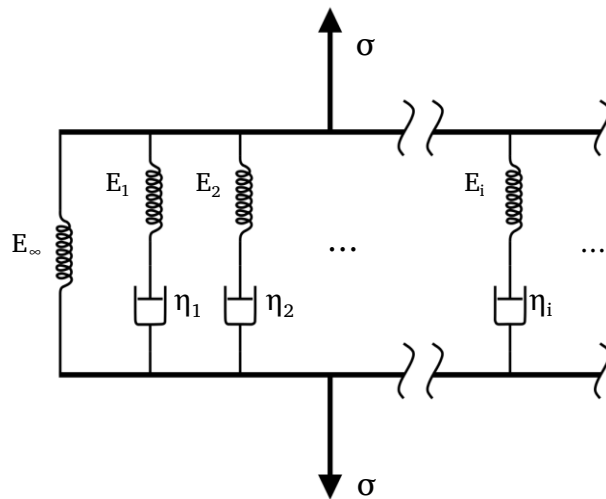
Where,

E_∞ Elastic modulus of the main elastic branch

i i^{th} branch

Figure 5.4: Generalized Maxwell model

Interestingly the generalized Maxwell model covers amorphous or cross-linked polymers [348]. The following equations 5.1, 5.2, 5.3, 5.4 and

5.5 can be obtained, where ε_i and σ_i are the strain and stress of the ith element in generalized Maxwell model.

$$\varepsilon = \varepsilon_0 = \varepsilon_i (i = 1,2,3 \dots n) \tag{5.1}$$

$$\sigma = \sigma_0 + \sum_{i=1}^{n} \sigma_i \tag{5.2}$$

$$\sigma_0 = E_0 \varepsilon_0 \tag{5.3}$$

For the ith Maxwell model, the following relationship was derived, taking $\tau = \eta/E$,

$$\left(\frac{d}{dt} + \frac{1}{\tau_i} \right) \sigma_i(t) = E_i \frac{d\varepsilon_i}{dt} \tag{5.4}$$

$$\sigma_i = \varepsilon E_i e^{\left(\frac{-t}{\tau_i} \right)} \tag{5.5}$$

Then the relaxation modulus E(t) can be given as,

$$E(t) = \frac{\sigma(t)}{\varepsilon} = E_0 + \sum_{i=1}^{n} E_i \, e^{\left(\frac{-t}{\tau_i} \right)} ; (t \geq 0) \tag{5.6}$$

Here, E_0 is the equilibrium modulus of the sample when it has fully relaxed; E_i and τ_i are Prony parameters and relaxation time, respectively. As illustrated in equation 5.6, it was clear that the relaxation modulus significantly varies over time at the glass transition temperature region. This principle depends on material viscoelastic behaviour at reference temperature (θ_0). The equation 5.7 is the relaxation modulus at any temperature (θ) and

time $(\alpha_T t)$ is equivalent to the relaxation modulus at reference temperature (θ_0) and time (t) [349].

$$E(t, \theta_0) = E(\alpha_T t, \theta) \qquad (5.7)$$

Where,

t   Time

θ_0 Reference temperature at relaxation data given

T   Temperature of interest

It is widely accepted for the polymer that has T_g, which is equal to θ_0 and the shift factor $(log_{10} (\alpha_T t))$ follows William-Landel-Ferry (WLF) equation 5.3 [349]. The C_1 and C_2 are constants in equation 5.8 obtained by fitting the WLF equation to the shift factors-temperature curve derived empirically. The DMA relaxation data were subjected to Time-Temperature Superposition (TTS), fitting the resulting master curve with the Prony series.

$$log_{10} (A) = - \frac{C_1(\theta - \theta_0)}{C_2 + (\theta - \theta_0)} \qquad (5.8)$$

Where,

C_1 and C_2 are material dependent calibration constants and calculated after plotting $log_{10} (\alpha_T t)$ versus $(\theta - \theta_0)$

If $\theta \leq \theta_0 - C_2$, $\theta \leq \theta_0$-C_2, deformation changes are assumed to be elastic based on the instantaneous modulus

The proposed method is robust and does not involve subroutines; thus, covers a large range of characteristic times in both experiments. However, the accuracy of predictions may vary with experimental data. Diania et al., Yu et al., and Shrotriya et al., revealed that the viscoelastic models had shown good consistency between prediction and experimental results even in large strain conditions [350-352]. Therefore, this method can be used to model the behaviour of any viscoelastic material.

5.2.1 Generalised Maxwell model parameter evaluation
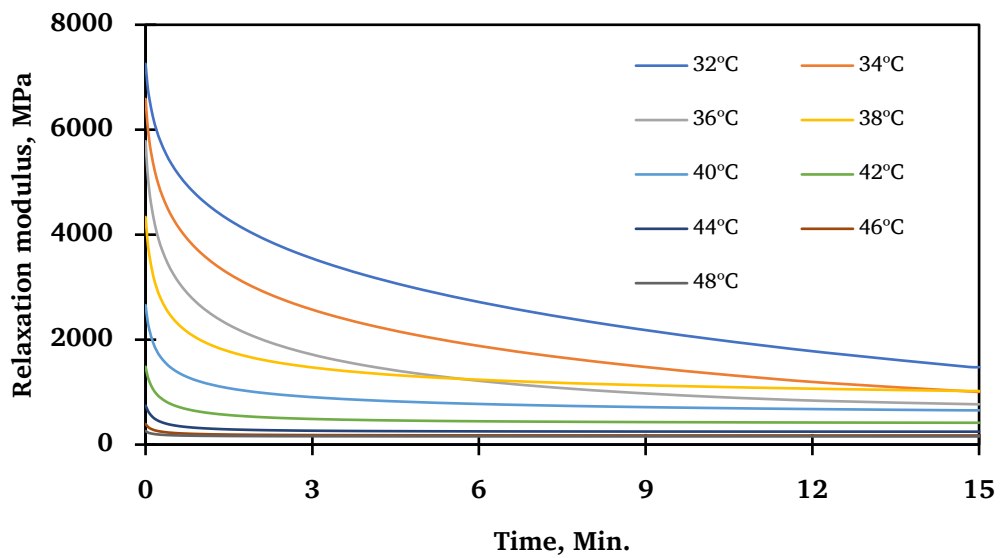
Figure 5.5: Ortho⁺ relaxation data

The synthesised Ortho⁺ was cut into $50 \times 8 \times 2$ mm³ specimens for the DMA relaxation test. TA instrument DMA Q800 stress relaxation mode was used to characterise the viscoelastic parameters. The specimen was mounted

using a dual cantilever clamp, and 0.25% strain was applied over 10 min. of relaxation and 2 min. of recovery. The furnace temperature increased by 2°C and the procedure was repeated until it reached 50°C. The obtained Ortho$^+$ relaxation data is illustrated in Figure 5.5.
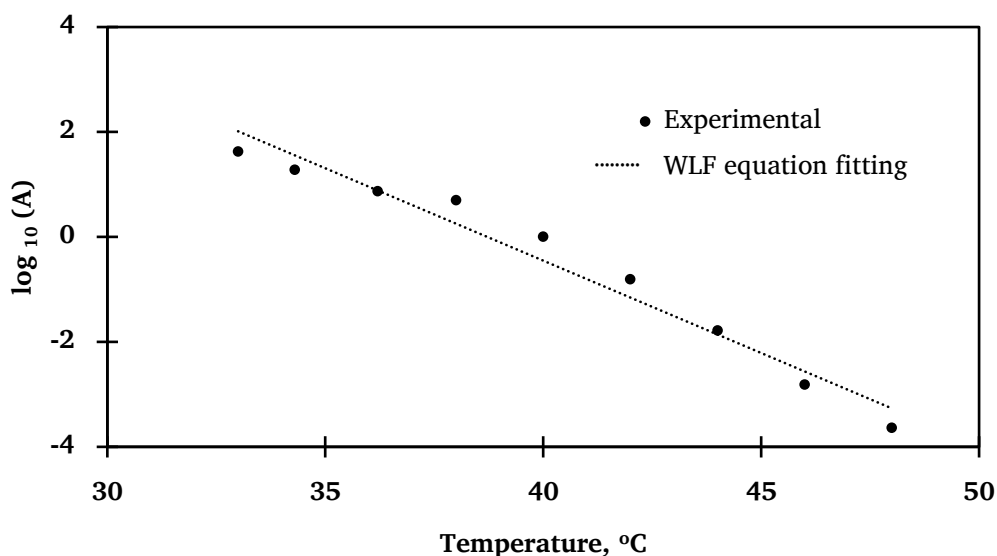
Figure 5.6: Shifting factors at 40°C reference temperature

After that, the relaxation data were exported into Advantage Software (*v*5.5.22) and shifting factors and master curve were generated according to equations 5.7 and 5.8. During the shift factor calculation, 40°C is taken as reference (θ_0) and generated shift factors fitted to the linear equation, as shown in Figure 5.6. The shift factors were revealed as C_1 and C_2, 7.18108 and 2.02108, respectively. It is important to note that shifting factors (log_{10} (A)) are temperature dependent. In addition, shift factors at lower temperatures were shifted to the left while those at higher temperatures were shifted to the

185

right to derive generalised master curve. The Ortho$^+$ master curve generated by the TTS technique is shown in Figure 5.7. Finally, equation 5.6 Prony series parameters were calculated by fitting them into Figure 5.7 relaxation master curves.
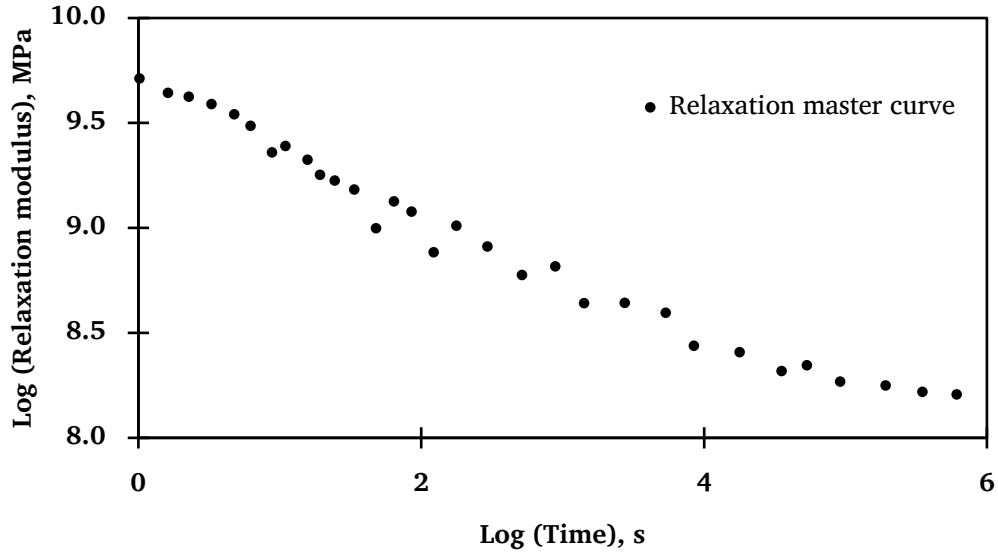
Figure 5.7: Ortho$^+$ Prony series master curve

5.2.2 ABAQUS finite element procedure for Ortho$^+$

A $250 \times 240 \times 2$ mm^3 sheet was created in finite element analysis ABAQUS CAE 2020 commercial software. The model contained C3D8R solid 8-node quadrilateral brick elements. The density and expansion coefficients were 1151.15 kg/m^3 and 3.5×10^{-4} ^{o}C^{-1}, respectively [80]. The Nlgeom option in ABAQUS was turned on at this step to enable geometric nonlinearity effects. A brief FEA model definition, steps and parameters are illustrated in Table 5-1. The FEA model was subjected to four steps similar to a thermomechanical

186

cycle, (i) heating above $\dot{T}_g$, (ii) wrapping around a cylindrical surface, (iii) allowing cool to room temperature while keeping constrained forces, and (iv) reheating above $\dot{T}_g$. A mesh sensitivity analysis was carried out to ensure the results' convergence and for each step, 600 s is considered. Figure 5.8 shows the extracted FEA strain contour at 650 s, 750 s, 1200 s, 1350 s, and 1500 s at 40°C programming temperature. In addition, Figure 5.12 provides a comprehensive average FEA strain result at 40°C, 50°C, 60°C and 70°C.

Table 5-1: Ortho$^+$ FEA modelling parameters

	Boundary condition	Predefined field	Deformation constraint
Initial	-	Created Set room temperature	-
Step #1	Created z-direction pinned	Modified Set element temperature $> \dot{T}_g$ *(i.e., 40ºC, 50ºC, 60ºC and 70ºC)*	Created Restrict all movements
Step #2	Propagated	Modified Set temperature $< \dot{T}_g$ *(i.e., 23ºC)*	Modified Deformation/ Displacement changed: moving rods 65 mm upward (+y) direction
Step #3	Propagated	Propagated Kept at 23ºC	Propagated
Step #4	Propagated	Modified Set element temperature $> \dot{T}_g$ *(i.e., 40ºC, 50ºC, 60ºC and 70ºC)*	Inactive Surface-to-surface body interactions inactivated
Step #5	Propagated	Modified Set temperature $< \dot{T}_g$ *(i.e., 23ºC)*	Propagated
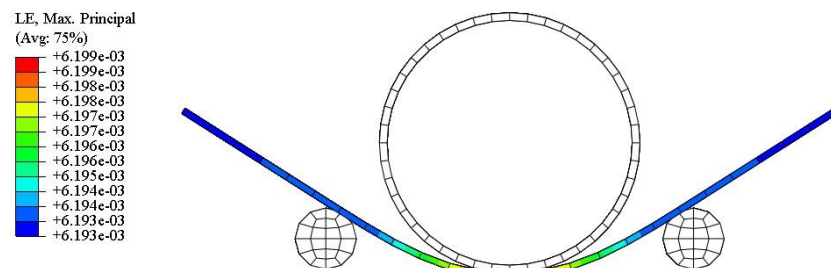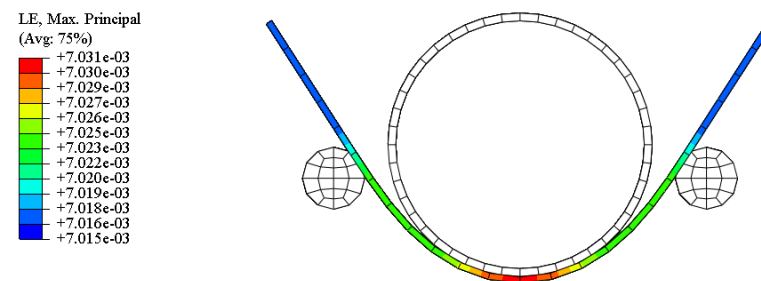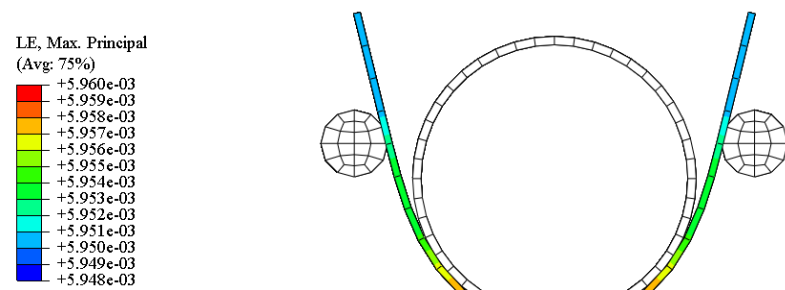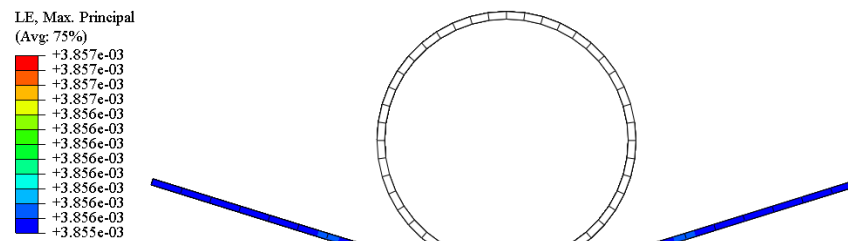
Figure 5.8: Strain nephogram at 40ºC (a) 650 s, (b) 750 s, (c) 1200 s, (d) 1350 s
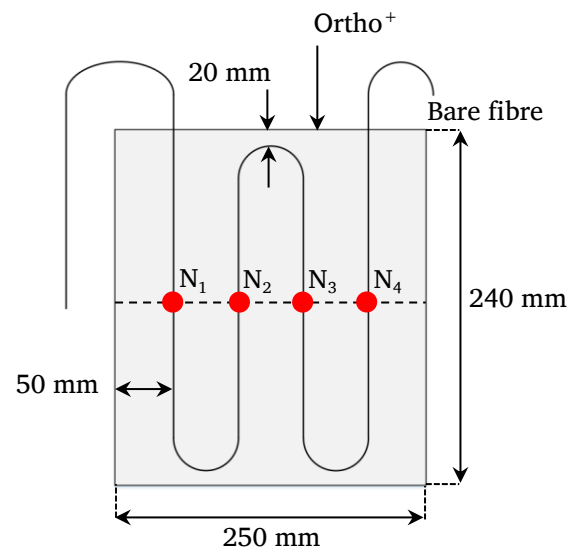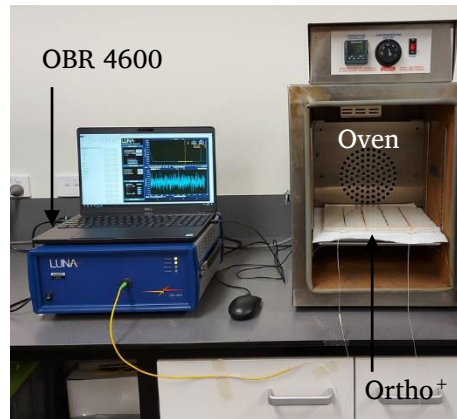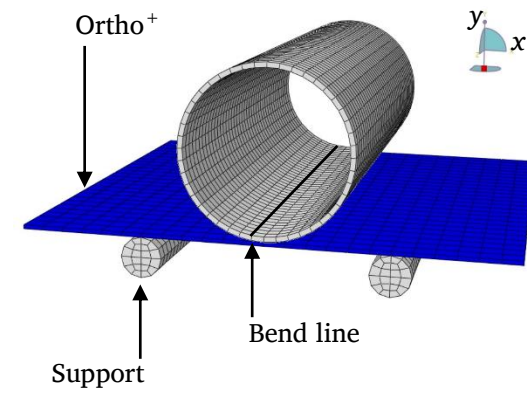
Figure 5.9: FEA validation (a) Ortho$^+$ with embedded optical fibre, (b) Experimental setup, (c) FEA boundary conditions

5.2.3 ABAQUS finite element model validation

The majority of FEA viscoelastic models were derived based on experimental results; thus, researchers are hardly interested in validating them. Therefore, in this research author propose a novel experimental strain model to validate the proposed FEA Ortho$^+$ model.

A 1:1 physical model, $250 \times 240 \times 2$ mm^3 was fabricated with embedded single-mode 125 μm bare optical fibre, as shown in Figure 5.9 (a) and (b). The sensing length was configured to 10 mm equal distances and recorded at four readings per minute under OBR 4600 dynamic mode, as shown in Figure 5.10. The strain reading was taken in four steps similar to SMP thermomechanical cycle, (i) heating, (ii) wrapping around a cylindrical surface, (iii) allowing cool to room temperature while keeping constrained forces, and (iv) recovery. As shown in Figure 5.9 (a) and (c), N_1, N_2, N_3, and N_4 were positioned along the cylindrical axis and Ortho$^+$ wrapped around it. The average strain reading of N_1, N_2, N_3, and N_4 were chosen for the data comparison with FEA analysis. The experiment was repeated for 40ºC, 50ºC, 60ºC and 70ºC temperatures.
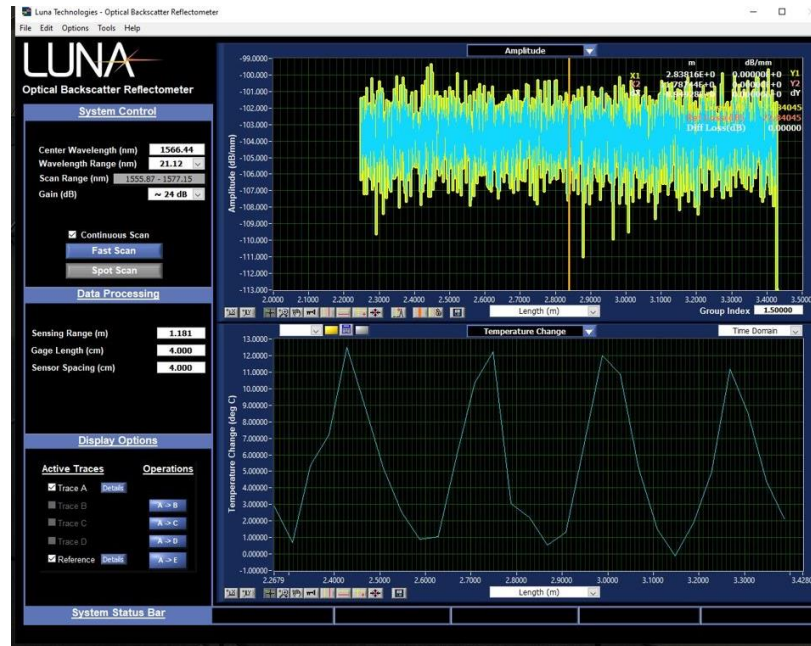
Figure 5.10: OBR 4600 software interface
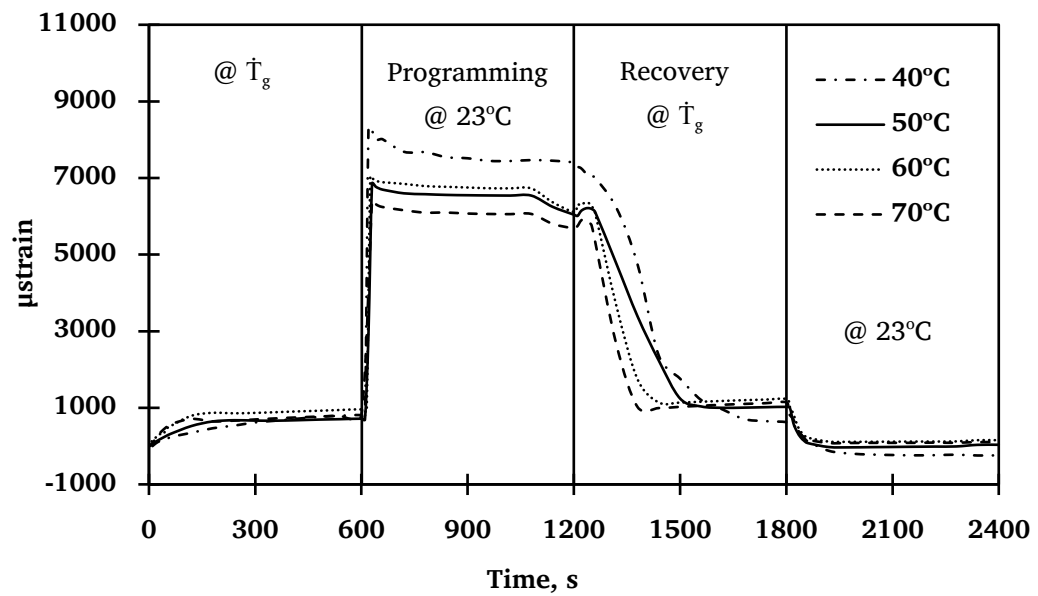
Figure 5.11: N_1, N_2, N_3 and N_4 average strain at 40ºC, 50ºC, 60ºC and 70ºC
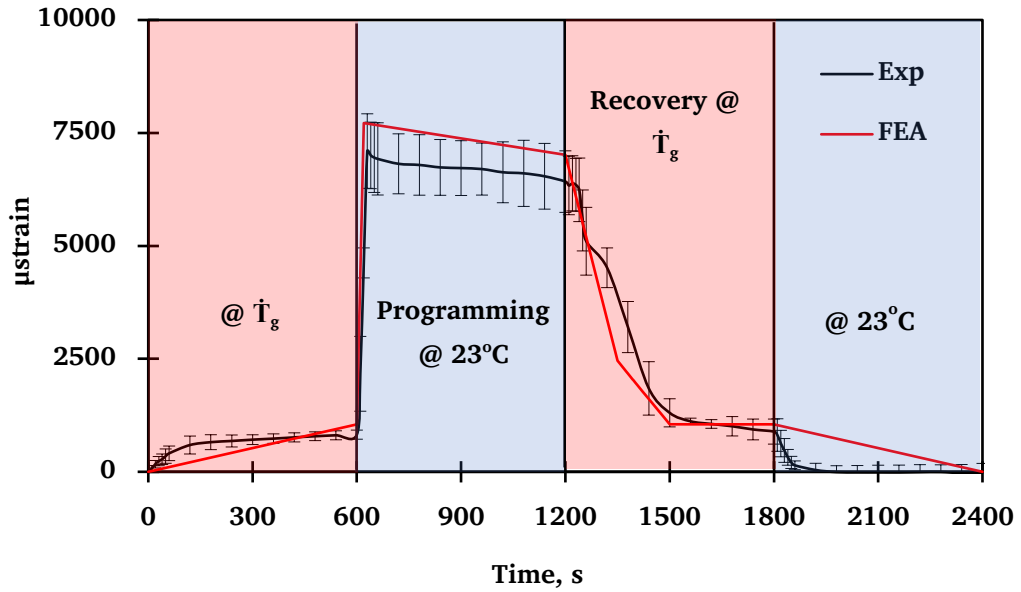
Figure 5.12: Average node element strain: experimental and FEA

The experimentally measured average strain values are illustrated in Figure 5.11. According to Figure 5.11, the strain readings did not show a discernible difference at 40°C, 50°C, 60°C and 70°C since material is in rubbery stage. Thus, obtained strain values are averaged compared with Chapter 5.2.2 FEA analysis. According to Figure 5.12, it is clear that the output of the FEA strain and experimental strain closely match each other. Thus, the proposed FEA model is robust and strongly recommended for predict viscoelastic behaviour when Ortho$^+$ is free formed into complex shapes. Therefore, the author of this thesis confidently concludes the proposed FEA model can forecast Ortho$^+$ accurately. Moreover, the FEA model can be used to optimise the Ortho$^+$ plaster geometrical parameters and dimensions.
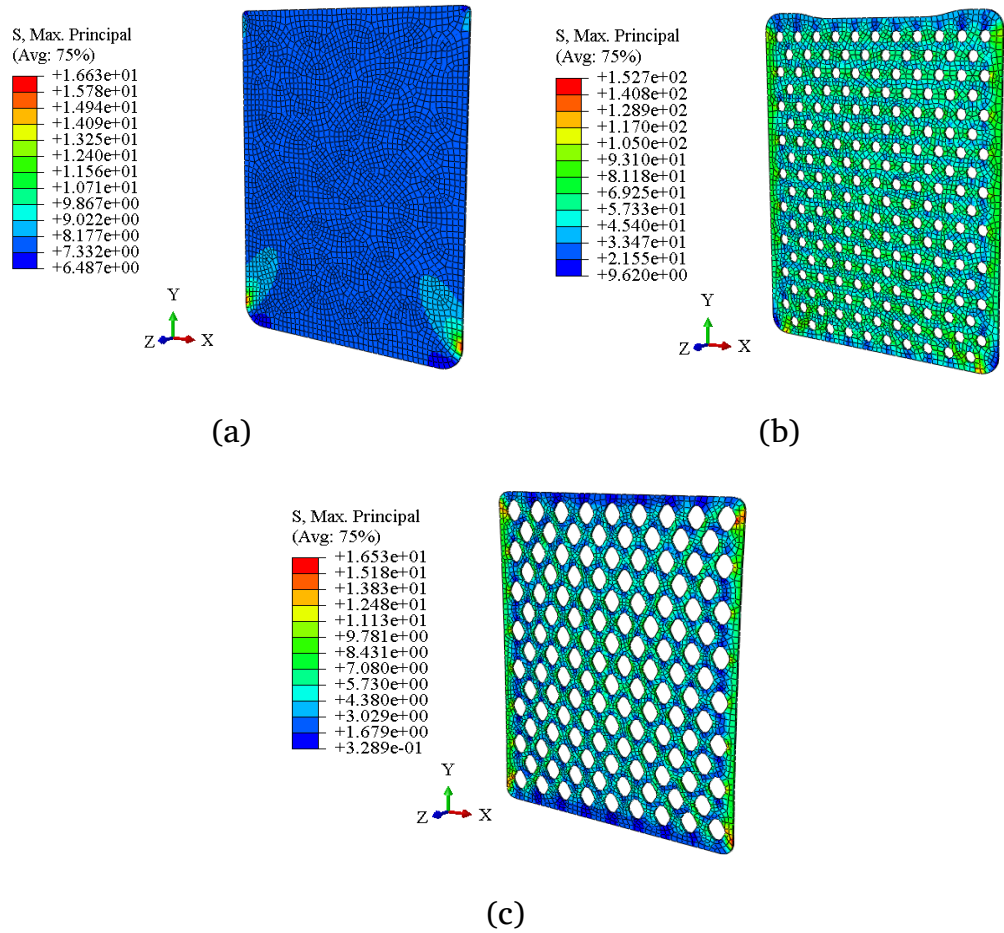
Figure 5.13: Ortho$^+$ FEA axial stress plot at room temperature

At room temperature, Ortho$^+$ was given a 5 mm displacement, and the results are shown in Figure 5.13 (a), (b), and (c). According to the FEA model the selected three Ortho$^+$ geometrical configurations were considered within the safe range, with a safety factor of over three. The maximum safety factor was seen in circular patterned Ortho$^+$ due to the low interruption of stress flow; however, the difference between circular and diamond patterns were insignificant. Therefore, the proposed methodology and validated FEA model

194

will benefit in predicting viscoelastic biomaterials behaviour under different temperatures and loading.

The model is basically used to predict the Ortho$^+$ shape fixity ratio, shape recovery ratio and shape recovery time. The author main intention is to use validate FEA model to use predict shape fixity and recovery during free from shapes. Moreover, the same FEA model is intended to use optimise cut-outs which improve undercast air circulation without scarifying strength of the Ortho$^+$. Therefore, the author mainly interested to provide required necessary parameters run Abaqus viscoelastic models without fatal error.

On the other hand, Ortho$^+$ T$_g$ is already tailored (<45ºC) to use in orthopaedic bone immobilisation. At this temperature, human skin can be retained without first degree of burn around 45 mins. according to the Hutchinson model. Moreover, during the Otho$^+$ application there will be no chemical reaction thus, no whatsoever risk with hotspots unlike POP or fibreglass casting techniques. Therefore, introducing heat flow parameters cannot make any significant contribution to the research outcome.

5.3   Ortho$^+$ time required for heating and cooling

Ortho$^+$ is thermally activated SMP; thus, the uniform through-thickness temperature distribution is important before programming. This helps to minimise the stress induced due to the programming and also it prevents delamination, wrinkles, and cracks. For the experimentation, 2 mm thick Ortho$^+$ was chosen with three different patterns (S$_0$, S$_1$ and S$_2$), as shown in

195

Figure 5.14. S_0 denotes plain (without pattern) Ortho$^+$ in this experimentation.

S_1 S_2

d = 10 mm   q = 20 mm

Minimum centre distance 18 mm   r = 15 mm
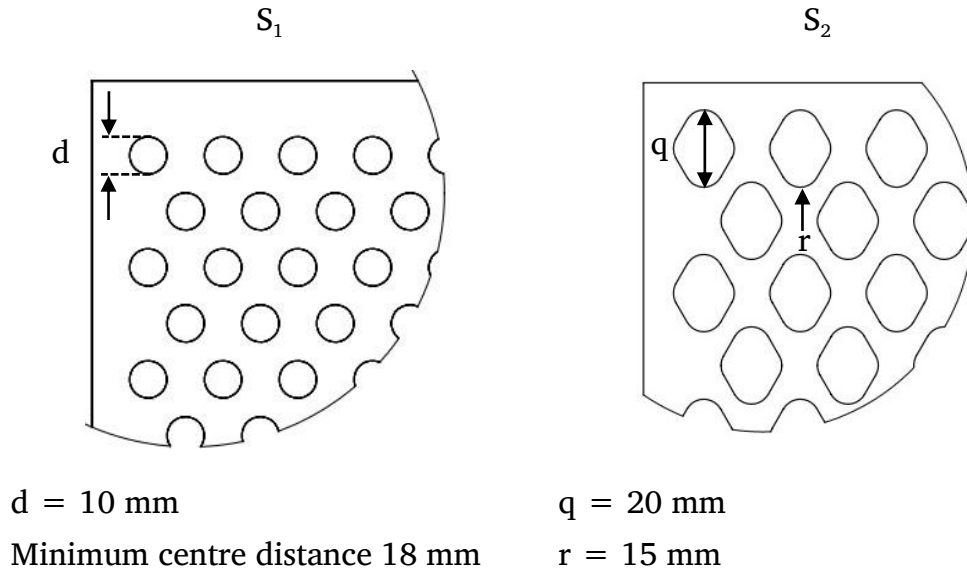
Figure 5.14: Ortho$^+$ experimented patterns (S_1 and S_2)

During the experimental program, the NovaTech heat plate was set to 40±0.5°C and allowed to be in a steady state. The Ortho$^+$ was then kept on the NovaTech heat plate, and respective temperature variations were captured by a FLIR A65 thermal imaging camera for around 10 min.. Then moved, the specimen away from the NovaTech heat plate and FLIR images were taken until Ortho$^+$ reached room temperature. The same procedure was repeated for 50°C and S_0 and S_1, two different configurations. The experimental setup is shown in Figure 5.15 and the temperature profiles were analysed using the ResearchIR software package.
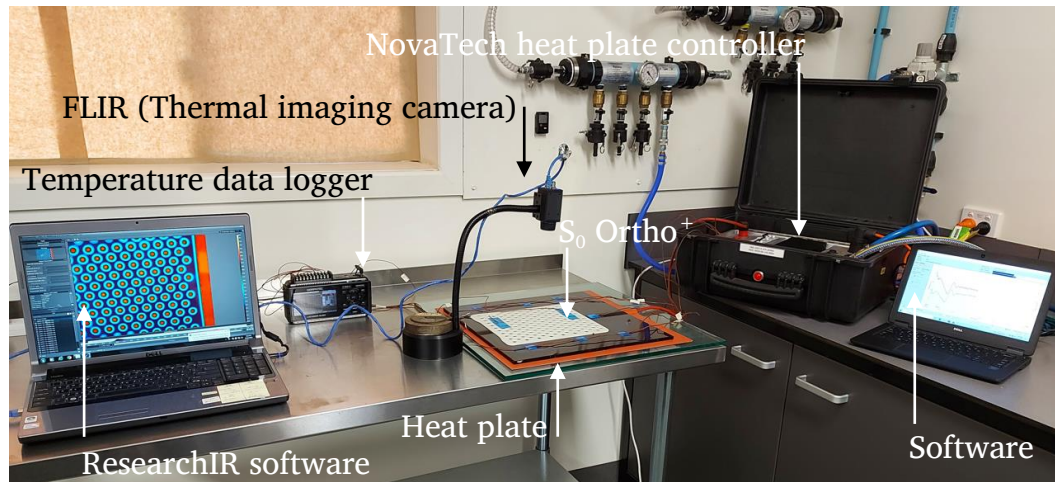
Figure 5.15: Thermal imaging experimental setup

Figure 5.16, Figure 5.17, Figure 5.18, Figure 5.19, Figure 5.20 and Figure 5.21 illustrate the FLIR temperature profiles of S_1 and S_2 configurations for heating and natural cooling. According to the FLIR data, the Ortho$^+$ reached the set temperatures in less than 3 min. and, during natural cooling, the temperature dropped less than 25°C in just 3 min.. Therefore, it is revealed that 2 mm thick Ortho$^+$ should heat for 3 min before programming and applying constraint forces for another 3 mins. while it is cooling.
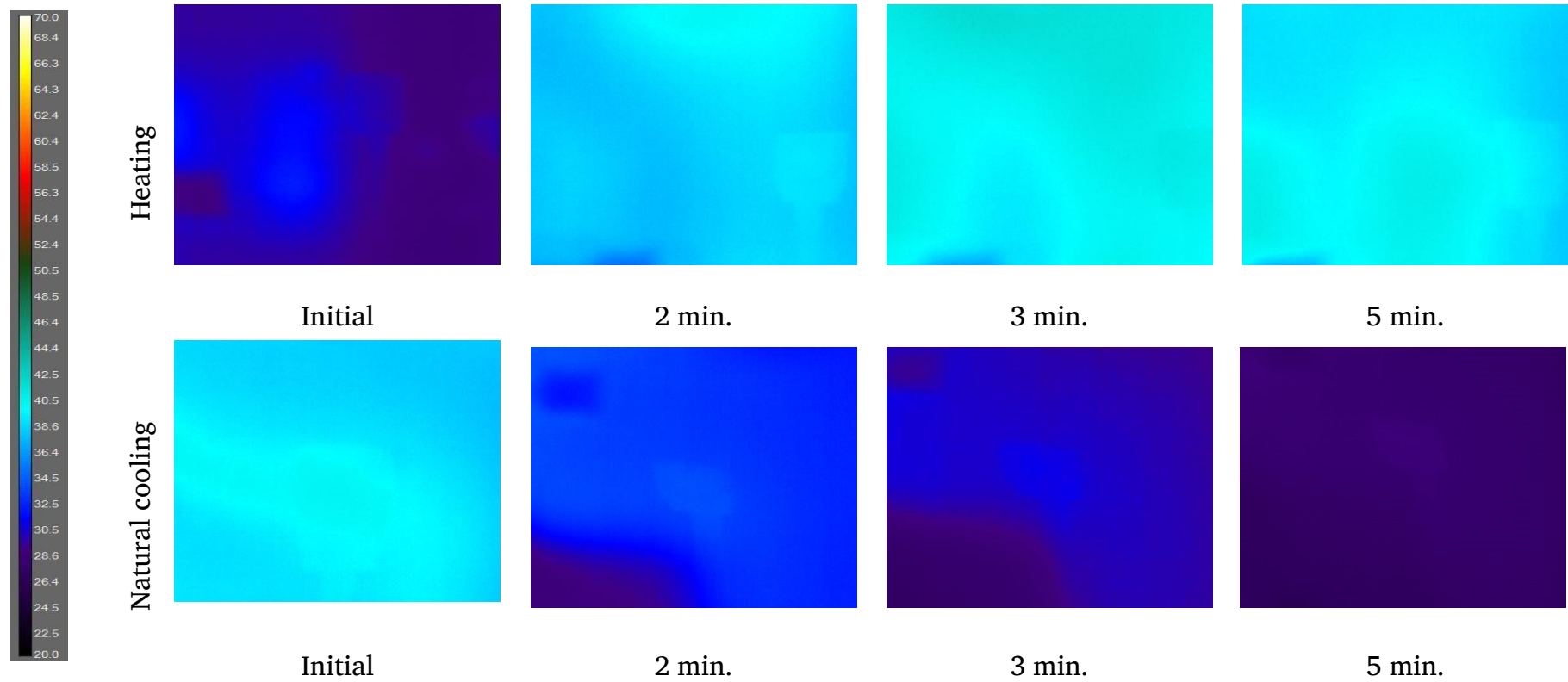
Figure 5.16: S_0 temperature profile at 40ºC
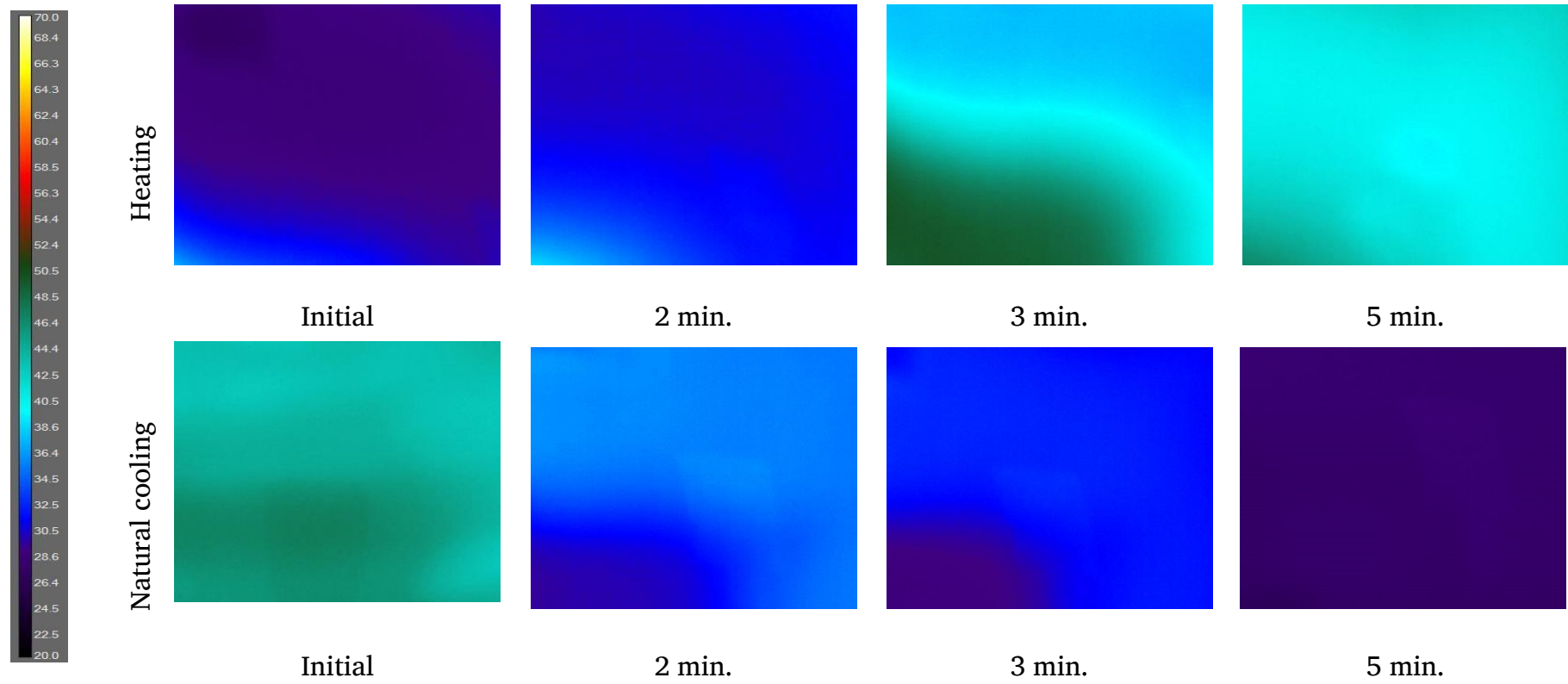
Figure 5.17: S_0 temperature profile at 50°C

199
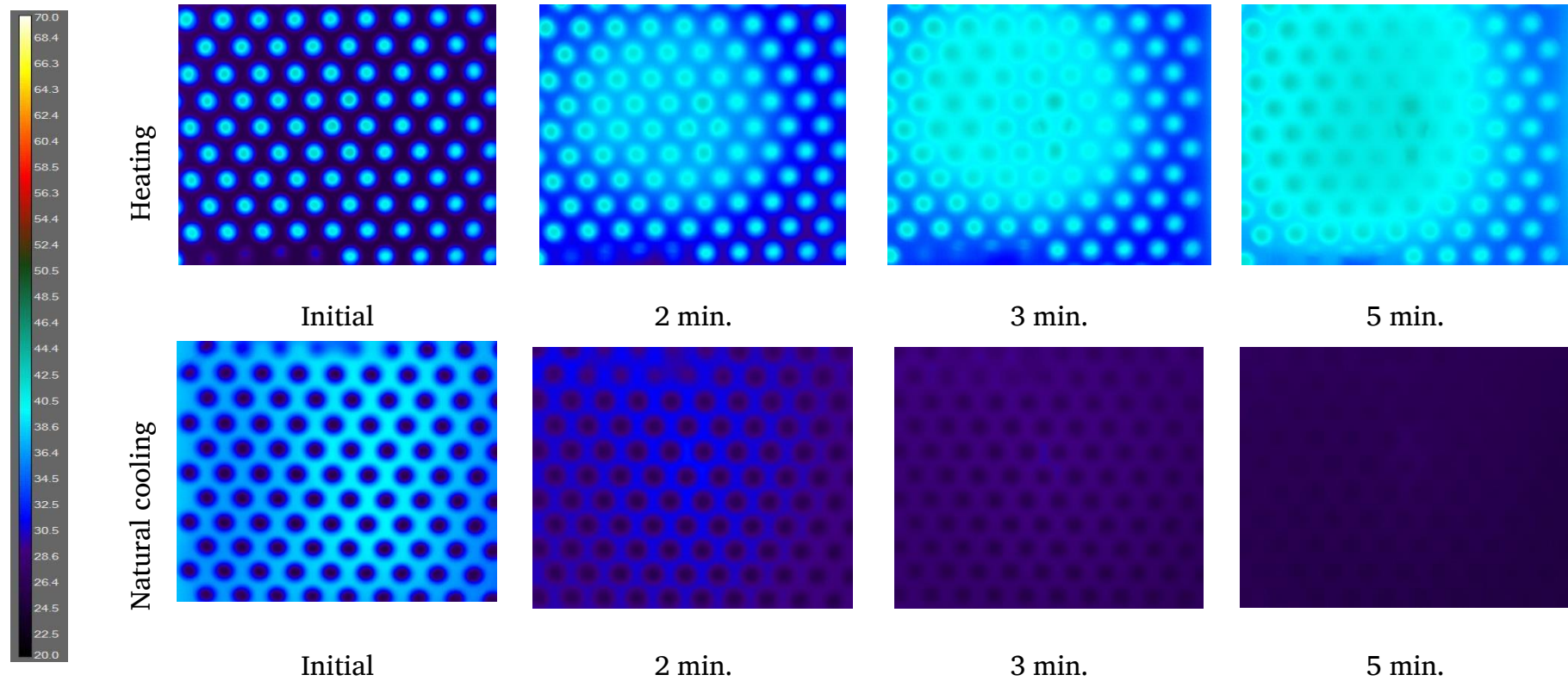
Figure 5.18: S$_1$ temperature profile at 40°C
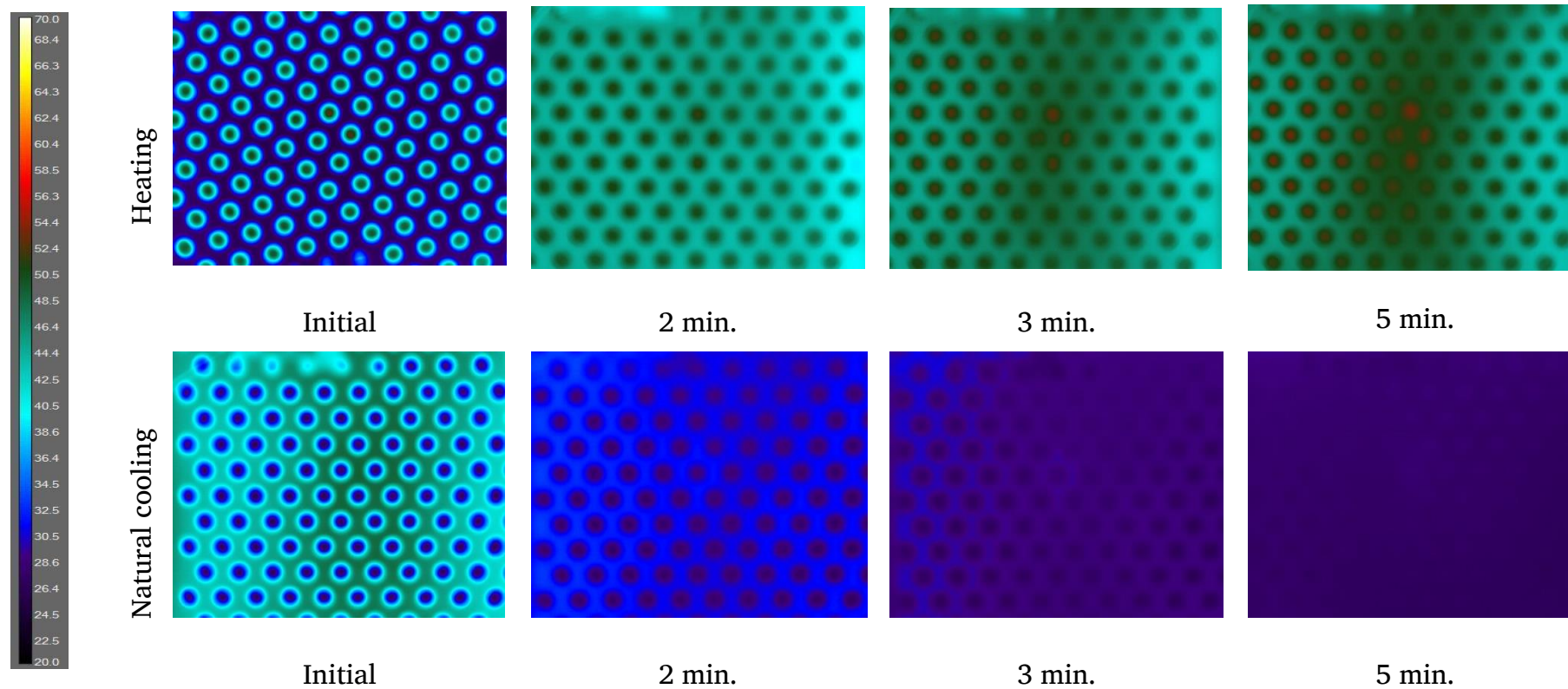
Figure 5.19: S_1 temperature profile at 50ºC
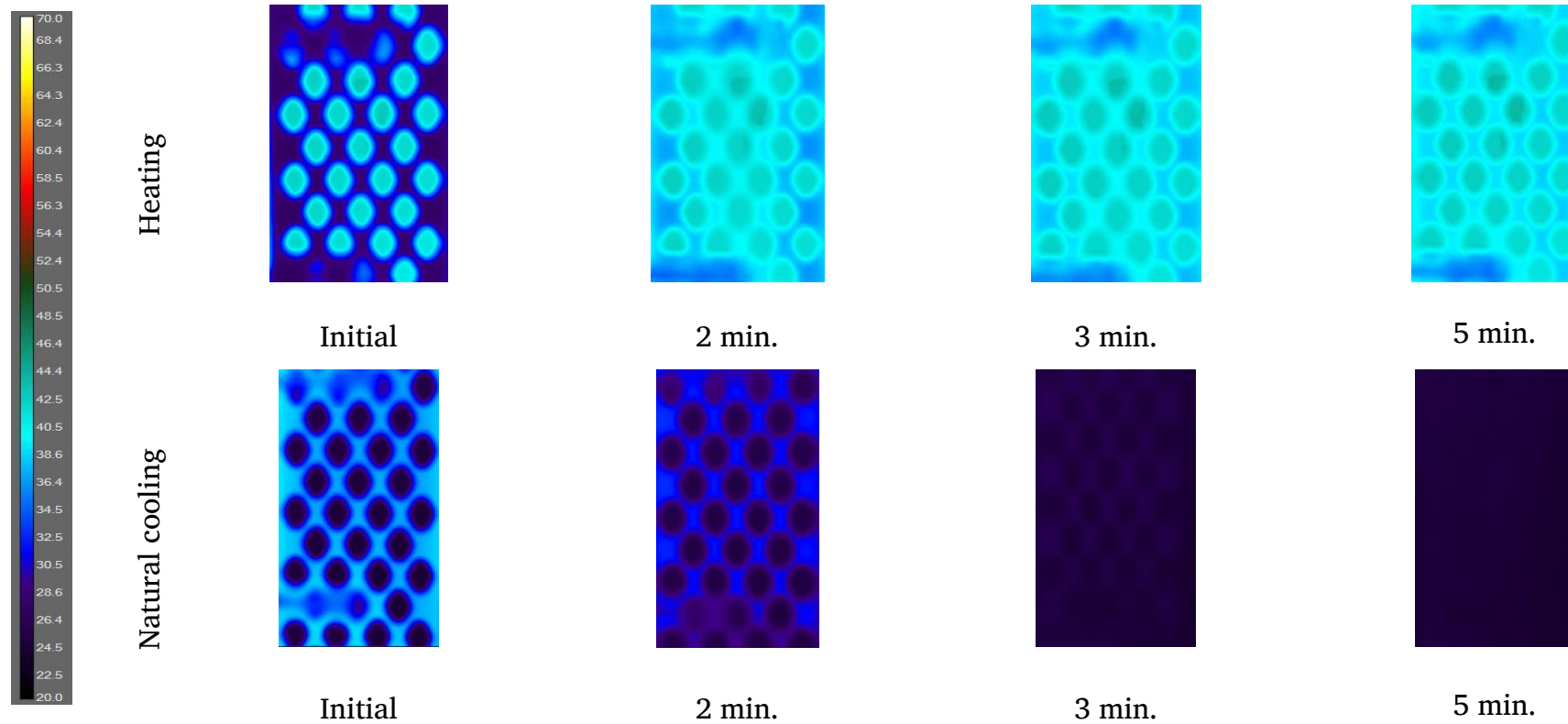
Figure 5.20: S_2 temperature profile at 40ºC
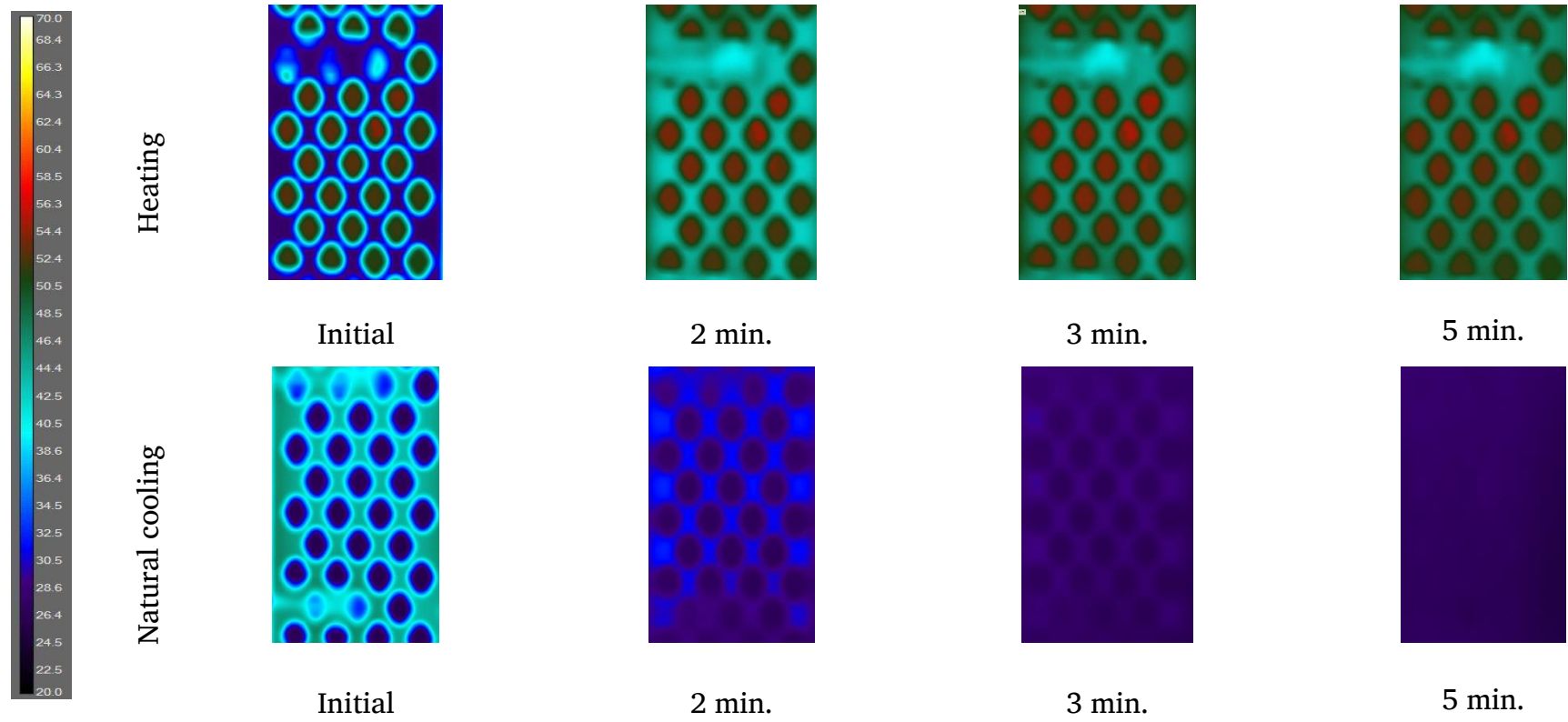
Figure 5.21: S_2 temperature profile at 50ºC

5.4   Undercast temperature distribution *vs* pressure

This chapter experimentally evaluates the undercast temperature distribution against different pressure conditions. According to the literature, POP and fibreglass undercast pressures vary between 20 mmHg to 85 mmHg. Therefore, $P_o = 20$ mmHg, $P_1 = 50$ mmHg and $P_2 = 75$ mmHg under cast pressure was applied and the temperature distribution by varying number of cotton webril layers ($L_1 = 1$, $L_2 = 2$ and $L_3 = 3$) and programming temperatures (50°C, 60°C and 70°C). In addition, S_0, S_1 and S_2, three different Ortho$^+$ patterns, were chosen for in-depth experimentation.

Throughout the experiment, the NovaTech heat plate maintained a constant 37 ± 0.5°C, representing the human body temperature. The experimental setup is shown in Figure 5.22 and Figure 5.23. The L_1 (closer to the heat plate) cotton webril temperature was measured for three pressure conditions (P_0, P_1 and P_2) and averaged. The results are presented against S_0, S_1, and S_2 in Figure 5.24.
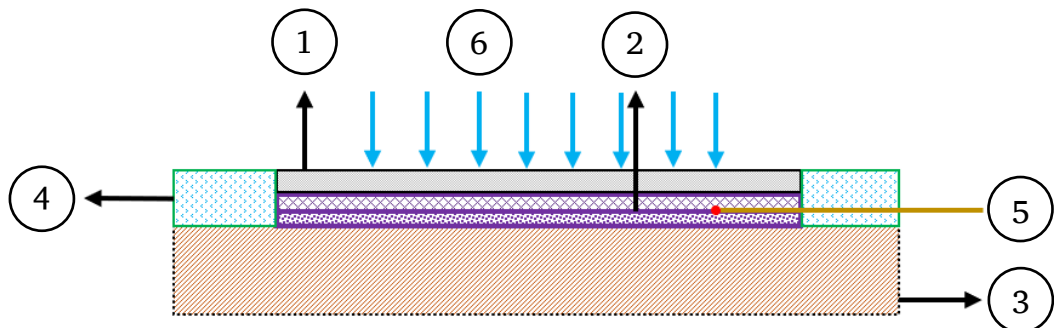
Part No.	Component
1	Ortho$^+$
2	Cotton webril layers
3	Heat plate
4	Insulation
5	Thermocouples
6	Applied pressure

Figure 5.22: Temperature/ pressure effects on Ortho$^+$: schematic view
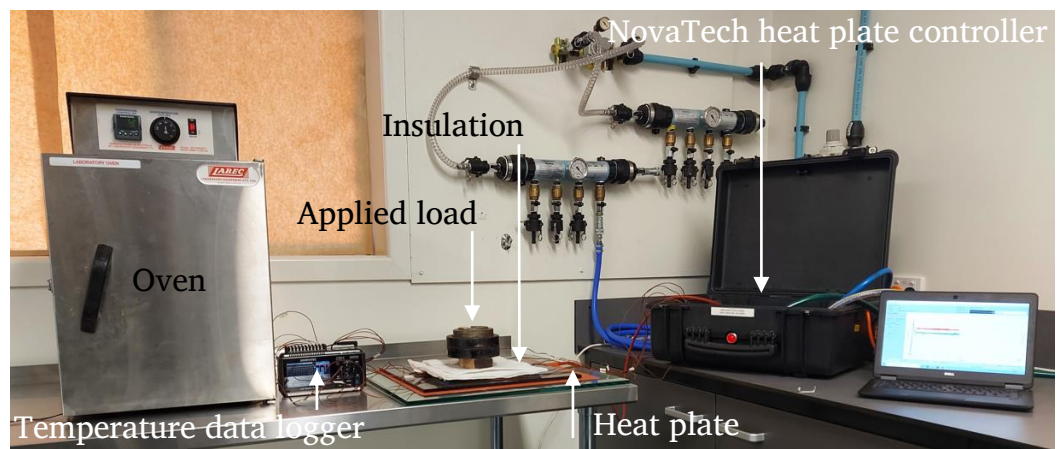
Figure 5.23: Temperature/ pressure effects on Ortho$^+$: experimental setup
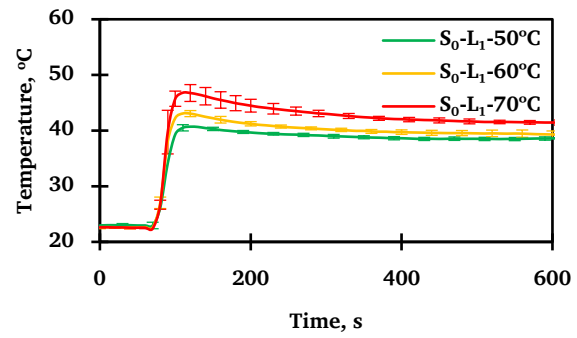
(a)
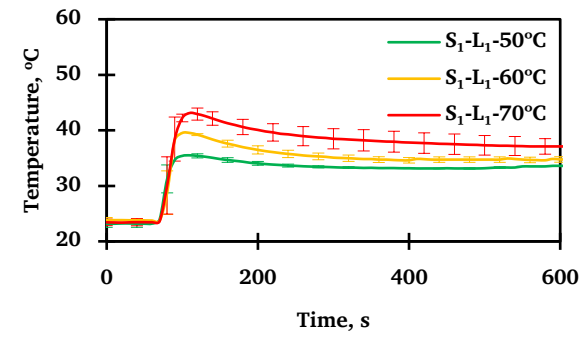
(b)
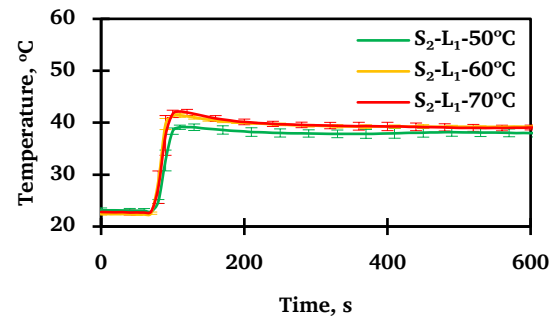
I

Figure 5.24: Averaged cotton webril temperature for P_0, P_1 and P_2

On the other hand, S_2 has lower mechanical strength than S_0 and S_1 due to the significant amount of material removal. During the first-hand experience, it was discovered that at 70°C, would be difficult for an orthopaedic technician to handle and hold Ortho$^+$. S_0 and S_1, on the other hand, exhibited low L_1 temperatures for 50°C and 60°C Ortho$^+$ programming temperatures (Figure 5.24.(a) and (b)). According to Figure 5.24, for 70°C, 60°C and 50°C temperatures, even the closest cotton webril to human skin was within the safe limit.

5.5   Ortho$^+$ smart plaster (Adaptive fracture fixator)

The author introduces Ortho$^+$ smart plaster (Ortho$^+$ SP) to treat orthopaedic bone immobilisation in this section. The fracture fixator's initial *vitro* demonstration was carried out on a 13 cm-diameter cylindrical surface. This is mainly to match a 12-year-old child's lower limb anatomy. However, human limbs have complex shapes, but a uniform diameter was chosen to compare temperature and pressure effectively at different locations. As indicated in Figure 5.25 and Figure 5.26, three T-type thermocouples (T#1, T#2, and T#3) and two (effective area 22 mm^2) Kikuhime pressure measuring probes (P#1 and P#2) were placed around the outer surface of the cylindrical surface. After that, 100% unbleached elasticised radial and longitudinal stretchable cotton stockinette was applied and wrinkles were smoothed out. This was followed by a 50% overlap cotton webril unrolled circumferentially. After that, three T-type thermocouples were symmetrically placed on the L_1

(T#4, T#5, T#6) and the L_2 (T#7, T#8, and T#9) and connected to the data logger.
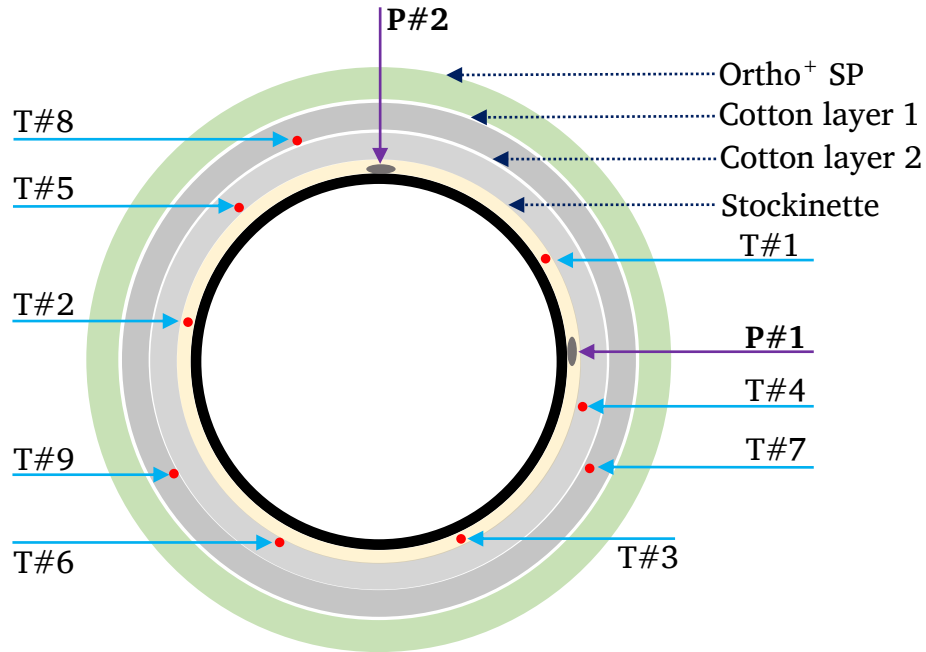
Figure 5.25: Temperature and pressure sensor arrangement: schematic view

The Ortho$^+$ was kept at an elevated temperature ($\geq \dot{T}_g$) and trimmed with scissors based on the circumference and length. Then, Ortho$^+$ was kept again at its reference temperature (i.e. 50°C and 60°C) for 5 min. before wrapping it around the cylindrical surface. The constrain forces were kept until the Ortho$^+$ temperature dropped below 30°C (approximately 3 min.) as per Chapter 5.3.
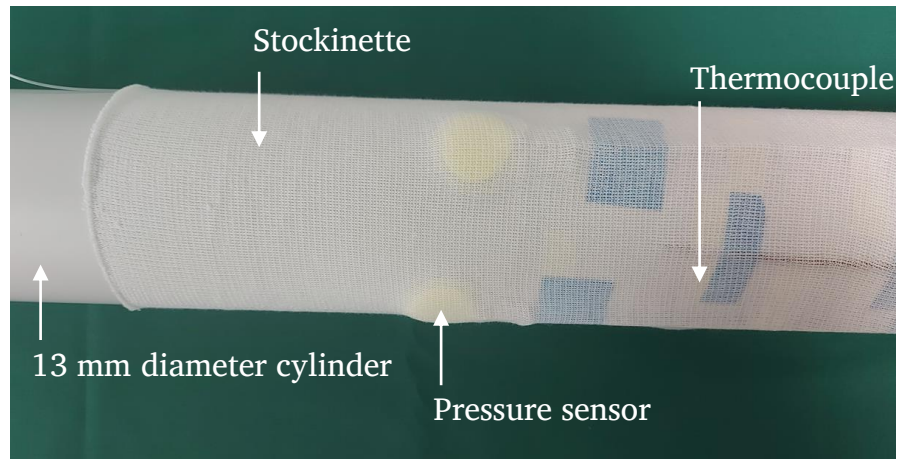
(a)
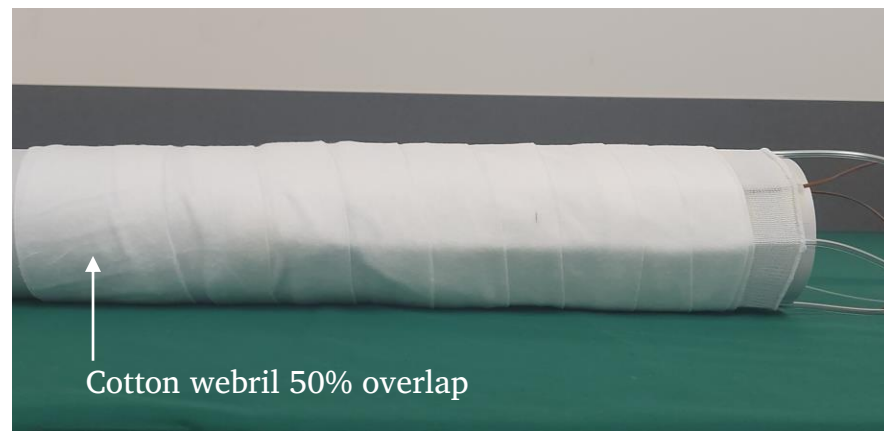
(b)

Figure 5.26: Experimental view of Ortho^{+} smart plaster temperature and

pressure sensor arrangement

Finally, as a secondary locking mechanism, a stretchy elastic bandage (pressure bandage) was applied to the Ortho^{+} SP to overcome self-recovery in extreme environments. Overall, the Ortho^{+} SP *vitro* experiment took approximately 10 min., comparatively less than the POP and fibreglass casting techniques. The Ortho^{+} SP important steps are illustrated in Figure 5.28.

During the Ortho$^+$ SP removal, first, the stretchable elastic bandage is removed. The Ortho$^+$ SP should then be heated with a heat gun (hairdryer), a hot water towel, or a heat blanket to around $\dot{T}_g$. After recovering to a sufficient extent (~25%), remove the Ortho$^+$ SP and keep it at an elevated temperature ($\geq \dot{T}_g$) for several minutes until the Ortho$^+$ SP is fully recovered. The SP protocol discussed above differs from the POP and fibreglass casting methods. The key differences are that POP is placed while in contact with the extremity surface and folds are produced with directional changes. In contrast, fibreglass castings are applied without folding and stretched to the contour [353].

(a)

(b)

(c)

211
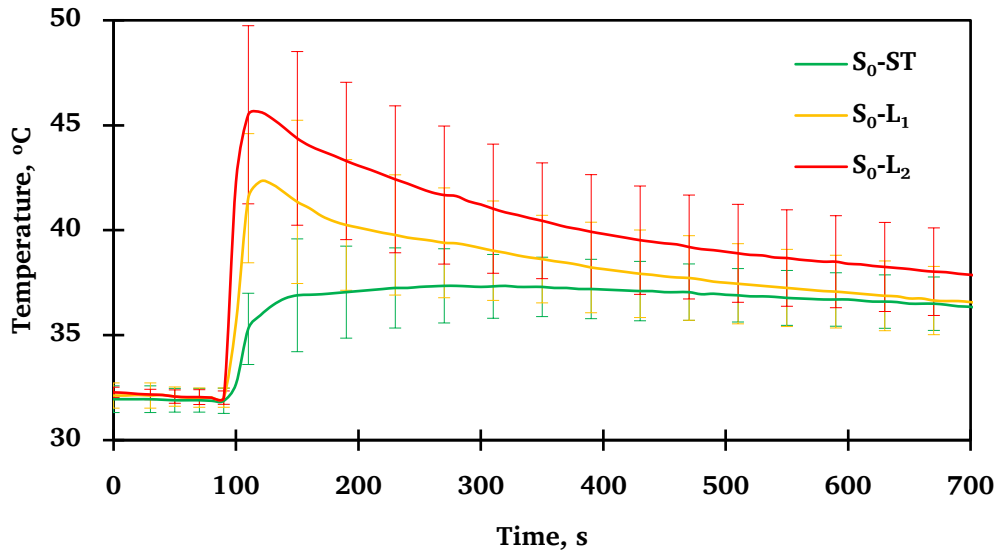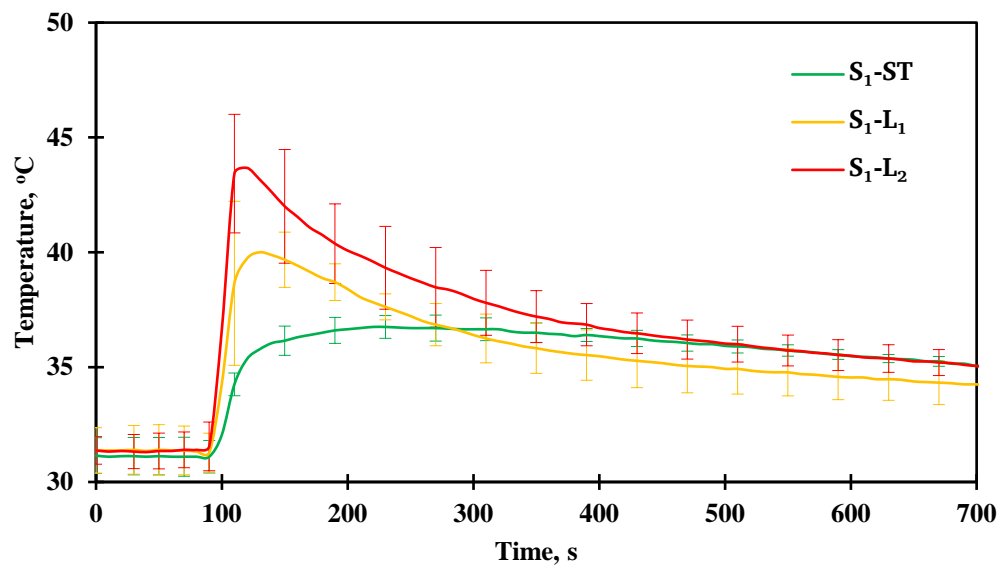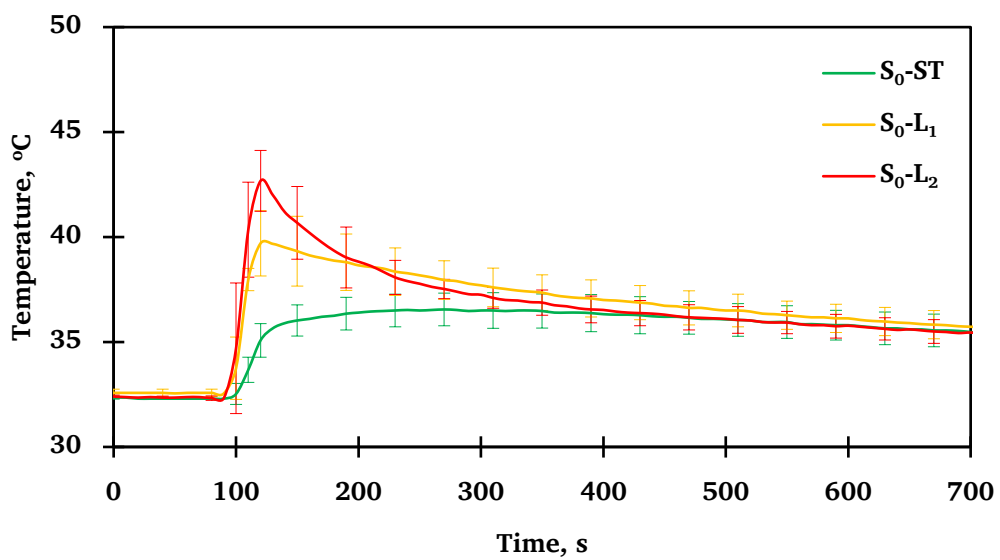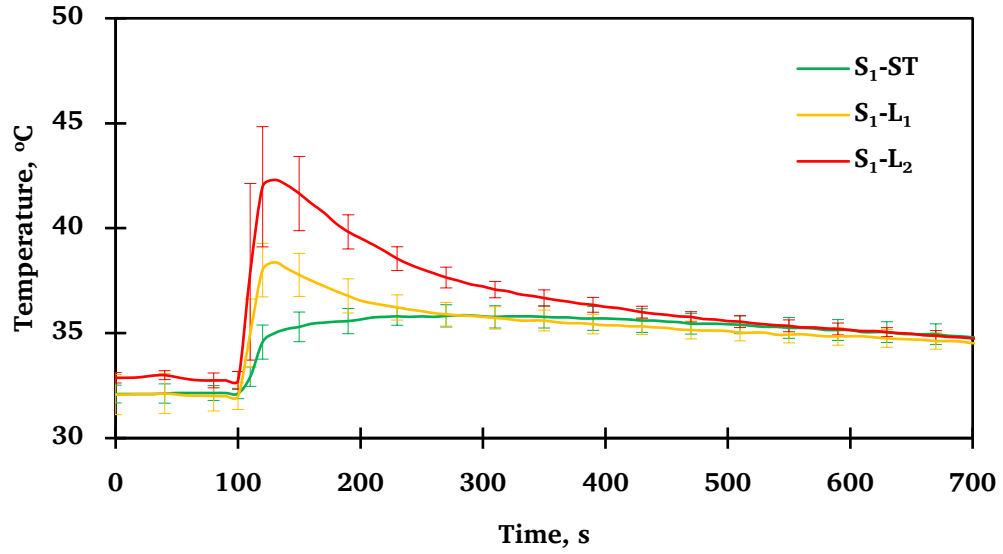
(d)

Figure 5.27: Underneath temperature profiles (a) S_o overlapped, (b) S_1

overlapped, (c) S_0 without overlapped, (d) S_1 without overlapped

In addition, the *vitro* demonstration was conducted for S_0 and S_1 for two

casting configurations: (a) Ortho$^+$ SP with overlap and (b) Ortho$^+$ SP without

overlap. The casting process was carried out at 50°C and 60°C. The average

temperatures of stockinette (S_x-ST), first webril layer (S_x-L_1) and second webril

layer (S_x-L_2) are illustrated in Figure 5.27 for both overlapping and without

overlapping, where $x = 0$ and 1 represent the Ortho$^+$ water jet cut pattern.

According to the findings, the heated Ortho$^+$ SP significantly increased

the temperature profiles beneath the cast. The highest temperature profile was

seen overlapped S_0-L_2, whereas the lowest temperature profile was seen in S_1-

ST without overlapping. However, for both the 50°C and 60°C programming

temperatures, the stockinette temperature stayed below-permitted thresholds

($<45^{\circ}$C) during the casting process. Interestingly, the standard deviation of Ortho$^+$ SP S_1 is less than S_0; thus, ensuring almost uniform temperature distribution and proper air circulation beneath the cast in S_1. Moreover, according to Figure 5.27 (a), (b), (c) and (d), the temperature beneath Ortho$^+$ SP became steady after 500 s from the initial contact. Furthermore, compared to POP and fibreglass casting, this ensured that the Ortho$^+$ SP would regain its original strength in a shorter time [354].

In addition, after the casting process was completed, the Ortho$^+$ SP intact pressure was measured and revealed to be 30.2 ± 5.2 mmHg for S_0 and 25.6 ± 5.8 mmHg for S_1. Blake et al. reported 30.45 ± 9.73 mmHg POP undercast pressure for a short leg cast, which is effectively identical to Ortho$^+$ SP [353]. A slight decrease in undercast pressure was observed in S_1, which might be attributed to inadequate contact with the pressure sensing area. On the other hand, there was no noticeable difference in undercast pressure between 50°C and 60°C programming temperatures. Moreover, there appeared to be no change in underlying pressure throughout the 30 days. Therefore, author state quite confidently the proposed Ortho$^+$ will fit around any free-form shape without sacrificing shape memory functionalities.

Finally, the Ortho$^+$ SP was applied to the mannequin and the key steps are presented in Figure 5.29.
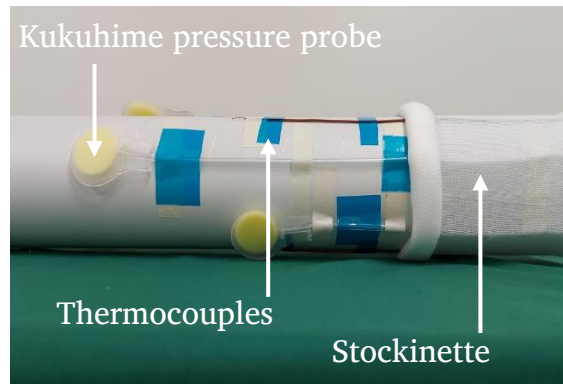
(a)
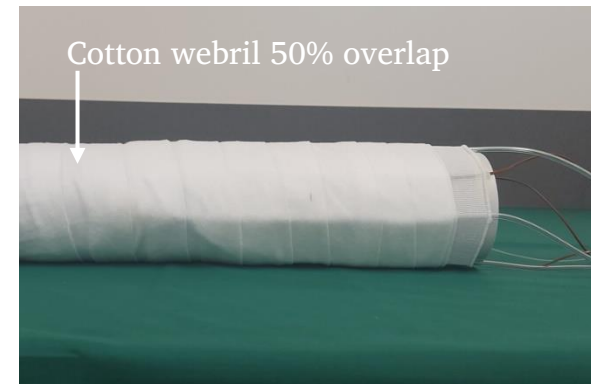
(b)
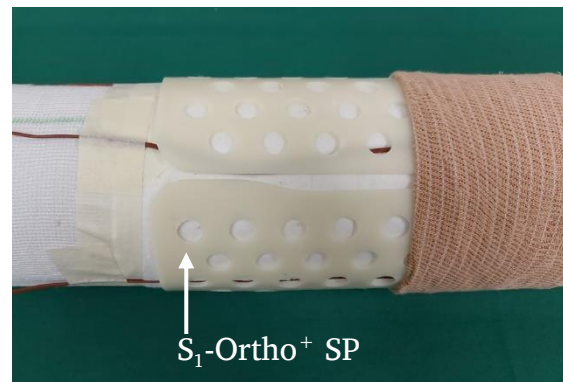
(c)
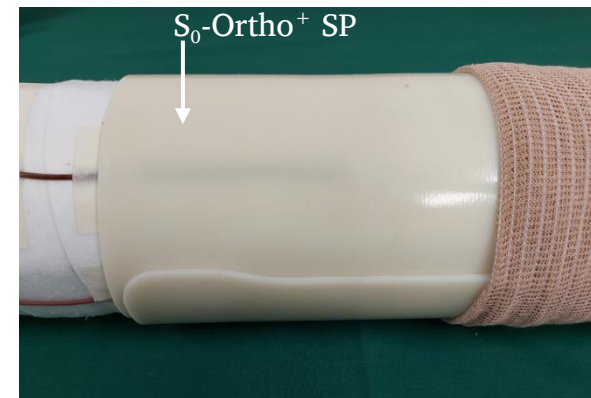
(d)
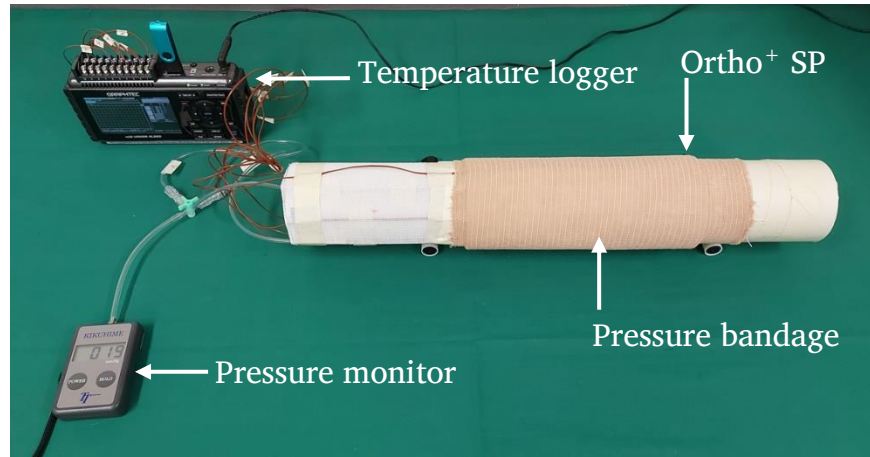
(e)

Figure 5.28: Smart plaster experimentation, (a) Temperature and pressure measuring, (b) Cotton webril 50% overlap, (c) S_1 without overlap, (d) S_o with overlap, (e) Complete measuring setup

The author has extensively considered the safe use of E-glass fibre in Ortho$^+$ fabrication. It is highly impossible to break Ortho$^+$ SP and there won't be any broken E-glass fibre pieces that could come out to the surface. Moreover, according to the Ortho$^+$ synthesis procedure, the E-glass fibre is unlikely to have direct contact with human skin since stockinette unrolls first. It is usually longer than the cast length, followed by cotton webril with 50% overlap. Additionally, the introduced secondary locking mechanism which further avoids direct contact. In addition, using FDA-certified latex surgical gloves are highly recommended for Ortho$^+$ initial measuring, sizing and during the casting process. Therefore, the author would confirm there is less probability of contacting E-glass fibre with human skin. After considering the overall effectiveness and the results revealed, the author of this thesis

confidently states that the novel Ortho⁺ SP can meet the demanded requirement for initial *vivo* trials.

(a)

(b)

(c)

(d)

(e)

(f)

Figure 5.29: Ortho$^+$ SP demonstration on mannequin, (a) Stockinette, (b) Cotton webril 50% overlap, (c) S_0 Ortho$^+$ SP, (d) S_1 Ortho$^+$ SP, (e) S_2 Ortho$^+$ SP, (f) Ortho$^+$ SP with secondary locking method

5.6 Unique features of Ortho$^+$ and Ortho$^+$ smart plaster

The proposed Ortho$^+$ material is a preferable alternative for POP and fibreglass materials since it can strictly meet the functionality of traditional orthopaedic casts while having other advantageous and inherent properties. At elevated temperatures ($\geq \dot{T}_g$), the Ortho$^+$ can be easily cut with a scissor according to the patient's anthropometric measurements. During the Ortho$^+$ SP forming into body shape, no exothermic or endothermic chemical reaction occurs, unlike POP and fibreglass casting; as a result, Ortho$^+$ SPs can avoid hot spots. From the orthopaedic technician's point of view, Ortho$^+$ SP is easy to apply, has less setting time (<3 min.), and the process is quicker and cleaner. On the other hand, from the patient's point of view, Ortho$^+$ SP is lightweight and more comfortable than POP. Moreover, Ortho$^+$ SP can be removed within less time (<2 min.) without using noisy electric oscillating saws or large cast scissors which may be frightening specially for paediatric patients. In addition, introduced circular and diamond shape patterns provide optimal air circulation between skin and the environment, which can minimise bacterial and fungal itchy infections. For fractures that require surgical reduction any bleeding from the surgical site can also be easily detected.

The Ortho$^+$ SP offers significant benefits compared to POP and fibreglass casting techniques since it allows multiple alterations. Therefore, the orthopaedic technician can immediately adjust it to fit better without wasting excess materials if an inaccurate shape is formed. This unique feature

is more useful for keeping the best fit since, during bone healing, swelling will be reduced. Additionally, the undercast pressure can be adjusted even after the Ortho$^+$ SP has been applied, thus preventing irreversible damage to muscles and nerves and reducing the severe outcomes associated with cast-induced compartment syndrome. Contrary to other medical supplies, Ortho$^+$ SP can be reused after thorough disinfection. Therefore, the Ortho$^+$ SP is an ideal solution for first aid and emergencies in remote or isolated locations where required medical facilities and assistance are not freely accessible. Finally, the author highly recommends Ortho$^+$ SP as a first-aid bone immobilisation solution for fractured limbs.

Table 5-2: Performance comparison of Ortho$^+$, POP, fiberglass, and wood casting materials

	Ortho$^+$	POP	Fibreglass	Wood
Weight	Low	High	Low	Low
Chemical reaction	No	Yes	Yes	Yes
Hotspots	No	Yes	Yes	Less
Setting time	~3 Min.	>3 Min.	>3 Min.	>3 Min.
Re-adjustment	Possible	Impossible	Impossible	Impossible
Pressure adjustment	Yes	No	No	No
Air circulation	Optimal	Low	Low	Low
Infection risk	Minimal	High	High	Low
Process time	Less	Extended	High	High
Removal	Easy	Difficult	Difficult	Easy
Required skill	Low	High	High	High
Reusability	Yes	No	No	No

5.7 Summary

In this chapter, Ortho$^+$ has been modelled in ABAQUS FEA and validated through a comprehensive experimental program. The proposed ABAQUS FEA model had good agreement with the experimental results. Therefore, the FEA model can be used effectively in designing and optimising Ortho$^+$ geometrical parameters without fabricating time-consuming and costly prototypes.

In addition, undercast temperature profiles and pressure were studied. During the Ortho$^+$ SP *vitro* trials, the number of cotton webril layers, programming temperatures and patterns were varied. The two layers of cotton webril and circular-patterned Ortho$^+$ SP with 50ºC programming temperature was given best results. The measured maximum skin temperature and pressure were less than 45ºC and 30.2±5.2 mmHg, respectively and within the safe range to initiate clinical trials. Overall, the Ortho$^+$ SP *vitro* experiment took approximately 10 min., which was comparatively less than traditional orthopaedic bone immobilisation techniques. Furthermore, Ortho$^+$ SP offers unique features, such as it allows multiple alterations; thus, the orthopaedic technician can adjust it to fit immediately. Moreover, the underneath pressure can be adjusted even after Ortho$^+$ SP is applied; as a result, it can prevent irreversible damage to muscles and nerves.

Therefore, the novel Ortho$^+$ SP showed superior performance compared to POP and fibreglass casting; thus, the author strongly recommends *vivo* trials to replace traditional bone fracture treatment practices

with Ortho$^+$ smart material. The next chapter presents the conclusions of the current study and suggestions to improve Ortho$^+$ for next-generation orthopaedic materials further.

CHAPTER 6: CONCLUSION

In this chapter, the author highlights the innovative contribution of this research for advancement of scientific knowledge. In this research, the objectives set forth in section 1.3. Chapter 2 were successfully accomplished. The author has comprehensively demonstrated the current research knowledge, the research gap, and the contributions of SMP materials to the biomedical field. The firsthand experiences of novel material Ortho$^+$ synthesis, fabrication, and characterisation are summarised in Chapters 3 and 4. Finally, in Chapter 5, the application of a lower limb leg cylindrical cast on a human mannequin using Ortho$^+$ is detailed to prove the concept. The innovative research findings are listed, along with the techniques used to synthesise Ortho$^+$.

The scientific knowledge revealed in this thesis was published in four peer reviewed Q_1 journal articles and five Scopus index conference proceedings. In order to promote the revolutionary Ortho$^+$ orthopaedic material and increase public awareness, a short video and a news article were published as detailed in the associated publication. For further investigations, the author has endorsed recommendations and future directions.

6.1 Key outcomes of the study

6.1.1 Firsthand experience and new knowledge

- **Novel SMP for non-invasive biomedical applications**

The key challenge has been to synthesise SMP for non-invasive biomedical applications. The author successfully tailored an SMP storage onset transition temperature of around 45°C. As this slightly above the average body temperature, it avoids self-recovery. Therefore, the synthesised Ortho⁺ is confidently recommended for orthosis and fracture fixator developments. The detailed methodology for chemical synthesis can be applied to any SMP-based research and development.

- **An innovative method to evaluate curing parameters**

The degree of curing significantly affects a composite's performance. DEA thermal analysis is a useful method for studying the curing behaviour of thermosetting composites. Further, DSC findings are used to obtain peak heat generation, and DMA provides material viscoelastic properties. Therefore, DSC and DMA results have been comprehensively used to identify curing performance, but their accuracy depends on the sensing location.

To avoid such discrepancies, the author proposed strain data to assess the curing kinetic; thus, DOFN was introduced. The DOFN was embedded before chemical pouring. The results proved that this method would not affect the composite's overall thermomechanical properties. Further, DOFN has shown its capability to measure in-situ data at curing and post-curing. This method can be further extended to quality control purposes.

With this method, the health of the final components can be monitored, even at mass-scale production.

- **Way to improve delicate shape memory properties**

SME merely relies on the molecular architecture of the matrix material and molecular parameters, such as the type of monomer or the comonomer ratios. Curing agents improve mechanical properties; however, they adversely affect delicate shape memory properties (e.g., shape fixity and retention ratios). Researchers have primarily focused on SMP synthesis; thus, there has been minimal attention to the importance of selecting a proper curing cycle. Therefore, the author of this thesis thoroughly examined the DEA and DSC results and introduced a custom curing schedule that improved delicate shape memory recovery properties by 25%.

- **Technique to optimise multiple fabrication parameters**

SMP applications demand mechanical strength as well as shape memory properties. The mechanical strength primarily drives fibres; on the other hand, fibres adversely affect the shape memory fixity and retention ratios. Moreover, these properties depend upon fabrication parameters such as the fibre type, fraction, and specimen thickness to name a few. Therefore, the author introduced a firsthand comprehensive experimental program and optimised fabrication parameters using a GRA combined method, for

the first time in smart material fabrication. This technique can be applied to optimise any SMP fabrication process.

- **A quick approach to find nanoparticle dispersion time**

The NP significantly contributes to improving SMP functional properties other than its mechanical strength. The homogeneous distribution of NPs is essential to obtain such an enhancement of the base material's properties. Different techniques are currently in use, among which ultrasonic irradiation has shown excellent emulsifying and crushing performance. However, sonication increases epoxy temperature, micro-bubbles, and cavitation. It also, break apart molecules and degrades the epoxy's performance. In the proposed method, NP dispersed epoxy FTIR spectroscopy was thoroughly examined and compared against the dispersion time. The suggested approach is cost effective since it can determine the ideal sonication time without actually curing the SMP epoxy. The same method can be used to disperse NPs in an epoxy.

6.1.2 SMP manufacturing processes

- **Validated FEA simulation model to predict Ortho$^+$ performances**

The presented SMP FEA models are based on experimentally obtained viscoelastic data. The TTS was employed to acquire material viscoelastic characteristics before incorporating them into ABAQUS commercial software. The FEA models can predict the spring-back effect, recovery

behaviour, and recovery time. The proposed innovative DOFN measured real-time strain during SMP programming and recovery and compared it with the ABAQUS FEA model. The revealed DOFN experimental strain and FEA model strain are in good agreement. Thus, the proposed FEA model is strongly recommended for predicting behaviour when Ortho$^+$ SP is formed into complex shapes. Moreover, this detailed methodology can be used to validate FEA models.

- **Fabrication and demonstration of SMP lower limb leg cylindrical cast**

A lower limb leg cylindrical cast was successfully demonstrated on a human mannequin using Ortho$^+$ to prove the concept. The initial preparation was similar to the POP casting, and the measured undercast temperature and pressure were within safe limits for human use. The fabricated Ortho$^+$ is lightweight and easy to apply. The process is quicker and cleaner than traditional materials. In addition, Ortho$^+$ SP offers unique features that are not available in other orthopaedic materials. Most importantly, Ortho$^+$ SP can be reused after disinfection. Therefore, the author encourages biomedical researchers to fabricate next-generation orthosis and fracture fixators with newly introduced Ortho$^+$.

- **Low-cost custom SMP-based orthopaedic solutions**

Above T_g, the synthesised SMP can be formed into any complex geometrical human body shape with high accuracy; thus, it allows health professionals to make high-quality and low-cost custom solutions while improving comfort and functional reliability. As a result, SMP-based devices may not require traditional biomedical rehabilitation methods.

6.2   Conclusions

Polymer researchers have shown greater interest in developing new medical devices with SMPs. However, none of the research groups has been able to fabricate non-invasive biomedical applications. This is because it is hard to synthesise the ideal SMP with the required structural properties for non-invasive applications. To fill this knowledge gap, in this thesis, DGEBA epoxy was synthesised with amine-based D-230 (di-amine) and NGDE chain extender. The SMP properties such as T_g (37°C$<T_g<$45°C), R_f ($>$98%), $R_{f,30}$ ($>$98%), and R_r ($>$85%) were comprehensively analysed and reported.

Delicate and weak SME must be improved in many synthesised SMPs before moving into the application stage; however, this is challenging. For the first time, in this research, it has been established that shape memory recovery depends on curing kinetics. Thus, SMP curing kinetics were thoroughly analysed through DEA and DSC trials. A customised curing cycle was introduced which involved curing at 65°C for 6 hrs. and then post-curing at

115°C for another hr. Remarkably, the proposed curing cycle improved shape recovery time by 25%.

On the other hand, when evaluating curing kinetics, researchers have often struggled with point-based sensors (DEA) and smaller test specimens (DSC) that do not adequately reflect the entire sample. In order to solve this pressing problem, the author proposed the innovative idea of DOFN and has successfully demonstrated its capability to measure in-situ data at curing. The author recommends further research on DOFN to achieve a breakthrough in technical improvement in order to monitor curing kinetics more accurately and efficiently. In addition, DOFN can be used for quality control in mass-scale production and further extended to health monitoring purposes.

It has been revealed that the inclusion of carbon and E-glass fibres significantly enhances the mechanical properties of composites. However, it has not yet been determined to what extent it is possible to strengthen composites without compromising their shape memory properties such as fixity and retention.

To resolve this issue, the author reinforced the epoxy with carbon and E-glass fibres following a Taguchi L_{18} ($2 \times 3 \times 3$) comprehensive experimental array. The fibre type, number of layers, and thickness were chosen as control variables. According to the results, E-glass fibres mainly dominated impact properties with a relative contribution of over 50%, followed by the number of layers. On the other hand, the number of fibre layers dominates R_f and R_r with over 60% relative contribution, while $R_{f,30}$ dominates both the number of

layers and the thickness. Thus, to find the optimum fabrication configuration for orthopaedic bone immobilisation, the most impacted T_g, σ_i, and $R_{f,30}$ multiple variables were selected and optimised with GRA integrated Taguchi analysis. The results showed that a single layer (GRA, mean 0.6173 and S/N ratio -4.275) of E-glass fibre (GRA, mean 0.5766 and S/N ratio -4.939) in a 2.5 mm thick (GRA, mean 0.5626 and S/N ratio -5.138) SMP sheet displayed the optimum characteristics. Further, the number of fibre layers (P-value 0.013, relative contribution >37.86%) was found to be the most critical parameter and the thickness was insignificant for overall performance.

Additionally, SMP was reinforced with TiO_2, MWCNT and graphene NPs with 0.4, 0.7, and 1.0 wt% under a Taguchi L_9 (3×3) orthogonal array. T_g, SM, σ_t, σ_c, σ_f, σ_i, R_f, $R_{f,30}$, and R_r were reduced to a single objective through a GRA combined Taguchi method. It was found that 0.4 wt% (S/N ratio -2.597) of TiO_2 (S/N ratio-4.022) optimised the selected variables. After carefully analysing the L_{18} and L_9 optimised parameters, one layer of E-glass fibre with 0.4 wt% of TiO_2 NPs was used to invent a novel orthopaedic material named Ortho$^+$. The Ortho$^+$ showed a 98.72 ± 0.5% cure percentage and contained 91.30 wt% of SMP. In between 315°C and 420°C, a rapid mass loss was reported due to the decomposition of the carbonate phase. Thus, Ortho$^+$ is thermally stable at an operational temperature range of between 40°C and 70°C. Furthermore, Ortho$^+$ transition temperatures range from 40°C to 56°C; hence, a significant influence on viscoelastic properties at room temperature has not been reported.

The remaining unresolved doubts of SMP for external orthopaedic applications were successfully answered by verifying Ortho$^+$'s environmental durability. At room temperature, Ortho$^+$ was shown to have SM $= 4.375 \pm 0.141$ GPa, $\sigma_t = 74.4 \pm 3.9$ MPa, $\sigma_c = 71.3 \pm 1.0$ MPa, $\sigma_f = 129.7 \pm 0.2$ MPa, $\sigma_i = 0.036$ J/mm, $R_f = 99.89\%$, and $R_r = 90.96\%$. Moreover, tensile and flexural experiments were concluded at elevated temperatures ($\leq 45°C$) and the strength and modulus were dropped following the second-order polynomial function. Therefore, the synthesised novel Ortho$^+$ successfully addressed synthesis, characterisation, and optimisation doubts. This material effectively solves the remaining issues in SMPs for external orthopaedic applications.

Researchers have proposed SMP ABAQUS FEA models to virtually test and predict the behaviour of SME to identify the critical geometrical parameters when subjected to different loading conditions. SMP time and temperature-dependent viscoelastic properties are fitted with the Prony series and the required parameters for FEA modelling are calculated. However, most viscoelastic FEA models are not validated. The author addresses this issue for the first time in this thesis by validating the FEA model outcome through an innovative DOFN experimental program. The proposed validation technique was relatively simple but robust; thus, the presented Ortho$^+$ FEA model predictions are reliable.

After effectively addressing many unresolved problems, an orthopaedic fracture fixator *vitro* demonstration was performed on a human mannequin.

The Ortho$^+$ SP was completed at 50ºC and 60ºC temperatures. On both occasions, the temperature beneath the stockinette remained within the permissible limits (<45ºC). The patterned (S_1) Ortho$^+$ SP ensured uniform temperature distribution and proper air circulation beneath the cast. This procedure was similar to POP and fibreglass casting techniques; however, Ortho$^+$ casting was completed in less than 10 mins. Moreover, the undercast temperature was steady after 500 s from the initial contact and Ortho$^+$ gained original strength in less than 2 mins., which was a significant achievement compared to POP and fibreglass casting. The patterned Ortho$^+$, S_0 and S_1 were found to have intact pressures of 30.2 ± 5.2 mmHg and 25.6 ± 5.8 mmHg, respectively.

In addition, Ortho$^+$ SP offers unique features such as no chemical reaction during the process, allowing multiple alterations, adjustable pressure, and optimum air circulation beneath the cast. Therefore, Ortho$^+$ SP prevents irreversible damage to muscles and nerves. This offers a significant reduction in severe life-threatening effects on the patient. Most importantly, Ortho$^+$ SP can be reused on multiple occasions after disinfection, supporting the circular economy model toward zero waste.

The successfully completed study has significantly contributed to the scientific knowledge base by establishing a novel SMP material and a development framework for biomedical non-invasive applications. The generated new knowledge and *vitro* demonstration established a solid platform for the scientific and engineering communities to use SMPs in

orthopaedic medical applications. In due course, future SMP based orthosis and fracture fixator custom devices will be the best candidate for the next generation of orthopaedic material.

6.3   Future Directions and Recommendations

In this thesis, primary attention was given to introducing SMP based material for non-invasive orthopaedic treatments. The author has comprehensively detailed the synthesis and characterisation of Ortho$^+$ and demonstrated a lower limb leg cylindrical cast in less than 10 mins. However, SMPs are still new to orthopaedic non-invasive applications; thus, there is still space for more research. Therefore, the author of this thesis highly recommends further research to enhance the synthesised Ortho$^+$ properties and fulfil commercialisation requirements.

- Orthopaedic materials demand mechanical properties at body temperature. Therefore, the author selected a commercially available, low-cost, high-structural analogy DGEBA epoxy, as a matrix material. Incorporated continuous E-glass fibres further improved the strength of Ortho$^+$. Also, it is worth exploring other reinforcement materials such as basalt, kevlar, natural fibres, and NPs. These may significantly improve Ortho$^+$'s mechanical and required functional properties such as fire resistance, thermal conductivity and soothing, among others.

- Ortho$^+$'s thermomechanical and shape memory properties depend upon fabrication parameters such as chemical configuration, thickness, fibre type, fraction, and NP content to name a few. As a result, improving one performance characteristic may affect other performance characteristics positively or negatively. For example, R_f and R_r are inversely proportional to the fibre fraction; however, fibre fraction dominates the mechanical properties. GRA and the robust Taguchi method have been successfully employed to overcome such optimisation of the multiple performance characteristics. However, there is more scope for further research on optimising the thermomechanical and shape memory properties against multiple variables in order to determine the best configuration recommended for fabricating Ortho$^+$.

- The CFRSMPC SEM images were magnified up to 30X and NRSMPCS were magnified till 30000X. The UniSQ Jeol Benchtop (JCM-6000) SEM machines images were not clear at higher magnification due to low thermal conductivity of the specimens. Therefore, we contacted Centre for Catalysis and Clean Energy at Griffith University, Gold Coast campus for in-depth analysis. They also confirmed that at higher magnification the synthesised SMP specimens' SEM images were not clear enough for a strong conclusion due to low thermal conductivity. Thus, the author claimed the synthesised SMPCs are free from voids

and cracks with regard to available resources. On the other hand, mechanical testing has not shown pre-mature failures compare to other published work which were referred similar SEM magnifications. Therefore, author recommend further investigation on this matter.

- Delamination occurs due to interlaminar stress and fibre-reinforced composites' most common failure mode. Manufacturing defects and fibre incompatibility also influence delamination. On the other hand, Ortho$^+$'s unique features allows the orthopaedic technician to make multiple alterations upon external stimulus. Due to this, there will be a high probability of the bond being weakening between the SMP matrix and the fibre; thus, the expected properties of Ortho$^+$ might decline. Therefore, the author recommends further investigations to determine the maximum permissible cycles without delamination, before reusing Ortho$^+$ in *vitro* trials.

- During Ortho$^+$ manufacturing, it is worth embedding DOFN, which can be used to monitor real-time strain at curing and the shape memory programming cycle. The same DOFN can be further extended to evaluate undercast temperature, pressure, delamination, and the overall health of the Ortho$^+$. As opposed to single-point sensors, this technique covers a significant area. As a result, the experimental data have a high degree of validity. Therefore, the author strongly

recommends further research to overcome current orthopaedic material requirements and challenges with distributed sensing.

- It is well known that polymeric materials have a limited life span due to environmental degradation. The research in this thesis has established a useful design space to discuss the Ortho$^+$ characterisation material framework before and after exposure to extreme environments. A baseline assessment was conducted according to the commonly accepted international standards. The study's results revealed that extreme environments negatively influenced Ortho$^+$ properties such as glassy modulus, rubbery modulus and most importantly, the shape fixity, and retention ratio. The author also noticed slight variations in the weight and colour of Ortho$^+$ in the conditioned specimens. Therefore, further research recommended to confirm the Ortho$^+$ durability assessment under many common environmental factors, including moisture, oil, UV radiation, etc.

- The shape of the human body varies from person to person and is mainly determined by the distribution of muscles, fat, and the skeletal structure. The orthopaedic technician wraps Ortho$^+$ around the fractured limb and forms the shape during the treatment. The casting process might take 10 mins. and varies depending on the thickness and pattern of the Ortho$^+$. Therefore, further research is advised to

establish a correlation between thickness and the smallest bend radius that avoids delamination and minimises spring back. This will give additional flexibility to the orthopaedic technician for selecting the appropriate Ortho$^+$ pattern on the fractured location and the required strength.

- As a secondary locking mechanism, a pressure bandage was used to avoid an unexpected shape recovery of Ortho$^+$. At the same time, this can be used to regulate undercast pressure. On the other hand, this secondary locking mechanism allows additional control since the orthopaedic technician can allow for natural swelling after an acute injury. Therefore, it is worth studying further the secondary locking mechanism generated under cast pressure against the locking material.

- Undercast infections are the most common complication in POP and fibreglass bone immobilisation methods. The infection starts with skin irritation and a foul odour, or a cast discharge can be occurred. This might result in a permanent loss of body parts or a severe life-threatening condition; thus, treatment is needed immediately. However, to minimise such discomfort and diseases, TiO$_2$ NPs have been introduced. According to the literature, TiO$_2$ has shown excellent antifungal and antibacterial effects due to its physico-chemical properties. For example, TiO$_2$ powder has been heavily researched for

the photocatalytic decomposition of organic pollutants. Thus, the author recommends further research to investigate the undercast antibacterial effect with Ortho⁺ smart plaster.

- Healthcare facilities around the world generate a large amount of non-infected plastic waste, but only a small amount is recyclable. Medical plastic recycling is difficult, expensive, and time-consuming since it needs sorting and cleaning. If Ortho⁺ can be 100% recyclable, it can gain a significant boost towards zero waste. Therefore, it is worth investigating recycling methods for Ortho⁺ in order for the material to gain widespread acceptance from the medical community.

- The author completed the needed tasks within the time frame to demonstrate that SMPs are viable options for external orthopaedic applications. However, further research is strongly recommended under the supervision of healthcare professionals to review and assess the impact of Ortho⁺ SP on orthopaedic treatments. This would accelerate the legal authorisation to undertake *vivo* trials and FDA approvals, translating the research into a consumable product benefiting patients in accidents and emergencies.

REFERENCES

1. Apostolakos, J., T.J. Durant, et al., *The enthesis: a review of the tendon-to-bone insertion.* Muscles, ligaments and tendons journal, 2014. **4**(3): p. 333.

2. Ganveer, G.B. and R.R. Tiwari, *Injury pattern among non-fatal road traffic accident cases: a cross-sectional study in Central India.* 2005.

3. Sheen, J.R. and V.V. Garla, *Fracture healing overview*, in *StatPearls [Internet].* 2021, StatPearls Publishing.

4. Fischgrund, J., D. Paley, et al., *Variables affecting time to bone healing during limb lengthening.* Clinical orthopaedics and related research, 1994(301): p. 31-37.

5. Lusardi, M.M., M. Jorge, et al., *Orthotics and prosthetics in rehabilitation-e-book.* 2013: Elsevier Health Sciences.

6. Schwendenwein, E., S. Hajdu, et al., *Displaced fractures of the proximal humerus in children require open/closed reduction and internal fixation.* European journal of pediatric surgery, 2004. **14**(01): p. 51-55.

7. Halanski, M. and K.J. Noonan, *Cast and splint immobilization: complications.* JAAOS-Journal of the American Academy of Orthopaedic Surgeons, 2008. **16**(1): p. 30-40.

8. Sharma, H. and D. Prabu, *Plaster of Paris: past, present and future.* Journal of Clinical Orthopaedics & Trauma, 2013. **4**(3): p. 107-109.

9. Hammond, R., *Advantages and disadvantages of plaster-of-Paris as a fixative apparatus.* Medical Record (1866-1922), 1912. **82**(1): p. 18.

10. Hernigou, P., *Plaster of Paris: the orthopaedic surgeon heritage.* International orthopaedics, 2016. **40**(8): p. 1767-1779.

11. Lindfors, N. and J. Salo, *New ecological wood–plastic composite materials for scaphoid-type casting: Material properties and clinical evaluation.* Hand Therapy, 2014. **19**(3): p. 67-72.

12. Prior, M. and S. Miles, *Casting: part one.* EMERGENCY nurse, 1999. **7**(2).

13. Deignan, B.J., J.M. Iaquinto, et al., *Effect of pressure applied during casting on temperatures beneath casts.* Journal of Pediatric Orthopaedics, 2011. **31**(7): p. 791-797.

14. Jeewantha, J., C. Emmanuel, et al. *Development and characterization of shape memory polymers for non-invasive biomedical applications*. in *Smart Materials, Adaptive Structures and Intelligent Systems*. 2021. American Society of Mechanical Engineers.

15. Liu, C., H. Qin, et al., *Review of progress in shape-memory polymers.* Journal of materials chemistry, 2007. **17**(16): p. 1543-1558.

16. Lendlein, A. and O.E. Gould, *Reprogrammable recovery and actuation behaviour of shape-memory polymers.* Nature Reviews Materials, 2019. **4**(2): p. 116-133.

17. Lendlein, A., M. Behl, et al., *Shape-memory polymers as a technology platform for biomedical applications.* Expert review of medical devices, 2010. **7**(3): p. 357-379.

18. Liang, R., H. Yu, et al., *Triple and two-way reversible shape memory polymer networks with body temperature and water responsiveness.* Chemistry of Materials, 2021. **33**(4): p. 1190-1200.

19. Herath, H., J. Epaarachchi, et al., *Structural performance and photothermal recovery of carbon fibre reinforced shape memory polymer.* Composites Science and Technology, 2018. **167**: p. 206-214.

20. Pisani, S., I. Genta, et al., *Shape-Memory Polymers Hallmarks and Their Biomedical Applications in the Form of Nanofibers.* International Journal of Molecular Sciences, 2022. **23**(3): p. 1290.

21. Safranski, D. and J.C. Griffis, *Shape-memory polymer device design.* 2017: William Andrew.

22. Yakacki, C.M. and K. Gall, *Shape-memory polymers for biomedical applications.* Shape-memory polymers, 2009: p. 147-175.

23. Delaey, J., P. Dubruel, et al., *Shape-memory polymers for biomedical applications.* Advanced Functional Materials, 2020. **30**(44): p. 1909047.

24. Gayathri, A., J.N. Sajja, et al. *An Extensive Review of Shape Memory Polymers for Biomedical Applications*. in *IOP Conference Series: Materials Science and Engineering*. 2020. IOP Publishing.

25. Correia, C.O. and J.F. Mano, *Chitosan scaffolds with a shape memory effect induced by hydration.* Journal of Materials Chemistry B, 2014. **2**(21): p. 3315-3323.

26.   Behl, M. and A. Lendlein, *Shape-memory polymers.* Materials today, 2007. **10**(4): p. 20-28.

27.   Ohki, T., Q.-Q. Ni, et al., *Mechanical and shape memory behavior of composites with shape memory polymer.* Composites Part A: applied science and manufacturing, 2004. **35**(9): p. 1065-1073.

28.   Gall, K., M. Mikulas, et al., *Carbon fiber reinforced shape memory polymer composites.* Journal of intelligent material systems and structures, 2000. **11**(11): p. 877-886.

29.   Lan, X., Y. Liu, et al., *Fiber reinforced shape-memory polymer composite and its application in a deployable hinge.* Smart Materials and Structures, 2009. **18**(2): p. 024002.

30.   Li, H., J. Liu, et al., *The low velocity impact response of shape memory alloy hybrid polymer composites.* Polymers, 2018. **10**(9): p. 1026.

31.   Boudjellal, A., D. Trache, et al., *Stimulation and reinforcement of shape-memory polymers and their composites: A review.* Journal of Thermoplastic Composite Materials, 2020: p. 0892705720930775.

32.   Nabipour Chakoli, A., *Composites Based on Shape Memory Materials.* Handbook of Polymer and Ceramic Nanotechnology, 2021: p. 603-637.

33.   Tan, L., L. Gan, et al., *Functional shape memory composite nanofibers with graphene oxide filler.* Composites Part A: Applied Science and Manufacturing, 2015. **76**: p. 115-123.

34.   Lu, H., M. Lei, et al., *Shape memory polymer nanocomposites: nano-reinforcement and multifunctionalization.* Nanoscience and Nanotechnology Letters, 2014. **6**(9): p. 772-786.

35.   Dhanasekaran, R., S.S. Reddy, et al., *Shape memory materials for bio-medical and aerospace applications.* Materials Today: Proceedings, 2018. **5**(10): p. 21427-21435.

36.   Tobushi, H., S. Hayashi, et al., *Bending actuation characteristics of shape memory composite with SMA and SMP.* Journal of Intelligent Material Systems and Structures, 2006. **17**(12): p. 1075-1081.

37.   Mu, T., L. Liu, et al., *Shape memory polymers for composites.* Composites Science and Technology, 2018. **160**: p. 169-198.

38. Sokolowski, W., A. Metcalfe, et al., *Medical applications of shape memory polymers.* Biomedical Materials, 2007. **2**(1): p. S23.

39. Pilate, F., A. Toncheva, et al., *Shape-memory polymers for multiple applications in the materials world.* European Polymer Journal, 2016. **80**: p. 268-294.

40. Herath, H., J. Epaarachchi, et al., *Carbon fibre reinforced shape memory polymer composites for deployable space habitats.* Engineer, 2019. **52**(1): p. 1-9.

41. Emmanuel, K., H. Herath, et al., *Thermomechanical and fire performance of DGEBA based shape memory polymer composites for constructions.* Construction and Building Materials, 2021. **303**: p. 124442.

42. Fu, Y.Q., W.M. Huang, et al., *Polyurethane shape-memory polymers for biomedical applications*, in *Shape Memory Polymers for Biomedical Applications*. 2015, Elsevier. p. 167-195.

43. Small IV, W., T.S. Wilson, et al., *Laser-activated shape memory polymer intravascular thrombectomy device.* Optics Express, 2005. **13**(20): p. 8204-8213.

44. Maitland, D.J., M.F. Metzger, et al., *Photothermal properties of shape memory polymer micro-actuators for treating stroke.* Lasers in Surgery and Medicine: The Official Journal of the American Society for Laser Medicine and Surgery, 2002. **30**(1): p. 1-11.

45. Maitland, D.J., W. Small IV, et al., *Prototype laser-activated shape memory polymer foam device for embolic treatment of aneurysms.* Journal of biomedical optics, 2007. **12**(3): p. 030504.

46. Small, W., P.R. Buckley, et al., *Shape memory polymer stent with expandable foam: a new concept for endovascular embolization of fusiform aneurysms.* IEEE Transactions on Biomedical Engineering, 2007. **54**(6): p. 1157-1160.

47. Serrano, M.C. and G.A. Ameer, *Recent insights into the biomedical applications of shape-memory polymers.* Macromolecular bioscience, 2012. **12**(9): p. 1156-1171.

48. Alteheld, A., Y. Feng, et al., *Biodegradable, amorphous copolyester-urethane networks having shape-memory properties.* Angewandte Chemie International Edition, 2005. **44**(8): p. 1188-1192.

49. Jung, Y.C. and J.W. Cho, *Application of shape memory polyurethane in orthodontic.* Journal of Materials Science: Materials in Medicine, 2010. **21**(10): p. 2881-2886.

50. Liu, Y.-f., J.-l. Wu, et al., *Thermo-mechanical properties of glass fiber reinforced shape memory polyurethane for orthodontic application.* Journal of Materials Science: Materials in Medicine, 2018. **29**(9): p. 1-11.

51. Bruni, A., F.G. Serra, et al., *Shape-memory polymers in dentistry: systematic review and patent landscape report.* Materials, 2019. **12**(14): p. 2216.

52. Zhao, W., L. Liu, et al., *Shape memory polymers and their composites in biomedical applications.* Materials Science and Engineering: C, 2019. **97**: p. 864-883.

53. Biswas, A., A.P. Singh, et al., *Biodegradable toughened nanohybrid shape memory polymer for smart biomedical applications.* Nanoscale, 2018. **10**(21): p. 9917-9934.

54. Wischke, C., A.T. Neffe, et al., *Evaluation of a degradable shape-memory polymer network as matrix for controlled drug release.* Journal of Controlled Release, 2009. **138**(3): p. 243-250.

55. Wischke, C., A.T. Neffe, et al., *Controlled drug release from biodegradable shape-memory polymers.* Shape-Memory Polymers, 2009: p. 177-205.

56. Wache, H., D. Tartakowska, et al., *Development of a polymer stent with shape memory effect as a drug delivery system.* Journal of Materials Science: Materials in Medicine, 2003. **14**(2): p. 109-112.

57. Peterson, G.I., A.V. Dobrynin, et al., *Biodegradable shape memory polymers in medicine.* Advanced healthcare materials, 2017. **6**(21): p. 1700694.

58. Pfau, M.R. and M.A. Grunlan, *Smart scaffolds: shape memory polymers (SMPs) in tissue engineering.* Journal of Materials Chemistry B, 2021. **9**(21): p. 4287-4297.

59. Yakacki, C.M., R. Shandas, et al., *Unconstrained recovery characterization of shape-memory polymer networks for cardiovascular applications.* Biomaterials, 2007. **28**(14): p. 2255-2263.

60. Yang, P., *Research on the structure of space deployable antenna based on shape memory polymer composites.* 2011, Dissertation for the Master Degree in Engineering, School of Astronautic

61.   Keller, P., M. Lake, et al. *Development of elastic memory composite stiffeners for a flexible precision reflector.* in *47th AIAA/ASME/ASCE/AHS/ASC Structures, Structural Dynamics, and Materials Conference 14th AIAA/ASME/AHS Adaptive Structures Conference 7th.* 2006.

62.   Hu, J., H. Meng, et al., *A review of stimuli-responsive polymers for smart textile applications.* Smart Materials and Structures, 2012. **21**(5): p. 053001.

63.   Wu, H., O. Wang, et al., *Selective laser sintering-based 4D printing of magnetism-responsive grippers.* ACS applied materials & interfaces, 2020. **13**(11): p. 12679-12688.

64.   Al Azzawi, W., M. Herath, et al., *Modeling, analysis, and testing of viscoelastic properties of shape memory polymer composites and a brief review of their space engineering applications.* Creep and Fatigue in Polymer Matrix Composites, 2019: p. 465-495.

65.   Liu, T., L. Liu, et al., *Integrative hinge based on shape memory polymer composites: material, design, properties and application.* Composite Structures, 2018. **206**: p. 164-176.

66.   Xin, X., L. Liu, et al., *Mechanical models, structures, and applications of shape-memory polymers and their composites.* Acta Mechanica Solida Sinica, 2019. **32**(5): p. 535-565.

67.   Liu, Z., X. Lan, et al., *Design, material properties and performances of a smart hinge based on shape memory polymer composites.* Composites Part B: Engineering, 2020. **193**: p. 108056.

68.   Jeewantha, L.H.J., J.A. Epaarachchi, et al., *Early research of shape memory polymer vascular stents.* Express Polymer Letters, 2022. **16**(9).

69.   Jeewantha, L., K. Emmanuel, et al., *Investigation of curing kinetics and internal strains to enhance performances of bisphenol A based shape memory polymers.* Materialia, 2022. **21**: p. 101264.

70.   Hutchinson, M.J. and M.R. Hutchinson, *Factors contributing to the temperature beneath plaster or fiberglass cast material.* Journal of orthopaedic surgery and research, 2008. **3**(1): p. 1-8.

71.   Read, J., N. Ferguson, et al., *Plaster cast burns: the reality.* Emergency Medicine Journal, 2008. **25**(12): p. 827-828.

72. Liu, Y., H. Du, et al., *Shape memory polymers and their composites in aerospace applications: a review.* Smart materials and structures, 2014. **23**(2): p. 023001.

73. Zhang, F., Y. Xia, et al., *Nano/microstructures of shape memory polymers: From materials to applications.* Nanoscale horizons, 2020. **5**(8): p. 1155-1173.

74. Cheng, X., Y. Chen, et al., *Bending shape memory behaviours of carbon fibre reinforced polyurethane-type shape memory polymer composites under relatively small deformation: Characterisation and computational simulation.* Journal of the mechanical behavior of biomedical materials, 2019. **100**: p. 103372.

75. Lendlein, A. and S. Kelch, *Shape-memory polymers.* Angewandte Chemie International Edition, 2002. **41**(12): p. 2034-2057.

76. Yakacki, C.M., N.S. Satarkar, et al., *Shape-memory polymer networks with Fe3O4 nanoparticles for remote activation.* Journal of Applied Polymer Science, 2009. **112**(5): p. 3166-3176.

77. Kang, H., H. Lai, et al., *Restoration of superwetting switching on TiO2 coated shape memory polymer arrays.* Chemical Engineering Journal, 2020. **394**: p. 124996.

78. Majumdar, D., *Ultrasound-Assisted Synthesis, Exfoliation and Functionalisation of Graphene Derivatives*, in *Graphene Functionalization Strategies*. 2019, Springer. p. 63-103.

79. Bittmann, B., F. Haupert, et al., *Ultrasonic dispersion of inorganic nanoparticles in epoxy resin.* Ultrasonics sonochemistry, 2009. **16**(5): p. 622-628.

80. Al Azzawi, W., J. Epaarachchi, et al., *Implementation of a finite element analysis procedure for structural analysis of shape memory behaviour of fibre reinforced shape memory polymer composites.* Smart Materials and Structures, 2017. **26**(12): p. 125002.

81. Tao, R., Q.-S. Yang, et al., *Parametric analysis and temperature effect of deployable hinged shells using shape memory polymers.* Smart Materials and Structures, 2016. **25**(11): p. 115034.

82. Ukani, A.M. and K.N. Gopal, *Analysis of bending and torsion of shape memory polymer beams.*

83. Wagermaier, W., K. Kratz, et al., *Characterization methods for shape-memory polymers.* Shape-memory polymers, 2009: p. 97-145.

84.   Jang, J.H., S.B. Hong, et al., *Long-term properties of carbon fiber-reinforced shape memory epoxy/polymer composites exposed to vacuum and ultraviolet radiation.* Smart Materials and Structures, 2019. **28**(11): p. 115013.

85.   Quadrini, F., L. Iorio, et al., *Durability of Shape Memory Polymer Composite Laminates under Thermo-Mechanical Cycling.* Journal of Composites Science, 2022. **6**(3): p. 91.

86.   Wong, Y., J. Kong, et al., *Biomedical applications of shape-memory polymers: how practically useful are they?* Science China Chemistry, 2014. **57**(4): p. 476-489.

87.   Hu, J., Y. Zhu, et al., *Recent advances in shape–memory polymers: Structure, mechanism, functionality, modeling and applications.* Progress in polymer science, 2012. **37**(12): p. 1720-1763.

88.   Otsuka, K. and C.M. Wayman, *Shape memory materials.* 1999: Cambridge university press.

89.   Huang, W., Z. Ding, et al., *Shape memory materials.* Materials today, 2010. **13**(7-8): p. 54-61.

90.   Jeewantha, L., K. Emmanuel, et al., *Multi-attribute parametric optimisation of shape memory polymer properties for adaptive orthopaedic plasters.* Materialia, 2022. **21**: p. 101325.

91.   Zhao, W., L. Liu, et al., *Adaptive repair device concept with shape memory polymer.* Smart Materials and Structures, 2017. **26**(2): p. 025027.

92.   Funakubo, H. and J. Kennedy, *Shape memory alloys.* Gordon and Breach, xii + 275, 15 x 22 cm, Illustrated, 1987.

93.   Jena, A., B.B. Samal, et al., *Analysis of electro-thermo-mechanical behavior of thin film Ni50-Ti50 and Ni40-Ti50-Cu10 shape memory alloys for application in thermal actuators.* Materials Today: Proceedings, 2021. **47**: p. 4578-4583.

94.   Alaneme, K.K. and E.A. Okotete, *Reconciling viability and cost-effective shape memory alloy options–A review of copper and iron based shape memory metallic systems.* Engineering Science and Technology, an International Journal, 2016. **19**(3): p. 1582-1592.

95.   Alaneme, K.K., E.A. Okotete, et al., *Structural vibration mitigation–a concise review of the capabilities and applications of Cu and Fe based shape memory alloys in civil structures.* Journal of Building Engineering, 2019. **22**: p. 22-32.

96.   Cladera, A., B. Weber, et al., *Iron-based shape memory alloys for civil engineering structures: An overview.* Construction and building materials, 2014. **63**: p. 281-293.

97.   Kausar, A., *Shape memory polymer/graphene nanocomposites: State-of-the-art.* e-Polymers, 2022. **22**(1): p. 165-181.

98.   Chen, X. and T.D. Nguyen, *Influence of thermoviscoelastic properties and loading conditions on the recovery performance of shape memory polymers.* Mechanics of Materials, 2011. **43**(3): p. 127-138.

99.   Xiao, R., C. Zhang, et al., *Programming of Shape-Memory Polymers: The Temperature Memory Effect and Triple/Multiple-Shape-Memory Effect in Polymers.* Shape-Memory Polymer Device Design; Safranski, DL, Griffis, JC, Eds, 2017: p. 113-137.

100.   Coccia, M., E. Farotti, et al., *Effects of temperature, strain and strain rate on shape memory thermoplastic polyurethane processed by injection molding.* Journal of Intelligent Material Systems and Structures, 2022: p. 1045389X221121917.

101.   Li, G. and A. Wang, *Cold, warm, and hot programming of shape memory polymers.* Journal of Polymer Science Part B: Polymer Physics, 2016. **54**(14): p. 1319-1339.

102.   Hu, J.L., F.L. Ji, et al., *Dependency of the shape memory properties of a polyurethane upon thermomechanical cyclic conditions.* Polymer international, 2005. **54**(3): p. 600-605.

103.   Gall, K., M.L. Dunn, et al., *Shape memory polymer nanocomposites.* Acta Materialia, 2002. **50**(20): p. 5115-5126.

104.   Hiltz, J.A., *Shape Memory Polymers-Literature Review.* 2002.

105.   Hiltz, J.A., *Shape Memory Polymers.* Lit Rev, 2002. **36**.

106.   El Feninat, F., G. Laroche, et al., *Shape memory materials for biomedical applications.* Advanced Engineering Materials, 2002. **4**(3): p. 91-104.

107.   Shirai, Y., *Development of polymeric shape memory material.* Mitsubishi Technical Bulletin, 1988.

108.   Guo, J., Z. Wang, et al., *Shape memory and thermo-mechanical properties of shape memory polymer/carbon fiber composites.* Composites Part A: Applied Science and Manufacturing, 2015. **76**: p. 162-171.

109. Abrahamson, E.R., M.S. Lake, et al., *Shape memory mechanics of an elastic memory composite resin.* Journal of intelligent material systems and structures, 2003. **14**(10): p. 623-632.

110. Mather, P.T., X. Luo, et al., *Shape memory polymer research.* Annual Review of Materials Research, 2009. **39**(1): p. 445-471.

111. Meng, Q. and J. Hu, *A review of shape memory polymer composites and blends.* Composites Part A: Applied Science and Manufacturing, 2009. **40**(11): p. 1661-1672.

112. Leng, J., X. Lan, et al., *Shape-memory polymers and their composites: stimulus methods and applications.* Progress in Materials Science, 2011. **56**(7): p. 1077-1135.

113. Liu, Y., H. Lv, et al., *Review of electro-active shape-memory polymer composite.* Composites Science and Technology, 2009. **69**(13): p. 2064-2068.

114. Hager, M.D., S. Bode, et al., *Shape memory polymers: Past, present and future developments.* Progress in Polymer Science, 2015. **49**: p. 3-33.

115. Lendlein, A. and R. Langer, *Biodegradable, elastic shape-memory polymers for potential biomedical applications.* Science, 2002. **296**(5573): p. 1673-1676.

116. Ruiz-Rubio, L., L. Pérez-Álvarez, et al., *Biodegradable shape-memory polymers,* in *Shape Memory Polymers, Blends and Composites.* 2020, Springer. p. 219-236.

117. Yakacki, C.M., R. Shandas, et al., *Strong, tailored, biocompatible shape-memory polymer networks.* Advanced functional materials, 2008. **18**(16): p. 2428-2435.

118. Song, J.J., H.H. Chang, et al., *Biocompatible shape memory polymer actuators with high force capabilities.* European Polymer Journal, 2015. **67**: p. 186-198.

119. Scalet, G. *Two-way and multiple-way shape memory polymers for soft robotics: An overview.* in *Actuators.* 2020. MDPI.

120. Robinson, H.A., R. Ruggy, et al., *Elasto-Viscous and Stress-Optical Properties of Commercial Polymerized Methyl Methacrylate as a Function of Temperature.* Journal of Applied Physics, 1944. **15**(4): p. 343-351.

121. Lanza, V.L. and P.M. Cook, *A technical paper on the irradiation induced elastic memory of polymers.* 1960, RAYCHEM CORP REDWOOD CITY CALIF.

122. Rezanejad, S. and M. Kokabi, *Shape memory and mechanical properties of cross-linked polyethylene/clay nanocomposites.* European Polymer Journal, 2007. **43**(7): p. 2856-2865.

123. Tobushi, H., S. Hayashi, et al., *Mechanical properties of shape memory polymer of polyurethane series: basic characteristics of stress-strain-temperature relationship.* JSME international journal. Ser. 1, Solid mechanics, strength of materials, 1992. **35**(3): p. 296-302.

124. Takahashi, T., N. Hayashi, et al., *Structure and properties of shape-memory polyurethane block copolymers.* Journal of Applied Polymer Science, 1996. **60**(7): p. 1061-1069.

125. Hewage, J.J.L., S. Jayalath, et al., *Shape memory polymer smart plaster for orthopaedic treatments.* Smart Materials and Structures, 2022.

126. Sokolowski, W.M., *Shape-memory polymer foam and applications*, in *Shape-Memory Polymers and Multifunctional Composites*. 2010, CRC Press. p. 277-302.

127. Yang, L., J. Lou, et al., *A review of shape memory polymers based on the intrinsic structures of their responsive switches.* RSC advances, 2021. **11**(46): p. 28838-28850.

128. Behl, M., M.Y. Razzaq, et al., *Multifunctional shape-memory polymers.* Advanced materials, 2010. **22**(31): p. 3388-3410.

129. Zhang, X., G. Sun, et al., *A novel thermoplastic shape memory polymer with solid-state plasticity derived from exchangeable hydrogen bonds.* RSC advances, 2020. **10**(16): p. 9387-9395.

130. Haskew, M. and J. Hardy, *A mini-review of shape-memory polymer-based materials: stimuli-responsive shape-memory polymers.* Johnson Matthey Technology Review, 2020. **64**(4).

131. Lakhera, N., C.M. Yakacki, et al., *Partially constrained recovery of (meth) acrylate shape-memory polymer networks.* Journal of Applied Polymer Science, 2012. **126**(1): p. 72-82.

132. Hanzon, D.W., K. Yu, et al., *Activation mechanisms of shape-memory polymers.* Shape-Memory Polymer Device Design; Elsevier: Amsterdam, The Netherlands, 2017: p. 139-187.

133. Wang, W., Y. Liu, et al., *Recent developments in shape memory polymer nanocomposites: Actuation methods and mechanisms.* Coordination Chemistry Reviews, 2016. **320**: p. 38-52.

134. Sun, L., W.M. Huang, et al., *Stimulus-responsive shape memory materials: a review.* Materials & Design, 2012. **33**: p. 577-640.

135. Fu, X., Y. Yuan, et al., *Thermoplastic shape memory polymers with tailor-made trigger temperature.* European Polymer Journal, 2017. **93**: p. 307-313.

136. Lendlein, A., H. Jiang, et al., *Light-induced shape-memory polymers.* Nature, 2005. **434**(7035): p. 879-882.

137. Chen, S., S. Yang, et al., *Electroactive two-way shape memory polymer laminates.* Polymer Composites, 2015. **36**(3): p. 439-444.

138. Xiao, R., J. Guo, et al., *Solvent-driven temperature memory and multiple shape memory effects.* Soft matter, 2015. **11**(20): p. 3977-3985.

139. Lu, H., Y. Liu, et al., *Qualitative separation of the effect of the solubility parameter on the recovery behavior of shape-memory polymer.* Smart materials and structures, 2009. **18**(8): p. 085003.

140. Leng, J., W. Huang, et al., *Significantly reducing electrical resistivity by forming conductive Ni chains in a polyurethane shape-memory polymer/carbon-black composite.* Applied Physics Letters, 2008. **92**(20): p. 204101.

141. Xie, T., *Tunable polymer multi-shape memory effect.* Nature, 2010. **464**(7286): p. 267-270.

142. Safranski, D. and J. Griffis, *Mechanical properties of shape-memory polymers for biomedical applications*, in *Shape Memory Polymers for Biomedical Applications*. 2015, Elsevier. p. 9-33.

143. Gu, J., X. Zhang, et al., *A hygro-thermo-mechanical constitutive model for shape memory polymers filled with nano-carbon powder.* International Journal of Smart and Nano Materials, 2021. **12**(3): p. 286-306.

144. Rajak, D.K., D.D. Pagar, et al., *Fiber-reinforced polymer composites: Manufacturing, properties, and applications.* Polymers, 2019. **11**(10): p. 1667.

145. Goh, G.D., Y.L. Yap, et al., *Recent progress in additive manufacturing of fiber reinforced polymer composite.* Advanced Materials Technologies, 2019. **4**(1): p. 1800271.

146. Emmanuel, K., J. Jeewantha, et al. *Effect of Thickness on the Shape Memory Properties of Bisphenol A Epoxy Based Shape Memory Polymer Composites*. in *Smart Materials, Adaptive Structures and Intelligent Systems*. 2021. American Society of Mechanical Engineers.

147. Meng, H. and G. Li, *A review of stimuli-responsive shape memory polymer composites.* polymer, 2013. **54**(9): p. 2199-2221.

148. Liu, T., T. Zhou, et al., *Stimulus methods of multi-functional shape memory polymer nanocomposites: A review.* Composites Part A: Applied Science and Manufacturing, 2017. **100**: p. 20-30.

149. Jordan, J., K.I. Jacob, et al., *Experimental trends in polymer nanocomposites—a review.* Materials science and engineering: A, 2005. **393**(1-2): p. 1-11.

150. Sahoo, N.G., S. Rana, et al., *Polymer nanocomposites based on functionalized carbon nanotubes.* Progress in polymer science, 2010. **35**(7): p. 837-867.

151. Li, W., Y. Liu, et al., *Selectively actuated multi-shape memory effect of a polymer multicomposite.* Journal of Materials Chemistry A, 2015. **3**(48): p. 24532-24539.

152. Gall, K., M.L. Dunn, et al., *Internal stress storage in shape memory polymer nanocomposites.* Applied Physics Letters, 2004. **85**(2): p. 290-292.

153. Zhao, L., J. Zhao, et al., *Continuously tunable wettability by using surface patterned shape memory polymers with giant deformability.* Small, 2016. **12**(24): p. 3327-3333.

154. Hassanzadeh-Aghdam, M.K., R. Ansari, et al., *Thermo-mechanical properties of shape memory polymer nanocomposites reinforced by carbon nanotubes.* Mechanics of Materials, 2019. **129**: p. 80-98.

155. Kazakevičiūtė-Makovska, R., A. Özlem Özarmut, et al., *Characterization of shape memory polymer estane by means of dynamic mechanical thermal analysis technique.* Smart Materials Research, 2014. **2014**.

156. Liu, Y., C. Han, et al., *Thermal, mechanical and shape memory properties of shape memory epoxy resin.* Materials Science and Engineering: A, 2010. **527**(10-11): p. 2510-2514.

157. Dyamenahalli, K., A. Famili, et al., *Characterization of shape-memory polymers for biomedical applications*, in *Shape memory polymers for biomedical applications*. 2015, Elsevier. p. 35-63.

158. Rottiers, W., L. Van den Broeck, et al. *Shape Memory Materials and their applications*. in *Korolev's readings: conference proceedings*. 2011. Samara State Aerospace University.

159. Ohki, T., *Q.-Q. Ni, N. Ohsako, M. Iwamoto*. Compos. Part A Appl. Sci. Manuf, 2004. **35**: p. 1065.

160. Lv, H., J. Leng, et al., *Shape-memory polymer in response to solution*. Advanced Engineering Materials, 2008. **10**(6): p. 592-595.

161. Parameswaranpillai, J., S. Siengchin, et al., *Shape memory polymers, blends and composites*. 2020: Springer.

162. Kalita, H., *5. Applications of shape memory polymers*, in *Shape Memory Polymers*. 2018, De Gruyter: Berlin, Boston. p. 121-136.

163. Lei, M., Z. Chen, et al., *Recent progress in shape memory polymer composites: methods, properties, applications and prospects*. Nanotechnology reviews, 2019. **8**(1): p. 327-351.

164. Wang, L., F. Zhang, et al., *Shape memory polymer fibers: materials, structures, and applications*. Advanced Fiber Materials, 2021: p. 1-19.

165. Santo, L., F. Quadrini, et al., *Applications of shape-memory polymers, and their blends and composites*, in *Shape Memory Polymers, Blends and Composites*. 2020, Springer. p. 311-329.

166. Liu, Y. and J. Leng, *Applications of shape-memory polymers in aerospace*, in *Shape-memory polymers and multifunctional composites*. 2010, CRC Press. p. 243-276.

167. Santo, L., *Shape memory polymer foams*. Progress in Aerospace Sciences, 2016. **81**: p. 60-65.

168. Fabrizio, Q., S. Loredana, et al., *Shape memory epoxy foams for space applications*. Materials letters, 2012. **69**: p. 20-23.

169. Santo, L., F. Quadrini, et al., *Shape memory composites for self-deployable structures in aerospace applications*. Procedia Engineering, 2014. **88**: p. 42-47.

170. Lin, J., C. Knoll, et al. *Shape memory rigidizable inflatable (RI) structures for large space systems applications*. in *47th AIAA/ASME/ASCE/AHS/ASC Structures, Structural Dynamics, and Materials Conference 14th AIAA/ASME/AHS Adaptive Structures Conference 7th*. 2006.

171. Small IV, W., P. Singhal, et al., *Biomedical applications of thermally activated shape memory polymers.* Journal of materials chemistry, 2010. **20**(17): p. 3356-3366.

172. Meng, H. and G. Li, *Shape-memory and self-reinforcing polymers as sutures*, in *Shape Memory Polymers for Biomedical Applications.* 2015, Elsevier. p. 281-300.

173. Erel, V., *Critical Material Parameters for Modeling Devices Made from an Epoxy-Based Shape Memory Polymer.* 2014.

174. Leng, J. and S. Du, *Shape-memory polymers and multifunctional composites.* 2010: CRC Press.

175. Wang, K., S. Strandman, et al., *A mini review: Shape memory polymers for biomedical applications.* Frontiers of Chemical Science and Engineering, 2017. **11**(2): p. 143-153.

176. Yahia, L., *Introduction to shape-memory polymers for biomedical applications*, in *Shape Memory Polymers for Biomedical Applications.* 2015, Elsevier. p. 3-8.

177. Sabahi, N., W. Chen, et al., *A review on additive manufacturing of shape-memory materials for biomedical applications.* Jom, 2020. **72**(3): p. 1229-1253.

178. Liang, X., *Designing and Synthesis of Shape-Memory Polymers for Biomedical Application.* 2010.

179. Tamada, J. and R. Langer, *Erosion kinetics of hydrolytically degradable polymers.* Proceedings of the National Academy of Sciences, 1993. **90**(2): p. 552-556.

180. McClure, M., P. Wolfe, et al., *Bioengineered vascular grafts: Improving vascular tissue engineering through scaffold design.* Journal of drug delivery science and technology, 2011. **21**(3): p. 211-227.

181. Bal, Z., T. Kaito, et al., *Bone regeneration with hydroxyapatite-based biomaterials.* Emergent Materials, 2020. **3**(4): p. 521-544.

182. Santos, D., D.M. Silva, et al., *Multifunctional PLLA-ceramic fiber membranes for bone regeneration applications.* Journal of colloid and interface science, 2017. **504**: p. 101-110.

183. Annunziata, M., L. Nastri, et al., *The use of Poly-d, l-lactic acid (PDLLA) devices for bone augmentation techniques: A systematic review.* Molecules, 2017. **22**(12): p. 2214.

184. Xue, L., S. Dai, et al., *Biodegradable shape-memory block co-polymers for fast self-expandable stents.* Biomaterials, 2010. **31**(32): p. 8132-8140.

185. Boire, T.C., M.K. Gupta, et al., *Pendant allyl crosslinking as a tunable shape memory actuator for vascular applications.* Acta biomaterialia, 2015. **24**: p. 53-63.

186. Wendels, S. and L. Avérous, *Biobased polyurethanes for biomedical applications.* Bioactive Materials, 2021. **6**(4): p. 1083-1106.

187. Tamai, H., K. Igaki, et al., *Initial and 6-month results of biodegradable poly-l-lactic acid coronary stents in humans.* Circulation, 2000. **102**(4): p. 399-404.

188. Venkatraman, S.S., L.P. Tan, et al., *Biodegradable stents with elastic memory.* Biomaterials, 2006. **27**(8): p. 1573-1578.

189. Sonawane, V.C., M.P. More, et al., *Fabrication and characterization of shape memory polymers based bioabsorbable biomedical drug eluting stent.* Artificial cells, nanomedicine, and biotechnology, 2017. **45**(8): p. 1740-1750.

190. Lauto, A., M. Ohebshalom, et al., *Self-expandable chitosan stent: design and preparation.* Biomaterials, 2001. **22**(13): p. 1869-1874.

191. Chen, M.-C., H.-W. Tsai, et al., *Rapidly self-expandable polymeric stents with a shape-memory property.* Biomacromolecules, 2007. **8**(9): p. 2774-2780.

192. Chen, M.-C., Y. Chang, et al., *The characteristics and in vivo suppression of neointimal formation with sirolimus-eluting polymeric stents.* Biomaterials, 2009. **30**(1): p. 79-88.

193. Duarah, R., Y.P. Singh, et al., *High performance bio-based hyperbranched polyurethane/carbon dot-silver nanocomposite: a rapid self-expandable stent.* Biofabrication, 2016. **8**(4): p. 045013.

194. Zheng, Y., Y. Li, et al., *Biocompatible shape memory blend for self-expandable stents with potential biomedical applications.* ACS applied materials & interfaces, 2017. **9**(16): p. 13988-13998.

195. Yu, X., L. Wang, et al., *A shape memory stent of poly (ε-caprolactone-co-DL-lactide) copolymer for potential treatment of esophageal stenosis.* Journal of Materials Science: Materials in Medicine, 2012. **23**(2): p. 581-589.

196. Ajili, S.H., N.G. Ebrahimi, et al., *Polyurethane/polycaprolactane blend with shape memory effect as a proposed material for cardiovascular implants.* Acta biomaterialia, 2009. **5**(5): p. 1519-1530.

197. Ansari, M., M. Golzar, et al., *Shape memory characterization of poly (ε-caprolactone)(PCL)/polyurethane (PU) in combined torsion-tension loading with*

potential applications in cardiovascular stent. Polymer Testing, 2018. **68**: p. 424-432.

198. Chasse, B., H. Xu, et al., *In-vitro biodegradation study of poly (ε-caprolactone) films using a 3D printed helical flow prototype to simulate the physiological conditions for cardiovascular implanted devices.* Biomedical Physics & Engineering Express, 2019. **5**(6): p. 065021.

199. Park, J.Y., J.B. Lee, et al., *Nasolacrimal stent with shape memory as an advanced alternative to silicone products.* Acta Biomaterialia, 2020. **101**: p. 273-284.

200. Gu, S.Y., K. Chang, et al., *A dual-induced self-expandable stent based on biodegradable shape memory polyurethane nanocomposites (PCLAU/Fe3O4) triggered around body temperature.* Journal of Applied Polymer Science, 2018. **135**(3): p. 45686.

201. Gu, S.-Y., S.-P. Jin, et al., *Polylactide-based polyurethane shape memory nanocomposites (Fe3O4/PLAUs) with fast magnetic responsiveness.* Smart Materials and Structures, 2016. **25**(5): p. 055036.

202. Zhou, B., Y. Liu, et al. *Modeling the shape memory effect of shape memory polymer.* in *Second International Conference on Smart Materials and Nanotechnology in Engineering*. 2009. SPIE.

203. Baer, G.M., W. Small, et al., *Fabrication and in vitro deployment of a laser-activated shape memory polymer vascular stent.* Biomedical engineering online, 2007. **6**(1): p. 1-8.

204. Zhang, H., H. Wang, et al., *A novel type of shape memory polymer blend and the shape memory mechanism.* Polymer, 2009. **50**(6): p. 1596-1601.

205. Goraltchouk, A., J. Lai, et al., *Shape-memory self-retaining sutures, methods of manufacture, and methods of use.* 2011, Google Patents.

206. Toncheva, A., F. Khelifa, et al., *Fast IR-actuated shape-memory polymers using in situ silver nanoparticle-grafted cellulose nanocrystals.* ACS applied materials & interfaces, 2018. **10**(35): p. 29933-29942.

207. Guo, Q., C.J. Bishop, et al., *Entanglement-based thermoplastic shape memory polymeric particles with photothermal actuation for biomedical applications.* ACS applied materials & interfaces, 2018. **10**(16): p. 13333-13341.

208. Fang, L., T. Fang, et al., *Near-Infrared Light Triggered Soft Actuators in Aqueous Media Prepared from Shape-Memory Polymer Composites.* Macromolecular Materials and Engineering, 2016. **301**(9): p. 1111-1120.

209. Bettuchi, M. and R. Heinrich, *Novel surgical fastener.* 2009, Google Patents.

210. Ortega, J.M., W. Small, et al., *A shape memory polymer dialysis needle adapter for the reduction of hemodynamic stress within arteriovenous grafts.* IEEE Transactions on Biomedical Engineering, 2007. **54**(9): p. 1722-1724.

211. Metzger, M.F., T.S. Wilson, et al., *Mechanical properties of mechanical actuator for treating ischemic stroke.* Biomedical Microdevices, 2002. **4**(2): p. 89-96.

212. Sharp, A.A., H.V. Panchawagh, et al., *Toward a self-deploying shape memory polymer neuronal electrode.* Journal of neural engineering, 2006. **3**(4): p. L23.

213. Hampikian, J.M., B.C. Heaton, et al., *Mechanical and radiographic properties of a shape memory polymer composite for intracranial aneurysm coils.* Materials Science and Engineering: C, 2006. **26**(8): p. 1373-1379.

214. Marco, D. and S. Eckhouse, *Biodegradable self-inflating intragastric implants for curbing appetite.* WO, 2006. **92789**: p. A2.

215. Mather, P., C. Burstone, et al., *Shape memory polymer orthodontic appliances, and methods of making and using the same.* 2006, Google Patents.

216. Nakasima, A., J.R. Hu, et al., *Potential application of shape memory plastic as elastic material in clinical orthodontics.* The European Journal of Orthodontics, 1991. **13**(3): p. 179-186.

217. Masuda, T., K. Miyazawa, et al., *Development of an orthodontic elastic material using EMA-based resin combined with 1-butanol.* Dental materials journal, 2011: p. 1109210178-1109210178.

218. Wu, T., X. Chen, et al., *Development and application of metal materials in terms of vascular stents.* Bio-medical materials and engineering, 2015. **25**(4): p. 435-441.

219. Tsimikas, S., *Drug-eluting stents and late adverse clinical outcomes: lessons learned, lessons awaited.* 2006, American College of Cardiology Foundation Washington, DC. p. 2112-2115.

220. Novitzke, J., *A patient guide to brain stent placement.* Journal of Vascular and Interventional Neurology, 2009. **2**(2): p. 177.

221.   Guerra, A.J. and J. Ciurana, *Stent's manufacturing field: past, present, and future prospects.* Angiography, 2019. **73817**: p. 41-60.

222.   Joner, M., A.V. Finn, et al., *Pathology of drug-eluting stents in humans: delayed healing and late thrombotic risk.* Journal of the American College of Cardiology, 2006. **48**(1): p. 193-202.

223.   Hirano, S., H. Tsuchida, et al., *N-acetylation in chitosan and the rate of its enzymic hydrolysis.* Biomaterials, 1989. **10**(8): p. 574-576.

224.   Bellin, I., S. Kelch, et al., *Polymeric triple-shape materials.* Proceedings of the National Academy of Sciences, 2006. **103**(48): p. 18043-18047.

225.   Landsman, T.L., R.L. Bush, et al., *Design and verification of a shape memory polymer peripheral occlusion device.* Journal of the mechanical behavior of biomedical materials, 2016. **63**: p. 195-206.

226.   Rodriguez, J.N., M.W. Miller, et al., *Reticulation of low density shape memory polymer foam with an in vivo demonstration of vascular occlusion.* Journal of the mechanical behavior of biomedical materials, 2014. **40**: p. 102-114.

227.   Safranski, D. and J. Griffis, *MedShape, Inc., Atlanta, GA, USA.* Shape Memory Polymers for Biomedical Applications, 2015: p. 9.

228.   Smith, K.E., M. Garcia, et al., *Anterior cruciate ligament fixation: is radial force a predictor of the pullout strength of soft-tissue interference devices?* The Knee, 2012. **19**(6): p. 786-792.

229.   Kumar, B., J. Hu, et al., *Smart medical stocking using memory polymer for chronic venous disorders.* Biomaterials, 2016. **75**: p. 174-181.

230.   Ahmad, M., J. Luo, et al., *Feasibility study of polyurethane shape-memory polymer actuators for pressure bandage application.* Science and technology of advanced materials, 2012.

231.   Tobushi, H., T. Hashimoto, et al., *Thermomechanical constitutive modeling in shape memory polymer of polyurethane series.* Journal of intelligent material systems and structures, 1997. **8**(8): p. 711-718.

232.   Shojaei, A. and G. Li, *Thermomechanical constitutive modelling of shape memory polymer including continuum functional and mechanical damage effects.* Proceedings of the Royal Society A: Mathematical, Physical and Engineering Sciences, 2014. **470**(2170): p. 20140199.

233.   Voyiadjis, G.Z., A. Shojaei, et al., *A theory of anisotropic healing and damage.*

234. Emmanuel, K., L. Jeewantha, et al., *Damage onset analysis of optimized shape memory polymer composites during programming into curved shapes.* Materialia, 2022: p. 101599.

235. Palanikumar, K., L. Karunamoorthy, et al., *Assessment of factors influencing surface roughness on the machining of glass fiber-reinforced polymer composites.* Materials & design, 2006. **27**(10): p. 862-871.

236. Latha, B. and V. Senthilkumar, *Analysis of thrust force in drilling glass fiber-reinforced plastic composites using fuzzy logic.* Materials and Manufacturing processes, 2009. **24**(4): p. 509-516.

237. Azmi, A., R. Lin, et al., *Machinability study of glass fibre-reinforced polymer composites during end milling.* Int J Adv Manuf Technol, 2013. **64**(1-4): p. 247-261.

238. Noryani, M., S. Sapuan, et al., *A statistical framework for selecting natural fibre reinforced polymer composites based on regression model.* Fibers and Polymers, 2018. **19**: p. 1039-1049.

239. Steele, D.G. and C.A. Bramblett, *The anatomy and biology of the human skeleton.* 1988: Texas A&M University Press.

240. Robey, P.G. and A.L. Boskey, *The composition of bone.* Primer on the metabolic bone diseases and disorders of mineral metabolism, 2008. **7**: p. 32-38.

241. Buckwalter, J. and R. Cooper, *Bone structure and function.* Instructional course lectures, 1987. **36**: p. 27-48.

242. Hossain, M.A., *Significance of the structure of human skeleton.* American Journal of Medical Science and Medicine, 2018. **6**(1): p. 1-4.

243. Fazzalari, N., *Bone fracture and bone fracture repair.* Osteoporosis international, 2011. **22**(6): p. 2003-2006.

244. Singh, V., *Medicinal plants and bone healing.* National journal of maxillofacial surgery, 2017. **8**(1): p. 4.

245. Boyd, A.S., H.J. Benjamin, et al., *Splints and casts: indications and methods.* American family physician, 2009. **80**(5): p. 491-499.

246. Smith and Nephew, *The History and Function of Plaster of Paris in Surgery.* 1967: Smith & Nephew.

247. Nemeth, B.A., M.A. Halanski, et al., *Cast and Splint Immobilization.* Rockwood and Wilkins Fractures in Children, 2019.

248. Pifer, G., *Casting and splinting: Prevention of complications.* Advanced Emergency Nursing Journal, 2000. **22**(3): p. 48-54.

249. Bowker, P. and E. Powell, *A clinical evaluation of plaster-of-Paris and eight synthetic fracture splinting materials.* Injury, 1992. **23**(1): p. 13-20.

250. Hefti, F., *Pediatric orthopedics in practice.* 2007: Springer Science & Business Media.

251. Singh, N. and B. Middendorf, *Calcium sulphate hemihydrate hydration leading to gypsum crystallization.* Progress in crystal growth and characterization of materials, 2007. **53**(1): p. 57-77.

252. Burghardt, R.D., J.G. Anderson, et al., *Exothermic properties of plaster–synthetic composite casts.* Journal of Children's Orthopaedics, 2014. **8**(2): p. 193-201.

253. Ngaaje, N.N., *Physico-Mechanical Properties of Plaster of Paris (Gypsum Plaster) Reinforced with Paper Pulp.* European Journal of Engineering and Technology Research, 2021. **6**(1): p. 124-132.

254. Szostakowski, B., P. Smitham, et al., *Plaster of Paris–short history of casting and injured limb immobilzation.* The Open Orthopaedics Journal, 2017. **11**: p. 291.

255. Silfverskiold, J.P., *Fiberglass versus plaster casts: How to choose between them.* Postgraduate Medicine, 1989. **86**(5): p. 71-74.

256. Marshall, P., A. Dibble, et al., *When should a synthetic casting material be used in preference to plaster-of-Paris? A cost analysis and guidance for casting departments.* Injury, 1992. **23**(8): p. 542-544.

257. Pirhonen, E., A. Pärssinen, et al., *Comparative study on stiffness properties of WOODCAST and conventional casting materials.* Prosthetics and Orthotics International, 2013. **37**(4): p. 336-339.

258. Hirsimäki, J., N. Lindfors, et al., *Novel ankle cast designs with non-toxic material.* Foot Ankle Online J., 2014. **7**: p. 1-5.

259. Halanski, M.A., *How to avoid cast saw complications.* Journal of Pediatric Orthopaedics, 2016. **36**: p. S1-S5.

260. Sadruddin, N., M.A. Chinoy, et al., *Soak the cast off.* J Coll Physicians Surg Pak, 2007. **17**(6): p. 380-1.

261. Bakody, E., *Orthopaedic plaster casting: nurse and patient education.* Nursing Standard (through 2013), 2009. **23**(51): p. 49.

262. Hui, C., E. Joughin, et al., *Comparison of cast materials for the treatment of congenital idiopathic clubfoot using the Ponseti method: a prospective randomized controlled trial.* Canadian Journal of Surgery, 2014. **57**(4): p. 247.

263. Davids, J.R., S.L. Frick, et al., *Skin surface pressure beneath an above-the-knee cast: plaster casts compared with fiberglass casts.* JBJS, 1997. **79**(4): p. 565-9.

264. NC, L., *A novel nontoxic wood-plastic composite cast.* The Open Medical Devices Journal, 2012. **4**(1).

265. Smith, G.D., R.G. Hart, et al., *Fiberglass cast application.* The American journal of emergency medicine, 2005. **23**(3): p. 347-350.

266. Wytch, R., C. Mitchell, et al., *Mechanical assessment of polyurethane impregnated fibreglass bandages for splinting.* Prosthetics and Orthotics International, 1987. **11**(3): p. 128-134.

267. Davie , B. and B. Dooley, *New fibreglass casting system in orthopaedic practice.* Medical Journal of Australia, 1976. **1**(26): p. 1010-1012.

268. Bitar, K., M. Ferdhany, et al., *Physical and clinical evaluation of hip spica cast applied with three-slab technique using fibreglass material.* Malaysian orthopaedic journal, 2016. **10**(3): p. 17.

269. Wilson, D.G., *An evaluation of fiberglass cast application techniques.* Veterinary Surgery, 1995. **24**(2): p. 118-121.

270. Conroy, S.M., D. Ward, et al., *Laboratory investigation into optimal temperature for plaster of Paris application.* Emergency Medicine Australasia, 2007. **19**(4): p. 320-324.

271. Williamson, C. and J.R. Scholtz, *Time-temperature relationships in thermal blister formation.* Journal of Investigative Dermatology, 1949. **12**(1): p. 41-47.

272. Pechar, J. and M.M. Lyons, *Acute compartment syndrome of the lower leg: a review.* The Journal for Nurse Practitioners, 2016. **12**(4): p. 265-270.

273. Harrison, D.A., G. D'Amico, et al., *The Pancreatitis Outcome Prediction (POP) Score: a new prognostic index for patients with severe acute pancreatitis.* Critical care medicine, 2007. **35**(7): p. 1703-1708.

274. Baller, L.S. and D.A. Hendrickson, *Management of equine orthopedic pain.* Veterinary Clinics: Equine Practice, 2002. **18**(1): p. 117-131.

275. Whiteing, N.L., *Fractures: pathophysiology, treatment and nursing care.* Nursing Standard (through 2013), 2008. **23**(2): p. 49.

276.   Chadburn, L., *Cast care.* Practices in Children's Nursing E-Book, 2010: p. 200.

277.   Rezaei, R., *The Easy Wrap Orthopedic Cast.* 2017: Rochester Institute of Technology.

278.   Welch-Phillips, A., D. Gibbons, et al., *What is finite element analysis?* Clinical Spine Surgery, 2020. **33**(8): p. 323-324.

279.   Westbrook, K.K., P.H. Kao, et al., *A 3D finite deformation constitutive model for amorphous shape memory polymers: a multi-branch modeling approach for nonequilibrium relaxation processes.* Mechanics of Materials, 2011. **43**(12): p. 853-869.

280.   Yu, K., A.J. McClung, et al., *A thermomechanical constitutive model for an epoxy based shape memory polymer and its parameter identifications.* Mechanics of Time-Dependent Materials, 2014. **18**: p. 453-474.

281.   Mailen, R.W., Y. Liu, et al., *Modelling of shape memory polymer sheets that self-fold in response to localized heating.* Soft Matter, 2015. **11**(39): p. 7827-7834.

282.   Eladak, S., T. Grisin, et al., *A new chapter in the bisphenol A story: bisphenol S and bisphenol F are not safe alternatives to this compound.* Fertility and sterility, 2015. **103**(1): p. 11-21.

283.   Shahi, K., R. Boomurugan, et al. *Cold programming of epoxy-based shape memory polymer.* in *Structures.* 2021. Elsevier.

284.   Xie, T. and I.A. Rousseau, *Facile tailoring of thermal transition temperatures of epoxy shape memory polymers.* Polymer, 2009. **50**(8): p. 1852-1856.

285.   Chen, J., L. Fang, et al., *Self-healing epoxy coatings curing with varied ratios of diamine and monoamine triggered via near-infrared light.* Progress in Organic Coatings, 2016. **101**: p. 543-552.

286.   Fang, L., J. Chen, et al., *Self-healing epoxy coatings via focused sunlight based on photothermal effect.* Macromolecular Materials and Engineering, 2017. **302**(9): p. 1700059.

287.   Fan, M., H. Yu, et al., *Thermomechanical and shape-memory properties of epoxy-based shape-memory polymer using diglycidyl ether of ethoxylated bisphenol-A.* Smart materials and structures, 2013. **22**(5): p. 055034.

288.   Vyazovkin, S., *Kissinger method in kinetics of materials: Things to beware and be aware of.* Molecules, 2020. **25**(12): p. 2813.

289. González, M.G., J.C. Cabanelas, et al., *Applications of FTIR on epoxy resins-identification, monitoring the curing process, phase separation and water uptake.* Infrared Spectroscopy-Materials Science, Engineering and Technology, 2012. **2**: p. 261-284.

290. Herath, M., J. Epaarachchi, et al., *Light activated shape memory polymers and composites: A review.* European Polymer Journal, 2020. **136**: p. 109912.

291. Herath, M., J. Epaarachchi, et al., *Remote actuation of light activated shape memory polymers via D-shaped optical fibres.* Smart Materials and Structures, 2020. **29**(4): p. 047001.

292. Said, M.S.M., J.A. Ghani, et al. *Comparison between Taguchi method and response surface methodology (RSM) in optimizing machining condition.* in *Proceeding of 1st International Conference on Robust Quality Engineering.* 2013.

293. Kıvak, T., *Optimization of surface roughness and flank wear using the Taguchi method in milling of Hadfield steel with PVD and CVD coated inserts.* Measurement, 2014. **50**: p. 19-28.

294. Achuthamenon Sylajakumari, P., R. Ramakrishnasamy, et al., *Taguchi grey relational analysis for multi-response optimization of wear in co-continuous composite.* Materials, 2018. **11**(9): p. 1743.

295. Li, A., A. Challapalli, et al., *4D printing of recyclable lightweight architectures using high recovery stress shape memory polymer.* Scientific reports, 2019. **9**(1): p. 1-13.

296. Li, Z. and C. Wang, *Effects of working parameters on electrospinning,* in *One-dimensional nanostructures.* 2013, Springer. p. 15-28.

297. Chrissafis, K., G. Antoniadis, et al., *Comparative study of the effect of different nanoparticles on the mechanical properties and thermal degradation mechanism of in situ prepared poly (ε-caprolactone) nanocomposites.* Composites science and technology, 2007. **67**(10): p. 2165-2174.

298. Sprenger, S., *Improving mechanical properties of fiber-reinforced composites based on epoxy resins containing industrial surface-modified silica nanoparticles: review and outlook.* Journal of composite materials, 2015. **49**(1): p. 53-63.

299. Zare, Y. and K.Y. Rhee, *The mechanical behavior of CNT reinforced nanocomposites assuming imperfect interfacial bonding between matrix and nanoparticles and percolation of interphase regions.* Composites Science and Technology, 2017. **144**: p. 18-25.

300. Chellvarajoo, S., M. Abdullah, et al., *Effects of Fe2NiO4 nanoparticles addition into lead free Sn–3.0 Ag–0.5 Cu solder pastes on microstructure and mechanical properties after reflow soldering process.* Materials & Design, 2015. **67**: p. 197-208.

301. Cacciotti, I., E. Fortunati, et al., *Effect of silver nanoparticles and cellulose nanocrystals on electrospun poly (lactic) acid mats: Morphology, thermal properties and mechanical behavior.* Carbohydrate polymers, 2014. **103**: p. 22-31.

302. Wichmann, M.H., J. Sumfleth, et al., *Glass-fibre-reinforced composites with enhanced mechanical and electrical properties–benefits and limitations of a nanoparticle modified matrix.* Engineering fracture mechanics, 2006. **73**(16): p. 2346-2359.

303. Lee, C.H., A. Khalina, et al., *Importance of interfacial adhesion condition on characterization of plant-fiber-reinforced polymer composites: A review.* Polymers, 2021. **13**(3): p. 438.

304. Hearle, J.W., *High-performance fibres.* 2001: Elsevier.

305. Kobets, L. and I. Deev, *Carbon fibres: structure and mechanical properties.* Composites science and technology, 1998. **57**(12): p. 1571-1580.

306. Jones, F., *Glass fibres.* 2001: Woodhead Publishing Limited and CRC Press LLC.

307. Aspell, C., *Polymer science VR Gowariker, NV Viswanathan and Jayadev Sreedhar, Halsted Press (John Wiley & Sons), New York, 1986. pp. xv+ 505, price£ 38.50. ISBN 0-470-20322-6.* 1988, Wiley Online Library.

308. Keddie, J.L., R.A. Jones, et al., *Size-dependent depression of the glass transition temperature in polymer films.* EPL (Europhysics Letters), 1994. **27**(1): p. 59.

309. Rimdusit, S., M. Lohwerathama, et al., *Shape memory polymers from benzoxazine-modified epoxy.* Smart materials and structures, 2013. **22**(7): p. 075033.

310. D'Elia, E., H.S. Ahmed, et al., *Electrically-responsive graphene-based shape-memory composites.* Applied Materials Today, 2019. **15**: p. 185-191.

311. Artemenko, S., *Polymer composite materials made from carbon, basalt, and glass fibres. Structure and properties.* Fibre Chemistry, 2003. **35**(3): p. 226-229.

312. Rout, S., R.K. Nayak, et al., *Development of improved flexural and impact performance of kevlar/carbon/glass fibers reinforced polymer hybrid composites.* Journal of Composites Science, 2022. **6**(9): p. 245.

313. Yang, K., S. Wu, et al., *Enhancing the mechanical toughness of epoxy-resin composites using natural silk reinforcements.* Scientific reports, 2017. **7**(1): p. 11939.

314. Yang, K., S. Wu, et al., *Enhancing the mechanical toughness of epoxy-resin composites using natural silk reinforcements.* Scientific reports, 2017. **7**(1): p. 1-9.

315. Suzuki, N., O. Ogikubo, et al., *The prognosis for pain, disability, activities of daily living and quality of life after an acute osteoporotic vertebral body fracture: its relation to fracture level, type of fracture and grade of fracture deformation.* European Spine Journal, 2009. **18**(1): p. 77-88.

316. Meng, Q., J. Hu, et al., *Properties of shape memory polyurethane used as a low-temperature thermoplastic biomedical orthotic material: influence of hard segment content.* Journal of Biomaterials Science, Polymer Edition, 2008. **19**(11): p. 1437-1454.

317. Nishikawa, M., K. Wakatsuki, et al., *Effect of fiber arrangement on shape fixity and shape recovery in thermally activated shape memory polymer-based composites.* Composites Part A: Applied Science and Manufacturing, 2012. **43**(1): p. 165-173.

318. Shi, K., D. Zhang, et al., *Optimization of process parameters for surface roughness and microhardness in dry milling of magnesium alloy using Taguchi with grey relational analysis.* The International Journal of Advanced Manufacturing Technology, 2015. **81**(1): p. 645-651.

319. Kumar, R., R. Singh, et al., *Joining of 3D printed dissimilar thermoplastics with friction welding: A case study.* 2020.

320. Akbari, M., P. Asadi, et al., *Artificial neural network and optimization.* Advances in friction-stir welding and processing, 2014: p. 543-599.

321. Malek, A., S. Ebrahimnejad, et al., *An improved hybrid grey relational analysis approach for green resilient supply chain network assessment.* Sustainability, 2017. **9**(8): p. 1433.

322. Daniel, S.A.A., R. Pugazhenthi, et al., *Multi objective prediction and optimization of control parameters in the milling of aluminium hybrid metal matrix composites*

using ANN and Taguchi-grey relational analysis. Defence Technology, 2019. **15**(4): p. 545-556.

323. Khan, I., K. Saeed, et al., *Nanoparticles: Properties, applications and toxicities.* Arabian journal of chemistry, 2019. **12**(7): p. 908-931.

324. Al-Kayiem, H.H., S.C. Lin, et al., *Review on nanomaterials for thermal energy storage technologies.* Nanoscience & Nanotechnology-Asia, 2013. **3**(1): p. 60-71.

325. Díez-Pascual, A.M., *Surface Engineering of Nanomaterials with Polymers, Biomolecules, and Small Ligands for Nanomedicine.* Materials, 2022. **15**(9): p. 3251.

326. Verma, A. and M. Yadav, *Application of nanomaterials in architecture–An overview.* Materials Today: Proceedings, 2021. **43**: p. 2921-2925.

327. Mogal, S.I., M. Mishra, et al. *Metal doped titanium dioxide: synthesis and effect of metal ions on physico-chemical and photocatalytic properties.* in *Materials Science Forum.* 2013. Trans Tech Publ.

328. Tayade, R.J. and D. Key. *Synthesis and characterization of titanium dioxide nanotubes for photocatalytic degradation of aqueous nitrobenzene in the presence of sunlight.* in *Materials science forum.* 2010. Trans Tech Publ.

329. Tayade, R.J., *Photocatalytic Materials & Surfaces for Environmental Cleanup-II.* 2012: Trans Tech Publications Ltd.

330. Liu, Y., K. Gall, et al., *Thermomechanics of shape memory polymer nanocomposites.* Mechanics of Materials, 2004. **36**(10): p. 929-940.

331. Hashtjin, A.M. and S. Abbasi, *Optimization of ultrasonic emulsification conditions for the production of orange peel essential oil nanoemulsions.* Journal of food science and technology, 2015. **52**(5): p. 2679-2689.

332. Yang, C. and S.-W. Hung, *Optimising the thermoforming process of polymeric foams: an approach by using the Taguchi method and the utility concept.* The International Journal of Advanced Manufacturing Technology, 2004. **24**: p. 353-360.

333. Vankanti, V.K. and V. Ganta, *Optimization of process parameters in drilling of GFRP composite using Taguchi method.* Journal of Materials Research and Technology, 2014. **3**(1): p. 35-41.

334.   Emmanuel, K., L. Jeewantha, et al., *Damage onset analysis of optimized shape memory polymer composites during programming into curved shapes.* Materialia, 2022. **26**: p. 101599.

335.   Ajibade, O., J. Agunsoye, et al., *Optimisation of water absorption parameters of dual-filler filled composites using Taguchi and moderated Taguchi techniques.* Kufa Journal of Engineering, 2019. **10**(2): p. 134-151.

336.   Eslami, S., M. De Figueiredo, et al., *Parameter optimisation of friction stir welded dissimilar polymers joints.* The International Journal of Advanced Manufacturing Technology, 2018. **94**: p. 1759-1770.

337.   Palanikumar, K., *Experimental investigation and optimisation in drilling of GFRP composites.* Measurement, 2011. **44**(10): p. 2138-2148.

338.   Mather, P.T., X. Luo, et al., *Shape memory polymer research.* Annual Review of Materials Research, 2009. **39**: p. 445-471.

339.   Liu, Y., K. Gall, et al., *Thermomechanics of shape memory polymers: uniaxial experiments and constitutive modeling.* International Journal of Plasticity, 2006. **22**(2): p. 279-313.

340.   Rajabi, K. and S. Hosseini-Hashemi, *On the application of viscoelastic orthotropic double-nanoplates systems as nanoscale mass-sensors via the generalized Hooke's law for viscoelastic materials and Eringen's nonlocal elasticity theory.* Composite Structures, 2017. **180**: p. 105-115.

341.   Rao, K.V., G. Ananthapadmanabha, et al., *Effect of cross-linking density on creep and recovery behavior in epoxy-based shape memory polymers (SMEPs) for structural applications.* Journal of Materials Engineering and Performance, 2016. **25**(12): p. 5314-5322.

342.   Yu, K., T. Xie, et al., *Mechanisms of multi-shape memory effects and associated energy release in shape memory polymers.* Soft Matter, 2012. **8**(20): p. 5687-5695.

343.   Chen, J., L. Liu, et al., *Thermoviscoelastic shape memory behavior for epoxy-shape memory polymer.* Smart Materials and Structures, 2014. **23**(5): p. 055025.

344.   Lin, C.-Y., *Alternative form of standard linear solid model for characterizing stress relaxation and creep: Including a novel parameter for quantifying the ratio of fluids to solids of a viscoelastic solid.* Frontiers in materials, 2020. **7**: p. 11.

345. Sethuraman, V., K. Makornkaewkeyoon, et al., *Influence of scaffold forming techniques on stress relaxation behavior of polycaprolactone scaffolds.* Journal of Applied Polymer Science, 2013. **130**(6): p. 4237-4244.

346. Feng, Z., D. Seya, et al., *Viscoelastic characteristics of contracted collagen gels populated with rat fibroblasts or cardiomyocytes.* Journal of Artificial Organs, 2010. **13**(3): p. 139-144.

347. Findley, W.N. and K. Onaran, *Incompressible and linearly compressible viscoelastic creep and relaxation.* 1974.

348. Jalocha, D., A. Constantinescu, et al., *Revisiting the identification of generalized Maxwell models from experimental results.* International Journal of Solids and Structures, 2015. **67**: p. 169-181.

349. Ferry, J.D., *Viscoelastic properties of polymers.* 1980: John Wiley & Sons.

350. Diani, J., P. Gilormini, et al., *Predicting thermal shape memory of crosslinked polymer networks from linear viscoelasticity.* International Journal of Solids and Structures, 2012. **49**(5): p. 793-799.

351. Shrotriya, P. and N.R. Sottos, *Creep and relaxation behavior of woven glass/epoxy substrates for multilayer circuit board applications.* Polymer composites, 1998. **19**(5): p. 567-578.

352. Yu, K., A.J. McClung, et al., *A thermomechanical constitutive model for an epoxy based shape memory polymer and its parameter identifications.* Mechanics of Time-Dependent Materials, 2014. **18**(2): p. 453-474.

353. Marson, B.M. and M. Keenan, *Skin surface pressures under short leg casts.* Journal of orthopaedic trauma, 1993. **7**(3): p. 275-278.

354. Berman, A.L., *Cathy.* Suicide and Life-Threatening Behavior, 1990. **20**(1): p. 85-92.

APPENDIX A

Table A01: 2E SMP mechanical properties summary

Parameter		2E
Tensile strength		40.51
Tensile modulus	MPa	2600
Compression strength		43.60
Compression modulus		708.2
Flexural load	N	77.23
Flexural strength	MPa	78.86
Flexural modulus		2395
Impact load	kN	0.252
Impact resistance	J/mm	0.048

Note: Test methods are comprehensively discussed and compared in Chapter 4.4

APPENDIX B

Table B01: FRSMPC Taguchi L_{18} design of experiments

Sample name	Fibre type	Layers	Thickness (mm)
1C-2.0	Carbon	1	2.0
1C-2.5	Carbon	1	2.5
1C-3.0	Carbon	1	3.0
2C-2.0	Carbon	2	2.0
2C-2.5	Carbon	2	2.5
2C-3.0	Carbon	2	3.0
3C-2.0	Carbon	3	2.0
3C-2.5	Carbon	3	2.5
3C-3.0	Carbon	3	3.0
1G-2.0	E-glass	1	2.0
1G-2.5	E-glass	1	2.5
1G-3.0	E-glass	1	3.0
2G-2.0	E-glass	2	2.0
2G-2.5	E-glass	2	2.5
2G-3.0	E-glass	2	3.0
3G-2.0	E-glass	3	2.0
3G-2.5	E-glass	3	2.5
3G-3.0	E-glass	3	3.0

APPENDIX C

Table C01: FRSMPC viscoelastic summary

Sample name	Transition temperature, (ºC)				Viscoelastic behaviour		
	Storage onset	Min. storge of	Loss modulus	Tan δ peak	Storage	Peak of loss	Tan δ peak
1C-2.0 [92.9†]	37.38 ± 0.08	44.83 ± 0.26	44.63 ± 0.13	52.27 ± 0.46	4.366 ± 0.42	0.431 ± 0.08	0.820 ± 0.02
1C-2.5 [96.5†]	38.66 ± 0.10	46.30 ± 0.38	46.11 ± 0.41	54.65 ± 0.09	3.861 ± 0.25	0.353 ± 0.01	1.038 ± 0.02
1C-3.0 [97.2†]	38.90 ± 0.09	48.22 ± 0.32	49.02 ± 0.10	58.04 ± 0.38	2.617 ± 0.17	0.231 ± 0.01	0.905 ± 0.07
2C-2.0 [83.2†]	40.20 ± 0.20	49.26 ± 0.23	50.13 ± 0.27	54.06 ± 0.15	5.664 ± 0.02	0.658 ± 0.18	0.848 ± 0.05
2C-2.5 [89.9†]	40.00 ± 0.40	48.12 ± 0.24	48.78 ± 0.23	55.94 ± 0.16	5.124 ± 0.29	0.696 ± 0.03	1.065 ± 0.00
2C-3.0 [91.9†]	41.74 ± 0.20	50.35 ± 0.17	49.25 ± 0.47	58.57 ± 0.37	4.718 ± 0.38	0.738 ± 0.02	0.995 ± 0.01
3C-2.0 [79.2†]	40.43 ± 0.22	49.99 ± 0.46	50.97 ± 0.13	55.86 ± 0.11	6.200 ± 0.43	1.272 ± 0.11	1.015 ± 0.00
3C-2.5 [82.1†]	41.00 ± 0.29	51.37 ± 0.33	51.66 ± 0.25	56.78 ± 0.29	5.334 ± 0.40	0.630 ± 0.13	1.189 ± 0.03
3C-3.0 [86.7†]	43.13 ± 0.18	50.59 ± 0.46	51.89 ± 0.02	58.55 ± 0.44	4.820 ± 0.43	0.813 ± 0.06	0.952 ± 0.05
1G-2.0 [89.1†]	39.47 ± 0.07	45.40 ± 0.42	46.38 ± 0.44	54.07 ± 0.01	3.912 ± 0.01	0.394 ± 0.00	0.711 ± 0.00
1G-2.5 [90.4†]	37.12 ± 0.24	45.04 ± 0.45	46.03 ± 0.05	55.95 ± 0.43	3.190 ± 0.07	0.301 ± 0.01	0.713 ± 0.05
1G-3.0 [91.5†]	43.22 ± 0.27	49.69 ± 0.43	49.29 ± 0.08	60.24 ± 0.27	2.928 ± 0.10	0.300 ± 0.49	0.725 ± 0.04
2G-2.0 [78.7†]	39.70 ± 0.41	49.41 ± 0.49	50.03 ± 0.40	54.92 ± 0.37	5.940 ± 0.48	0.682 ± 0.14	0.745 ± 0.24
2G-2.5 [83.6†]	38.37 ± 0.21	45.37 ± 0.48	49.22 ± 0.48	57.30 ± 0.20	4.085 ± 0.29	0.336 ± 0.03	0.834 ± 0.01
2G-3.0 [84.6†]	41.32 ± 0.35	52.77 ± 0.39	53.11 ± 0.04	58.88 ± 0.31	3.340 ± 0.47	0.305 ± 0.08	0.971 ± 0.00
3G-2.0 [74.9†]	41.02 ± 0.45	49.42 ± 0.07	50.24 ± 0.18	55.20 ± 0.42	6.146 ± 0.34	0.746 ± 0.08	0.885 ± 0.00
3G-2.5 [76.2†]	41.44 ± 0.38	51.49 ± 0.42	52.47 ± 0.33	57.50 ± 0.10	4.150 ± 0.07	0.449 ± 0.02	0.901 ± 0.09
3G-3.0 [79.3†]	43.89 ± 0.39	53.15 ± 0.31	53.46 ± 0.43	58.85 ± 0.42	3.861 ± 0.30	0.521 ± 0.06	0.944 ± 0.02
Average	40.39 ± 1.92	48.93 ± 2.63	49.59 ± 2.53	56.54 ± 2.12	4.459 ± 1.106	0.548 ± .0259	0.903 ± 0.133

Table C02: FRSMPC mechanical properties summary

Sample name	Tensile properties, (MPa)		Compression properties, (MPa)		Flexural properties, (MPa)		Impact strength, J/mm
	Strength	Modulus	Strength	Modulus	Strength	Modulus	
1C-2.0 [92.9ᶲ]	119	8315	71	**567↓**	172	4339	**0.023↓**
1C-2.5 [96.5ᶲ]	95	6517	73	667	158	4814	0.046
1C-3.0 [97.2ᶲ]	91	6867	75	826	162	5089	0.050
2C-2.0 [83.2ᶲ]	168	12662	97	1333	271	6086	0.040
2C-2.5 [89.9ᶲ]	145	9974	100	1422	266	8442	0.062
2C-3.0 [91.9ᶲ]	132	9597	107	1565	231	7601	0.074
3C-2.0 [79.2ᶲ]	**280†**	**20868†**	112	1900	**341†**	**11563†**	0.068
3C-2.5 [82.1ᶲ]	206	15298	119	**2029†**	282	9800	0.071
3C-3.0 [86.7ᶲ]	180	12499	**128†**	2030	254	8773	0.085
1G-2.0 [89.1ᶲ]	**81↓**	**4470↓**	59	928	164	**4184↓**	0.081
1G-2.5 [90.4ᶲ]	86	4585	**53↓**	905	157	4523	0.096
1G-3.0 [91.5ᶲ]	97	4828	67	953	**148↓**	5269	0.084
2G-2.0 [78.7ᶲ]	137	7452	72	1103	238	6450	0.127
2G-2.5 [83.6ᶲ]	140	6248	84	1293	215	7847	0.173
2G-3.0 [84.6ᶲ]	141	6487	91	1223	221	7181	0.141
3G-2.0 [74.9ᶲ]	195	11023	92	1255	257	10313	0.180
3G-2.5 [76.2ᶲ]	177	8634	92	1594	247	8397	0.222
3G-3.0 [79.3ᶲ]	161	8262	98	1343	242	8932	**0.270†**

ᶲ SMP weight fraction, † Maximum, ↓ Minimum